

**DOCTORAL THESIS**

Development of  
Semi-Transparent  $\text{Sb}_2\text{S}_3$   
Solar Cells with Fluorene-based  
Compounds as Hole Transport  
Materials

Nimish Juneja

TALLINN UNIVERSITY OF TECHNOLOGY  
DOCTORAL THESIS  
68/2024

# **Development of Semi-Transparent $\text{Sb}_2\text{S}_3$ Solar Cells with Fluorene-based Compounds as Hole Transport Materials**

NIMISH JUNEJA



TALLINN UNIVERSITY OF TECHNOLOGY  
School of Engineering  
Department of Materials and Environmental Technology

This dissertation was accepted for the defence of the degree 07/11/2024

**Supervisor:** Prof. Dr. Malle Krunks  
School of Engineering  
Tallinn University of Technology  
Tallinn, Estonia

**Co-supervisor:** Prof. Dr. Nicolae Spalatu  
School of Engineering  
Tallinn University of Technology  
Tallinn, Estonia

**Opponents:** Prof. Dr. Elisa Artegiani  
Laboratory for Photovoltaics and Solid State Physics  
University of Verona  
Verona, Italy

Prof. Dr. Sven Lange  
Institute of Physics  
Tartu University  
Tartu, Estonia

**Defence of the thesis:** 17/12/2024, Tallinn

**Declaration:**

Hereby I declare that this doctoral thesis, my original investigation and achievement, submitted for the doctoral degree at Tallinn University of Technology has not been submitted for doctoral or equivalent academic degree.

Nimish Juneja



-----  
signature

Copyright: Nimish Juneja, 2024  
ISSN 2585-6898 (publication)  
ISBN 978-9916-80-227-4 (publication)  
ISSN 2585-6901 (PDF)  
ISBN 978-9916-80-228-1 (PDF)  
DOI <https://doi.org/10.23658/taltech.68/2024>  
Printed by EVG Print

Juneja, N. (2024). *Development of Semi-Transparent Sb<sub>2</sub>S<sub>3</sub> Solar Cells with Fluorene-based Compounds as Hole Transport Materials* [TalTech Press]. <https://doi.org/10.23658/taltech.68/2024>

TALLINN UNIVERSITY OF TECHNOLOGY  
DOCTORAL THESIS  
68/2024

**Polläbipaistvate  $Sb_2S_3$  päikesepatareide  
arendus: fluoreenipõhised ühendid aukude  
transportkihi materjalina**

NIMISH JUNEJA





# Contents

List of Publications .....	7
Author's Contribution to the Publications .....	8
Introduction .....	9
Abbreviations, Terms, and Symbols.....	12
1 Literature Overview .....	14
1.1 Evolution of PV technologies.....	14
1.1.1 Established PV technologies dominating the market .....	14
1.1.2 Established thin film PV technologies.....	15
1.2 Emerging thin film PV technologies.....	16
1.3 Antimony sulfide based thin film PV technology.....	18
1.3.1 Properties of antimony sulfide .....	18
1.3.2 Sb <sub>2</sub> S <sub>3</sub> solar cells: architecture and device configurations .....	19
1.3.3 Methods for Sb <sub>2</sub> S <sub>3</sub> thin film preparation .....	20
1.3.4 Successfully implemented deposition routes and state of the art in Sb <sub>2</sub> S <sub>3</sub> solar cells development.....	23
1.3.5 Strategies for optimization of solution processed Sb <sub>2</sub> S <sub>3</sub> material and device.....	26
1.4 Selective contacts for Sb <sub>2</sub> S <sub>3</sub> solar cells .....	27
1.4.1 Electron transport layer .....	27
1.4.2 Hole transport layer .....	28
1.4.3 Challenges with conventional HTMs in developing semi-transparent solar cells.....	31
1.5 Summary of the literature review and the aim of the thesis .....	32
2 Experimental .....	35
2.1 Preparation of Sb <sub>2</sub> S <sub>3</sub> thin films solar cells.....	35
2.2 Characterization of solar cell component layers and solar cell device.....	36
3 Results and Discussions.....	38
3.1 Properties of ultrasonically sprayed Sb <sub>2</sub> S <sub>3</sub> absorber film .....	38
3.2 Development of technology for deposition of HTM thin films.....	39
3.3 Solar cells with fluorene-based HTMs with aliphatic chains (V1275, V1235, V1236, V1461) .....	41
3.4 Solar cells with fluorene-based HTMs with thiophene end units (V808, V1385 and V1386) .....	46
3.5 Solar cells with fluorene-based HTMs with dimers linked with thiophene units (V1422, V1423, V1454, V1455) .....	50
Conclusion.....	57
References .....	60
Acknowledgements.....	71
Abstract.....	72

Lühikokkuvõte.....	75
Appendix 1 .....	77
Appendix 2 .....	129
Curriculum vitae.....	133
Elulookirjeldus.....	135

## List of Publications

The list of the author's publications based on which the thesis has been written:

- I. **Nimish Juneja**, Sreekanth Mandati, Atanas Katerski, Nicolae Spalatu, Šarūnė Daškevičiūtė-Gegužienė, Aivars Vembris, Smagul Karazhanov, Vytautas Getautis, Malle Krunk, and Ilona Oja Açıık, "Sb<sub>2</sub>S<sub>3</sub> solar cells with a cost-effective and dopant-free fluorene-based enamine as a hole transport material", *Sustainable Energy and Fuels* 6, 13, 3220–29, 2022, doi: 10.1039/d2se00356b.
- II. Sreekanth Mandati, **Nimish Juneja**, Atanas Katerski, Aisté Jegorovė, Raitis Gržibovskis, Aivars Vembris, Tatjana Dedova, Nicolae Spalatu, Artiom Magomedov, Smagul Karazhanov, Vytautas Getautis, Malle Krunk, and Ilona Oja Açıık, "4.9 % efficient Sb<sub>2</sub>S<sub>3</sub> solar cells from semitransparent absorbers with fluorene-based thiophene-terminated hole conductors", *ACS Applied Energy Materials*, 6, 3822–33, 2023, doi: 10.1021/acsaem.2c04097.
- III. **Nimish Juneja**, Šarūnė Daškevičiūtė-Gegužienė, Nicolae Spalatu, Sreekanth Mandati, Atanas Katerski, Raitis Gržibovskis, Aivars Vembris, Smagul Karazhanov, Vytautas Getautis, Malle Krunk, and Ilona Oja Açıık, "Employment of dopant-free fluorene-based enamines as innovative hole transport materials to boost the transparency and performance of Sb<sub>2</sub>S<sub>3</sub> based solar cells", *Materials Science in Semiconductor Processing*, 169, 107934, 2024, doi: 10.1016/j.mssp.2023.107934.
- IV. **Nimish Juneja**, Aisté Jegorovė, Raitis Grzibovskis, Atanas Katerski, Maryte Daskeviciene, Tadas Malinauskas, Aivars Vembris, Smagul Karazhanov, Nicolae Spalatu, Vytautas Getautis, Malle Krunk and Ilona Oja Açıık, "Dopant-free fluorene based dimers linked with thiophene units as prospective hole transport materials for Sb<sub>2</sub>S<sub>3</sub> solar cells", *Sustainable Energy and Fuels*, 8, 4324–4334, 2024, doi: 10.1039/D4SE00472H.

## Author's Contribution to the Publications

- I. Deposition of  $\text{TiO}_2$  and  $\text{Sb}_2\text{S}_3$  thin films by Ultrasonic Spray Pyrolysis (USP). Characterization of structural, vibrational, optical properties of glass/FTO/ $\text{TiO}_2$ / $\text{Sb}_2\text{S}_3$  stacks by X-ray diffraction (XRD), Raman spectroscopy, and ultraviolet-visible spectroscopy (UV-VIS). Deposition of novel Hole Transport Materials (HTMs) onto the glass/FTO/ $\text{TiO}_2$ / $\text{Sb}_2\text{S}_3$  stack. Characterization of solar cells using current-voltage (J-V), external quantum efficiency (EQE) and ultraviolet-visible spectroscopy (UV-VIS); visualization; major role in writing.
- II. Deposition of  $\text{TiO}_2$  and  $\text{Sb}_2\text{S}_3$  thin films by USP. Characterization of structural, vibrational and optical properties of glass/FTO/ $\text{TiO}_2$ / $\text{Sb}_2\text{S}_3$  stacks by XRD, Raman spectroscopy, and UV-VIS. Deposition of novel HTMs on the glass/FTO/ $\text{TiO}_2$ / $\text{Sb}_2\text{S}_3$  stack. Characterization of solar cell using J-V, EQE and UV-VIS; data analysis; visualization; minor role in writing.
- III. Deposition of  $\text{TiO}_2$  and  $\text{Sb}_2\text{S}_3$  thin films by USP. Characterization of structural, vibrational and optical properties of glass/FTO/ $\text{TiO}_2$ / $\text{Sb}_2\text{S}_3$  stacks by XRD, Raman spectroscopy, and UV-VIS. Deposition of novel HTMs on the glass/FTO/ $\text{TiO}_2$ / $\text{Sb}_2\text{S}_3$  stack. Characterization of solar cell, data analysis using J-V, EQE and UV-VIS; data analysis; visualization; major role in writing.
- IV. Deposition of  $\text{TiO}_2$  and  $\text{Sb}_2\text{S}_3$  thin films by USP. Characterization of structural, vibrational and optical properties of glass/FTO/ $\text{TiO}_2$ / $\text{Sb}_2\text{S}_3$  stacks by XRD, Raman spectroscopy, and UV-VIS. Deposition of novel HTMs on the glass/FTO/ $\text{TiO}_2$ / $\text{Sb}_2\text{S}_3$  stack. Characterization of solar cell using J-V, EQE and UV-VIS, data analysis; visualization; major role in writing.

## Introduction

The energy crisis is among the major problems of the present day's world with ever increasing need for resources. Fossil fuels being the prime source of energy, besides their limited availability, seriously contribute to environmental pollution through the emission of pollutant gases like carbon dioxide (CO<sub>2</sub>), sulfur dioxide (SO<sub>2</sub>), nitrogen dioxide (NO<sub>2</sub>), and carbon monoxide (CO) [1,2]. Addressing these issues corresponds to the UN policy on net zero emission by 2050 and several countries' policies on clean energy production; hence, the actual need to develop alternative, clean, and abundant energy source technologies. Solar photovoltaic material is considered one of the most promising technologies due to its superior capability to harness solar energy efficiently and convert it into electricity in an environmentally friendly way [3,4]. Furthermore, building-integrated photovoltaics (BIPVs) are developing technology whereby the integration of solar panels is made into buildings to help them provide part of the energy requirement of the building. Energy-efficient buildings form part of smart city development and relate very well to any strategy aimed at net-zero emissions. Semi-transparent solar cells could be integrated into windows, thereby opening new avenues within the domain of BIPVs. New material development and new device architectures are being pursued to enhance the efficiency and applicability of semi-transparent solar cells, thus contributing to the advancement of BIPV technology.

At this scale, a new photovoltaic technology must not only compete with existing c-Si or CdTe thin film technologies in terms of performance and stability but also be environmentally sustainable and composed of earth abundant elements. A developing category of prospective cost-effective photovoltaic materials, including antimony and bismuth-based chalcogenides [5–7] and lead-free chalcogenide perovskites [8] is presently being explored within the PV community. Antimony chalcogenides, including Sb<sub>2</sub>S<sub>3</sub>, Sb<sub>2</sub>Se<sub>3</sub>, and Sb<sub>2</sub>(S,Se)<sub>3</sub>, have demonstrated a promising trajectory of rapid performance enhancement, achieving power conversion efficiencies (PCE) of 8.0%, 10.57%, and 10.75%, respectively [9–11]. These materials have attracted significant efforts in R&D within the photovoltaic community due to their advantageous properties, including abundance in nature, environmentally friendly elemental components, suitable optoelectronic characteristics and stability [6,12,13]. The distinct characteristics of Sb<sub>2</sub>S<sub>3</sub> absorbers, such as a bandgap of ca. 1.7 eV, a high absorption coefficient of 10<sup>5</sup> cm<sup>-1</sup> at 450 nm, and long-term stability, make them suitable for semi-transparent solar cell devices [4,13–15]. Additionally, these characteristics also qualify them to be integrated into tandem cell device as top cell and for applications such as solar windows.

Addressing the considerable challenges in improving power conversion efficiencies (PCEs) of the solar cell devices, the fabrication method for Sb<sub>2</sub>S<sub>3</sub> absorbers is crucial for scaling up production. While high-efficiency Sb<sub>2</sub>S<sub>3</sub> solar cells have primarily been prepared using spin coating and chemical bath deposition (CBD) techniques, each method presents its own limitations [9,16]. Spin coating, despite offering precise parameter control and reproducibility, is constrained to laboratory-scale production and results in significant material wastage. Conversely, CBD shows promise for large-scale applications but demands extended deposition times at relatively low temperatures to achieve the desired absorber thickness. In contrast, the ultrasonic spray pyrolysis method offers advantages such as large-area uniformity and is an industrially scalable technique with low capex requirements.

A crucial component in the  $\text{Sb}_2\text{S}_3$  cell stack is the hole transporting material (HTM), which is responsible for extracting and transporting photogenerated charge carriers from the absorber layer to the electrode. Additionally, the HTM acts as a barrier against electron leakage and provides protection against oxygen and moisture exposure for the active layer [14,17]. The ideal HTM should possess an abundance of holes, high hole mobility, minimal defect density, excellent stability, and compatibility with adjacent layers [6,17]. Various organic and inorganic HTMs have been tested extensively. The most conventional organic HTMs utilized in  $\text{Sb}_2\text{S}_3$  solar cell fabrication are poly(3-hexylthiophene) (P3HT) [13,14,18], 2,2',7,7'-tetrakis[N,N-di(4-methoxyphenyl)amino]-9,9'-spirobifluorene (Spiro-OMeTAD) [9,16], and poly{4,4-dialkyl-4H-cyclopenta[2,1-b;3,4-b']-dithiophene-2,6-diyl-alt-2,1,3-benzothiadiazole-4,7-diyl} (PCPDTBT) [19,20]. However, these materials come with their own set of drawbacks such as high cost and complex synthesis processes, hindering their scalability for commercial applications. In addition, P3HT, due to its bandgap of 1.8 eV, exhibits parasitic absorption in the visible spectrum, leading to reduced total transmittance of the solar cell [14]. Additionally, P3HT requires post-coating activation at temperatures around 170 °C, further complicating the manufacturing process [13,18]. Spiro-OMeTAD also faces challenges due to its synthesis involving a multi-step reaction scheme conducted at low temperatures (-78 °C) and requires sensitive reagents such as n-butyllithium or Grignard reagents [21,22]. Furthermore, doping Spiro-OMeTAD with Li-based salt to enhance its hole transporting ability increases costs and compromises device stability, given that the dopant, Lithium bis(trifluoromethylsulphonyl)imide (LiTFSI), is hygroscopic in nature [23].

Considering the aforementioned HTM related drawbacks, the aim of this doctoral study is the development of semitransparent  $\text{Sb}_2\text{S}_3$  thin film solar cells employing novel dopant-free fluorene-based enamines as hole transport materials. The novelty of the study is that these new HTMs are used for the first time as alternative charge selective layers in  $\text{Sb}_2\text{S}_3$  thin film devices. In this doctoral thesis, we explored the use of three groups of novel, dopant-free hole transport materials in  $\text{Sb}_2\text{S}_3$ -based PV devices. The first group consists of fluorene-based enamines with aliphatic chains (V1275, V1235, V1236 and V1461). The second group comprised of fluorene-based molecules with thiophene end units, mimicking P3HT (V808, V1385 and V1386). The third group consists of fluorene-based dimers linked with thiophene units (V1422, V1423, V1454 and V1455), drawing inspiration from structure of Spiro-OMeTAD. The thickness of these fluorene-based HTMs were systematically varied and the impact on the  $\text{Sb}_2\text{S}_3$  device performance is investigated. The novel HTMs were synthesized at the Department of Organic Chemistry, Kaunas University of Technology, Lithuania, and characterization of physical and chemical properties of compounds was performed in cooperation with Kaunas University of Technology and Institute of Solid State Physics, University of Latvia. Various characterization methods applied to the materials, interfaces and devices provide insights on the functionality of these new family of dopant-free HTMs for Sb-chalcogenide-based solar cells.

This thesis is based on four published articles and is divided into three main chapters. The first chapter consists of a literature review of the present and emerging solar PV technologies. This is followed by an introduction to the Sb – chalcogenide absorber materials and solar cells, and most widely used organic and inorganic HTMs in  $\text{Sb}_2\text{S}_3$  based solar cells. The second chapter includes the experimental details and characterization methods used. The third chapter summarizes the development of technology for the deposition of HTM films and the results and discussion of the study

based on the three distinct groups of HTMs investigated. The thesis concludes with a summary showcasing the main goals achieved during the study.

The study received financial support from Iceland, Liechtenstein and Norway through the EEA Grants. The aim of the project was to develop new approach based on novel materials and structures and production technologies, which are the key to further increase the share, and range of application of PV in areas with sub-average sunlight, including Baltic and Nordic countries. Therefore, development of resource saving, cost-effective and efficient PV devices is a primary challenge of this project. Project contract with the Research Council of Lithuania (LMTLT) No is S-BMT-21-1(LT08-2-LMT-K-01-003). The research was also supported by Estonian Research Council, projects PRG627 "Antimony chalcogenide thin films for next-generation semi-transparent solar cells applicable in electricity producing windows"; European Union's Horizon 2020 - ERA Chair project 5GSOLAR (grant No. 952509); H2020-WIDESPREAD-01-2016-2017-TeamingPhase2 (grant No. 739508, project CAMART<sup>2</sup>); European Cooperation in Science and Technology (COST) project RENEW-PV (CA21148) and by the Estonian Ministry of Education and Research (project TK210; TK210U8 "Center of Excellence in Sustainable Green Hydrogen and Energy Technologies").

## Abbreviations, Terms, and Symbols

ALD	Atomic layer deposition
AM1.5G	Air mass 1.5 global
a-Si	Amorphous silicon
AVT	Average visible transmittance
BIPV	Building integrated photovoltaics
CBD	Chemical bath deposition
CIGS	$\text{Cu}(\text{In,Ga})(\text{S,Se})_2$
c-Si	Crystalline silicon
CSS	Close spaced sublimation
CZTS	$\text{Cu}_2\text{ZnSn}(\text{S,Se})_4$
DSSC	Dye sensitized solar cells
$E_g$	Band gap
EQE	External quantum efficiency
ETL	Electron transport layer
FF	Fill factor
HOMO	Highest occupied molecular orbital
HTL	Hole transport layer
HTM	Hole transport material
J-V	Current density-voltage
$J_{sc}$	Short circuit current density
LUMO	Lowest unoccupied molecular orbital
NMR	Nuclear magnetic resonance spectroscopy
OSC	Organic solar cell
P3HT	Poly(3-hexylthiophene-2,5-diyl)
PCPDTBT	Poly(2,6-(4,4-bis-(2-ethylhexyl)-4Hcyclopenta[2,1-b;3,4-b']dithiophene)-alt-4,7(2,1,3 benzothiadiazole)
PEDOT:PSS	Poly(3,4-ethylenedioxythiophene) polystyrene sulfonate
PSC	Perovskite solar cell
PV	Photovoltaic
QD	Quantum dot
$R_s$	Series resistance
$R_{sh}$	Shunt resistance
RT	Room temperature
SEM	Scanning electron microscopy
Spiro-OMeTAD	2,2',7,7'-tetrakis-(N,N-di-p-methoxyphenylamine)-9,9'-spirobifluorene
TCO	Transparent conductive oxide
$\theta$	X-ray diffraction incidence angle

TU	Thiourea
USP	Ultrasonic chemical spray pyrolysis
UV-VIS	Ultraviolet-visible light
$V_{oc}$	Open-circuit voltage
XPS	X-ray photoelectron spectroscopy
XRD	X-ray diffraction
PCE	Power conversion efficiency
PYS	Photoelectron Yield Spectroscopy

# 1 Literature overview

Solar photovoltaic (PV) technology is clean way of generating electric power directly from solar radiation. The industry has seen remarkable metamorphosis, and have achieved an annual installation rate of 30–40% in years 2000–2022 [24]. Globally, a combined 239 GW of new capacity was added in the grid. Photovoltaics have reached a total global installed capacity of almost 1.2 TW by the end of the year 2022 [25]. However, despite the tremendous growth of solar power, surpassing that of any other power generation technology, its share in global electricity generation still lies at around 4.5% [25]. Policymakers' awareness of the importance of establishing local renewable power generation capacities for the purpose of energy security and price volatility was significantly elevated by the global energy crisis in 2022, which served as a major inflection point. The surge in solar installations is not merely the result of supportive governmental policies; but it is also supported by a substantial reduction in the levelized cost of electricity of PV power plants, rendering them more economically viable than their counterparts producing electricity using coal and gas [25]. An overview on established and emerging photovoltaic technologies is provided below.

## 1.1 Evolution of PV technologies

### 1.1.1 Established PV technologies dominating the market

#### *Crystalline Si-based PV technologies*

Silicon (Si) based solar cells are considered as the first generation of solar cell technology. These are based on a bulk material p-n junction represented by the silicon PV cells made of mono or polycrystalline wafers [26]. The past few decades have witnessed a persistent enhancement in the efficiency of silicon wafer-based commercial PV modules. The current record device efficiency of Si-based solar cells have reached 27.3% [27]. This efficiency is around 80% of the Shockley-Queisser limit for single junction cells with bandgap value of 1.1 eV [26]. The dominance of crystalline silicon (mono-Si and multi-Si) PV remains unchallenged, commanding a 95% market share [26].

Silicon tandem devices can combine conventional silicon solar cells and additional materials, that are typically perovskites and enhance the overall efficiency. By stacking a perovskite layer on top of a silicon layer, the tandem cells can utilize a broader spectrum of sunlight that can significantly increase the energy conversion efficiency. Recent advancements have led to remarkable efficiency records for perovskite/c-Si two terminal solar cells with reported efficiencies reaching 34.6%, as of today [27].

#### *Gallium arsenide (GaAs)*

III-V compound solar cells, including GaAs, have significant advantages over crystalline Si solar cells due to their high efficiency potential, suitability for thin-film applications, advantageous temperature coefficient, radiation resistance, and potential use in multi-junction configurations [26]. These solar cells have made significant contributions to space and concentrator applications and serve as crucial sub-cells in multi-junction solar cell configurations. Notably, R&D efforts have resulted in record efficiencies, with GaAs achieving 27.8% in single-junction solar cells [28]. GaAs cells can be used in multi-junction configuration with enhanced performance by use of layering. Multiple layers with distinct compositions and bandgaps can be incorporated to absorb light

across specific wavelengths [26]. By optimizing the spectral absorption across various layers, multi-junction solar cells achieve higher efficiencies than conventional single-layer configurations. Recently, triple-junction PV cells have reached efficiency of 37.9% [28].

### **1.1.2 Established thin film PV technologies**

Established thin film PV technologies consists of amorphous silicon (a-Si), cadmium telluride/cadmium sulfide (CdTe/CdS) and copper indium gallium selenide (CIGS). The film's thickness is up to a few micrometres ( $\mu\text{m}$ ). The aim of thin film solar cells was to reduce the amount of material required for solar cell absorber layer compared with wafer based solar cells production and introduce usage of cheaper substrates [26]. The remaining 5% of the market share, aside from Si, is held by thin-film photovoltaics, including CdTe, CIGS, and a-Si solar cells. CdTe holds more than half of the thin-film market, leaving 2 percent to CIGS and amorphous silicon. However, CdTe has challenges attributed to tellurium scarcity [29] and the lingering negative perceptions surrounding cadmium [30].

#### ***Amorphous silicon (a-Si)***

Amorphous Si solar cells, showcase efficiencies from 14.0% with double and triple-junction designs [28]. Despite advancements, operational challenges, notably susceptibility to sunlight-induced degradation remains [31]. Multi-junction devices exhibit better efficiency and moderate stability. Various groups are exploring integration possibilities with nc-Si or a-SiGe alloys for multi-junction cells [60]. Amorphous Si has a high bandgap of 1.7 eV offer a unique advantage in light absorptivity which is 40 times higher than mono-crystalline silicon [31] and holds a share of 2% in the PV market [26].

#### ***Cadmium telluride (CdTe)***

Recognized for its favorable semiconductor properties, CdTe demonstrates strong absorption through the solar spectrum, and a favorable direct bandgap of 1.45 eV [29]. Most important, record efficiencies of 23.0% by First Solar [28], together with continuous improvements in commercial module efficiencies [26], has put CdTe in one of the top places among thin-film solar cells. Besides that, CdTe thin film almost rivals c-Si solar cells in cost/watt terms [26]. Researchers are exploring alternative material systems using abundant and non-toxic elements, in order to address concerns about the toxicity of elemental cadmium and the scarcity of tellurium [29].

#### ***Copper indium gallium di-selenide (CIGS)***

Copper Indium Gallium Di-Selenide (CIGS) stands out as a prominent material in thin-film solar PV cells, characterized by the general formula  $\text{Cu}(\text{In}_x\text{Ga}_{1-x})\text{Se}_2$ . The band gap of CIGS varies in the range of 1.0–1.7 eV, based on the In-Ga ratio [26]. CIGS solar cells have achieved device efficiency of 23.6% [28]. Despite advancements, CIGS technology faces key challenges, including high variability in film stoichiometry, limited understanding of grain boundary effects, structural and electronic inhomogeneity causing low open-circuit voltage, and the need to engineer higher-bandgap alloys for multijunction devices [31]. The scarcity of indium limits widespread deployment of CIGS technologies [29]. The ability to deposit CIGS on metal or polymer substrates aids production of flexible cells [26].

## 1.2 Emerging thin film PV technologies

Emerging PV technologies aim to achieve both high efficiency ( $\geq 20\%$ ) and low cost. These technologies employ thin-layer deposition techniques from the established PV technologies, while exploring new configurations, materials, and novel nanostructured or organic elements [26]. Crucially, the emerging photovoltaics prioritize the use of non-toxic and abundant materials for large-scale implementation [31]. Considerable attention is dedicated to optimizing charge collection, and improving energy capture within the solar spectrum [31].

### ***Dye sensitized solar cells (DSSC)***

Dye-sensitized solar cells (DSSCs) stand out as leading nanotechnology-based materials for solar photovoltaic technologies [32,33]. DSSCs adopt a hybrid organic-inorganic design, featuring a porous, nano-crystalline titanium dioxide ( $\text{TiO}_2$ ) film as the electron conductor. This film is in contact with an electrolyte solution containing organic light-absorbing dyes. Charge transfer occurs at the interface, facilitating the transportation of holes in the electrolyte. The novelty of DSSCs is the photosensitization of nano-grained  $\text{TiO}_2$  coatings, using visible optically active dyes to achieve efficiencies above 10.0% [32,33]. Device efficiencies of approximately 13.0% have been reported in year 2020 [28]. The efforts towards the commercialization of dye-sensitized photovoltaic modules are underway.

### ***Quantum Dot (QD) solar cells***

Quantum dots (QDs) are nano-crystalline structures ranging in size from 2 to 10 nm, resembling porous Si or  $\text{TiO}_2$  [34,35]. Solar cells crafted from these materials are termed Quantum Dot (QD) Solar Cells, also known as Nano-crystal Solar Cells. These structures are epitaxially grown on a substrate crystal, with the quantum dots enclosed by high potential barriers in a three-dimensional configuration. The discrete energy levels of electrons and electron holes within the quantum dot arise from their confinement in a confined space [36]. The energy states of electrons and electron holes in quantum dots are linked to the size of the quantum dot [36]. The epitaxial growth method on a substrate crystal ensures that quantum dots assume a three-dimensional shape which contributes to their unique electronic properties. The record efficiency of QD solar cells have increased from 4% in 2010 to 19.1% in 2023 [28].

### ***Perovskite solar cells (PSC)***

Perovskite solar cell (PSC), with the general crystal structure  $\text{ABX}_3$ , is seen as an alternative for silicon solar-cells. Here, A represents a larger monovalent cation, B is bivalent metal cation and X is a halide anion [37]. The most common A cations are organic or inorganic ions such as methylammonium ( $\text{CH}_3\text{NH}_3^+$ ), cesium ( $\text{Cs}^+$ ), and formamidinium ( $\text{FA}^+$ ). The B sites are metals like lead ( $\text{Pb}^{2+}$ ) or tin ( $\text{Sn}^{2+}$ ). The X anion is usually a halide i.e. chloride ( $\text{Cl}^-$ ), bromide ( $\text{Br}^-$ ), or iodide ( $\text{I}^-$ ). The tunability of the  $\text{ABX}_3$  structure, is based on the choice of A, B, and X components, which allows for adjustable band gaps, making perovskites incredibly versatile in photovoltaic applications [38,39,40]. The extensively studied perovskite solar cell features methylammonium lead trihalide ( $\text{CH}_3\text{NH}_3\text{PbX}_3$ , where X is a halogen ion like  $\text{I}^-$ ,  $\text{Br}^-$ ,  $\text{Cl}^-$ ) with an optical bandgap ranging from 1.6 eV to 2.3 eV, depending on halide type [38]. The structure of the perovskite solar cells consists of an absorber layer in between the electron transport layer (ETL) and hole transport

material (HTM) [38]. The biggest drawback of PSC is their poor environmental stability, caused by the instability of the perovskite layer when in contact with moisture [40].

PSCs have undergone a remarkable efficiency increase from 3.8% in 2009 to 26.7% in 2024 for single-junction architectures [28]. Perovskite/silicon tandem solar cells have further improved toward high efficiency and lately reached a record efficiency of 34.6% [28]. In addition, semi-transparent perovskite solar cells, which recently have been developed for their potential use as solar windows, have demonstrated efficiency of 15.5% along with an AVT of 20.7% [41].

### ***Organic solar cells (OSC)***

Organic solar cells (OSC) represent a transformative technology employing conductive organic polymers or small organic molecules for light absorption and charge transport [37]. The active layer is composed of a blend of donor and acceptor materials. Common materials include conjugated polymers and fullerene derivatives [37]. The intrinsic flexibility of OSCs, typically on a polymer substrate, adds versatility to their applications in areas such as wearable electronics and portable devices. Solution-based processing techniques, such as roll-to-roll printing, reduce costs in the production of large-scale fabrication [37]. The PCE of organic and polymer solar cells are generally lower than that of Si-based or perovskite cells. Current OSC efficiencies stands at 19.2% [28]. Organic cells can be made semi-transparent, making them ideal for applications in building-integrated photovoltaics (BIPV), such as windows and facades [37].

### ***Kesterite solar cells***

Kesterite solar cell, typically based on compound  $\text{Cu}_2\text{ZnSn}(\text{S},\text{Se})_4$  (CZTSSe) has garnered significant attention due to its inherent environmental friendliness and cost-effectiveness. They are seen as a transition from CIGS which has high cost and low material availability [37]. The wide bandgap range of CZTSSe, varying from 1.0 to 1.5 eV through the tuning of the S/Se ratio, enables a theoretical maximum efficiency within the range of 28% to 32%, according to the Shockley-Queisser limit [42]. This tunable bandgap allows good spectral matching for a range of working conditions. Similar to CIGS, kesterite also has a comparable lattice and energy band structure with a high absorption coefficient  $> 10^4 \text{ cm}^{-1}$  and an intrinsic p-type conductivity of  $10^{-2} \text{ S cm}^{-1}$  [37]. Record device efficiency has been successively reached up to 14.9% for CZTSSe solar cells, which was reported in the year 2023 [28].

This improvement in the performances of solar cells comes after a very long period of stagnation while efficiencies were about 12.0% for the years between 2010 to 2022 [28]. Even with the recent efficiency improvements, CZTSSe photovoltaic devices still operate under their theoretical limit and other equivalents like CIGS; hence, the potential for efficiency improvements in kesterite solar cells remains. Doping/alloying, defects regulation, thermal treatment, crystallization pathway intervention, interface passivation, and bandgap manipulation are some of the numerous approaches that have been developed for performance enhancement in kesterite solar cells [42].

### ***Antimony chalcogenide solar cells***

Recent interest in antimony chalcogenides, including antimony sulfide ( $\text{Sb}_2\text{S}_3$ ), antimony selenide ( $\text{Sb}_2\text{Se}_3$ ), and antimony sulfoselenide  $\text{Sb}_2(\text{S}_x\text{Se}_{1-x})_3$ , has surged among PV researchers due to their remarkable stability, abundance of constituent elements, non-toxicity, and high absorption coefficient ( $> 10^4 \text{ cm}^{-1}$ ) [43].  $\text{Sb}_2\text{S}_3$  solar cells are similar

to CdTe and PSC device structure i.e. thin-film configuration with layered architecture comprising of TCO, absorber, and charge transport layers [4]. However, in contrast to the complexity associated with kesterite materials in solar cells, antimony-based chalcogenides present a more straightforward binary phase structure, that facilitates simpler fabrication processes [37]. The isomorphous nature of  $\text{Sb}_2\text{S}_3$  results in an orthorhombic crystal structure with quasi-one-dimensional ribbons. The ribbons facilitate charge carrier transport and contributes to anisotropic properties. Additionally, a tunable bandgap (1.1 to 1.7 eV), makes antimony chalcogenides suitable for various PV applications, including two-cell tandems [44].

Sustained R&D efforts in the past decade have significantly advanced the performance of antimony chalcogenide solar cells. In year 2022,  $\text{Sb}_2\text{S}_3$  based solar cells achieved PCE of 8.0%, and cells utilizing  $\text{Sb}_2\text{Se}_3$  and  $\text{Sb}_2(\text{S,Se})_3$  reached PCEs of 10.57% and 10.75%, respectively [9,10,45]. At the current stage,  $\text{Sb}_2\text{X}_3$  solar cells have achieved the same PCE as CdTe and CIGS solar cells, when they were initially considered for commercialization [46].

### 1.3 Antimony sulfide based thin film PV technology

#### 1.3.1 Properties of antimony sulfide

$\text{Sb}_2\text{S}_3$  exhibits an orthorhombic crystal structure with lattice constants of  $a \approx 11.31 \text{ \AA}$ ,  $b \approx 3.83 \text{ \AA}$ , and  $c \approx 11.22 \text{ \AA}$  [47]. The crystal structure of  $\text{Sb}_2\text{S}_3$  has been shown in Fig. 1.1a. This unit structure that builds the  $\text{Sb}_2\text{S}_3$  crystal consists of infinite 1D  $(\text{Sb}_4\text{S}_6)_n$  ribbons oriented along the [001] direction, which interlinks to form zigzag sheets perpendicular to the [100] plane as shown in Fig. 1.1b. These ribbons are interconnected by weak van der Waals forces [48]. Each chain comprises two trigonal  $\text{Sb}_2\text{S}_3$  and two  $\text{SbS}_5$  square pyramids with slightly varied bond lengths due to distinct coordination conditions [49,50]. Experimental observations reveal that single crystals can be easily cleaved perpendicular to the [100] plane, and the grain orientation has a substantial effect on solar cell performance, with the [hk1] orientation offering better charge carrier mobility and transport [48].

Polycrystalline  $\text{Sb}_2\text{S}_3$  has an optical bandgap ( $E_g$ ) of approximately 1.7 eV [13,18,51] along with a high optical absorption coefficient ranging from  $10^4$ – $10^5 \text{ cm}^{-1}$ , which positions it as an excellent candidate for semi-transparent applications [56]. These attributes contribute to the versatility of  $\text{Sb}_2\text{S}_3$ , facilitating its implementation in various optoelectronic applications such as solar cells, both in single-junction and tandem configurations, as well as in photocatalysis and energy storage systems [4].

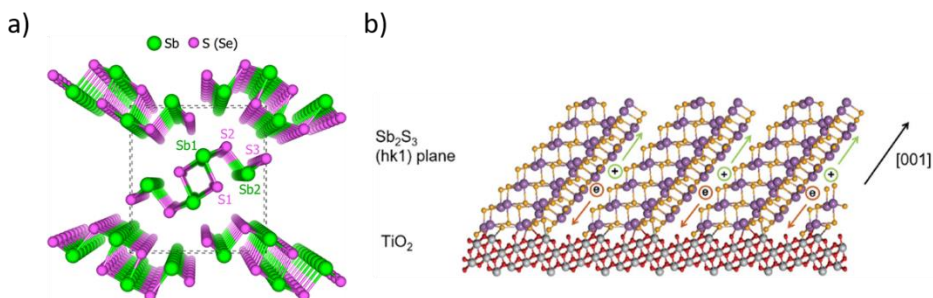


Figure 1.1. (a) Crystal structure of  $\text{Sb}_2\text{S}_3$  [52] and (b) [hk1] orientation  $\text{Sb}_2\text{S}_3$  ribbons deposited on  $\text{TiO}_2$  film [53].

### 1.3.2 Sb<sub>2</sub>S<sub>3</sub> solar cells: architecture and device configurations

Sb<sub>2</sub>S<sub>3</sub>-based solar cells can be broadly categorized into two architecture types – Planar and Mesoporous. Mesoporous Sb<sub>2</sub>S<sub>3</sub>-sensitized solar cells are inspired from the Dye-Sensitized Solar Cells on porous TiO<sub>2</sub> and have achieved noteworthy PCE of 7.5% in year 2014 [54]. On the other hand, the planar architecture is inspired from CdTe and perovskite solar cells and have achieved PCE of 8.0% in year 2022 [9]. Planar have become more popular than mesoporous solar cells because of their lower cost of fabrication and higher V<sub>OC</sub> values [55]. The planar Sb<sub>2</sub>S<sub>3</sub> solar cells can be prepared in both superstrate and substrate configurations as demonstrated in Fig. 1.2. Most of the research work is focused on the superstrate structure due to its simple fabrication process for Sb<sub>2</sub>S<sub>3</sub> absorber layer [56,57]. Only a few studies have explored the substrate structured in development of Sb<sub>2</sub>S<sub>3</sub> thin film devices [58,59]. The highest device efficiency obtained for Sb<sub>2</sub>S<sub>3</sub> solar cells in a superstrate configuration was 8.0% in the year 2022 [9]. In contrast, for the substrate configuration, the efficiency achieved was 1.75%, reported in the year 2019 [58].

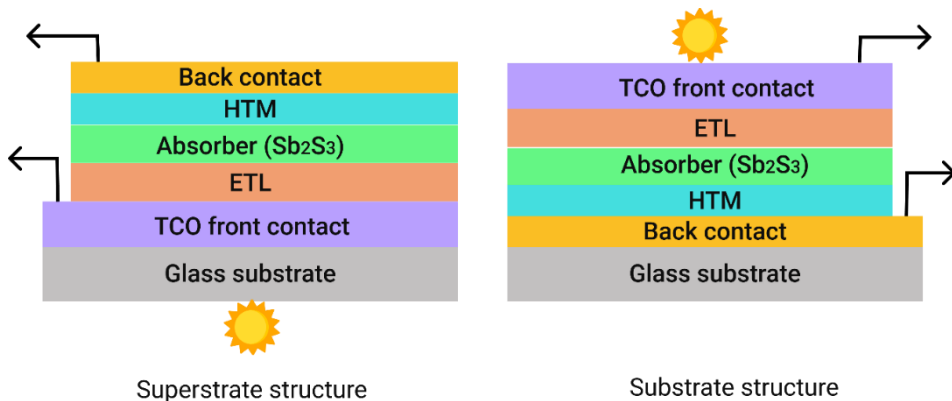


Figure 1.2. Schematics of the Sb<sub>2</sub>S<sub>3</sub> thin film solar cell in superstrate and substrate structures. Modified from [55]. TCO - transparent conducting oxide, ETL - electron transport layer, HTM - hole transport material.

The most essential components are TCO, ETL, light harvesting Sb<sub>2</sub>S<sub>3</sub> absorber, HTM and metal contacts. The most used TCOs are – Indium-doped tin oxide (ITO), Fluorine-doped tin oxide (FTO), and Aluminum-doped zinc oxide (AZO) [4]. The ETL, responsible for extracting and transporting the electrons from the absorber material are n-type materials like – Titanium dioxide (TiO<sub>2</sub>), Cadmium sulfide (CdS), Tin dioxide (SnO<sub>2</sub>) or Zinc oxide (ZnO) [55]. The HTM layer, could either be inorganic metal oxides like Copper oxide (CuO), Nickel oxide (NiO<sub>x</sub>), Vanadium oxide (V<sub>2</sub>O<sub>5</sub>) or organic ones like P3HT and Spiro-OMeTAD [4]. The common used ETLs and HTMs in Sb<sub>2</sub>S<sub>3</sub> based solar cells are shown in Fig. 1.3. The back contact includes metals with high work function like Gold (Au), Silver (Ag) or Nickel (Ni) [55].

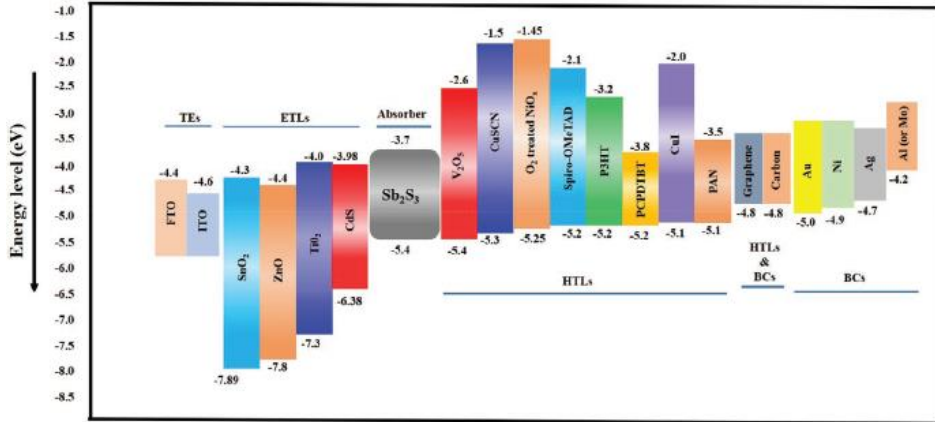


Figure 1.3. Band diagram of functional layers in  $Sb_2S_3$  solar cell stack [55].

The band energy levels of the functional layers of the solar cell stack are presented in Fig. 1.3. In general, the Ionization Potential ( $I_p$ ) energy level is generally denoted as the Valence Band Maxima (VBM) in inorganic materials and Highest Occupied Molecular Orbital (HOMO) in organic materials. Similarly, the Electron affinity ( $E_a$ ) level is denoted as Conduction Band Minima (CBM) in inorganic materials and Lowest Occupied Molecular Orbital (LUMO) in organic ones. For a suitable ETL, its CBM should be aligned to the CBM of the  $Sb_2S_3$  absorber ( $-3.7$  eV) with a maximum band offset of  $0.3$  eV [30]. The ETLs which are suitable to the  $Sb_2S_3$  solar cell stack are shown in Fig. 1.4. The HOMO level of the HTM should be aligned with the VBM of  $Sb_2S_3$  ( $-5.4$  eV) for the efficient transport of holes with maximum band offset of  $0.3$  eV [30]. A detailed discussion on most common used ETLs and HTMs in  $Sb_2S_3$  based solar cells is presented in section 1.7.

### 1.3.3 Methods for $Sb_2S_3$ thin film preparation

The preparation of thin films, especially those composed of  $Sb_2S_3$ , holds immense significance in the realm of solar cell technology. This section provides an overview of the methods employed in the deposition of  $Sb_2S_3$  thin films, delving into both physical and chemical approaches. The different physical deposition methods employed are thermal evaporation (TE) [60,61], magnetron sputtering [62,63], and close spaced sublimation (CSS) [64,65]. The widely used chemical methods are chemical bath deposition (CBD) [9,54], spin coating (SC) [16,66], atomic layer deposition (ALD) [67,68] and ultrasonic spray pyrolysis (USP) [13,18]. Table 1.1 presents the commonly used deposition techniques for  $Sb_2S_3$  film preparation along with the deposition temperature range, deposition time range, advantages, and disadvantages of each technique. The details of performance parameters of the fabricated solar cells obtained using different deposition techniques are presented in Table 1.2.

#### **Physical deposition methods:**

##### Thermal Evaporation (TE):

Thermal evaporation stands out as a prominent physical method for  $Sb_2S_3$  thin film preparation. This technique involves the controlled application of heat to elemental antimony and sulfur in a vacuum chamber.  $Sb_2S_3$  transforms into a vapor that subsequently condenses on a substrate, forming the desired thin film [60,61].

#### Magnetron Sputtering:

The process is driven by the application of high-power radio frequency (RF) or direct current (DC) to the target containing  $\text{Sb}_2\text{S}_3$ , facilitating the ejection of material from the targets. The ejected  $\text{Sb}_2\text{S}_3$  material is subsequently deposited onto a substrate [62,63].

#### Close Spaced Sublimation (CSS):

The precursor of  $\text{Sb}_2\text{S}_3$  powder is placed in a sealed vessel where they undergo congruent sublimation at temperatures of around 300 °C [69]. The sublimated  $\text{Sb}_2\text{S}_3$  vapor then condenses onto a cooler substrate to form the desired thin film [64,65].

#### ***Chemical deposition methods:***

##### Chemical Bath Deposition (CBD):

This technique involves the immersion of a substrate in a solution containing precursors that react to form  $\text{Sb}_2\text{S}_3$  thin films. The precursors used are Antimony trichloride ( $\text{SbCl}_3$ ), Antimony potassium tartrate ( $\text{C}_8\text{H}_4\text{K}_2\text{O}_{12}\text{Sb}_2 \cdot 3\text{H}_2\text{O}$ ) [70] or Antimony trioxide ( $\text{Sb}_2\text{O}_3$ ) [71] for antimony source and thioacetamide ( $\text{C}_2\text{H}_5\text{NS}$ ) [54,72], Thiourea ( $\text{CH}_4\text{N}_2\text{S}$ ) [73,74] or Sodium thiosulfate ( $\text{Na}_2\text{S}_2\text{O}_3$ ) [73,74] for sulfur source.

##### Hydrothermal Deposition (HD):

The hydrothermal process is a method of crystal growth that relies on the use of high-temperature aqueous solutions at high vapor pressures to dissolve and recrystallize materials. The process is similar to CBD in most aspects. The precursors used are Antimony trichloride ( $\text{SbCl}_3$ ) or Antimony potassium tartrate ( $\text{C}_8\text{H}_4\text{K}_2\text{O}_{12}\text{Sb}_2 \cdot 3\text{H}_2\text{O}$ ) for antimony source with Sodium thiosulfate ( $\text{Na}_2\text{S}_2\text{O}_3$ ) as sulfur source [75,76].

##### Atomic Layer Deposition (ALD):

Atomic Layer Deposition emerges as a precise and controlled chemical method for thin film deposition, offering atomic-level thickness control. The inherent advantages of ALD, such as uniformity, position it as a promising technique for  $\text{Sb}_2\text{S}_3$  thin solar cells [14]. The precursors used are tris-dimethylamido antimony ( $\text{Sb}(\text{N}(\text{CH}_3)_2)_3$ ) and hydrogen sulfide ( $\text{H}_2\text{S}$ ) for antimony and sulfur source, respectively [77,78].

Table 1.1. Summary of deposition temperatures, deposition time, advantages and disadvantages of the  $Sb_2S_3$  film preparation techniques.

Methods	Deposition temperature	Deposition time	Advantages	Disadvantages	Ref.
Thermal Evaporation (TE)	Source: 600–800 °C, Substrate: RT–200 °C	10–30 minutes	Rapid deposition, good adhesion to substrates	High temperature, vacuum required	[61, 82, 83]
Magnetron Sputtering	100–300 °C, followed by 200–400 °C annealing	1–3 hours	Uniform film, good control over film thickness	Complex and expensive equipment	[62, 84]
Closed Space Sublimation (CSS)	Source: 400–450 °C, Substrate: 200–350 °C	1–3 minutes	Rapid deposition	High temperature, vacuum required	[85]
Chemical Bath Deposition (CBD)	50–80 °C	1–3 hours	Low-temperature, cost-effective and simple	Limited control over film thickness	[9, 54, 86]
Hydro-thermal Deposition (HD)	150–200 °C	2–24 hours	Low-temperature, cost-effective and simple process	High pressure required, long processing time, complex equipment	[87]
Atomic Layer Deposition (ALD)	100–250 °C	2–4 hours	Precise thickness control conformal coating	Long processing time, limited for large-area coatings, high setup cost	[14, 67, 77]
Ultrasonic Spray Pyrolysis (USP)	180–250 °C, followed by crystallization in inert environment at 200–300 °C	10–40 minutes	Suitable for large-area coatings, scalable, high throughput	Need for careful deposition parameter optimization	[13, 18, 51, 72]
Spin Coating (SC)	RT followed by annealing in inert environment at 150–300 °C	Coating: seconds to minutes	Rapid and cost-effective, versatile for various substrates	Limited scalability for large-scale production, potential non-uniformities	[56, 88, 89]

#### Ultrasonic Spray Pyrolysis (USP):

This technique involves the deposition of precursor solutions using ultrasonic spray setup onto a heated substrate, forming a thin film upon solvent evaporation and precursors thermal decomposition [72]. The precursors used are antimony trichloride ( $\text{SbCl}_3$ ) [13,18] for antimony source with Thiourea ( $\text{CH}_4\text{N}_2\text{S}$ ) [13,18] or Thioacetamide ( $\text{C}_2\text{H}_5\text{NS}$ ) [72] as sulfur source. Other precursors used are Antimony ethyl xanthate ( $\text{C}_9\text{H}_{15}\text{O}_3\text{S}_6\text{Sb}$ ) with Thiourea [72]. Primarily, organic solvents such as ethanol, methanol or dimethyl sulfoxide (DMSO) are commonly used [13,18].

#### Spin Coating (SC):

This technique involves spinning a liquid precursor onto a substrate. The solvent evaporates during spinning, leaving behind a uniform layer of the precursor material. A subsequent annealing step is required to obtain  $\text{Sb}_2\text{S}_3$  thin film. The precursors used are Antimony trichloride ( $\text{SbCl}_3$ ) with Thiourea ( $\text{CH}_4\text{N}_2\text{S}$ ) [79,80] or Thioacetamide ( $\text{C}_2\text{H}_5\text{NS}$ )[81] in organic solvents such as ethanol, methanol, or dimethyl sulfoxide (DMSO) [79–81].

In summary, the most commonly used deposition techniques for  $\text{Sb}_2\text{S}_3$  thin films are chemical deposition methods. These methods offer significant advantages, such as scalability, the ability to deposit thin films at low temperatures, and the use of a straightforward and cost-effective setup [13,72]. To date, the highest-efficiency  $\text{Sb}_2\text{S}_3$  solar cells have been achieved using these chemical deposition processes (see Table 1.2).

### **1.3.4 Successfully implemented deposition routes and state of the art in $\text{Sb}_2\text{S}_3$ solar cells development**

In 1994, researchers developed the first planar  $\text{Sb}_2\text{S}_3$  thin film solar cell with the configuration ITO/ $\text{Sb}_2\text{S}_3$ / $\text{WO}_3$ /Pt using CBD as deposition technique for the absorber layer. The resulting devices yielded PCE of 5.6% [71]. Table 1.2 presents the compiled data on planar  $\text{Sb}_2\text{S}_3$  thin films, including the device configuration and the deposition techniques used for preparing the  $\text{Sb}_2\text{S}_3$  absorber. Additionally, the table provides information on the  $\text{Sb}_2\text{S}_3$  layer thickness, the HTM used and the performance parameters of representative  $\text{Sb}_2\text{S}_3$  solar cells. This thesis includes solar cell results published up until the completion of the thesis in November 2024. Although  $\text{Sb}_2\text{S}_3$  solar cells can be fabricated using both physical and chemical deposition techniques, a review of the literature makes it evident that more R&D efforts have been dedicated to  $\text{Sb}_2\text{S}_3$  films deposited through chemical deposition methods (see Table 1.2).

Before the start of the study in October 2020, the highest efficiency of planar FTO/ $\text{TiO}_2$ / $\text{Sb}_2\text{S}_3$ /PCPDTBT/PEDOT:PSS/Au solar cell devices was 7.5% (reported in 2014), obtained using chemical deposition method for the absorber preparation [54]. The record efficiency using physical deposition technique for  $\text{Sb}_2\text{S}_3$  was obtained by Lan et al, using thermal evaporation for  $\text{Sb}_2\text{S}_3$  preparation in the year 2018 [77]. The fabricated device in configuration FTO/ $\text{TiO}_2$ / $\text{Sb}_2\text{S}_3$ /Spiro-OMeTAD/Ag yielded efficiency of 3.8% [83]. After the start of the present study,  $\text{Sb}_2\text{S}_3$  solar cell results with PCE of 8.0% were published by Wang et al. (FTO/CdS/ $\text{Sb}_2\text{S}_3$ /Spiro-OMeTAD/Au) using CBD for  $\text{Sb}_2\text{S}_3$  deposition [9]. Using physical deposition technique of thermal evaporation, Lian et al. fabricated devices in configuration FTO/CdS/ $\text{Sb}_2\text{S}_3$ /Spiro-OMeTAD/Au yielding efficiency of 6.2% [82]. In summary, with continuous R&D efforts in the last decade, the efficiency of  $\text{Sb}_2\text{S}_3$  solar devices has made promising progress, however there is significant room for R&D to boost the PCE of this device.

Table 1.2. An overview of planar  $Sb_2S_3$  solar cells fabricated with different HTMs and the output parameters of corresponding solar cells, reported till November 2024.

HTM	Device configuration	$Sb_2S_3$ deposition method	$Sb_2S_3$ thickness [nm]	$V_{oc}$ [mV]	$J_{sc}$ [mA/cm <sup>2</sup> ]	FF [%]	PCE [%]	Ref.	Year
P3HT	ITO/ZnO/ $Sb_2S_3$ /P3HT/Ag	TE	210	450	12.6	42	2.4	[61]	2012
	ITO/TiO <sub>2</sub> / $Sb_2S_3$ /P3HT/Au	CBD	200	630	6.1	35	1.4	[90]	2013
	ITO/TiO <sub>2</sub> / $Sb_2S_3$ /P3HT/Ag	ALD	155	732	9.3	62	4.3	[14]	2015
	FTO/TiO <sub>2</sub> / $Sb_2S_3$ /P3HT/Au	SC	n.m.	616	8.1	46	2.3	[81]	2015
	ITO/TiO <sub>2</sub> / $Sb_2S_3$ /P3HT/Au	USP	150	618	6.0	51	1.9	[91]	2016
	ITO/TiO <sub>2</sub> / $Sb_2S_3$ /P3HT/Au	USP	100	693	13.8	58	5.5	[18]	2019
Spiro-OMeTAD	FTO/TiO <sub>2</sub> / $Sb_2S_3$ /Spiro-OMeTAD/Ag	TE	300	620	10.7	56	3.8	[83]	2018
	FTO/CdS/ $Sb_2S_3$ /Spiro-OMeTAD/Au	TE	200	720	15.9	54	6.2	[82]	2021
	FTO/TiO <sub>2</sub> / $Sb_2S_3$ /Spiro-OMeTAD/Au	CBD	84	690	13.4	50	4.6	[86]	2018
	FTO/TiO <sub>2</sub> / $Sb_2S_3$ /Spiro-OMeTAD/Au	SC	400	660	13.1	59	5.2	[88]	2019
	FTO/TiO <sub>2</sub> / $Sb_2S_3$ /Spiro-OMeTAD/Au	SC	162	650	17.7	62	7.1	[16]	2020
	FTO/CdS/ $Sb_2S_3$ /Spiro-OMeTAD/Au	HD	300	707	15.2	56	6.0	[92]	2020
	FTO/TiO <sub>2</sub> /CdS/ $Sb_2S_3$ /Spiro-OMeTAD/Au	HD	1000	748	15.3	57	6.5	[87]	2021

HTM	Device configuration	Sb <sub>2</sub> S <sub>3</sub> deposition method	Sb <sub>2</sub> S <sub>3</sub> thickness [nm]	V <sub>oc</sub> [mV]	J <sub>sc</sub> [mA/cm <sup>2</sup> ]	FF [%]	PCE [%]	Ref.	Year
	FTO/CdS/Sb <sub>2</sub> S <sub>3</sub> /Spiro-OMeTAD/Au	CBD	214	757	17.4	61	8.0	[9]	2022
PCPDTBT	FTO/TiO <sub>2</sub> /Sb <sub>2</sub> S <sub>3</sub> /PCPDTBT/Au	CBD	n.m.	616	15.0	66	6.2	[93]	2012
	FTO/TiO <sub>2</sub> /Sb <sub>2</sub> S <sub>3</sub> /PCPDTBT-PEDOT:PSS/Au	CBD	n.m.	711	16.1	65	7.5	[54]	2014
PEDOT:PSS	FTO/TiO <sub>2</sub> /Sb <sub>2</sub> S <sub>3</sub> /P3HT-PEDOT:PSS/Au	ALD	90	667	14.9	58	5.7	[77]	2014
	FTO/TiO <sub>2</sub> /ZnS/Sb <sub>2</sub> S <sub>3</sub> /P3HT-PEDOT:PSS/Au	ALD	75	626	15.7	52	5.1	[67]	2021
NiO <sub>x</sub>	FTO/TiO <sub>2</sub> /Sb <sub>2</sub> S <sub>3</sub> /NiO <sub>x</sub> /Au	SC	100	590	14.5	41	3.5	[89]	2018
V <sub>2</sub> O <sub>5</sub>	FTO/TiO <sub>2</sub> /Sb <sub>2</sub> S <sub>3</sub> /V <sub>2</sub> O <sub>5</sub> /Au	SC	87	590	15.3	53	4.8	[94]	2018

Note: TE – Thermal evaporation, CBD – Chemical bath deposition, SC – spin coating, ALD – Atomic layer deposition, USP – Ultrasonic spray pyrolysis, HD – Hydrothermal deposition, \*n.m. – not measured.

### 1.3.5 Strategies for optimization of solution processed Sb<sub>2</sub>S<sub>3</sub> material and device

Sb<sub>2</sub>S<sub>3</sub> solar cells face several challenges, including low efficiency caused by high recombination rates (including recombination in thin film absorber bulk and interface recombination), as well as difficulties in producing high-quality, large area uniform films, using scalable and cost-effective manufacturing techniques [6,63]. Several research studies have explored various strategies to tackle these challenges of Sb<sub>2</sub>S<sub>3</sub>-based solar cells, with focus on material and device engineering.

Precursor Engineering – One effective approach in improving the PCE of Sb<sub>2</sub>S<sub>3</sub> solar cells is through precursor engineering during the solution processing of the material. By carefully selecting and manipulating precursor materials, researchers have achieved significant advancements in efficiency. Zhou et al. added 4-Chloro-3-nitrobenzenesulfonyl Chloride (CSCI) in the Sb<sub>2</sub>S<sub>3</sub> precursor solution [95]. The resulting PCE increased from 4.2% to 5.8% due to enhanced crystallization and reduced trap states in the Sb<sub>2</sub>S<sub>3</sub> layer [95]. Li et al. introduced Ag ions within the Sb<sub>2</sub>S<sub>3</sub> sol-gel precursors of antimony acetate and thiourea [96]. The crystallinity of the Sb<sub>2</sub>S<sub>3</sub> crystal grains were enhanced from 36.6 nm to 42.2 nm and the charge carrier mobility was increased from  $1.4 \times 10^{-4}$  to  $3.5 \times 10^{-4} \text{ cm}^2 \text{ V}^{-1} \text{ s}^{-1}$ . This led significant improvements in the FF and V<sub>oc</sub> and yielded cells with record high PCE from 6.1% of 7.7% [96].

Growth Control – Controllable grain growth is essential for the vertical aligned growth of the absorber layer. This can be achieved by modifying the ETL surface or depositing a seed layer [88]. Zhang et al. used a thin Sb<sub>2</sub>S<sub>3</sub> seed layer on the TiO<sub>2</sub> substrate to assist the growth of the Sb<sub>2</sub>S<sub>3</sub> thin film during the hydrothermal process. The seed layer provides a high density of the nucleation site that helps in growth of Sb<sub>2</sub>S<sub>3</sub> layer with less structural defects [97]. The defect density (N<sub>t</sub>) in the seed assisted Sb<sub>2</sub>S<sub>3</sub> films decreased from  $10^{16}$  to  $10^{14} \text{ cm}^{-3}$  [97].

Post Deposition Treatment – Post deposition heat treatment of the absorber layer in vacuum, inert atmosphere or in a sulfurizing or selenizing atmosphere is often used for crystallization, grain growth control and surface/bulk modification of Sb<sub>2</sub>S<sub>3</sub> films [14,54,98,99]. Yuan et al. employed post-surface selenization in the fabrication of HTM-free planar Sb<sub>2</sub>S<sub>3</sub> solar cells. This process enabled Se-doping in the bulk, which effectively passivated both interface and bulk defects, leading to enhanced CdS/Sb<sub>2</sub>S<sub>3</sub> heterojunction quality. As a result, V<sub>oc</sub> increased from 692 to 714 mV, and the PCE improved from 3.3% to 4.1% [98].

Optimized Device Architecture – The device architecture of the solar cell can be improved by optimizing layer thickness (TCO, ETL, Absorber, HTM), and by incorporation of the interfacial and charge transport layers. The aim is to minimize both, electrical and optical losses and within the device [55].

Interface Engineering – Surface passivation techniques can reduce recombination losses at the absorber interfaces and enhance charge carrier lifetimes within the solar cell structure. Han et al. used SbCl<sub>3</sub> for post-treatment on Sb<sub>2</sub>S<sub>3</sub> films [100]. The result was a thin SbCl<sub>3</sub> layer formed on the Sb<sub>2</sub>S<sub>3</sub> surface which passivated the surface defects and suppressed the recombination. The fabricated device demonstrated a significant improvement in PCE from 5.9% to 7.1% [100]. Büttner et al. introduced a wide bandgap ZnS ultrathin interfacial layer, approximately 1–1.5 nm thick, between the TiO<sub>2</sub> and Sb<sub>2</sub>S<sub>3</sub> layers, passivating interface defects. This modification significantly improved the device's performance, leading to a PCE of 5.0 % [67].

Selective Contacts – Carrier-selective contacts are one of the basic requirements for solar cells. They work to collect and transport carriers generated in absorbers, realizing that electrons and holes are collected by two different terminals [63]. Hence, the performances of carrier-selective contacts directly affect the performance of solar cells. The choice and application of ETL and HTM are crucial in the performance of the device, especially for semi-transparent applications [55]. This will be discussed more in the next section.

## 1.4 Selective contacts for $\text{Sb}_2\text{S}_3$ solar cells

### 1.4.1 Electron transport layer

In the context of  $\text{Sb}_2\text{S}_3$  solar cells, ETL plays a crucial role in facilitating the transport of electrons from the  $\text{Sb}_2\text{S}_3$  absorber. In the case of superstrate  $\text{Sb}_2\text{S}_3$  thin film solar cells, the ETL material serves a dual purpose of facilitating electron transport and controlling the crystallites orientation in the  $\text{Sb}_2\text{S}_3$  film [55]. For effective performance, ETLs in  $\text{Sb}_2\text{S}_3$  solar cells need to possess specific characteristics. Firstly, the ETL should have high electron mobility to enable fast electron transportation and reduce sheet resistance. Conversely, it should establish significant hole-blocking barriers to prevent the recombination of photocarriers [6]. Secondly, the ETL material should be a wide bandgap semiconductor (see Fig. 1.3) to ensure high transparency and allow increased sunlight penetration. This transparency helps maximize light absorption by the  $\text{Sb}_2\text{S}_3$  absorber material [55]. Moreover, the CBM of the ETL must have a favorable band alignment with the CBM of the absorber. A large band offset between the VBM of the ETL and the VBM of the absorber helps block the holes from transporting towards the front contact [55]. Lastly, in the planar structure of  $\text{Sb}_2\text{S}_3$  solar cells, ETLs play a critical role in maintaining a compact and pinhole-free configuration [6,55]. This structural feature prevents direct contact between the absorber and the electron collection electrode, thereby minimizing shunting currents. Mainly, four different ETLs, such as  $\text{TiO}_2$  [13,18,51,55,72,101–103],  $\text{CdS}$  [87,104],  $\text{ZnO}$  [105] and  $\text{SnO}_2$  [53] have been utilized in  $\text{Sb}_2\text{S}_3$  solar cells.

$\text{TiO}_2$  is a n-type material with bandgap value of 3.2 eV and used as an ETL in  $\text{Sb}_2\text{S}_3$ -based solar cells [51,55,72]. Different strategies like doping and surface treatments of the  $\text{TiO}_2$  layer has been used by research groups in the past. Doping helps improve the electrical conductivity and electron mobility of the  $\text{TiO}_2$  layer, leading to better electron extraction and transport. Surface treatments of prepared  $\text{TiO}_2$  layers help passivate surface defects and reduces trap states at the  $\text{TiO}_2/\text{Sb}_2\text{S}_3$  interface. These traps often act as recombination centers, leading to efficiency losses. Odari et al. used Nb [101] and Lan et al. used Li [106] to dope  $\text{TiO}_2$  layer to improve the optoelectronic properties of  $\text{TiO}_2$ . Compared with the solar cells using undoped  $\text{TiO}_2$ , the solar cells with Li-doped  $\text{TiO}_2$  yielded improved PCE from 1.7% to 4.0% [106]. For post deposition of  $\text{TiO}_2$  treatments, Kim et al. used  $\text{Cs}_2\text{CO}_3$  [107], Han et al. used inorganic zinc halides ( $\text{ZnCl}_2$ ,  $\text{ZnBr}_2$ ,  $\text{ZnI}_2$ ) [100] and Tsujimoto et al. used  $\text{Mg}^{2+}$  and  $\text{Ba}^{2+}$  ions [102], showing various impacts of these treatments of the final device performance.

$\text{CdS}$ , another n-type material with its bandgap of 2.4 eV is a popular electron transport layer in  $\text{Sb}_2\text{S}_3$  based solar cells [9,55,82,87]. Lian et al. prepared solar cell with a PCE of 6.2%, which remains the highest in thermal evaporated  $\text{Sb}_2\text{S}_3$  solar cells [82]. Similar to  $\text{TiO}_2$ ,  $\text{CdS}$  layers can be doped to improve their electrical conductivity and electron mobility [108]. Ning et al. used  $\text{CdS}$  films doped with potassium and fabricated device yielding 6.5% PCE [108]. So far, the highest cell efficiency of 8.0% was obtained for the  $\text{Sb}_2\text{S}_3$  device with  $\text{CdS}$  ETL and using CBD for  $\text{Sb}_2\text{S}_3$  deposition [9].

Other ETLs in addition to TiO<sub>2</sub> and CdS, like ZnO and SnO<sub>2</sub> show promise to be employed in Sb<sub>2</sub>S<sub>3</sub> solar cell and have been explored by various research groups [61,109]. So far, the most suitable ETLs are TiO<sub>2</sub> and CdS offering a good platform for optimization of the absorber layer.

#### 1.4.2 Hole transport layer

In solar cell device structure, HTMs are an integral part and serve multiple tasks. They play a crucial role in facilitating the transportation of hole carriers to the counter electrode [4,55]. Additionally, they prevent the diffusion of metal from contacts, avoiding direct contact with the absorber, and suppress recombination losses at the back interface [55]. In the broader context, an ideal HTM candidate should possess high hole mobility and exhibit long-term stability in various environmental conditions. The HTM should have a large bandgap and be transparent in the visible spectral region for use in semi-transparent devices [55]. Their low cost, ease of preparation, and solution-processability is a crucial aspect, allowing for scalable manufacturing and commercial application [6,55]. Table 1.2 presents a summary of the solar cell performance results obtained with various organic and inorganic HTMs incorporated into planar Sb<sub>2</sub>S<sub>3</sub> solar cells up to the year 2024.

Spiro-OMeTAD remains a popular choice for high-performing Sb<sub>2</sub>S<sub>3</sub> solar cells (see Table 1.2), albeit with the need for dopants for optimal performance. Dopant-free HTMs such as P3HT and PCPDTBT have also been explored each with its set of advantages and disadvantages [13,72]. In addition to individual HTMs, combinations such as PCPDTBT/PEDOT:PSS and P3HT/PEDOT:PSS have also been utilized to improve the charge transport in Sb<sub>2</sub>S<sub>3</sub>-based solar cells [54,67,77]. Alternative inorganic HTMs, including CuSCN [110], NiO<sub>x</sub> [55] [89], CuI [111], V<sub>2</sub>O<sub>5</sub> [94], graphene [112], and carbon [113], have been also tested in Sb<sub>2</sub>S<sub>3</sub> solar cells by different research groups. Different experimental strategies, including HTM doping, post-treatments and thickness optimization have been employed to enhance PCE of the Sb<sub>2</sub>S<sub>3</sub> based devices. The efficacy of HTM in Sb<sub>2</sub>S<sub>3</sub> solar cells is contingent upon several key characteristics:

Band Energy Alignment: The HOMO level of the HTM must align with the VBM of the absorber Sb<sub>2</sub>S<sub>3</sub> (-5.4 eV) for efficient transport of the photo generated holes to the metal contact [55]. A larger band offset (> 0.3 eV) between the LUMO level of the HTM and the CBM of the absorber can prevent the electron from going towards the back contact (Fig. 1.3) [6,55].

Carrier Mobility and Lifetime: HTM must exhibit high carrier mobility ( $10^{-2}$  cm<sup>2</sup> V<sup>-1</sup> s<sup>-1</sup>), long diffusion length (> 100 nm), and extended carrier lifetime (hundreds of nanoseconds to a few microseconds). These characteristics play a vital role in rescuing carriers during extraction from the absorber and their subsequent transportation to the back-contact metal electrode [6].

Stability: Considering the significance of efficiency and stability in solar cells, the HTM selection should prioritize stability and resistance against environmental factors such as heat, moisture, oxygen, and ultraviolet (UV) light. The HTM should withstand both processing conditions and operational challenges [6,55].

**Deposition Compatibility:** The chosen deposition technique for HTM should be compatible with the underlying absorber layer, ensuring a seamless integration [6].

The subsequent section delves into the specifics of the most widely used organic and inorganic HTMs in  $\text{Sb}_2\text{S}_3$  solar cells.

## Organic HTMs

### ***2,2',7,7'-tetrakis-(N,N-di-p-methoxyphenylamine)-9fluorene (Spiro-OMeTAD)***

2,2',7,7'-tetrakis-(N,N-di-p-methoxyphenylamine)-9fluorene (Spiro-OMeTAD) has emerged as a highly regarded HTM in both perovskite and  $\text{Sb}_2\text{S}_3$  based solar cells. The chemical structure is presented in Fig. 1.4a. The wide band gap of ca. 3.0 eV makes it suitable for use in semi-transparent devices [55]. Conventionally, high-efficiency n-i-p structure PSCs have utilized Spiro-OMeTAD as an HTM [114]. Although Spiro-OMeTAD effectively facilitates extraction and transportation of holes from the absorber layer to the counter electrode, material is limited by the hole mobility of approximately  $2 \times 10^{-4} \text{ cm}^2 \text{ V}^{-1} \text{ s}^{-1}$  [115]. To overcome this, several dopants namely – lithium bis(trifluoromethyl-sulfonyl)-imide (LiTFSi), and 4-tert-butylpyridine (tBP) [115–117] are used. The incorporation of dopants in the HTMs increases the cost and can compromise the stability of devices, particularly because LiTFSi is hygroscopic in nature [23]. Additionally, the synthesis of Spiro-OMeTAD requires a multi-step process that necessitates low temperatures ( $-78^\circ\text{C}$ ) and sensitive reagents such as n-butyllithium or Grignard reagents [21,22]. The high synthesis cost of Spiro-OMeTAD ( $\sim 92$  Euro per g) [118] limits its commercial scalability.

A summary on  $\text{Sb}_2\text{S}_3$  thin films, employing various HTMs and the resulting photovoltaic performance parameters of solar cells is presented in Table 1.2. Moon et al. achieved 5.2% PCE in  $\text{Sb}_2\text{S}_3$  solar cells incorporating Spiro-OMeTAD as the hole transport layer [73]. Wang et al. reported a stable  $\text{Sb}_2\text{S}_3$ -based device with a PCE of 4.3% using Spiro-OMeTAD as the HTM [119]. Further enhancements have been realized by Chung et al., by employing dodecylphosphonic acid (DPA) and LiTFSi as dopants in Spiro-OMeTAD, and resulting in device yielding PCE of 6.0% [120]. The current state-of-the-art  $\text{Sb}_2\text{S}_3$  planar solar cell devices utilize Spiro-OMeTAD as the HTM, fabricated by Wang et al. has achieved a PCE of 8.0% [9].

### ***Poly(3-hexylthiophene) (P3HT)***

Poly(3-hexylthiophene) (P3HT), a well-known organic semiconductor. It has hole mobility of about  $0.1 \times 10^{-4} \text{ cm}^2 \text{ V}^{-1} \text{ s}^{-1}$  [13], good solubility, and thermal stability [115]. However, the similar bandgap of approximately 1.8 eV in P3HT compared to the ca. 1.7 eV of the  $\text{Sb}_2\text{S}_3$  absorber leads to parasitic absorption losses. This restricts its applicability in semi-transparent  $\text{Sb}_2\text{S}_3$  solar cells [13]. The chemical structure of P3HT contains thiophene units as shown in Fig. 1.4b. Recent studies by Jiang et al. and Xiang et al. have shown that the Sulphur atom in the thiophene unit with its lone pair of electrons can form a coordination bond with Sb in the absorber  $\text{Sb}_2(\text{S,Se})_3$  [121,122]. This led to an improvement of the interfacial properties between  $\text{Sb}_2(\text{S,Se})_3$  and the HTM [121,122]. As a general mechanism, it has been proposed that the interaction between thiophene and  $\text{Sb}_2(\text{S,Se})_3$  through the Sb-S bond improved the hole-extraction ability of the HTM, resulting in device PCE of 7.46% [121].

In the context of  $\text{Sb}_2\text{S}_3$ -based solar cells, Chang et al. pioneered the utilization of P3HT as an HTM, achieving a remarkable 5.0% PCE using CBD for preparing  $\text{Sb}_2\text{S}_3$  absorber layer [123]. To optimize the contact between P3HT and the back electrode Au, Gui et al. used a combination of P3HT and PEDOT:PSS as HTMs, resulting in better charge transfer

between  $\text{Sb}_2\text{S}_3/\text{P3HT}$  interfaces and enhancement in the PCE from 0.7% (for P3HT based device) to 2.3% for P3HT+PEDOT:PSS based cell [124]. In a different approach, Lim et al. proposed incorporation of Au nanoparticles into P3HT and demonstrated an improvement in the PCE from 4.0 to 4.9% [125].

Understanding the critical role of P3HT thickness, Liu et al. reported that a 40 nm thick P3HT film outperformed its 70 nm counterpart [126]. Gamboa et al. addressed the challenge of low hole mobility in P3HT by incorporating  $\text{NiO}_x$  nanoparticles, which resulted in a PCE of 2.90%, significantly higher than the 1.75% achieved with pristine P3HT in the control device [127].

Other HTMs like PCPBDBT [93] along with HTM combinations like P3HT: $\text{NiO}_x$  [127], P3HT/PEDOT:PSS [67], and PCPDTBT/PEDOT:PSS [54] have been explored by various research groups (see Table 1.2) with device efficiencies of up to 7.5% [54].

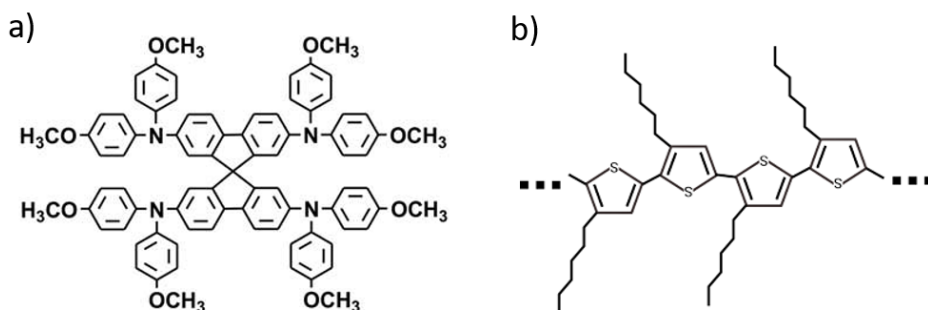


Figure 1.4. Chemical structures of conventionally used HTMs - (a) Spiro-OMeTAD [128] and (b) P3HT [129].

### ***Inorganic HTMs***

Copper thiocyanate (CuSCN) is an inorganic p-type semiconductor, with features such as high transparency over a broad-spectrum range, cost-effectiveness, and robust chemical stability [114]. Its wide bandgap of approximately 3.6 eV, coupled with a high hole mobility ranging from  $0.01$  to  $0.1 \text{ cm}^2 \text{ V}^{-1} \text{ s}^{-1}$ , positions CuSCN as an excellent candidate for deployment as an HTM in solar cells [55]. The inaugural utilization of CuSCN as an HTM in  $\text{Sb}_2\text{S}_3$ -based solar cells by Itzhaik et al. marked a significant breakthrough [110]. Post-treatments involving potassium thiocyanate (KSCN) or lithium thiocyanate (LiSCN) were introduced, resulting in enhanced p-type conductivity, reduced series resistance, and noteworthy PCEs [110]. The optimized thickness of the CuSCN layer was explored by Tsujimoto et al., revealing that thicknesses had a direct impact on PCE, with the optimum PCE of 3.7% achieved with a  $1 \mu\text{m}$  thick CuSCN layer [130].

$\text{NiO}_x$ , characterized by a wide bandgap ranging from 3.5 to 3.9 eV and a deep VBE ( $-5.2$  to  $-5.4$  eV), stands out as a p-type semiconductor [114]. Despite its hole mobility ranging from  $10^{-4}$  to  $10^{-2} \text{ cm}^2 \text{ V}^{-1} \text{ s}^{-1}$ ,  $\text{NiO}_x$  is exceptionally effective in hole extraction and transport, and electron blocking, owing conduction band edge at  $-1.5$  eV [55]. Jin et al. introduced  $\text{NiO}_x$  as an HTM in  $\text{Sb}_2\text{S}_3$ -based solar cells and fabricated devices with PCE of 3.5% [89].

Copper(I) iodide (CuI) is an inorganic p-type semiconductor, possessing a wide bandgap of 3.1 eV and hole mobility ranging from 0.5 to 2 cm<sup>2</sup> V<sup>-1</sup> s<sup>-1</sup> [114]. With a valence band maximum (VBM) of approximately -5.2 eV, CuI has advantages like inherent stability, organic solvent solubility, and cost-effectiveness [114]. In the context of Sb<sub>2</sub>S<sub>3</sub> solar cells, Dematage et al. pioneered the use of CuI as an HTM, resulting in a device achieving PCE of 2.5% [111]. Sun et al. introduced a spray technique for CuI deposition, outperforming drop coating and yielding a PCE of 1.1% [131].

Other inorganic materials such as V<sub>2</sub>O<sub>5</sub> [94], graphene [112], and carbon [113] have been also explored as HTMs in Sb<sub>2</sub>S<sub>3</sub>-based solar cells. Zhang et al., prepared V<sub>2</sub>O<sub>5</sub> HTM layer by thermal decomposition of spin-coated vanadium(V) triisopropoxide oxide solution, resulting in devices with PCE of 4.8% [94]. Graphene, introduced by Xiao et al., served both as a transparent electrode and HTM, achieving in device PCE of 1.6% [112]. Carbon as HTM and back contact was explored by Chen et al., yielding devices with PCE of 1.7% [113]. These diverse materials contribute to the evolving landscape of HTMs, each offering unique advantages and potential enhancements to solar cell performance.

### 1.4.3 Challenges with conventional HTMs in developing semi-transparent solar cells

The applicability of Sb<sub>2</sub>S<sub>3</sub> solar cells is constrained by their relatively low PCEs and the use of expensive HTMs. HTMs are essential components in the solar cell structures, performing multiple functions necessary for achieving high PCEs, particularly in semi-transparent devices [6]. There is a new grown interest in use of emerging photovoltaic technologies for semi-transparent applications like BIPV and solar windows [18,132–134]. This necessitates the need to evaluate the AVT in addition to PCE. Generally, solar cells are considered semi-transparent when they have an AVT > 20% in the visible region [18]. As of today, the most of R&D efforts were dedicated on development of semi-transparent organic and perovskite solar cells [41,132,133]. For OPV solar cell devices PCE of 10.8% and AVT of 50% in visible light has been reported [135]. Semitransparent halide perovskite solar cells have yielded PCE of 13% with AVT = 26% in the wavelength range of 350–900 nm [136]. Research on Sb<sub>2</sub>S<sub>3</sub>-based solar cells for semi-transparent applications is limited [18,134,137]. Pictures of semi-transparent perovskite solar cell and USP Sb<sub>2</sub>S<sub>3</sub> solar cells are presented in Fig. 1.5a and b, respectively.

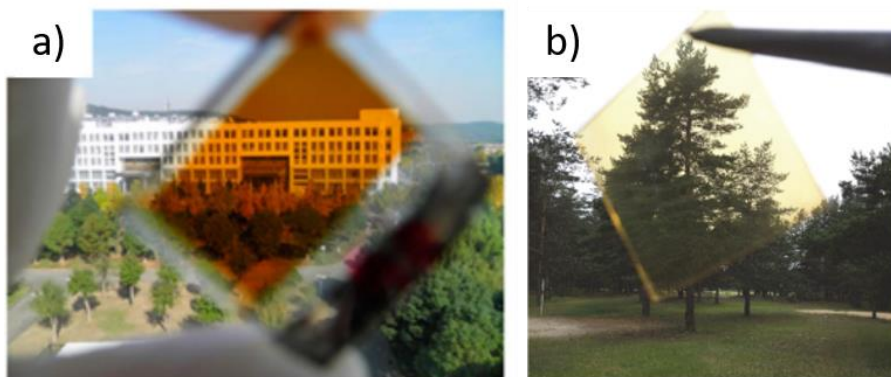


Figure 1.5. Picture of (a) semi-transparent perovskite solar cell [132] and (b) semi-transparent planar Sb<sub>2</sub>S<sub>3</sub> – based solar cell without contacts [18].

Eensalu et al. reported an AVT of 26% (shown in Fig. 1.5b) in a stack configuration of glass/ITO/TiO<sub>2</sub>/Sb<sub>2</sub>S<sub>3</sub> with a USP absorber thickness of 100 nm in 2019 [18]. These findings highlight the potential for sprayed Sb<sub>2</sub>S<sub>3</sub>-based solar cells to be used in semi-transparent applications, especially when combined with a suitably transparent back contact. In summary, since semi-transparent photovoltaics are expected to be the main application for Sb<sub>2</sub>S<sub>3</sub> thin-film solar cells, there is an urgent need to develop a transparent and stable hole transport layer and back contact.

The HTMs must exhibit high hole mobility, good thermal stability, high solubility in suitable solvents, and appropriate band edge positions compatible with Sb<sub>2</sub>S<sub>3</sub> [4]. Additionally, HTMs need to be transparent in the visible spectral region (400–800 nm) for use in semi-transparent solar cells [55]. Although a large number of novel organic HTMs have been tested successfully in perovskite solar cells [115,117,138], there is a significant lack of research on their application in Sb<sub>2</sub>S<sub>3</sub> solar cells.

In all the aforementioned solar cells, the high cost of HTMs like Spiro-OMeTAD ( $\approx$  92 Euro per g) [118] and P3HT ( $\approx$  45 Euro per g) [139] limits their commercial scalability. Spiro-OMeTAD is synthesized through a multi-step process that necessitates low temperatures ( $-78$  °C) and sensitive reagents [21,22]. Additionally, the use of Spiro-OMeTAD as HTM in solar cells requires dopants. LiTFSI – a lithium-based salt is used to enhance its hole transport capabilities. This doping process increases costs and reduces device stability, as the dopant is hygroscopic [23]. Limitations associated with the other commonly used HTM – P3HT is that it requires an additional activation step at temperatures around 170 °C in a vacuum or inert atmosphere [13,18]. Moreover, the similar bandgap values of P3HT (1.8 eV) and Sb<sub>2</sub>S<sub>3</sub> (ca. 1.7 eV) result in parasitic absorption losses, thereby limiting the overall transparency of the solar cells [13]. In this regard, the use of large bandgap HTMs and tailoring their thickness is crucial for achieving high-efficiency and semi-transparent solar cells.

Given the aforementioned limitations of conventional HTMs like Spiro-OMeTAD and P3HT, there is a clear need to explore alternative novel, dopant-free, transparent and low-cost HTMs. Daskeviciute et al., employed fluorene-based enamines (V1275, V1235 and V1236) as HTMs, as potential replacement of conventional Spiro-OMeTAD [140]. These new HTMs have the potential to be easily synthesized from commercially available starting materials while possessing desirable properties such as good thermal stability, appropriate solubility, and high hole mobility.

## 1.5 Summary of the literature review and the aim of the thesis

Antimony chalcogenides, including Sb<sub>2</sub>S<sub>3</sub>, Sb<sub>2</sub>Se<sub>3</sub>, and Sb<sub>2</sub>(S,Se)<sub>3</sub>, show great promise for photovoltaic applications owing to their abundance, non-toxic nature, and adjustable optoelectronic characteristics [6,67,106]. For Sb<sub>2</sub>S<sub>3</sub>, its anisotropic quasi - 1D structure, coupled with high optical absorption coefficients exceeding  $10^4$  cm<sup>-1</sup>, and bandgap of ca. 1.7 eV, makes it suitable candidates for both single-junction and tandem PV devices [4,63]. The band gap of Sb<sub>2</sub>S<sub>3</sub> absorber layer of ca. 1.7 eV allows for the fabrication of devices for semi-transparent applications and for use as a sub cell in tandem devices [4,63].

Several factors have been identified as critical for the performance of Sb<sub>2</sub>S<sub>3</sub> solar cells designed in both, non-transparent and transparent device concepts, including absorber and device optimization (e.g., interface engineering, selection of ETL and HTM) [6,67,106]. To address these challenges, various groups implemented strategies, including modifications to HTM and ETL layers, passivation techniques, novel synthesis approaches,

and doping strategies [6,67,106,134]. The device architecture of the solar cell can be improved by optimizing layer thickness (TCO, ETL, Absorber, HTM), interfaces and charge transport pathways [23]. Based on the literature overview, the following R&D advancements and challenges can be summarized:

1. Through continuous R&D efforts, antimony-based chalcogenides –  $\text{Sb}_2\text{S}_3$ ,  $\text{Sb}_2\text{Se}_3$ , and  $\text{Sb}_2(\text{S,Se})_3$  – have demonstrated significant improvements in solar cell applications, reaching PCEs of 8.0%, 10.57%, and 10.75%, respectively [9,10,45] within a span of about a decade. These advancements make antimony-based chalcogenides strong contenders for the next generation of emerging photovoltaic technologies. Antimony based chalcogenides are at the same stage as CdTe when it was considered as a potential candidate for commercialization [46].
2.  $\text{Sb}_2\text{S}_3$  thin films can be fabricated using a range of chemical and physical deposition methods. So far, high-efficiency  $\text{Sb}_2\text{S}_3$  solar cells have predominantly been prepared using cost-effective chemical methods such as spin coating and CBD. USP, which offers to cover large and is an industrially scalable technique with low capital has proven its ability to produce the devices with PCEs above 5% [13,18].
3. Solar cell device can be fabricated in both the substrate and superstrate configuration. The  $\text{Sb}_2\text{S}_3$  solar cell stack has a structural composition similar to CdTe and perovskite solar cells, incorporating an ETL, an absorber layer, HTM, and metal front and back contacts [37,55].
4. Various organic and inorganic materials have been explored as HTMs in  $\text{Sb}_2\text{S}_3$ -based solar cells. HTMs form a crucial component in solar cell structures that facilitate efficient extraction and transport of photogenerated holes, prevent metal diffusion, and suppress recombination losses at  $\text{Sb}_2\text{S}_3$ /HTM interface [6,55]. Ideal HTMs must possess high hole mobility, thermal stability, solubility, appropriate band edge positions compatible with absorber  $\text{Sb}_2\text{S}_3$  and transparency in the visible spectral region, especially for use in semi-transparent solar cells [55].
5. There are only a limited number of studies on the development of  $\text{Sb}_2\text{S}_3$  solar cells for semi-transparent applications. The integration of P3HT as a HTM in  $\text{Sb}_2\text{S}_3$  solar cells is constrained by its parasitic absorption in the visible spectrum, resulting in a reduction of the overall transmittance of the solar cell [14,55]. Additionally, P3HT also requires additional post-deposition activation at temperatures around 170 °C either in a vacuum or inert atmosphere [13,18]. Spiro-OMeTAD needs dopant which causes stability issues [23]. Conventional HTMs like Spiro-OMeTAD and P3HT utilized in  $\text{Sb}_2\text{S}_3$  based solar cells are expensive mainly due to their complex, expensive, and time-consuming synthesis processes.
6. Considering the limitation of conventional HTMs, there is a need for development of new alternative HTMs with suitable optoelectronic properties allowing efficient charge selectivity and transport in the  $\text{Sb}_2\text{S}_3$  solar cell device. This requires systematic optimization of HTM layers as well as fundamental understanding of the impact of these HTL on the functionality of the  $\text{Sb}_2\text{S}_3$  based solar cell devices.

Based on the literature review and the identified research gaps, the following hypothesis are proposed for this study:

1. The type, methodology for the application of HMT layer and HTM layer thicknesses have impact on the efficiency of charge transfer at the absorber/HTM interface and solar cell performance.
2. Dopant-free fluorene-based enamines are suitable as a hole selective contact in  $\text{Sb}_2\text{S}_3$  solar cells. The choice of HTM will affect band alignment at the back interface, which, in turn, affects hole extraction and the overall performance of the fabricated solar cells.
3. A combination of material and device characterization techniques will provide new insights into the functionality of fluorene-based compounds as HTMs, particularly in relation to their influence on the performance of  $\text{Sb}_2\text{S}_3$ -based semi-transparent devices.

### ***Aim of the thesis***

The main aim of this thesis is to develop semi-transparent  $\text{Sb}_2\text{S}_3$ -based solar cells with employment of new fluorene-based HTMs and provide understanding on the impact of these HTMs on efficacy of the charge transport in the solar cell device, including physical and chemical aspects of the phenomena occurring at the absorber-back contact interface. To achieve the aim, the research tasks were formulated as follows:

1. To fabricate planar glass/FTO/ $\text{TiO}_2$ / $\text{Sb}_2\text{S}_3$ /HTM/Au thin film solar cells, with  $\text{TiO}_2$  as ETL and  $\text{Sb}_2\text{S}_3$  absorber grown via USP, with a specific emphasis on developing the technology for application of novel HTM layers via spin coating.
2. To fabricate and characterize solar cells incorporating three distinct groups of fluorene-based enamines as dopant-free HTMs: fluorene-based compounds with aliphatic chains, fluorene-based compounds with thiophene end units and fluorene-based compounds with dimers linked with thiophene units.
3. To evaluate the solar cell performance along with an analysis of AVT, depending on each employed HTM group. To investigate and propose possible mechanism of inter relation between the overall device performance and HTM properties.

## 2 Experimental

In this chapter, the experimental methods utilized in articles I–IV for the preparation, characterization, and analysis of HTMs, solar cell component layers and  $\text{Sb}_2\text{S}_3$  solar cell devices are summarized.

### 2.1 Preparation of $\text{Sb}_2\text{S}_3$ thin films solar cells

Antimony sulfide solar cells were fabricated in a superstrate configuration (glass/FTO/ $\text{TiO}_2$ / $\text{Sb}_2\text{S}_3$ /HTM/Au) using a USP setup (Fig. 2.1a). The device configuration is depicted in Fig. 2.1b and the standard procedure for fabricating  $\text{Sb}_2\text{S}_3$  solar cells is illustrated in Fig. 2.1c.

#### ***Glass/FTO substrate***

FTO-coated glass substrate (25 mm × 25 mm) with a sheet resistivity  $\approx 10 \Omega \text{ sq}^{-1}$  were subjected to a thorough cleaning process. The samples were rinsed with deionized water, ethanol ( $\text{C}_2\text{H}_5\text{OH}$ ), and methanol ( $\text{CH}_3\text{OH}$ ), subsequently cleaned in boiling deionized water for 15 minutes, and dried with nitrogen before the deposition.

#### ***$\text{TiO}_2$ thin film deposition by ultrasonic spray pyrolysis***

The  $\text{TiO}_2$  precursor solution was prepared by mixing 0.2 M titanium (IV) isopropoxide (TTIP,  $\text{Ti}(\text{OC}_3\text{H}_7)_4$ ) with 0.2 M acetylacetonate (AcacH,  $(\text{CH}_3\text{CO})_2\text{CH}_2$ ) in solvent ethanol. Both,  $\text{TiO}_2$  as ETL and  $\text{Sb}_2\text{S}_3$  as absorber layer were deposited on the glass/FTO substrate using an indigenous and scalable USP setup. The USP procedure involves generating an aerosol from the precursor solution via an ultrasonic generator. This aerosol is sprayed on the substrate using compressed air. The directing gas nozzle generally operates inside the x-y plane to provide consistent coating.  $\text{TiO}_2$  was applied in over 75 cycles, utilizing approximately 80 ml of the solution in 35 minutes, with a carrier gas flow rate of 7.5 l/min and a spray rate of 2.5 ml/min. The substrate was kept on a hot plate at 340 °C in air. The prepared  $\text{TiO}_2$  films were thereafter annealed at 450 °C for 30 minutes in air.

#### ***$\text{Sb}_2\text{S}_3$ absorber thin film deposition by ultrasonic spray pyrolysis***

$\text{Sb}_2\text{S}_3$  absorber thin film was prepared in a 2-step process as pioneered previously in Laboratory for Thin Film Energy Materials in Tallinn University of Technology [13,51,72]. It involves the deposition of amorphous  $\text{Sb}_2\text{S}_3$  layer on top of glass/FTO/ $\text{TiO}_2$  substrate and thereafter crystallizing it by annealing in  $\text{N}_2$  environment [13,72]. The precursor solution was prepared by mixing 60 mM of antimony chloride ( $\text{SbCl}_3$ ) with 180 mM of thiourea ( $\text{SC}(\text{NH}_2)_2$ ) in the solvent methanol. The same USP setup was adopted for  $\text{Sb}_2\text{S}_3$ , with the substrate temperature maintained at 200 °C and the carrier gas flow rate at 2.5 l/min. The deposition utilized 40 cycles and approximately 60 ml of precursor. The deposition time was about 30 minutes, resulting in a spray rate of 1.5 ml/min. The as-deposited  $\text{Sb}_2\text{S}_3$  thin films were then annealed at 260 °C for 5 minutes in a nitrogen atmosphere.

#### ***Hole transport material layer deposition by spin coating***

The hole transport materials in powder form were synthesized by Prof. Vytautas Getautis group in Kaunas University of Technology in Lithuania. A detailed description of the HTM synthesis, their characterization and properties were published in articles [140], II–IV and is summarized in Appendix 2. The studied HTMs molecules have a central fluorene

scaffold, and these compounds can be synthesized in a straightforward condensation reaction from commercially available inexpensive materials. The as received HTM powders were then dissolved in solvent chlorobenzene ( $C_6H_5Cl$ ). To complete the solar cell fabrication, the HTM layers were spin-coated (3000 rpm, 30s) over glass/FTO/ $TiO_2$ / $Sb_2S_3$  stack from their respective precursor solutions. The concentration of the fluorene-based HTMs was systematically varied for all the HTMs to obtain the optimal value of thickness resulting in the highest PCE in solar cells. P3HT was dissolved in chlorobenzene and its concentration was fixed at 1 wt. %, as conventionally used [13,51,72]. Following the spin-coating of P3HT, the samples underwent heat treatment in a vacuum at 170 °C for 5 minutes to activate P3HT, while this step was not required for the new HTMs.

### **Back contact deposition by thermal evaporation**

Thermal evaporation process is employed to deposit an 80–100 nm-thick gold (Au) back contact using a shadow mask with the resulting contact area of 7.06 mm<sup>2</sup>.

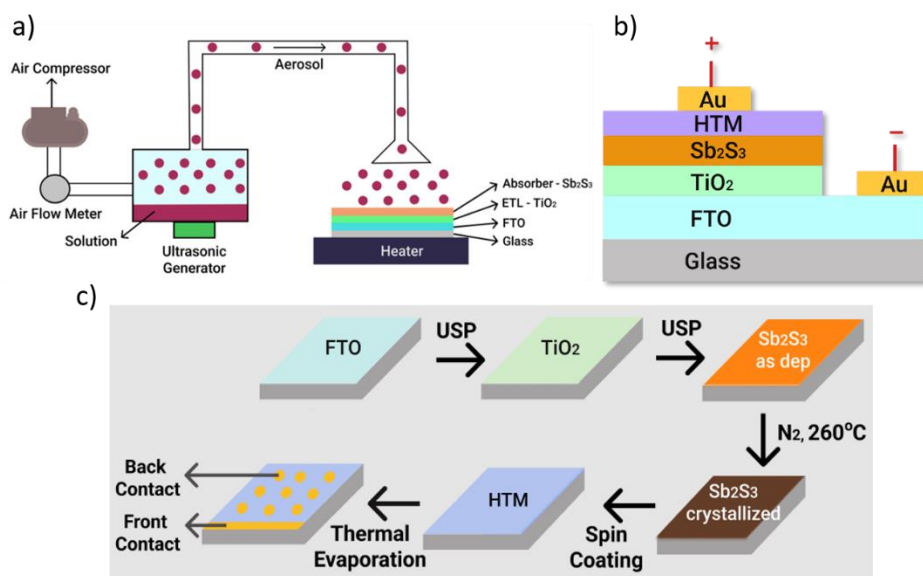


Figure 2.1. (a) Schematics of ultrasonic spray pyrolysis setup, (b) device configuration and (c) fabrication process of  $Sb_2S_3$  based solar cells.

## **2.2 Characterization of solar cell component layers and solar cell device**

The crystal structure and phase composition of the as-deposited and annealed  $Sb_2S_3$  thin films were analyzed using X-ray diffraction (XRD). Measurements were conducted on the glass/FTO/ $TiO_2$ / $Sb_2S_3$  stack, with a Rigaku Ultima-IV, utilizing a Cu  $K\alpha$  radiation source ( $\lambda = 1.5406 \text{ \AA}$ ) over a  $2\theta$  range of 10–80°. The recorded patterns were analyzed with a Rigaku PDXL2 software (I, II, IV). Micro-Raman spectra were obtained at ambient temperature for the glass/FTO/ $TiO_2$ / $Sb_2S_3$  stack utilizing a Horiba Labram HR 800 apparatus, which was fitted with a He-Ne laser attenuated to 143 mW/mm<sup>2</sup> and focused on a 5 mm diameter region. The thicknesses of the  $TiO_2$ ,  $Sb_2S_3$  absorber, and HTM layers were measured using scanning electron microscopy (SEM) with a Zeiss HR FESEM Ultra 55, operated at a 4 kV electron beam (I–IV). The total transmittance and reflectance

spectra for the glass/HTM, glass/FTO/HTM and glass/FTO/TiO<sub>2</sub>/Sb<sub>2</sub>S<sub>3</sub>/HTM cell stacks were recorded using an ultraviolet-visible (UV-VIS) spectrophotometer over the 300–1100 nm range. Average Visible Transmittance (AVT) values for both samples were calculated from transmittance spectra in the 400–800 nm range **(I–IV)**. The optical band gaps ( $E_g$ ) of the absorber and HTM films were calculated from the absorption spectra using Tauc plots **(I–IV)**. XRD, Raman, SEM and transmittance studies were conducted at Tallinn University of Technology **(I–IV)**.

Ionization potential ( $I_p$ ) values of functional layers were determined using self-built photoelectron emission yield spectroscopy (PYS) system. The measurements were conducted in a vacuum of approximately  $2 \times 10^{-5}$  mbar. The system includes the ENERGETIQ Laser-Driven Light Source (LDLS EQ-99) white light source, a Spectral Products DK240 1/4m monochromator for regulating the wavelength of UV radiation incident on the sample, and a Keithley 617 electrometer utilized as a voltage source and for electrical current measurements. The measurements were done between 4.00 and 6.00 eV photon energy with the step of 0.05 eV, registering the number of electrons emitted from the sample at each wavelength **(I–IV)**. The work function of gold metal contacts was determined utilizing a Kelvin probe. X-ray photoelectron spectroscopy (XPS) measurements of the stacks glass/FTO/TiO<sub>2</sub>/Sb<sub>2</sub>S<sub>3</sub> with and without HTM were made on a Thermo Fisher ESCALAB Xi system with a monochromatic Al Ka (1486.7 eV) X-ray source **(IV)**. The PYS and XPS measurements were made by Raitis Gržibovskis from the University of Latvia. Density Functional Theory (DFT) calculations were performed using the B3LYP functional and 6-31G(d,p) basis set to determine the highest occupied and lowest unoccupied molecular orbitals of the molecules, based on optimized ground-state geometries. All calculations were performed using the Gaussian 09W software, with graphical representations generated by the Avogadro program **(IV)**. The DFT calculations were conducted by Prof. Aivars Vembris from the University of Latvia.

J-V characteristics of the fabricated solar cells were measured under standard AM1.5G conditions (100 mW/cm<sup>2</sup> at room temperature) with irradiance utilizing a Wavelabs LS-2 LED solar simulator equipped with AUTOLAB PGSTAT 30 **(I–IV)**. The EQE spectra of solar cell devices were recorded with a Newport 300 W Xenon lamp, Newport Cornerstone 260 monochromator, a Merlin digital lock-in detector and a factory-calibrated silicon reference detector. J-V and EQE measurements of the solar cell stack were performed at Tallinn University of Technology **(I–IV)**.

### 3 Results and Discussions

This chapter presents the results of the study on  $\text{Sb}_2\text{S}_3$  solar cells incorporating novel, dopant-free fluorene-based compounds as HTMs. The solar cells were fabricated using thin-film  $\text{Sb}_2\text{S}_3$  in a superstrate configuration glass/FTO/ $\text{TiO}_2$ / $\text{Sb}_2\text{S}_3$ /HTM/Au. The chapter is organized into four sections. The first section covers the properties of the deposited  $\text{Sb}_2\text{S}_3$  absorber layer, followed by a section detailing the development of technology for deposition of the studied HTMs. The subsequent three sections present the results of solar cell fabrication and characterization, focusing on three distinct groups of fluorene-based compounds used as HTMs. These groups include fluorene-based molecules with aliphatic chains (V1275, V1235, V1236, V1461), fluorene-based molecules with thiophene end units (V808, V1385, V1386), and fluorene-based molecules with dimers linked with thiophene units (V1422, V1423, V1454, V1455). The results of the solar cell studies involving the first group of HTMs are detailed in articles I and III, the second group in article II, and the third group in article IV.

#### 3.1 Properties of ultrasonically sprayed $\text{Sb}_2\text{S}_3$ absorber film

Herein, the characterization of  $\text{Sb}_2\text{S}_3$  thin films grown by USP are detailed. The findings are published in articles I, II and IV. The quality of the as-deposited and annealed  $\text{Sb}_2\text{S}_3$  films were analyzed prior to their application in solar cells, with deposition parameters kept constant throughout the study.

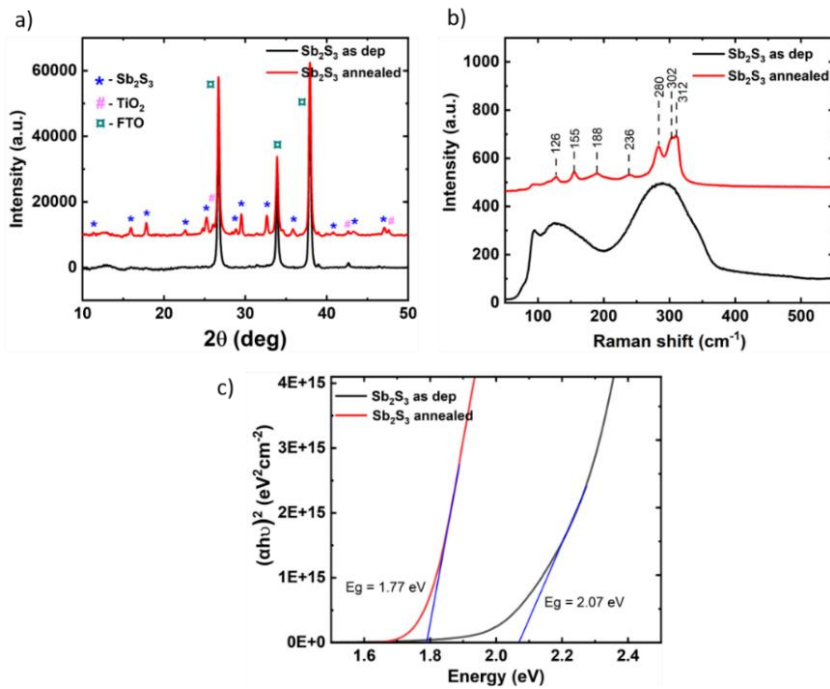


Figure 3.1. (a) XRD patterns, (b) Raman spectra, (c) Tauc plots of as-deposited and annealed  $\text{Sb}_2\text{S}_3$  films. Substrate: glass/FTO/ $\text{TiO}_2$ / $\text{Sb}_2\text{S}_3$ .

Optical microscopy images (Fig. S1 in SI, in article I and Fig. 2 in article II) showed that the as-deposited  $\text{Sb}_2\text{S}_3$  films conformally cover the  $\text{TiO}_2$  layer, devoid of pinholes or crystallization, which often occurs during deposition and can degrade film quality. Fig. 3.1a presents the XRD patterns of the as-deposited and annealed  $\text{Sb}_2\text{S}_3$  films on glass/FTO/ $\text{TiO}_2$  substrates. The as-deposited films exhibit only the peaks associated with the FTO and anatase  $\text{TiO}_2$  layers, indicating amorphous  $\text{Sb}_2\text{S}_3$  layer. After annealing, sharp peaks at  $2\theta$  values of  $15.9^\circ$ ,  $17.8^\circ$ ,  $29.2^\circ$ , and  $30.5^\circ$  appear, confirming the crystallization into orthorhombic  $\text{Sb}_2\text{S}_3$  (ICDD PDF 01-075-4013) [13,18,72]. No  $\text{Sb}_2\text{O}_3$  peaks, which appear at  $2\theta$  values of  $13.6^\circ$  and  $27.5^\circ$  are detected, indicating high-purity films quality devoid of impurities and undesired oxide phases. The transition from amorphous as deposited layer to crystalline  $\text{Sb}_2\text{S}_3$  layer after annealing is further confirmed by Raman spectroscopy (Fig. 3b). The sharp peaks observed at 128, 155, 188, 236, 280, 302, and  $312\text{ cm}^{-1}$ , are characteristic of the orthorhombic stibnite structure [13,18,72].

UV-Vis-NIR spectroscopy reveals that annealed  $\text{Sb}_2\text{S}_3$  films exhibit stronger absorption and a sharper edge at around 700 nm, compared to 650 nm for the amorphous films (article I and II). The optical band gaps were 1.77 eV for crystalline film after annealing and 2.07 eV for the as deposited amorphous films, as determined from the Tauc plot of the absorption spectra (Fig. 3.1c). The determined  $E_g$  values are similar to previously reported ones for sprayed  $\text{Sb}_2\text{S}_3$  films [13,18]. Optical, morphological, compositional and structural optical analyses indicate that annealed  $\text{Sb}_2\text{S}_3$  films provide good coverage, a single-phase stibnite structure, and a suitable bandgap of ca. 1.8 eV for solar cells. For each batch of solar cells prepared, the quality of the prepared  $\text{Sb}_2\text{S}_3$  absorber film was analyzed. The  $I_p$  of the  $\text{Sb}_2\text{S}_3$  layer was measured to be at 5.1 eV using the PYS technique. With a bandgap of 1.77 eV, the CBE is positioned at 3.4 eV (I–IV). The thickness of the  $\text{Sb}_2\text{S}_3$  absorber layer, as measured by SEM, ranged from 80 to 100 nm (I–IV). Next, for device fabrication, HTMs were spin-coated on the crystallized  $\text{Sb}_2\text{S}_3$ , followed by thermal evaporation of metal contacts.

### 3.2 Development of technology for deposition of HTM thin films

In this study, a total of eleven fluorene-based compounds were examined as HTMs for the first time in  $\text{Sb}_2\text{S}_3$  solar cells. These compounds are broadly categorized into three groups: fluorene-based HTMs with aliphatic chains (V1275, V1235, V1236, V1461), fluorene based HTMs with thiophene end units (V808, V1385 and V1386) and fluorene based HTMs with dimers linked with thiophene units. Three of the compounds – V1275, V1235 and V1236, from the first group have previously been synthesized, characterized and employed successfully as dopant-free HTMs in perovskite solar cells [140]. The remaining compounds were synthesized for the first time specifically for use in  $\text{Sb}_2\text{S}_3$  solar cells as HTMs. One of the aims of the present study was to develop the technology of application of these novel HTMs via spin coating. In prior applications, V1275, V1235 and V1236 were used at a concentration of 15 mM, producing HTM layers with a thickness of 70 nm in PSCs [140]. As fluorene-based compounds were applied as HTMs in  $\text{Sb}_2\text{S}_3$ -based solar cells for the first time, determining the appropriate layer thickness for highest efficiency was necessary. This was accomplished by changing the HTM concentration in the precursor solution to achieve the desired layer thickness suitable for the  $\text{Sb}_2\text{S}_3$  solar cell stack. Similarly, different concentrations of P3HT (0.5, 1 and 2% wt.) in the precursor solution were tested and optimized to maximize efficiency for the solar cell stack, as detailed in article I (Fig. S5 and Table S2, in SI).

Thin film  $\text{Sb}_2\text{S}_3$ -based solar cells were fabricated in the superstrate configuration of glass/FTO/ $\text{TiO}_2$ / $\text{Sb}_2\text{S}_3$ /HTM/Au, as illustrated in Fig. 2.1b, section 2.1. A systematic approach was used to optimize the concentration for all three groups of investigated fluorene-based compounds in their respective precursor solutions. For the first group of fluorene-based compounds with aliphatic chains (V1275, V1235, V1236, V1461), a 15 mM HTM precursor solution was initially used, a concentration that had previously been successful in PSCs [140]. However, the J-V characteristics of the prepared solar cell indicate low cell performance. Solar cell fabricated with 15 mM V1235 solution, exhibited a low  $J_{\text{SC}}$  of 0.8  $\text{mA}/\text{cm}^2$  and a high  $R_s$  of 23  $\Omega\cdot\text{cm}^2$  (see Table 3.1). Next, the HTM solutions were diluted to lower concentrations of 4, 2 and 1 mM. SEM cross-sectional images of solar cells with HTM layers from V1235 at various precursor concentrations are shown in Fig. 3.2.

Table 3.1. Effect of HTM V1235 precursor solution concentration on solar cell performance output parameters.

V1235 conc. [mM]	$V_{\text{OC}}$ [mV]	$J_{\text{SC}}$ [ $\text{mA}/\text{cm}^2$ ]	FF [%]	PCE [%]	$R_s$ [ $\Omega\cdot\text{cm}^2$ ]
15	490	0.8	21	0.8	23
4	570	12.5	42	3.0	2.1
2	587	15.5	47	4.3	1.3
1	582	14.1	45	3.7	1.0

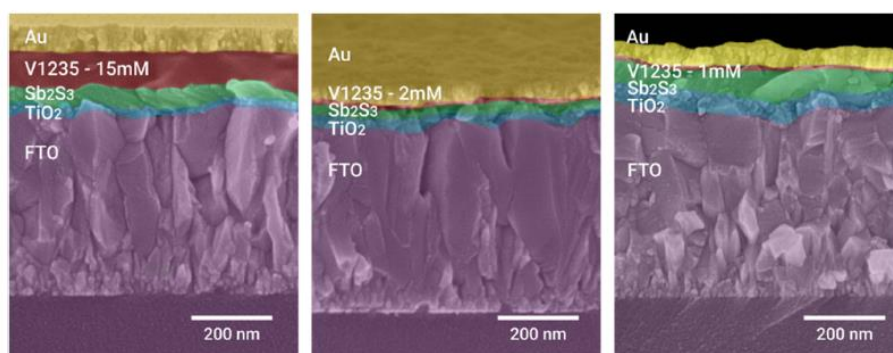


Figure 3.2. SEM cross-sectional images of  $\text{Sb}_2\text{S}_3$  solar cells with varying concentrations of HTM V1235 (15, 2, and 1 mM). Substrate – glass/FTO/ $\text{TiO}_2$ / $\text{Sb}_2\text{S}_3$ /HTM/Au.

As the concentration is decreased, HTM layer thicknesses also decrease: 120 nm for 15 mM, 25 nm for 2 mM, and 15 nm for 1 mM. This reduction in thickness correlates with a drop in  $R_s$  from 23 to 1.0  $\Omega\cdot\text{cm}^2$  as the concentration is reduced from 15 to 1 mM. For V1235, reducing the concentration to 2 mM increased resulting device  $V_{\text{OC}}$  to 587 mV,  $J_{\text{SC}}$  to 15.5  $\text{mA}/\text{cm}^2$ , FF to 47% and PCE to 4.3%. Conversely, further dilution to 1 mM reduced  $J_{\text{SC}}$  and PCE. Similar trends during concentration optimizations were observed for other HTMs V1275, V1236, and V1461 (Fig. 4a in article I and Fig. 3b-d in article III), with 2 mM giving the best results. Likely, very thin HTM layers (< 20 nm) may

not cover the absorber uniformly, causing pinholes and direct contact between the metal contact and the absorber. The molecular structure of the HTM influences layer formation, as seen in case of devices with V1275, which showed minimal performance decline at low thicknesses (see article III).

For the second group of fluorene-based compounds with thiophene end units (V808, V1385, and V1386), a concentration of 70 mM for V808 was initially tested. The resulting solar cell exhibited low PCE (< 1%) and very high  $R_s$  (> 100  $\Omega\text{-cm}^2$ ), likely due to the increased thickness from the high HTM concentration. Therefore, lower concentrations of 18, 9, and 4.5 mM were utilized. The J-V curves for the prepared solar cells with varying precursor concentrations of V808, V1385, and V1386 are presented in Fig. 3b-d, article III. The device PCEs with V808 at 70, 18, 9, and 4.5 mM were 0.1%, 2.0%, 4.7%, and 3.7%, respectively. A precursor concentration of 9 mM, producing a layer thickness of ca. 25 nm (Fig. 4c, article II), was determined to be optimal for all three investigated HTMs, leading to the highest device PCE.

For the third group of fluorene-based compounds with dimers linked with thiophene units (V1422, V1423, V1454, V1455), a similar systematic optimization of precursor solutions was carried on, as performed for the first two HTM groups. The impact of varying fluorene-based HTM solution concentrations (4, 2, 1, 0.6 mM) on solar cell performance was studied, with optimal cell performance observed at 2 mM, similar to the results obtained for HTMs with aliphatic chains (article I and III). Solar cells fabricated with 2 mM precursor solutions showed the highest performance, independent of the HTM used. The resulting solar cell performance parameters are presented in article IV (Table S1, in the SI).

In summary, a method for preparing layers of novel fluorene-based HTMs on USP deposited  $\text{Sb}_2\text{S}_3$  absorber layer via spin coating was developed. Systematic optimization of the concentration of the new compounds in the precursor solution led to HTM layers with an optimal thickness of 20–25 nm. In addition, a 1% wt. concentration of P3HT, resulting in an HTM layer thickness of about 80–100 nm, was found to be optimal for highest device performance in the  $\text{Sb}_2\text{S}_3$  solar cell stack.

### **3.3 Solar cells with fluorene-based HTMs with aliphatic chains (V1275, V1235, V1236, V1461)**

The first group of HTMs explored in antimony sulfide-based solar cells are fluorene-based compounds with aliphatic chains. The key distinction among these HTMs lies in the length of their aliphatic chains. The chemical structure of these HTMs – N2,N2,N7,N7-tetrakis[2,2-bis(4-methoxyphenyl)vinyl]-9H-fluorene-2,7-diamine (V1275), N2,N2,N7, N7-tetrakis[2,2-bis(4-methoxyphenyl)vinyl]-9,9-dipropyl-9H-fluorene-2,7-diamine (V1235), N2,N2,N7,N7-Tetrakis[2,2-bis(4-methoxyphenyl)vinyl]-9,9-dihexyl-9H-fluorene-2,7-diamine (V1236) and N2,N2,N7,N7-tetrakis[2,2-bis(4-methoxyphenyl)vinyl]-9,9-dinonyl-9H-fluorene-2,7-diamine (V1461) are presented in Fig. 3.3. Previously, V1275, V1235 and V1236 has been used in n-i-p perovskite solar cells as dopant-free HTMs with cells yielding PCE of up to 17.1% [140]. The synthesis route along with details of the characterization and properties of the HTMs are in articles [140], III and summarized in Table S1 in Appendix 2.

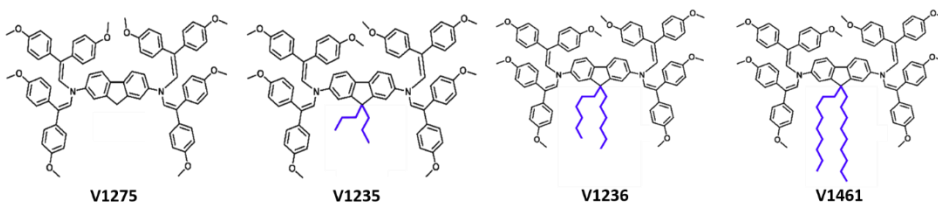


Figure 3.3. Chemical structures of fluorene-based compounds with different length of aliphatic chains – V1275, V1235, V1236 and V1461.

$\text{Sb}_2\text{S}_3$  solar cells were fabricated in superstrate configuration as shown in Fig 2.1b and the results of solar cell study are published in articles I and III. The devices were fabricated using an optimal 2 mM precursor solution concentrations of the HTMs V1275, V1235, V1236, and V1461, along with devices incorporating 1 wt. % P3HT, and a reference device without an HTM (glass/FTO/ $\text{TiO}_2$ / $\text{Sb}_2\text{S}_3$ /Au), all within the same batch. The J-V characteristics of the champion cells are presented in Fig. 3.4a, with corresponding data shown in Table 3.2. The reference device without any HTM exhibited a  $V_{\text{oc}}$  of 450 mV,  $J_{\text{sc}}$  of 12.8  $\text{mA}/\text{cm}^2$ , FF of 40%, and PCE of 2.1%.

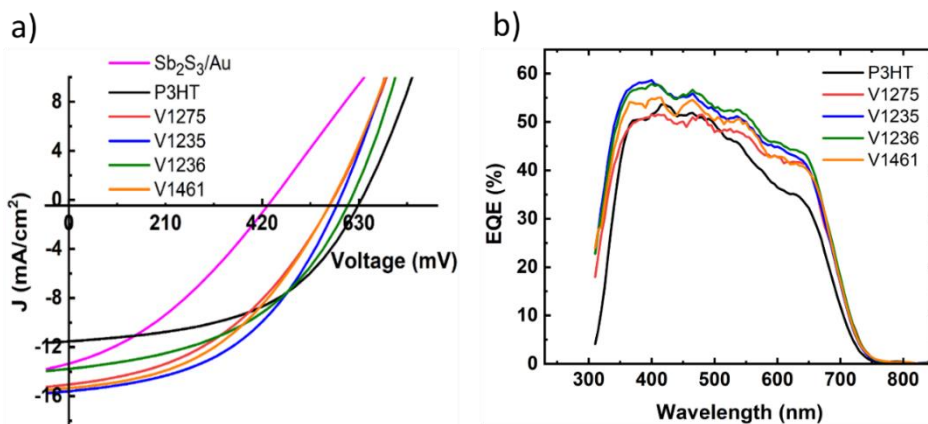


Figure 3.4. (a) J-V characteristics of champion cells without HTM and with HTMs (V1275, V1235, V1236, V1461 and P3HT), and (b) EQE curves of  $\text{Sb}_2\text{S}_3$  solar cells with different HTMs.

Table 3.2. Solar cell performance parameters of champion devices without HTM and with HTMs – V1275, V1235, V1236, V1461 and P3HT.

HTM	HTM conc.	$V_{\text{oc}}$ [mV]	$J_{\text{sc}}$ [ $\text{mA}/\text{cm}^2$ ]	FF [%]	PCE [%]	$R_{\text{s}}$ [ $\Omega \cdot \text{cm}^2$ ]	$R_{\text{sh}}$ [ $\Omega \cdot \text{cm}^2$ ]
No HTM	-	450	12.8	40	2.1	3.2	210
V1275	2 mM	572	15.3	44	3.9	1.2	390
V1235	2 mM	587	15.5	47	4.3	1.3	444
V1236	2 mM	612	13.8	46	3.9	0.6	384
V1461	2 mM	573	15.0	43	3.7	1.8	373
P3HT	1 wt. %	650	11.2	50	3.8	3.5	650

The inclusion of HTMs significantly improved the device  $V_{OC}$ , reaching 570–610 mV for the fluorene-based HTMs and 650 mV for P3HT, correlating with an increase in shunt resistance ( $R_{SH}$ ). The increase in  $V_{OC}$  by use of HTMs can be attributed to the prevention of direct contact between the Au electrode and the absorber layer, which reduces recombination losses at the back contact and enhances charge extraction. The highest device PCE of 4.3% was achieved with the HTM V1235, being higher than that demonstrated by the device with P3HT, which exhibited a PCE of 3.8%.

The external quantum efficiency (EQE) responses of the fabricated solar cells were analyzed and are presented in Fig. 3.4b. Solar cells with fluorene-based HTMs demonstrate higher EQE spectral response across entire wavelength range as compared to cells with P3HT. The P3HT cells exhibited a concave shape in the 500–700 nm region, while this feature is not expressed in the fluorene-based HTM cells. This concavity in EQE curve is linked to P3HT's lower bandgap value of ca. 1.8 eV, compared to the bandgap of novel HTMs of 2.8–3.0 eV ([140], III). It should be notified here that a mistake was made in determination of the band gap value for V1236 in article I, and thus we are using here and in the further analysis  $E_g$  of 2.8 eV as measured for the material by Daskeviciute et al. in [140].

The statistical box plots of solar cell performance parameters' ( $V_{OC}$ ,  $J_{SC}$ , FF and PCE) for devices with no HTM, with new HTMs (V1275, V1235, V1236, V1461) and with P3HT are presented in Fig. 3.5. Solar cell devices with all new HTMs exhibit higher  $J_{SC}$  but a lower  $V_{OC}$  compared to devices employing P3HT. The higher  $J_{SC}$  in cells with new HTMs are likely due to their lower thickness and higher  $E_g$  value of 2.8–3.0 eV compared to P3HT. However,  $V_{OC}$  values in devices are slightly lower with new HTMs (570–610 mV) compared to devices with P3HT (600–650 mV). The higher  $V_{OC}$  observed in devices using P3HT could be attributed to beneficial interactions at the  $Sb_2S_3$ /P3HT interface. The presence of the thiophene unit in P3HT's structure can enhance carrier collection and reduce recombination [23,141,142]. Additionally, new HTMs with a lower thickness (15–20 nm) may enable a direct Au contact with the absorber at some points, unlike in case of thicker P3HT film (ca. 100 nm).

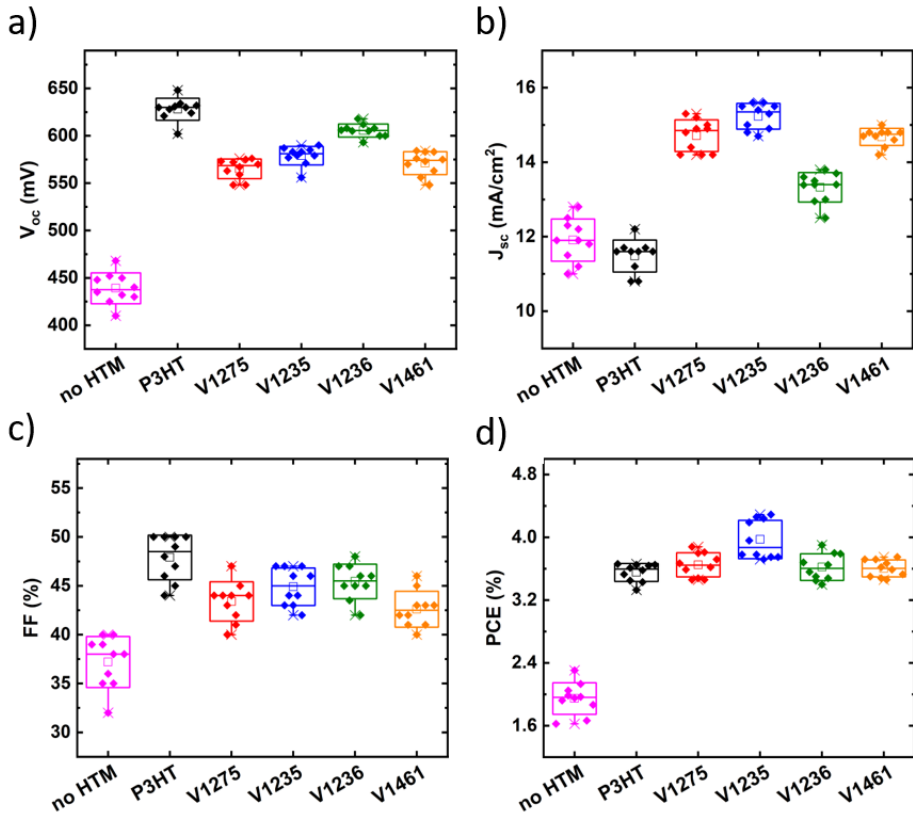


Figure 3.5. Box-plot diagrams of device performance parameters ( $V_{oc}$ ,  $J_{sc}$ , FF, PCE) of the fabricated solar cell devices without HTM and with various HTMs (P3HT, V1275, V1235, V1236 and V1461).

Interestingly, previous study with perovskite cells employing fluorene-based HTMs (70–150 nm) also yielded lower  $V_{oc}$  compared to devices with Spiro-OMeTAD [140]. Despite the reduced  $V_{oc}$ , the PCE of devices with HTMs V1275, V1235, V1236 and V1461 is comparable or higher than that obtained with P3HT. According to the Fig 3.5, the spread of the device performance parameters is reasonably small, demonstrating a good reproducibility of the fabricated solar cells.

Photoemission yield spectroscopy (PYS) was employed to measure the  $I_p$  values of all functional layers within the solar cell stack – FTO,  $TiO_2$ ,  $Sb_2S_3$ , and the investigated HTMs – in order to determine the band alignment. In TCO/ $TiO_2$ / $Sb_2S_3$ /HTM device, VBE values for FTO,  $TiO_2$ , and  $Sb_2S_3$  were at  $-8.7$ ,  $-7.4$  and  $-5.1$  eV, relative to the vacuum level, respectively. The measured work function of Au contact was at 5.1 eV. HOMO levels for organic HTMs – P3HT, V1275, V1235, V1236 and V1461 were determined to be at  $-4.6$ ,  $-4.9$ ,  $-4.8$ ,  $-5.0$  and  $-4.9$  eV, respectively. HOMO levels of new HTMs are close to that of Spiro-OMeTAD ( $-5.2$  eV) and PCPDTBT ( $-5.2$  eV), as reported in literature [6]. The determined  $E_g$  values were found to be 2.96 [III], 2.96 [III], 2.80 [140], and 2.98 eV [III] for V1275, V1235, V1236 and V1461, respectively.

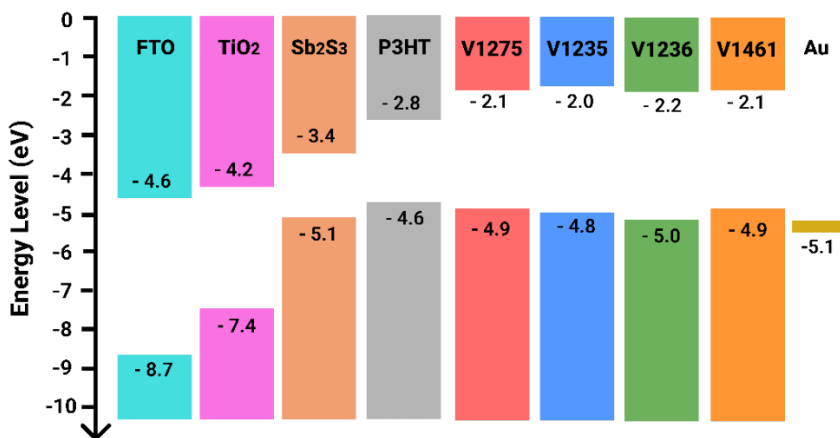


Figure 3.6. Band energy diagram of  $\text{Sb}_2\text{S}_3$  solar cells with functional layers (FTO,  $\text{TiO}_2$ ,  $\text{Sb}_2\text{S}_3$ , HTMs and Au).

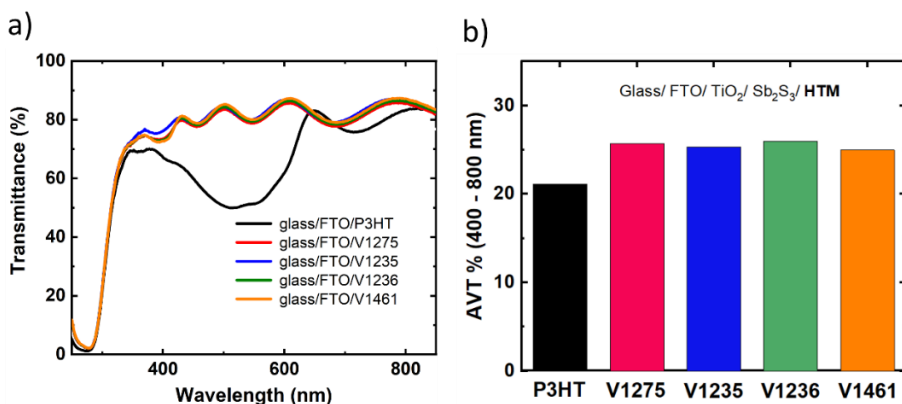


Figure 3.7. (a) Transmittance spectra of HTM layers deposited on glass/FTO substrate and (b) calculated average visible transmittance (AVT) values for solar cell devices in the 400–800 nm range.

Recombination losses are reduced by applying the new HTM, as their electron affinity ( $E_a$ ) or LUMO level (–2.0 to –2.2 eV, Fig. 3.6) is lower than the CBE of  $\text{Sb}_2\text{S}_3$  (–3.4 eV), effectively blocking electron transfer from the  $\text{Sb}_2\text{S}_3$  absorber to the HTM. The VBE of  $\text{Sb}_2\text{S}_3$  (–5.1 eV) and the new HTMs (–4.8 to –5.0 eV) allow for feasible photogenerated hole transfer, although HTMs with higher HOMO levels could offer improved performance.

The transmittance spectra of the HTM layers (V1275, V1235, V1236, V1461 and P3HT) deposited on a glass/FTO substrate are presented in Fig. 3.7a. Parasitic absorption is evident for P3HT within the 400–650 nm range, which is not observed for the new HTMs. The AVT values, calculated over the 400–800 nm range for all fabricated solar cell devices (glass/FTO/ $\text{Sb}_2\text{S}_3$ /HTM), are shown in Fig. 3.7b. Solar cells with P3HT exhibit AVT values of 23%, while those with fluorene-based HTMs reach up to 27%, offering about 20% higher transparency than P3HT-based devices. HTM film thicknesses are approximately 100 nm for P3HT and 25 nm for fluorene-based HTMs, optimized for maximum efficiency in  $\text{Sb}_2\text{S}_3$ -based solar cells. The increased transparency with fluorene-based HTMs underscores their potential for semi-transparent solar cell applications.

In summary, we have applied four dopant free fluorene-based compounds with different length of aliphatic chains in their structure – V1275, V1235, V1236 and V1461, as HTMs in antimony sulfide based solar cells. Band diagrams of solar cells employing the new HTMs reveal favorable band offsets for efficient charge transfer. Results demonstrated notable improvements in device performance with the introduction of new HTMs as compared to device without an HTM. Solar cells with optimized thicknesses of layers of HTMs V1275, V1235, V1236, and V1461 achieved efficiencies of 3.9%, 4.3%, 3.9%, and 3.7%, respectively, that are comparable or higher than obtained with P3HT based device (3.8%). Solar cells with the new HTMs achieve AVT values of up to 27% in the visible range, demonstrating their suitability for semi-transparent applications.

### 3.4 Solar cells with fluorene-based HTMs with thiophene end units (V808, V1385 and V1386)

The second group of HTMs explored in  $\text{Sb}_2\text{S}_3$  solar cells are fluorene-based molecules with thiophene end units, and the results are published in article II. The core distinction between these HTMs is the number of thiophene units present. The three HTMs explored were V808, V1385 and V1386 with one, two and three thiophene units, respectively. The chemical structure of these HTMs – *N2,N2,N7,N7*-tetrakis(4-methoxyphenyl)-9-(thiophen-2-ylmethylene)-9*H*-fluorene-2,7-diamine (V808), 9-([2,2':5',2''-terthiophen]-5-ylmethylene)-*N2,N2,N7,N7*-tetrakis(4-methoxyphenyl)-9*H*-fluorene-2,7-diamine (V1385), and 9-([2,2':-bithiophen]-5-ylmethylene)-*N2,N2,N7,N7*-tetrakis(4-methoxyphenyl)-9*H*-fluorene-2,7-diamine (V1386) are presented in Fig. 3.8. These compounds have been synthesized for the first time and are inspired from the structure of thiophene containing P3HT.

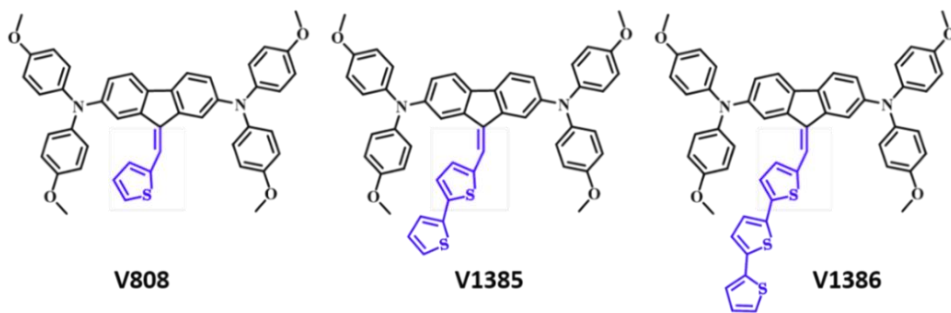


Figure 3.8. Chemical structures of the fluorene-based HTMs with different number of thiophene end units – V808, V1385, and V1386.

The objective of investigating thiophene-based HTMs was motivated by recent studies by various research groups demonstrating that thiophene units inside the HTM molecule may interact with Sb atoms in the absorber layer  $\text{Sb}_2(\text{S},\text{Se})_3$  [23,143,144]. This led to improvement in the interfacial characteristics between  $\text{Sb}_2(\text{S},\text{Se})_3$  and the HTM layers [23,143,144]. The interaction can create favorable hole transport pathways and may improve both the  $V_{\text{oc}}$  and FF relative to devices without any HTM layer. V808 molecule has a singular thiophene end unit with symmetrically attached 4,4-dimethoxydiphenylamine chromophores on either side of the fluorene core. Additionally, to investigate the possibility of enhanced Sb-S interaction, molecules incorporating two and three thiophene units into the fluorene core were also

synthesized, and are referred to as V1385 and V1386, respectively. Structural, thermal, optical and electrical properties of the synthesized HTMs were analyzed and the results are presented in article II and summarized in Table S1 in Appendix 2.

Solar cells were fabricated using novel HTMs – V808, V1385, and V1386 in the same batch and were compared to the devices without HTM and with conventional HTM – P3HT. Solar cells were fabricated using 9 mM precursor solution concentrations of the HTMs V808, V1385, and V1386, as had been previously optimized for the solar cell stack (see section 3.2). Fabricated devices without an HTM demonstrated a  $V_{OC}$  of 430 mV, a  $J_{SC}$  of 12.0 mA/cm<sup>2</sup>, FF of 41% and PCE of 2.10%, consistent with the behavior of bare Sb<sub>2</sub>S<sub>3</sub>-based solar cells (as shown in section 3.3). The J-V characteristics of the champion Sb<sub>2</sub>S<sub>3</sub> solar cells without and with HTMs (V808, V1385, V1386 and P3HT) are presented in Fig. 3.9a, along with device parameters are detailed in Table 3.3.

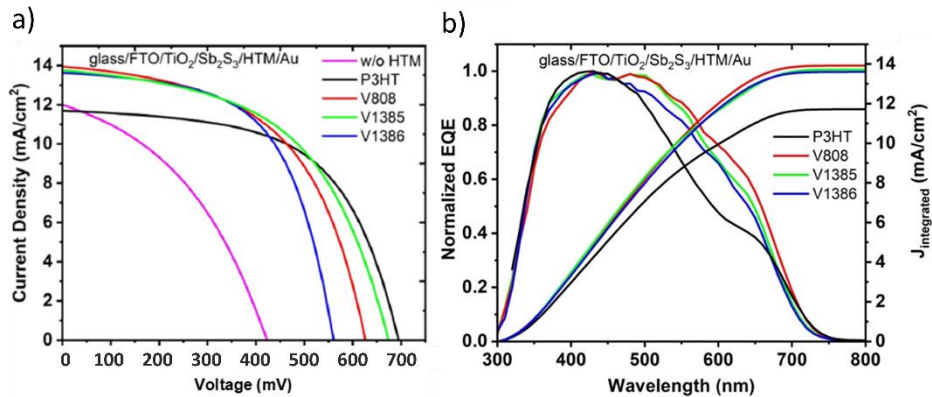


Figure 3.9. (a) J-V characteristics of champion solar cells without HTM and with HTMs – P3HT, V808, V1385 and V1386 and (b) Normalized EQE curves with the integrated  $J_{SC}$  of Sb<sub>2</sub>S<sub>3</sub> solar cells with different HTMs.

Devices with the new HTMs achieved PCE of 4.73%, 4.94%, and 4.50% with V808, V1385, and V1386, respectively, that is significantly higher than 2.1% recorded for the device without any HTM. Open circuit voltages for devices with the new HTMs are in the range of 560–680 mV, that is slightly lower compared to 690 mV measured for P3HT-based solar cells. It should be noted here the  $V_{OC}$  values in the solar cell device decrease with an increase in the number of thiophene moieties in HTM molecule (from V808 to V1386) as can be clearly seen from J-V curves in Fig. 3.9a and box-plots of the device output parameters, in Fig. 3.10. Solar cells with new HTMs exhibit similarly high  $J_{SC}$  values up to 14 mA/cm<sup>2</sup> (Fig. 3.9a, Fig. 3.10b) that is higher compared to ca. 12.0 mA/cm<sup>2</sup> for devices without any HTM or with P3HT.

Table 3.3. Device performance parameters of champion  $Sb_2S_3$  solar cells with HTMs – V808, V1385, V1386 and P3HT.

HTM	HTM conc.	$V_{oc}$ [mV]	$J_{sc}$ [mA/cm <sup>2</sup> ]	FF [%]	PCE [%]	$R_s$ [ $\Omega \cdot cm^2$ ]	$R_{SH}$ [ $\Omega \cdot cm^2$ ]
no HTM	-	430	12.0	41	2.1	1.3	167
V808	9 mM	630	13.9	54	4.7	1.0	586
V1385	9 mM	680	13.7	53	4.9	2.3	569
V1386	9 mM	560	13.6	59	4.5	0.9	844
P3HT	1 wt. %	690	11.7	58	4.7	2.1	1190

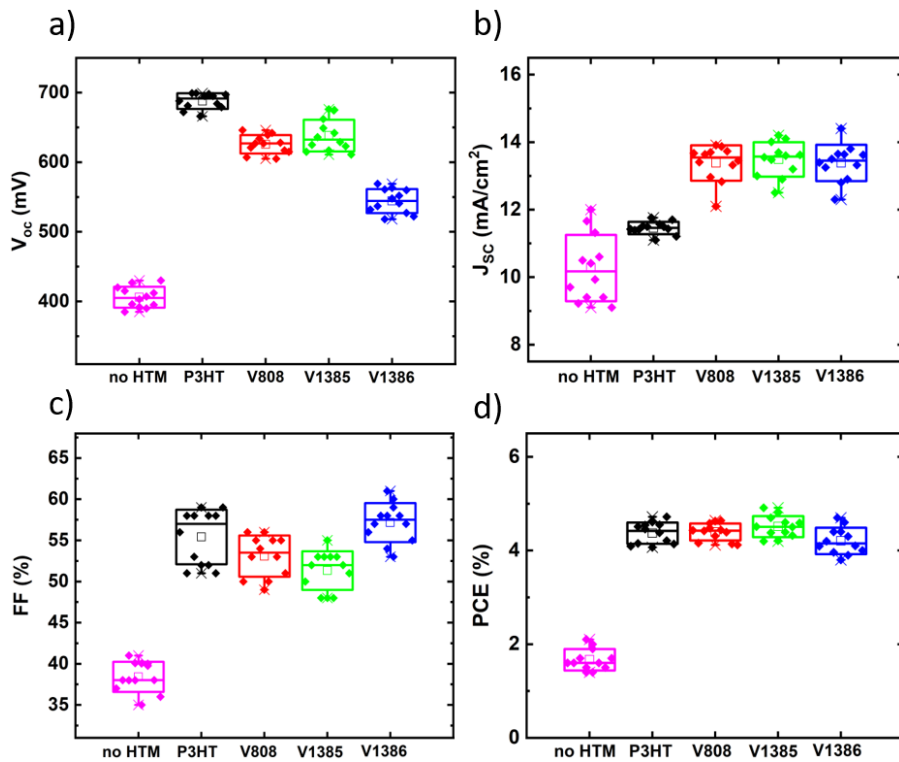


Figure 3.10. Box-plot diagrams of performance parameters of the fabricated solar cell devices without any HTM and incorporating various HTMs (P3HT, V808, V1385, and V1386).

Solar cells with fluorene-based HTMs with thiophene end units exhibit fill factor values around 55% (Fig. 3.10c) and very similar average PCEs at around 4.7%, comparable to that with P3HT (Fig. 3.10d), except for V1386, which shows slightly lower efficiency due to a reduced  $V_{oc}$ . The statistical box plots in Fig. 3.10 also demonstrates a relatively good reproducibility of device performance parameters, including nearly identical efficiency spread for both P3HT and the new HTM devices, with average efficiencies in a similar range. The normalized EQE curves of solar cells employing both new HTM layers and P3HT are presented in Fig. 3.9b. Notably, solar cells with P3HT ( $E_g = 1.8$  eV) show a dip in

EQE within the 500–650 nm range, indicating parasitic absorption losses. In contrast, new HTMs with band gap values in the range of 2.3 to 2.9 eV do not exhibit this dip.

The HOMO levels for new HTMs – V808, V1385, and V1386 were determined to be positioned at –4.9, –5.0 and –5.0 eV, respectively, according to  $I_p$  measurements via PYS technique. The  $E_g$  values of V808, V1385, and V1386 are estimated to be 2.8, 2.5, and 2.3 eV, respectively, based on the absorption coefficient-derived Tauc’s plots. The energy band diagram, as depicted in Fig. 3.11, illustrates agreeable band offsets conducive to the transport of photogenerated holes from the absorber to the metal back contact. Although, despite exhibiting favorable band edge positions, solar cell devices with fluorene-based HTMs have led to slightly lower  $V_{oc}$  values compared to P3HT. This may be attributed to additional factors such as interfacial recombination at the  $Sb_2S_3$ /HTM interface. Two potential sources of recombination could be the direct contact between the electrode and absorber layer, leading to creation of micro shunts, due to thinner new HTM layers and the quality of the interface between the absorber and HTM layer.



Figure 3.11. Band energy diagram of  $Sb_2S_3$  solar cell stack with different HTMs (P3HT, V808, V1385 and V1386).

An assessment of the overall optical transparency of device stacks without the top metal contact was conducted. Optical transmittance studies conducted for P3HT and the new HTM layers (V808, V1385, and V1386) on glass/FTO substrates, as depicted in Fig. 3.12a, corroborate the absorption by P3HT, as evidenced by the dip in transmittance curve within the 400–650 nm region.

Fig. 3.12b presents the AVT of the solar cells as calculated from total transmittance spectra within the 400–800 nm range for the devices (without metal contact) employing P3HT, V808, V1385, and V1386 HTMs, yielding values of approximately 26, 33, 30 and 28%, respectively. It can be concluded that the number of thiophene units affect the value of the band gap and this is reflected in the final AVT of the device.

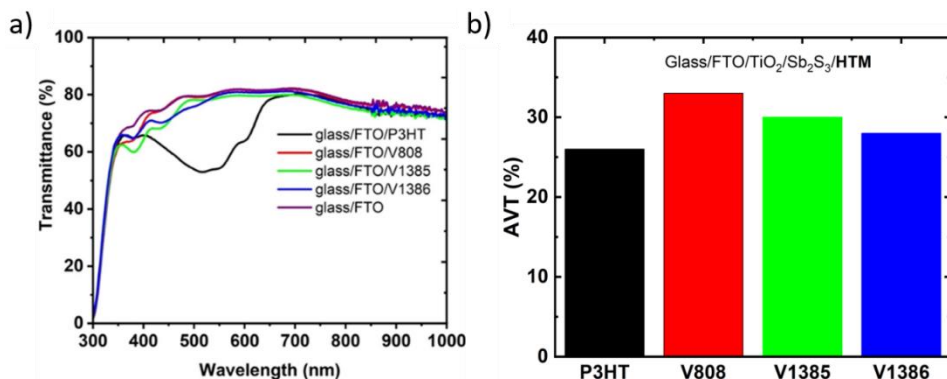


Figure 3.12. (a) Transmittance curves of glass/FTO and glass/FTO/HTM stacks and (b) calculated AVT for solar cells without metal contact in range of 400–800 nm, sample – glass/FTO/TiO<sub>2</sub>/Sb<sub>2</sub>S<sub>3</sub>/HTM.

In summary, novel fluorene-based HTMs with varying number of thiophene end units (V808, V1385, and V1386) were introduced for the first time in semi-transparent Sb<sub>2</sub>S<sub>3</sub> solar cells. The fabricated devices exhibited PCE between 4.5% and 4.9%, and an AVT of 30% to 33% in the wavelength range of 400 to 800 nm. In contrast, solar cells utilizing conventional P3HT as the HTM achieved a PCE of 4.7%, with lower transparency (AVT – 26%), which is attributed to inherent parasitic absorption losses. The band diagram reveals favorable band offsets for the new HTMs, confirming their suitability as HTMs in Sb<sub>2</sub>S<sub>3</sub> solar cells for semi-transparent applications.

### 3.5 Solar cells with fluorene-based HTMs with dimers linked with thiophene units (V1422, V1423, V1454, V1455)

The third group of HTMs explored in antimony sulfide-based solar cells are dimers linked with thiophene units. The synthesis route of the HTMs along with their characterization and properties are published in article IV and summarized in Table S1 in Appendix 2. The solar cell results are presented in article IV. The chemical structure of these HTMs – 9,9'-[(2,2'-Bithiophene)-5,5'-diylbis(methanylylidene)]bis[N2 ,N2 ,N7 ,N7 -tetrakis(4-methoxyphenyl)-9H-fluorene-2,7-diamine] (V1422), 9,9'-[(2,2':5',2''-Terthiophene)-5,5'-diylbis(methanylylidene)]bis[N2 ,N2 ,N7 ,N7 -tetrakis(4- methoxyphenyl)-9H-fluorene-2,7-diamine] (V1423), 4,4',4'',4''''-([2,2'-bithiophene)-5,5'-diylbis(methanylylidene)]bis(9H-fluorene-2,7-diyl-9-ylidene))tetrakis(N, N-bis(4-methoxyphenyl)aniline) (V1454) and 4,4',4'',4''''-([2,2':5',2''-terthiophene)-5,5''-diylbis(methanylylidene)]bis(9H-fluorene-2,7-diyl-9-ylidene))tetrakis(N, N-bis(4-methoxyphenyl)aniline) (V1455) are presented in Fig. 3.13. The chemical structure has 4,40-dimethoxydiphenylamine-substituted fluorene fragments, commonly utilized in organic HTMs such as Spiro-OMeTAD [143]. The dimer structure is inspired from Spiro-OMeTAD and incorporates thiophene units as found in P3HT. The investigated HTMs, feature diphenylamine (V1422 and V1423) or triphenylamine (V1454 and V1455) side fragments, with all sharing a central core containing varying numbers of thiophene moieties.

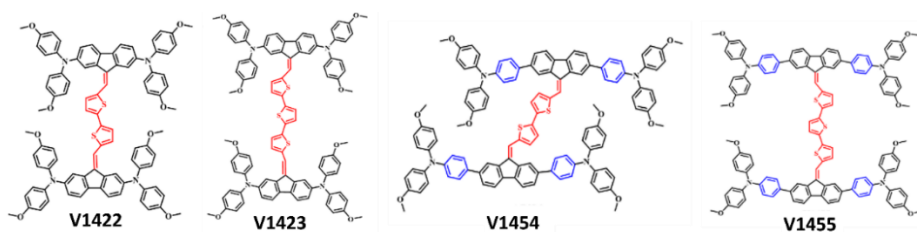


Figure 3.13. Chemical structures of fluorene-based compounds with dimers linked with thiophene units - V1422, V1423, V1454 and V1455.

The J-V characteristics of the champion devices using dimer-type HTMs are depicted in Fig. 3.14a, with the resulting output parameters shown in Table 3.4. Solar cells were fabricated using 2 mM precursor solution concentrations of the HTMs V1422, V1423, V1454, and V1455, as previously optimized for the  $\text{Sb}_2\text{S}_3$  solar cell stack (see section 3.2). These concentrations had been previously optimized for the  $\text{Sb}_2\text{S}_3$  solar cell stack (see section 3.2). The reference device without any HTM, yielded a  $V_{oc}$  of 478 mV,  $J_{sc}$  of 8.7  $\text{mA}/\text{cm}^2$ , FF of 46 %, and a PCE of 1.9%.

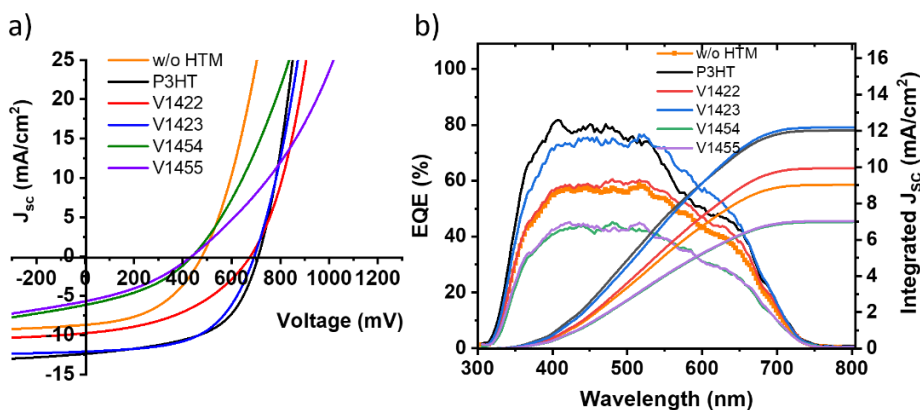


Figure 3.14. (a) J-V characteristics of champion cells without HTM and with HTMs (V1422, V1423, V1454, V1455 and P3HT) and (b) EQE curves with calculated integrated  $J_{sc}$  values of  $\text{Sb}_2\text{S}_3$  solar cells with different HTMs.

Table 3.4. Key performance metrics of champion  $\text{Sb}_2\text{S}_3$  solar cells without any HTM and with HTMs (V1422, V1423, V1454 V1455 and P3HT).

HTM	HTM conc.	$V_{oc}$ [mV]	$J_{sc}$ [ $\text{mA}/\text{cm}^2$ ]	FF [%]	PCE [%]	$R_s$ [ $\Omega \cdot \text{cm}^2$ ]	$R_{sh}$ [ $\Omega \cdot \text{cm}^2$ ]
no HTM	-	478	8.7	46	1.9	1.1	514
V1422	2 mM	656	9.7	43	3.9	1.7	436
V1423	2 mM	673	12.1	56	4.5	1.3	1005
V1454	2 mM	439	5.7	35	0.8	2.7	192
V1455	2 mM	437	6.1	33	0.7	4.9	198
P3HT	1 wt. %	689	12.2	55	4.7	1.8	526

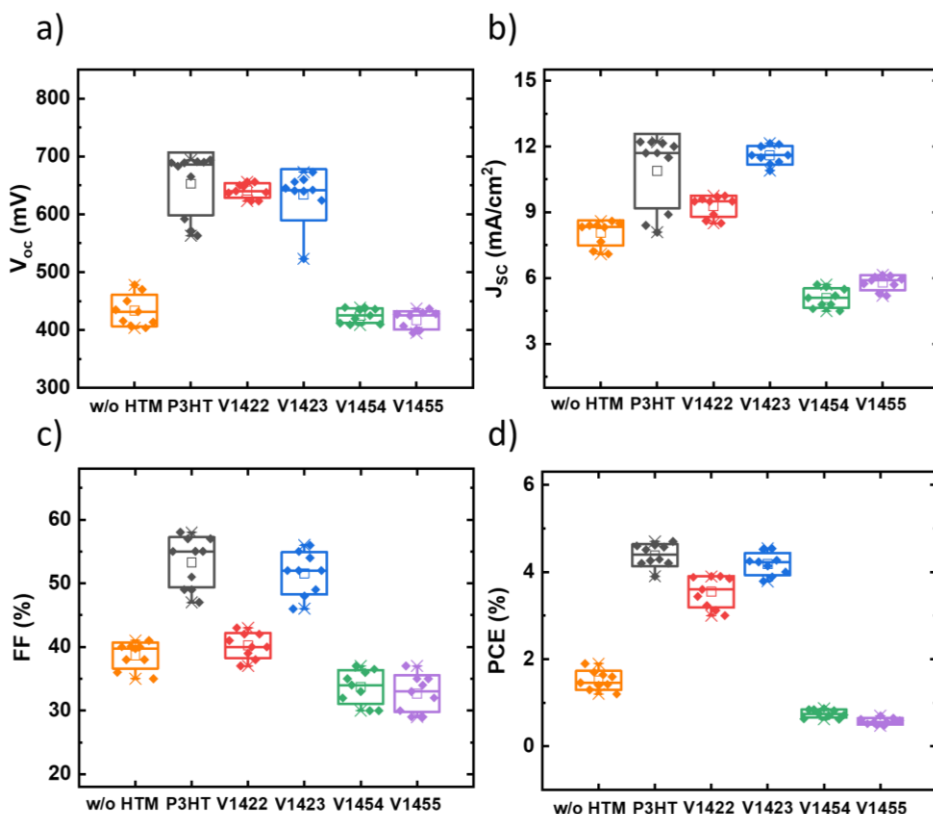


Figure 3.15. Box plots of  $Sb_2S_3$  solar cells with P3HT, V1422, V1423, V1454 and V1455 as HTMs: a)  $V_{oc}$ , b)  $J_{sc}$ , c) FF and d) PCE.

The introduction of HTM V1423 significantly improved the  $V_{oc}$  from 478 to 673 mV,  $J_{sc}$  from 8.7 to 12.1  $mA/cm^2$ , FF from 46% to 56%, and PCE from 1.9% to 4.5%, compared to a device without an HTM. Devices with V1422 and V1423, containing diphenylamine side units show significant improvement in output parameters (Fig. 3.14.a and Fig. 3.15) than devices with HTMs V1454 and V1455, which have triphenylamine side fragments, that showed no improvement in  $V_{oc}$ ,  $J_{sc}$ , FF and PCE compared to the device without an HTM. Thus, only the use of HTMs V1422 and V1423 significantly reduced carrier recombination at the back interface, enhancing carrier collection.

The EQE curves for champion devices with and without HTM layers, as well as those with various HTMs, are shown in Fig. 3.14b. A dip in the spectral response of the P3HT device is observed, due to its characteristic parasitic absorption losses (I, II, III). EQE concavity is less pronounced with the new HTMs, which have a comparable bandgap (1.9 eV) but are much thinner (20–25 nm) than P3HT (80–100 nm). The calculated integrated  $J_{sc}$  based on EQE spectra (Fig. 3.14b), closely correspond to the values obtained from the J-V curves (see Table 3.4). A statistical representation in form of box plots of cell parameters, both without any HTM and with investigated HTMs (see Fig. 3.15), underscore the high reproducibility of the results.

To evaluate the energy level alignment between the synthesized HTMs,  $Sb_2S_3$ , and the metal back contact, PYS was used to measure the  $I_p$ . The HOMO levels of V1422, V1423, V1454, and V1455 were determined to be at  $-4.94$ ,  $-4.94$ ,  $-5.05$ , and  $-5.08$  eV relative

to the vacuum level, respectively. The  $E_g$  values, as determined from Tauc plots were found to be 1.87, 1.90, 1.88, and 1.89 eV for V1422, V1423, V1454, and V1455, respectively. The constructed energy band diagram, as depicted in Fig. 3.16, illustrates agreeable band offsets conducive to the transport of photogenerated carriers from the absorber to the metal back contact. A larger barrier ( $> 0.3$  eV) between the CBE of  $\text{Sb}_2\text{S}_3$  ( $-3.4$  eV) and the LUMO levels of the new HTMs ( $-3.0$  to  $-3.2$  eV) further ensures effective electron blocking at the back interface.

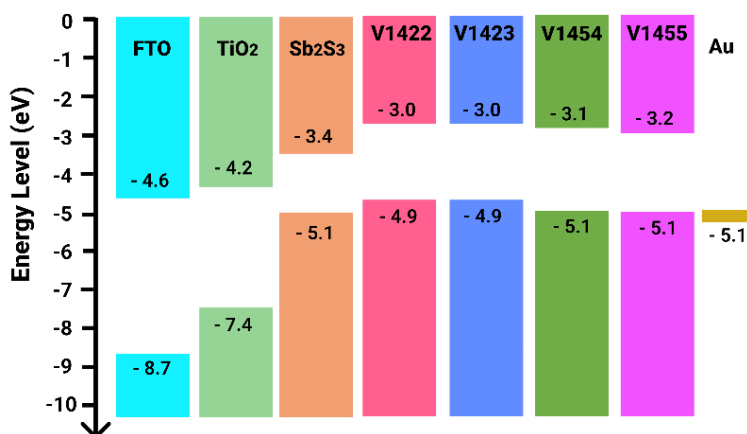


Figure 3.16. (a) Band energy diagram of  $\text{Sb}_2\text{S}_3$  cell with different HTMs.

Band energy diagram of  $\text{Sb}_2\text{S}_3$  solar cell with different HTMs (V1422, V1423, V1454, V1455 and P3HT) is presented in Fig. 3.16, based on  $I_p$  and  $E_g$  values measured by PYS and optical spectroscopy techniques, respectively. The HOMO levels of V1422, V1423, V1454, and V1455 were determined to be at  $-4.94$ ,  $-4.94$ ,  $-5.05$ , and  $-5.08$  eV relative to the vacuum level, respectively. The  $E_g$  values, as determined from Tauc plots were found to be 1.87, 1.90, 1.88, and 1.89 eV for V1422, V1423, V1454, and V1455, respectively. The energy band diagram, as depicted in Fig. 3.16, illustrates agreeable band offsets conducive to the transport of photogenerated holes from the absorber to the metal back contact. A barrier between the CBE of  $\text{Sb}_2\text{S}_3$  ( $-3.4$  eV) and the LUMO levels of the V1422 and V1423 ( $-3.0$  eV) is larger than 0.3 eV, ensuring effective electron blocking at the back interface. In case of V1454 and V1455, this condition is not fulfilled.

Fig. 3.17a presents the total transmittance spectra of HTM layers on glass substrates. In case of P3HT, a dip can be seen in the total transmittance spectrum (Fig. 3.17a), in region 400–700 nm. Nevertheless, all HTMs used here exhibit similar bandgap value of 1.8–1.9 eV, this cavity is much lower for V1422, V1423, V1454, V1455 as the thickness of these layers is ca. 20–25 nm, while P3HT layer is ca. 100 nm thick. This is also the main reason why solar cells with fluorene-based HTMs show a higher AVT (24–26%) than P3HT-based devices (21%) (Fig. 3.17b).

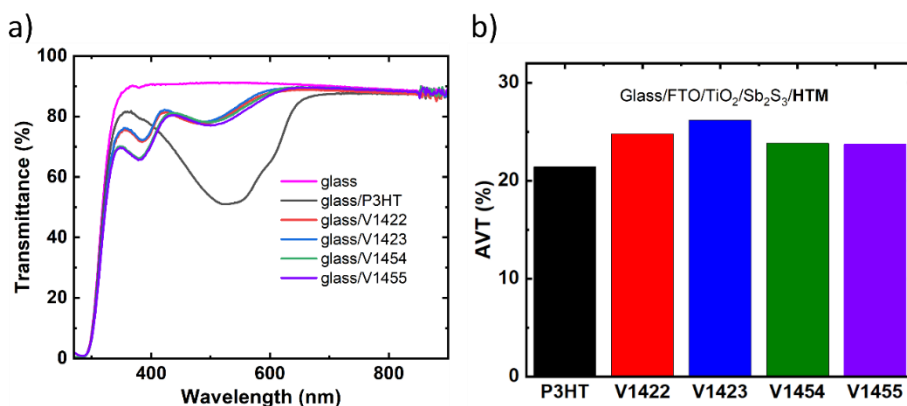


Figure 3.17. (a) Transmittance spectra of HTM layers deposited on glass substrate and (b) Calculated average visible transmittance (AVT) values for solar cell devices without Au contact, in the 400–800 nm range.

The inclusion of thiophene into the molecular structure is anticipated to facilitate interactions of S - Sb atoms at the absorber/HTM interface, potentially leading to an improvement in the interfacial properties as demonstrated in studies by many groups [23,141,142]. Our results show that the use of dimers, especially of V1454 and V1455 does not lead to similar results as obtained with HTMs containing thiophene end units (V808, V1385 and V1386). A question arises about chemical interaction at Sb<sub>2</sub>S<sub>3</sub>/HTM interface and X-ray photoelectron spectroscopy (XPS) studies were conducted to elucidate the problem.

Fluorene-based HTMs on glass substrates as well as within Sb<sub>2</sub>S<sub>3</sub> solar cell stacks were analyzed. The XPS spectra for the Sb 3d and S 2p regions of Sb<sub>2</sub>S<sub>3</sub>/HTM samples (V1422, V1423, V1454, V1455) with different etching times are presented in Fig. S6 and S7, in the SI of article IV. For the Sb<sub>2</sub>S<sub>3</sub> pristine sample (Fig. 3.18a), the Sb 3d core level peaks are observed at 539.7 eV (Sb 3d<sub>3/2</sub>) and 530.3 eV (Sb 3d<sub>5/2</sub>). With application of V1423, these peaks shifted to lower binding energy (BE) values of 539.2 eV and 529.9 eV, respectively. A similar shift is seen in case of V1454 (Fig. 3.18b), indicating an increase in electron density around Sb atoms. Comparable shifts in the Sb 3d core level peak was observed when applying dithieno[3,2-b:20,30-d]pyrrole-cored (DTPTThMe-ThTPA) [122] and thiophene-modified quinoxaline-core small molecules [23] to Sb<sub>2</sub>(S,Se)<sub>3</sub> films.

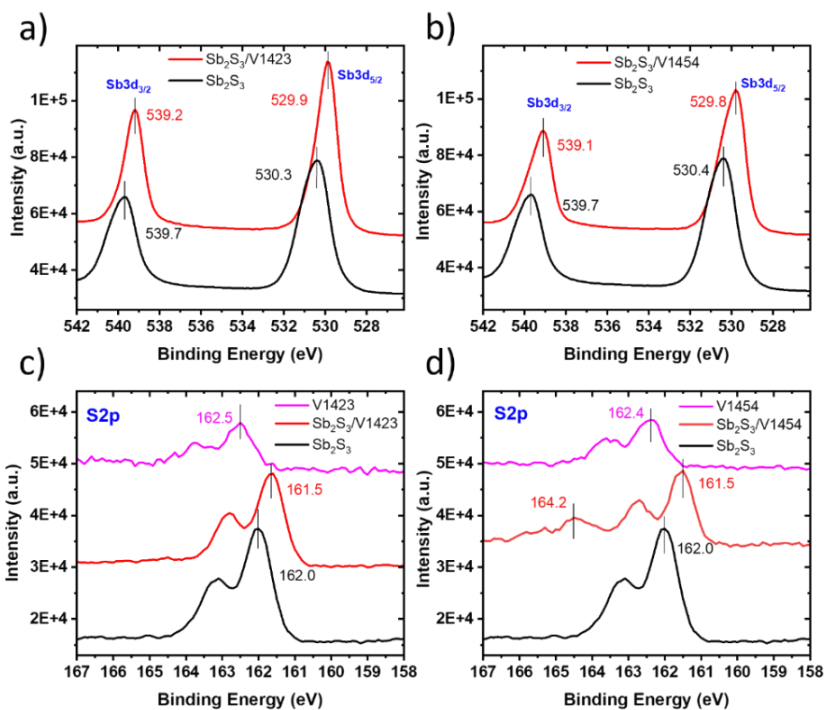


Figure 3.18. XPS core-level spectra: (a) Sb 3d for  $\text{Sb}_2\text{S}_3$  and  $\text{Sb}_2\text{S}_3/\text{V1423}$ , (b) Sb 3d for  $\text{Sb}_2\text{S}_3$  and  $\text{Sb}_2\text{S}_3/\text{V1454}$ , (c) S 2p for  $\text{Sb}_2\text{S}_3$ , V1423, and  $\text{Sb}_2\text{S}_3/\text{V1423}$  and (d) S 2p for  $\text{Sb}_2\text{S}_3$ , V1454, and  $\text{Sb}_2\text{S}_3/\text{V1454}$ .

The S 2p core level spectra for  $\text{Sb}_2\text{S}_3$  films, HTMs – V1423, V1454, and  $\text{Sb}_2\text{S}_3/\text{HTM}$  samples are shown in Fig. 3.18c and d, respectively. For  $\text{Sb}_2\text{S}_3$  and  $\text{Sb}_2\text{S}_3/\text{V1423}$  samples, the S  $2p_{3/2}$  peaks are located at 162.0 eV and 161.5 eV, respectively. A similar shift to lower BE is observed with V1454 on  $\text{Sb}_2\text{S}_3$ . For V1454 on a glass substrate, the S  $2p_{3/2}$  peak is at 162.4 eV. This peak shifts to 164.2 eV when deposited on  $\text{Sb}_2\text{S}_3$ . As seen in previous studies by other research groups, thiophene-modified quinoxaline-core molecules exhibit similar shifts in the S 2p peak to a lower binding energy [23]. The shifts in the Sb 3d and S 2p peaks of  $\text{Sb}_2\text{S}_3$ , and in the S 2p peaks of the HTMs, suggest interactions between sulfur in electron rich thiophene units and antimony in absorber  $\text{Sb}_2\text{S}_3$ . These interactions are expected to improve interfacial carrier extraction, and may enhance  $V_{\text{OC}}$  and overall solar cell performance by passivating interfacial states.

According to XPS results the interaction at  $\text{Sb}_2\text{S}_3/\text{HTM}$  interface is independent of the number of phenylamine side fragments or number of thiophene moieties in central core of HTM molecule. Thus, there are other possible reasons for poor performance of devices using V1454 and V1455 as HTMs. Some possibilities to explain this phenomenon such as dipole effect at absorber/HTM interface and positioning of LUMO level on the thiophene groups are proposed in article IV.

In summary, four dopant-free fluorene-based HTMs with dimers linked with thiophene units (V1422, V1423, V1454, V1455) were applied in  $\text{Sb}_2\text{S}_3$  solar cells. These organic semiconductors have an  $E_{\text{g}}$  of ca. 1.9 eV and HOMO levels at 4.9–5.1 eV. Energy level diagrams demonstrated agreeable band offsets for transport of holes to the metal back contact. The application of the new HTM layer shifted the Sb 3d core level peak to

lower binding energies, indicating increased electron density around Sb atoms and supporting thiophene-Sb interactions. HTMs with diphenylamine units (V1422, V1423) improved device performance, with V1423 showing notable gains:  $V_{OC}$  increased from 478 mV to 673 mV, FF from 46% to 56%, and PCE from 1.9% to 4.5%. In contrast, V1454 and V1455, containing triphenylamine units, did not enhance performance.  $V_{OC}$  remained at 430 mV, FF dropped to 30–35%, and PCE was below 1%. The poor performance of V1454 and V1455 suggests presence of additional factors. Quantum chemical simulations indicate that for better charge separation and selectivity, the HTM's HOMO level should be associated with thiophene groups. Dimer-based HTMs are not recommended for use in semi-transparent  $Sb_2S_3$  solar cells due to their similar bandgap values to P3HT and only slightly higher AVT values, which are attributed to their lower layer thicknesses compared to P3HT.

## Conclusion

In this thesis, we developed semi-transparent  $\text{Sb}_2\text{S}_3$ -based solar cells with employment of new fluorene-based HTMs and provided understanding on the impact of these HTMs on efficacy of the charge transport in the solar cell device. The technological methodology for the preparation of novel HTM layers on  $\text{Sb}_2\text{S}_3$  absorber layer via spin coating was successfully developed. We have successfully demonstrated, that the utilization of organic, cost-effective and wide bandgap fluorene-based enamines can boost both, the PCE as well as the AVT of  $\text{Sb}_2\text{S}_3$  based devices, compared to conventional P3HT-based solar cells.

The main highlights from the thesis can be summarized as follows:

1. A method for preparing layers of novel HTMs on USP deposited  $\text{Sb}_2\text{S}_3$  absorber layer via spin coating technique was developed via systematic altering the HTM concentration in the precursor solution. Appropriate concentrations were determined for all three groups of studied HTMs to obtain layer thicknesses of 20–25 nm, that were found to be optimal for the highest performance of USP  $\text{Sb}_2\text{S}_3$  absorber solar cell.
2. Novel fluorene-based HTMs reveal HOMO level at around  $-5.0$  eV (from  $-4.8$  eV to  $-5.1$  eV) and USP  $\text{Sb}_2\text{S}_3$  absorber VBE at  $-5.1$  eV as determined by photoelectron yield spectroscopy. According to the solar cell band diagram, the transfer of photogenerated holes from the absorber to the HTM is feasible in case of all fluorene-based molecules used. The band offset between CBE of the  $\text{Sb}_2\text{S}_3$  absorber ( $-3.4$  eV) and LUMO levels in fluorene-based HTM molecules with aliphatic chains (ca.  $-2.1$  eV) and molecules with thiophene end units (from  $-2.1$  to  $-2.7$  eV depending on number of thiophene units in the structure) is big enough to block the transfer of electrons at the back interface.
3. Compared to devices without any HTM, application of fluorene-based compounds as HTMs led to a significant gain in device performance. An improvement in PCE can be attributed to the HTM preventing direct contact between the Au electrode and the absorber layer with reduction of recombination losses at the back contact and enhancement of charge extraction. The results reveal the crucial role of HTMs in solar cell stack, especially when very thin absorber layer ( $<100$  nm) is used.
4. The devices utilizing fluorene-based molecules with aliphatic chains (V1275, V1235, V1236, V1461,  $E_g$  of ca. 3.0 eV) as HTM with optimized layer thicknesses of ca. 20 nm achieved PCE values of 3.9%, 4.3%, 3.9%, and 3.7% for V1275, V1235, V1236, and V1461, respectively. The obtained PCE values are comparable to or higher than 3.8% recorded for the P3HT based device. AVT values (without the metal electrode) of solar cell devices reached up to 27% in the 400–800 nm spectral range, representing a 20% increase in transparency over P3HT-based counterparts (AVT 22%), verifying their applicability in semi-transparent  $\text{Sb}_2\text{S}_3$  solar cells.
5. The employment of fluorene-based molecules with thiophene end units (V808, V1385, V1386) as HTMs in  $\text{Sb}_2\text{S}_3$  solar cell yielded device PCE of 4.5–4.9 % and AVT of 30–33% (without the metal back contact) in the 400–800 nm range. In comparison, solar cell devices utilizing conventional P3HT as HTM have yielded PCE of 4.7% and exhibited lower transparency (AVT 26%) due to

parasitic absorption losses in P3HT. An increase in the number of thiophene units from one to three in a molecule led to a decrease in the bandgap from 2.8 eV to 2.3 eV, which reflected in slightly reduced AVT value. For instance, devices using HTM V1386, with an  $E_g$  of 2.3 eV, exhibited AVT of 28%, whereas devices with HTM V808, which has a larger  $E_g$  of 2.8 eV, achieved an AVT of 33%, validating their adaptability for semi-transparent solar cells.

6. Fluorene-based dimers linked with thiophene units (V1422, V1423, V1454, V1455) as HTMs in solar cell resulted in mixed performance outcomes. Application of HTMs – V1422 and V1423, comprising of diphenylamine units in their structure, significantly improved device metrics. The highest boost in device performance compared to the device without any HTM was observed for V1423, which raised  $V_{OC}$  from 478 mV to 673 mV, FF from 46% to 56%, and PCE from 1.9% to 4.5%. However, devices with V1454 and V1455, containing triphenylamine units, showed poor performance (PCE < 1%), confirming our hypothesis that molecular structure strongly influences HTM functionality. As  $E_g$  values of novel dimer molecules and P3HT are similar, in the order of 1.8–1.9 eV, solar cell devices with dimer molecules as HTMs showed only slightly higher AVT values compared to P3HT counterpart, due to HTM layer lower thicknesses and thus cannot be recommended as an HTM for semi-transparent devices.
7. By XPS studies it has been proved that an interaction between the S atoms from thiophene units and Sb atoms from the absorber occurs at the  $Sb_2S_3$ /HTM interface when thiophene group containing HTMs on top of the  $Sb_2S_3$  absorber are applied. Namely, the application of a thiophene group containing HTM on  $Sb_2S_3$  absorber layer causes a shift in the Sb 3d core level peak to lower binding energies indicative of the increased electron density surrounding the Sb atoms. Such a shift confirms the interaction between S atoms from thiophene units and Sb atoms from the absorber, which can favor the transfer of charge carriers. Overall, the research confirms that fluorene-based compounds, particularly those with thiophene end units (V808, V1385 and V1386), are promising candidates for hole-selective contacts in  $Sb_2S_3$  solar cells. Future work should focus on refining HTM/ $Sb_2S_3$  interfaces to improve the  $V_{OC}$  and further improve device efficiency. This study provides a foundation for the development of high-performance, semi-transparent  $Sb_2S_3$  solar cells and opens new avenues for advancing Sb-chalcogenide photovoltaic materials and device architectures.

### ***Challenges and opportunities: outlook and practical applications***

The future outlook of  $Sb_2S_3$ -based solar cells for semi-transparent applications is promising, as these materials exhibit several advantages that make them suitable for this application.  $Sb_2S_3$ -based solar cells have a suitable bandgap of 1.7 eV [144], which is essential for semi-transparent applications as they can absorb a significant portion of the solar spectrum while remaining relatively transparent to visible light [55]. Additionally, the integration of  $Sb_2S_3$ -based solar cells into tandem solar cells is being explored, as they can serve as the top sub-cell in such systems [144]. Recent advances in  $Sb_2S_3$ -based solar cells include the development of efficient devices with a PCE of 8.0% using CBD techniques [9]. This has been achieved after intensive R&D efforts of many research groups. Compared to CBD technique, there are less R&D efforts on development of  $Sb_2S_3$  solar cells by USP. However, the learning curve shows promising results with a milestone

of semi-transparent device yielding PCE of 5.5% [18]. Exploring transparent metal contacts, such as graphene, ultra-thin metal films (Au, Ag), and metallic nanowires (Au, Ag), could significantly advance the performance of transparent  $\text{Sb}_2\text{S}_3$  solar cells. However, several challenges remain in order to fully realize the potential of  $\text{Sb}_2\text{S}_3$ -based solar cells for semi-transparent applications. Key areas of improvement include enhancing the stability and durability of the materials, as well as optimizing the device architecture and surface passivation techniques to minimize recombination losses and enhance charge transport properties. In conclusion, the future outlook of  $\text{Sb}_2\text{S}_3$ -based solar cells for semi-transparent applications is promising, with ongoing research focusing on improving their efficiency and stability. The intrinsic properties of the materials together with the flexibility of the device design allows for its integration into a wide range of applications like BIPV, indoor PV and other customized applications.

## References

- [1] D. Gielen, F. Boshell, D. Saygin, M.D. Bazilian, N. Wagner, R. Gorini, The role of renewable energy in the global energy transformation, *Energy Strategy Reviews* 24 (2019) 38–50. <https://doi.org/10.1016/j.esr.2019.01.006>.
- [2] S.G. Yalaw, M.T.H. van Vliet, D.E.H.J. Gernaat, F. Ludwig, A. Miara, C. Park, E. Byers, E. De Cian, F. Piontek, G. Iyer, I. Mouratiadou, J. Glynn, M. Hejazi, O. Dessens, P. Rochedo, R. Pietzcker, R. Schaeffer, S. Fujimori, S. Dasgupta, S. Mima, S.R.S. da Silva, V. Chaturvedi, R. Vautard, D.P. van Vuuren, Impacts of climate change on energy systems in global and regional scenarios, *Nature Energy* 5 (2020) 794–802. <https://doi.org/10.1038/s41560-020-0664-z>.
- [3] E. Kabir, P. Kumar, S. Kumar, A.A. Adelodun, K.-H. Kim, Solar energy: Potential and future prospects, *Renewable and Sustainable Energy Reviews* 82 (2018) 894–900. <https://doi.org/10.1016/j.rser.2017.09.094>.
- [4] R. Kondrotas, C. Chen, J. Tang, Sb<sub>2</sub>S<sub>3</sub> Solar Cells, *Joule* 2 (2018) 857–878. <https://doi.org/10.1016/j.joule.2018.04.003>.
- [5] N. Cates, M. Bernechea, Research Update: Bismuth based materials for photovoltaics, *APL Materials* 6 (2018). <https://doi.org/10.1063/1.5026541>.
- [6] S. Barthwal, R. Kumar, S. Pathak, Present Status and Future Perspective of Antimony Chalcogenide (Sb<sub>2</sub>X<sub>3</sub>) Photovoltaics, *ACS Applied Energy Materials* 5 (2022) 6545–6585. <https://doi.org/10.1021/acsaem.2c00420>.
- [7] M. Koltsov, S.V. Gopi, T. Raadik, J. Krustok, R. Josepson, R. Gržibovskis, A. Vembris, N. Spalatu, Development of Bi<sub>2</sub>S<sub>3</sub> thin film solar cells by close-spaced sublimation and analysis of absorber bulk defects via in-depth photoluminescence analysis, *Solar Energy Materials and Solar Cells* 254 (2023) 112292. <https://doi.org/10.1016/j.solmat.2023.112292>.
- [8] C. Comparotto, P. Ström, O. Donzel-Gargand, T. Kubart, J.J.S. Scragg, Synthesis of BaZrS<sub>3</sub> Perovskite Thin Films at a Moderate Temperature on Conductive Substrates, *ACS Applied Energy Materials* 5 (2022) 6335–6343. <https://doi.org/10.1021/acsaem.2c00704>.
- [9] S. Wang, Y. Zhao, B. Che, C. Li, X. Chen, R. Tang, J. Gong, X. Wang, G. Chen, T. Chen, J. Li, X. Xiao, A Novel Multi-Sulfur Source Collaborative Chemical Bath Deposition Technology Enables 8%-Efficiency Sb<sub>2</sub>S<sub>3</sub> Planar Solar Cells, *Advanced Materials* 34 (2022). <https://doi.org/10.1002/adma.202206242>.
- [10] Y. Zhao, S. Wang, C. Li, B. Che, X. Chen, H. Chen, R. Tang, X. Wang, G. Chen, T. Wang, J. Gong, T. Chen, X. Xiao, J. Li, Regulating deposition kinetics *via* a novel additive-assisted chemical bath deposition technology enables fabrication of 10.57%-efficiency Sb<sub>2</sub>Se<sub>3</sub> solar cells, *Energy Environmental Science* 15 (2022) 5118–5128. <https://doi.org/10.1039/D2EE02261C>.
- [11] Y. Zhao, S. Wang, C. Jiang, C. Li, P. Xiao, R. Tang, J. Gong, G. Chen, T. Chen, J. Li, X. Xiao, Regulating Energy Band Alignment via Alkaline Metal Fluoride Assisted Solution Post-Treatment Enabling Sb<sub>2</sub>(S,Se)<sub>3</sub> Solar Cells with 10.7% Efficiency, *Advanced Energy Materials* 12 (2022). <https://doi.org/10.1002/aenm.202103015>.
- [12] A.A.F. Husain, W.Z.W. Hasan, S. Shafie, M.N. Hamidon, S.S. Pandey, A review of transparent solar photovoltaic technologies, *Renewable and Sustainable Energy Reviews* 94 (2018) 779–791. <https://doi.org/10.1016/j.rser.2018.06.031>.

- [13] J.S. Eensalu, A. Katerski, E. Kärber, I. Oja Acik, A. Mere, M. Krunks, Uniform Sb<sub>2</sub>S<sub>3</sub> optical coatings by chemical spray method, *Beilstein Journal of Nanotechnology* 10 (2019) 198–210. <https://doi.org/10.3762/bjnano.10.18>.
- [14] E. Zimmermann, T. Pfadler, J. Kalb, J.A. Dorman, D. Sommer, G. Hahn, J. Weickert, L. Schmidt-Mende, Toward High-Efficiency Solution-Processed Planar Heterojunction Sb<sub>2</sub>S<sub>3</sub> Solar Cells, *Advanced Science* 2 (2015) 1500059. <https://doi.org/10.1002/advs.201500059>.
- [15] J.R.- Castro, P. Dale, M.F. Mahon, K.C. Molloy, L.M. Peter, Deposition of Antimony Sulfide Thin Films from Single-Source Antimony Thiolate Precursors, *Chemistry of Materials* 19 (2007) 3219–3226. <https://doi.org/10.1021/cm070405j>.
- [16] J. Han, X. Pu, H. Zhou, Q. Cao, S. Wang, Z. He, B. Gao, T. Li, J. Zhao, X. Li, Synergistic Effect through the Introduction of Inorganic Zinc Halides at the Interface of TiO<sub>2</sub> and Sb<sub>2</sub>S<sub>3</sub> for High-Performance Sb<sub>2</sub>S<sub>3</sub> Planar Thin-Film Solar Cells, *ACS Applied Materials and Interfaces* 12 (2020) 44297–44306. <https://doi.org/10.1021/acscami.0c11550>.
- [17] V.K.H. Bui, T.P. Nguyen, *Advances in Hole Transport Materials for Layered Casting Solar Cells*, *Polymers (Basel)* 15 (2023) 4443. <https://doi.org/10.3390/polym15224443>.
- [18] J.S. Eensalu, A. Katerski, E. Kärber, L. Weinhardt, M. Blum, C. Heske, W. Yang, I. Oja Acik, M. Krunks, Semitransparent Sb<sub>2</sub>S<sub>3</sub> thin film solar cells by ultrasonic spray pyrolysis for use in solar windows, *Beilstein Journal of Nanotechnology* 10 (2019) 2396–2409. <https://doi.org/10.3762/bjnano.10.230>.
- [19] R. Nie, S. Il Seok, Efficient Antimony-Based Solar Cells by Enhanced Charge Transfer, *Small Methods* 4 (2020) 1900698. <https://doi.org/10.1002/smt.201900698>.
- [20] R. Nie, H. Yun, M. Paik, A. Mehta, B. Park, Y.C. Choi, S. Il Seok, Efficient Solar Cells Based on Light-Harvesting Antimony Sulfoiodide, *Advanced Energy Materials* 8 (2018). <https://doi.org/10.1002/aenm.201701901>.
- [21] T.P.I. Saragi, T. Spehr, A. Siebert, T. Fuhrmann-Lieker, J. Salbeck, Spiro Compounds for Organic Optoelectronics, *Chemical Reviews* 107 (2007) 1011–1065. <https://doi.org/10.1021/cr0501341>.
- [22] J.P. Chen, H. Tanabe, X.-C. Li, T. Thoms, Y. Okamura, K. Ueno, Novel organic hole transport material with very high T<sub>g</sub> for light-emitting diodes, *Synthetic Metals* 132 (2003) 173–176. [https://doi.org/10.1016/S0379-6779\(02\)00203-5](https://doi.org/10.1016/S0379-6779(02)00203-5).
- [23] Y. Xiang, H. Guo, Z. Cai, C. Jiang, C. Zhu, Y. Wu, W.-H. Zhu, T. Chen, Dopant-free hole-transporting materials for stable Sb<sub>2</sub>(S,Se)<sub>3</sub> solar cells, *Chemical Communications* 58 (2022) 4787–4790. <https://doi.org/10.1039/D1CC07041J>.
- [24] Y. Chen, D. Chen, P.P. Altermatt, S. Zhang, L. Wang, X. Zhang, J. Xu, Z. Feng, H. Shen, P.J. Verlinden, Technology evolution of the photovoltaic industry: Learning from history and recent progress, *Progress in Photovoltaics: Research and Applications* 31 (2023) 1194–1204. <https://doi.org/10.1002/pip.3626>.
- [25] Global Market Outlook For Solar Power 2023 - 2027, <https://www.solarpowereurope.org/> (accessed September 30, 2024).
- [26] A.S. Al-Ezzi, M.N.M. Ansari, Photovoltaic Solar Cells: A Review, *Applied System Innovation* 5 (2022) 67. <https://doi.org/10.3390/asi5040067>.
- [27] F. Feldmann, M. Bivour, C. Reichel, M. Hermle, S.W. Glunz, Passivated rear contacts for high-efficiency n-type Si solar cells providing high interface passivation quality and excellent transport characteristics, *Solar Energy Materials and Solar Cells* 120 (2014) 270–274. <https://doi.org/10.1016/j.solmat.2013.09.017>.

- [28] NREL, Best Research-Cell Efficiency Chart. Photovoltaic Research | NREL. <https://www.nrel.gov/pv/cell-efficiency.html>, (2024).
- [29] T.T. Werner, G.M. Mudd, S.M. Jowitt, Indium: key issues in assessing mineral resources and long-term supply from recycling, *Applied Earth Science* 124 (2015) 213–226. <https://doi.org/10.1179/1743275815Y.0000000007>.
- [30] S.H.- Werner, S. Roland, *Chalcogenide Photovoltaics: Physics, Technologies, and Thin Film Devices*, 1st ed., Wiley, 2011.
- [31] B. Parida, S. Iniyar, R. Goic, A review of solar photovoltaic technologies, *Renewable and Sustainable Energy Reviews* 15 (2011) 1625–1636. <https://doi.org/10.1016/j.rser.2010.11.032>.
- [32] B. O'Regan, M. Grätzel, A low-cost, high-efficiency solar cell based on dye-sensitized colloidal TiO<sub>2</sub> films, *Nature* 353 (1991) 737–740. <https://doi.org/10.1038/353737a0>.
- [33] A. Hagfeldt, G. Boschloo, L. Sun, L. Kloo, H. Pettersson, Dye-Sensitized Solar Cells, *Chemical Reviews* 110 (2010) 6595–6663. <https://doi.org/10.1021/cr900356p>.
- [34] S. Almosni, A. Delamarre, Z. Jehl, D. Suchet, L. Cojocar, M. Giteau, B. Behaghel, A. Julian, C. Ibrahim, L. Tatry, H. Wang, T. Kubo, S. Uchida, H. Segawa, N. Miyashita, R. Tamaki, Y. Shoji, K. Yoshida, N. Ahsan, K. Watanabe, T. Inoue, M. Sugiyama, Y. Nakano, T. Hamamura, T. Toupance, C. Olivier, S. Chambon, L. Vignau, C. Geffroy, E. Cloutet, G. Hadziioannou, N. Cavassilas, P. Rale, A. Cattoni, S. Collin, F. Gibelli, M. Paire, L. Lombez, D. Aureau, M. Bouttemy, A. Etcheberry, Y. Okada, J.-F. Guillemoles, Material challenges for solar cells in the twenty-first century: directions in emerging technologies, *Science Technology Advanced Energy Materials* 19 (2018) 336–369. <https://doi.org/10.1080/14686996.2018.1433439>.
- [35] J. Tian, G. Cao, Semiconductor quantum dot-sensitized solar cells, *Nano Reviews* 4 (2013) 22578. <https://doi.org/10.3402/nano.v4i0.22578>.
- [36] J. Ya'u Muhammad, A. Bello Waziri, A. Muhammad Shitu, U. Muhammad Ahmad, M. Hassan Muhammad, Y. Alhaji, A. Taofeek Olaniyi, A. Abdulkadir Bala, Recent Progressive Status of Materials for Solar Photovoltaic Cell: A Comprehensive Review, *Science Journal of Energy Engineering* 7 (2019) 77. <https://doi.org/10.11648/j.sjee.20190704.14>.
- [37] J. Pastuszak, P. Węgierek, Photovoltaic Cell Generations and Current Research Directions for Their Development, *Materials* 15 (2022) 5542. <https://doi.org/10.3390/ma15165542>.
- [38] N. Suresh Kumar, K. Chandra Babu Naidu, A review on perovskite solar cells (PSCs), materials and applications, *Journal of Materiomics* 7 (2021) 940–956. <https://doi.org/10.1016/j.jmat.2021.04.002>.
- [39] J.H. Noh, S.H. Im, J.H. Heo, T.N. Mandal, S. Il Seok, Chemical Management for Colorful, Efficient, and Stable Inorganic–Organic Hybrid Nanostructured Solar Cells, *Nano Letters* 13 (2013) 1764–1769. <https://doi.org/10.1021/nl400349b>.
- [40] Q. Dong, Y. Fang, Y. Shao, P. Mulligan, J. Qiu, L. Cao, J. Huang, Electron-hole diffusion lengths > 175 μm in solution-grown CH<sub>3</sub>NH<sub>3</sub>PbI<sub>3</sub> single crystals, *Science* (1979) 347 (2015) 967–970. <https://doi.org/10.1126/science.aaa5760>.
- [41] J.C. Yu, B. Li, C.J. Dunn, J. Yan, B.T. Diroll, A.S.R. Chesman, J.J. Jasieniak, High-Performance and Stable Semi-Transparent Perovskite Solar Cells through Composition Engineering, *Advanced Science* 9 (2022). <https://doi.org/10.1002/advs.202201487>.

- [42] I. Boerasu, B.S. Vasile, Current Status of the Open-Circuit Voltage of Kesterite CZTS Absorber Layers for Photovoltaic Applications—Part I, a Review, *Materials* 15 (2022) 8427. <https://doi.org/10.3390/ma15238427>.
- [43] R. Kondrotas, C. Chen, J. Tang, Sb<sub>2</sub>S<sub>3</sub> Solar Cells, *Joule* 2 (2018) 857–878. <https://doi.org/10.1016/j.joule.2018.04.003>.
- [44] P. Würfel, *Physics of Solar Cells*, Wiley, 2005. <https://doi.org/10.1002/9783527618545>.
- [45] Y. Zhao, S. Wang, C. Jiang, C. Li, P. Xiao, R. Tang, J. Gong, G. Chen, T. Chen, J. Li, X. Xiao, Regulating Energy Band Alignment via Alkaline Metal Fluoride Assisted Solution Post-Treatment Enabling Sb<sub>2</sub>(S,Se)<sub>3</sub> Solar Cells with 10.7% Efficiency, *Advanced Energy Materials* 12 (2022). <https://doi.org/10.1002/aenm.202103015>.
- [46] J. Wang, K. Li, J. Tang, C. Chen, A Perspective of Antimony Chalcogenide Photovoltaics toward Commercialization, *Solar RRL* 7 (2023). <https://doi.org/10.1002/solr.202300436>.
- [47] P. Bayliss, W. Nowacki, Refinement of the crystal structure of stibnite, Sb<sub>2</sub>S<sub>3</sub><sup>1</sup>, *Zeitschrift Für Kristallographie* 135 (1972) 308–315. <https://doi.org/10.1524/zkri.1972.135.3-4.308>.
- [48] R.X. Yang, K.T. Butler, A. Walsh, Assessment of Hybrid Organic–Inorganic Antimony Sulfides for Earth-Abundant Photovoltaic Applications, *The Journal of Physical Chemistry Letters* 6 (2015) 5009–5014. <https://doi.org/10.1021/acs.jpcclett.5b02555>.
- [49] T. Fujita, K. Kurita, K. Takiyama, T. Oda, Near band edge photoluminescence in Sb<sub>2</sub>S<sub>3</sub>, *Journal of Luminescence* 39 (1988) 175–180. [https://doi.org/10.1016/0022-2313\(88\)90028-2](https://doi.org/10.1016/0022-2313(88)90028-2).
- [50] B. Roy, B.R. Chakraborty, R. Bhattacharya, A.K. Dutta, Electrical and magnetic properties of antimony sulphide (Sb<sub>2</sub>S<sub>3</sub>) crystals and the mechanism of carrier transport in it, *Solid State Communication* 25 (1978) 937–940. [https://doi.org/10.1016/0038-1098\(78\)90306-X](https://doi.org/10.1016/0038-1098(78)90306-X).
- [51] Eensalu Jako, Deposition of Sb<sub>2</sub>S<sub>3</sub> Thin Films by Ultrasonic Spray Pyrolysis for Photovoltaic Applications, Tallinn University of Technology, 2022.
- [52] Z. Cai, S. Chen, Extrinsic dopants in quasi-one-dimensional photovoltaic semiconductor Sb<sub>2</sub>S<sub>3</sub>: A first-principles study, *Journal of Applied Physics* 127 (2020). <https://doi.org/10.1063/1.5140751>.
- [53] H. Deng, Y. Zeng, M. Ishaq, S. Yuan, H. Zhang, X. Yang, M. Hou, U. Farooq, J. Huang, K. Sun, R. Webster, H. Wu, Z. Chen, F. Yi, H. Song, X. Hao, J. Tang, Quasiepitaxy Strategy for Efficient Full-Inorganic Sb<sub>2</sub>S<sub>3</sub> Solar Cells, *Advance Functional Materials* 29 (2019). <https://doi.org/10.1002/adfm.201901720>.
- [54] Y.C. Choi, D.U. Lee, J.H. Noh, E.K. Kim, S. Il Seok, Highly Improved Sb<sub>2</sub>S<sub>3</sub> Sensitized-Inorganic–Organic Heterojunction Solar Cells and Quantification of Traps by Deep-Level Transient Spectroscopy, *Advance Functional Materials* 24 (2014) 3587–3592. <https://doi.org/10.1002/adfm.201304238>.
- [55] U.A. Shah, S. Chen, G.M.G. Khalaf, Z. Jin, H. Song, Wide Bandgap Sb<sub>2</sub>S<sub>3</sub> Solar Cells, *Advance Functional Materials* 31 (2021). <https://doi.org/10.1002/adfm.202100265>.
- [56] S. Yuan, H. Deng, D. Dong, X. Yang, K. Qiao, C. Hu, H. Song, Z. He, H. Song, J. Tang, Efficient planar antimony sulfide thin film photovoltaics with large grain and preferential growth, in: *Asia Communications and Photonics Conference 2016*, OSA, Washington, D.C., 2016: p. AF2A.82. <https://doi.org/10.1364/ACPC.2016.AF2A.82>.

- [57] X. Wang, J. Li, W. Liu, S. Yang, C. Zhu, T. Chen, A fast chemical approach towards  $\text{Sb}_2\text{S}_3$  film with a large grain size for high-performance planar heterojunction solar cells, *Nanoscale* 9 (2017) 3386–3390. <https://doi.org/10.1039/C7NR00154A>.
- [58] G. Pan, D. Wang, S. Gao, P. Gao, Q. Sun, X. Liu, Z. Zhou, Y. Sun, Y. Zhang, Substrate structured  $\text{Sb}_2\text{S}_3$  thin film solar cells fabricated by rapid thermal evaporation method, *Solar Energy* 182 (2019) 64–71. <https://doi.org/10.1016/j.solener.2019.02.014>.
- [59] L. Zhang, D. Zhuang, M. Zhao, Q. Gong, L. Guo, L. Ouyang, R. Sun, Y. Wei, X. Lyu, X. Peng,  $\text{Sb}_2\text{S}_3$  thin films prepared by vulcanizing evaporated metallic precursors, *Materials Letters* 208 (2017) 58–61. <https://doi.org/10.1016/j.matlet.2017.05.040>.
- [60] E. Gnenna, N. Khemiri, M. Kong, M. Isabel Alonso, M. Kanzari, Effect of vacuum annealing on the properties of one step thermally evaporated  $\text{Sb}_2\text{S}_3$  thin films for photovoltaic applications, *The European Physical Journal Applied Physics* 96 (2021) 20301. <https://doi.org/10.1051/epjap/2021210101>.
- [61] C.P. Liu, H.E. Wang, T.W. Ng, Z.H. Chen, W.F. Zhang, C. Yan, Y.B. Tang, I. Bello, L. Martinu, W.J. Zhang, S.K. Jha, Hybrid photovoltaic cells based on  $\text{ZnO}/\text{Sb}_2\text{S}_3/\text{P3HT}$  heterojunctions, *Physics Status Solidi B* 249 (2012) 627–633. <https://doi.org/10.1002/pssb.201147393>.
- [62] J. Luo, W. Xiong, G. Liang, Y. Liu, H. Yang, Z. Zheng, X. Zhang, P. Fan, S. Chen, Fabrication of  $\text{Sb}_2\text{S}_3$  thin films by magnetron sputtering and post-sulfurization/selenization for substrate structured solar cells, *Journal of Alloys and Compounds* 826 (2020) 154235. <https://doi.org/10.1016/j.jallcom.2020.154235>.
- [63] M.Y. Versavel, J.A. Haber, Structural and optical properties of amorphous and crystalline antimony sulfide thin-films, *Thin Solid Films* 515 (2007) 7171–7176. <https://doi.org/10.1016/j.tsf.2007.03.043>.
- [64] L. Guo, B. Zhang, S. Li, Q. Zhang, M. Buettner, L. Li, X. Qian, F. Yan, Scalable and efficient  $\text{Sb}_2\text{S}_3$  thin-film solar cells fabricated by close space sublimation, *APL Materials* 7 (2019) 041105. <https://doi.org/10.1063/1.5090773>.
- [65] Y. Zeng, F. Liu, M. Green, X. Hao, Fabrication of  $\text{Sb}_2\text{S}_3$  planar thin film solar cells with closed-space sublimation method, in: 2018 IEEE 7th World Conference on Photovoltaic Energy Conversion (WCPEC) (A Joint Conference of 45th IEEE PVSC, 28th PVSEC & 34th EU PVSEC), IEEE, 2018: pp. 0870–0872. <https://doi.org/10.1109/PVSC.2018.8547305>.
- [66] E. Moustafa, J.G. Sánchez, L.F. Marsal, J. Pallarès, Stability Enhancement of High-Performance Inverted Polymer Solar Cells Using  $\text{ZnO}$  Electron Interfacial Layer Deposited by Intermittent Spray Pyrolysis Approach, *ACS Applied Energy Materials* 4 (2021) 4099–4111. <https://doi.org/10.1021/acsaem.1c00455>.
- [67] P. Büttner, F. Scheler, C. Pointer, D. Döhler, T. Yokosawa, E. Spiecker, P.P. Boix, E.R. Young, I. Mínguez-Bacho, J. Bachmann,  $\text{ZnS}$  Ultrathin Interfacial Layers for Optimizing Carrier Management in  $\text{Sb}_2\text{S}_3$ -based Photovoltaics, *ACS Applied Materials and Interfaces* 13 (2021) 11861–11868. <https://doi.org/10.1021/acsaem.1c021365>.
- [68] H.-J. Jo, S.H. Kim, J.S. Kim, S.-J. Lee, D.-H. Kim, Time-resolved photocurrent of an organic-inorganic hybrid solar cell based on  $\text{Sb}_2\text{S}_3$ , *Journal of the Korean Physical Society* 69 (2016) 541–546. <https://doi.org/10.3938/jkps.69.541>.

- [69] N. Spalatu, R. Krautmann, A. Katerski, E. Karber, R. Josepson, J. Hiie, I.O. Acik, M. Krunks, Screening and optimization of processing temperature for Sb<sub>2</sub>Se<sub>3</sub> thin film growth protocol: Interrelation between grain structure, interface intermixing and solar cell performance, *Solar Energy Materials and Solar Cells* 225 (2021) 111045. <https://doi.org/10.1016/j.solmat.2021.111045>.
- [70] H. Maghraoui-Meherzi, T. Ben Nasr, N. Kamoun, M. Dachraoui, Structural, morphology and optical properties of chemically deposited Sb<sub>2</sub>S<sub>3</sub> thin films, *Physica B Condensed Matter* 405 (2010) 3101–3105. <https://doi.org/10.1016/j.physb.2010.04.020>.
- [71] O. Savadogo, K.C. Mandal, Studies on new chemically deposited photoconducting antimony trisulphide thin films, *Solar Energy Materials and Solar Cells* 26 (1992) 117–136. [https://doi.org/10.1016/0927-0248\(92\)90131-8](https://doi.org/10.1016/0927-0248(92)90131-8).
- [72] J.S. Eensalu, K. Tõnsuaadu, I. Oja Acik, M. Krunks, Sb<sub>2</sub>S<sub>3</sub> thin films by ultrasonic spray pyrolysis of antimony ethyl xanthate, *Materials Science in Semiconductor Processing* 137 (2022) 106209. <https://doi.org/10.1016/j.mssp.2021.106209>.
- [73] S. Ito, K. Tsujimoto, D.-C. Nguyen, K. Manabe, H. Nishino, Doping effects in Sb<sub>2</sub>S<sub>3</sub> absorber for full-inorganic printed solar cells with 5.7% conversion efficiency, *International Journal of Hydrogen Energy* 38 (2013) 16749–16754. <https://doi.org/10.1016/j.ijhydene.2013.02.069>.
- [74] J.C. Cardoso, C.A. Grimes, X. Feng, X. Zhang, S. Komarneni, M.V.B. Zanoni, N. Bao, Fabrication of coaxial TiO<sub>2</sub>/Sb<sub>2</sub>S<sub>3</sub> nanowire hybrids for efficient nanostructured organic–inorganic thin film photovoltaics, *Chemical Communications* 48 (2012) 2818. <https://doi.org/10.1039/c2cc17573h>.
- [75] R. Tang, X. Wang, W. Lian, J. Huang, Q. Wei, M. Huang, Y. Yin, C. Jiang, S. Yang, G. Xing, S. Chen, C. Zhu, X. Hao, M.A. Green, T. Chen, Hydrothermal deposition of antimony selenosulfide thin films enables solar cells with 10% efficiency, *Nature Energy* 5 (2020) 587–595. <https://doi.org/10.1038/s41560-020-0652-3>.
- [76] M. Liu, Y. Gong, Z. Li, M. Dou, F. Wang, A green and facile hydrothermal approach for the synthesis of high-quality semi-conducting Sb<sub>2</sub>S<sub>3</sub> thin films, *Applied Surface Science* 387 (2016) 790–795. <https://doi.org/10.1016/j.apsusc.2016.06.126>.
- [77] D.-H. Kim, S.-J. Lee, M.S. Park, J.-K. Kang, J.H. Heo, S.H. Im, S.-J. Sung, Highly reproducible planar Sb<sub>2</sub>S<sub>3</sub>-sensitized solar cells based on atomic layer deposition, *Nanoscale* 6 (2014) 14549–14554. <https://doi.org/10.1039/C4NR04148H>.
- [78] H. Wedemeyer, J. Michels, R. Chmielowski, S. Bourdais, T. Muto, M. Sugiura, G. Dennler, J. Bachmann, Nanocrystalline solar cells with an antimony sulfide solid absorber by atomic layer deposition, *Energy & Environmental Science* 6 (2013) 67–71. <https://doi.org/10.1039/C2EE23205G>.
- [79] Y.C. Choi, S. Il Seok, Efficient Sb<sub>2</sub>S<sub>3</sub>-Sensitized Solar Cells Via Single-Step Deposition of Sb<sub>2</sub>S<sub>3</sub> Using S/Sb-Ratio-Controlled SbCl<sub>3</sub>-Thiourea Complex Solution, *Advance Functional Materials* 25 (2015) 2892–2898. <https://doi.org/10.1002/adfm.201500296>.
- [80] W. Wang, F. Strössner, E. Zimmermann, L. Schmidt-Mende, Hybrid solar cells from Sb<sub>2</sub>S<sub>3</sub> nanoparticle ink, *Solar Energy Materials and Solar Cells* 172 (2017) 335–340. <https://doi.org/10.1016/j.solmat.2017.07.046>.
- [81] M.S. You, C.-S. Lim, D.H. Kwon, J.H. Heo, S.H. Im, K.J. Chae, Oxide-free Sb<sub>2</sub>S<sub>3</sub> sensitized solar cells fabricated by spin and heat-treatment of Sb(III)(thioacetamide)<sub>2</sub>Cl<sub>3</sub>, *Organic Electronics* 21 (2015) 155–159. <https://doi.org/10.1016/j.orgel.2015.02.015>.

- [82] W. Lian, C. Jiang, Y. Yin, R. Tang, G. Li, L. Zhang, B. Che, T. Chen, Revealing composition and structure dependent deep-level defect in antimony trisulfide photovoltaics, *Nature Communications* 12 (2021). <https://doi.org/10.1038/s41467-021-23592-0>.
- [83] C. Lan, G. Liang, H. Lan, H. Peng, Z. Su, D. Zhang, H. Sun, J. Luo, P. Fan, Microstructural and Optical Properties of  $Sb_2S_3$  Film Thermally Evaporated from Antimony Pentasulfide and Efficient Planar Solar Cells, *Physica Status Solidi (RRL) - Rapid Research Letters* 12 (2018) 1800025. <https://doi.org/10.1002/pssr.201800025>.
- [84] M.A. Farhana, A. Manjceevan, J. Bandara, Recent advances and new research trends in  $Sb_2S_3$  thin film based solar cells, *Journal of Science: Advanced Materials and Devices* 8 (2023) 100533. <https://doi.org/10.1016/j.jsamd.2023.100533>.
- [85] R. Krautmann, N. Spalatu, R. Josepson, R. Nedzinskas, R. Kondrotas, R. Gržibovskis, A. Vembris, M. Krunks, I. Oja Acik, Low processing temperatures explored in  $Sb_2S_3$  solar cells by close-spaced sublimation and analysis of bulk and interface related defects, *Solar Energy Materials and Solar Cells* 251 (2023) 112139. <https://doi.org/10.1016/j.solmat.2022.112139>.
- [86] Y. Zhang, S. Li, R. Tang, X. Wang, C. Chen, W. Lian, C. Zhu, T. Chen, Phosphotungstic Acid Regulated Chemical Bath Deposition of  $Sb_2S_3$  for High-Efficiency Planar Heterojunction Solar Cell, *Energy Technology* 6 (2018) 2126–2131. <https://doi.org/10.1002/ente.201800238>.
- [87] H. Ning, H. Guo, J. Zhang, X. Wang, X. Jia, J. Qiu, N. Yuan, J. Ding, Enhancing the efficiency of  $Sb_2S_3$  solar cells using dual-functional potassium doping, *Solar Energy Materials and Solar Cells* 221 (2021) 110816. <https://doi.org/10.1016/j.solmat.2020.110816>.
- [88] J. Chen, J. Qi, R. Liu, X. Zhu, Z. Wan, Q. Zhao, S. Tao, C. Dong, G.Y. Ashebir, W. Chen, R. Peng, F. Zhang, S. Yang, X. Tian, M. Wang, Preferentially oriented large antimony trisulfide single-crystalline cuboids grown on polycrystalline titania film for solar cells, *Communications Chemistry* 2 (2019) 121. <https://doi.org/10.1038/s42004-019-0225-1>.
- [89] X. Jin, Y. Yuan, C. Jiang, H. Ju, G. Jiang, W. Liu, C. Zhu, T. Chen, Solution processed  $NiO_x$  hole-transporting material for all-inorganic planar heterojunction  $Sb_2S_3$  solar cells, *Solar Energy Materials and Solar Cells* 185 (2018) 542–548. <https://doi.org/10.1016/j.solmat.2018.06.017>.
- [90] B. Reeja-Jayan, A. Manthiram, Effects of bifunctional metal sulfide interlayers on photovoltaic properties of organic–inorganic hybrid solar cells, *RSC Advances* 3 (2013) 5412. <https://doi.org/10.1039/c3ra23055d>.
- [91] E. Kärber, A. Katerski, I. Oja Acik, A. Mere, V. Mikli, M. Krunks,  $Sb_2S_3$  grown by ultrasonic spray pyrolysis and its application in a hybrid solar cell, *Beilstein Journal of Nanotechnology* 7 (2016) 1662–1673. <https://doi.org/10.3762/bjnano.7.158>.
- [92] R. Tang, X. Wang, W. Lian, J. Huang, Q. Wei, M. Huang, Y. Yin, C. Jiang, S. Yang, G. Xing, S. Chen, C. Zhu, X. Hao, M.A. Green, T. Chen, Hydrothermal deposition of antimony selenosulfide thin films enables solar cells with 10% efficiency, *Nature Energy* 5 (2020) 587–595. <https://doi.org/10.1038/s41560-020-0652-3>.
- [93] J.A. Chang, S.H. Im, Y.H. Lee, H. Kim, C.-S. Lim, J.H. Heo, S. Il Seok, Panchromatic Photon-Harvesting by Hole-Conducting Materials in Inorganic–Organic Heterojunction Sensitized-Solar Cell through the Formation of Nanostructured Electron Channels, *Nano Letters* 12 (2012) 1863–1867. <https://doi.org/10.1021/nl204224v>.

- [94] L. Zhang, C. Jiang, C. Wu, H. Ju, G. Jiang, W. Liu, C. Zhu, T. Chen,  $V_2O_5$  as Hole Transporting Material for Efficient All Inorganic  $Sb_2S_3$  Solar Cells, *ACS Applied Materials and Interfaces* 10 (2018) 27098–27105. <https://doi.org/10.1021/acsami.8b09843>.
- [95] H. Zhou, J. Han, X. Pu, X. Li, Effective additive for enhancing the performance of  $Sb_2S_3$  planar thin film solar cells, *Journal of Materiomics* 7 (2021) 1074–1082. <https://doi.org/10.1016/j.jmat.2021.02.001>.
- [96] Y. Li, R. Li, Z. Jia, B. Yu, Y. Yang, S. Bai, M. Pollard, Y. Liu, Y. Ma, H. Kampwerth, Q. Lin, Precursor Engineering of Solution-Processed  $Sb_2S_3$  Solar Cells, *Small* 20 (2024). <https://doi.org/10.1002/smll.202308895>.
- [97] L. Zhang, W. Lian, X. Zhao, Y. Yin, T. Chen, C. Zhu,  $Sb_2S_3$  Seed-Mediated Growth of Low-Defect  $Sb_2S_3$  on a  $TiO_2$  Substrate for Efficient Solar Cells, *ACS Applied Energy Materials* 3 (2020) 12417–12422. <https://doi.org/10.1021/acsaem.0c02400>.
- [98] S. Yuan, H. Deng, X. Yang, C. Hu, J. Khan, W. Ye, J. Tang, H. Song, Postsurface Selenization for High Performance  $Sb_2S_3$  Planar Thin Film Solar Cells, *ACS Photonics* 4 (2017) 2862–2870. <https://doi.org/10.1021/acsp Photonics.7b00858>.
- [99] M.I. Medina-Montes, Z. Montiel-González, N.R. Mathews, X. Mathew, The influence of film deposition temperature on the subsequent post-annealing and crystallization of sputtered  $Sb_2S_3$  thin films, *Journal of Physics and Chemistry of Solids* 111 (2017) 182–189. <https://doi.org/10.1016/j.jpcs.2017.07.035>.
- [100] J. Han, S. Wang, J. Yang, S. Guo, Q. Cao, H. Tang, X. Pu, B. Gao, X. Li, Solution-Processed  $Sb_2S_3$  Planar Thin Film Solar Cells with a Conversion Efficiency of 6.9% at an Open Circuit Voltage of 0.7 V Achieved via Surface Passivation by a  $SbCl_3$  Interface Layer, *ACS Applied Materials and Interfaces* 12 (2020) 4970–4979. <https://doi.org/10.1021/acsami.9b15148>.
- [101] V. Odari, R. Musembi, J. Mwabora, Enhanced performance of  $Sb_2S_3$  mesoscopic sensitized solar cells employing  $TiO_2:Nb$  compact layer, *Journal of Materials Science: Materials in Electronics* 29 (2018) 16359–16368. <https://doi.org/10.1007/s10854-018-9726-4>.
- [102] K. Tsujimoto, D.C. Nguyen, S. Ito, H. Nishino, H. Matsuyoshi, A. Konno, G.R.A. Kumara, K. Tennakone,  $TiO_2$  surface treatment effects by  $Mg^{2+}$ ,  $Ba^{2+}$ , and  $Al^{3+}$  on  $Sb_2S_3$  extremely thin absorber solar cells, *Journal of Physical Chemistry C* 116 (2012) 13465–13471. <https://doi.org/10.1021/jp208937j>.
- [103] C. Lan, J. Luo, H. Lan, B. Fan, H. Peng, J. Zhao, H. Sun, Z. Zheng, G. Liang, P. Fan, Enhanced charge extraction of Li-doped  $TiO_2$  for efficient thermal-evaporated  $Sb_2S_3$  thin film solar cells, *Materials* 11 (2018). <https://doi.org/10.3390/ma11030355>.
- [104] W. Lian, C. Jiang, Y. Yin, R. Tang, G. Li, L. Zhang, B. Che, T. Chen, Revealing composition and structure dependent deep-level defect in antimony trisulfide photovoltaics, *Nature Communications* 12 (2021) 3260. <https://doi.org/10.1038/s41467-021-23592-0>.
- [105] C.P. Liu, H.E. Wang, T.W. Ng, Z.H. Chen, W.F. Zhang, C. Yan, Y.B. Tang, I. Bello, L. Martinu, W.J. Zhang, S.K. Jha, Hybrid photovoltaic cells based on  $ZnO/Sb_2S_3/P3HT$  heterojunctions, *Physica Status Solidi (b)* 249 (2012) 627–633. <https://doi.org/10.1002/pssb.201147393>.
- [106] C. Lan, J. Luo, H. Lan, B. Fan, H. Peng, J. Zhao, H. Sun, Z. Zheng, G. Liang, P. Fan, Enhanced Charge Extraction of Li-Doped  $TiO_2$  for Efficient Thermal-Evaporated  $Sb_2S_3$  Thin Film Solar Cells, *Materials* 11 (2018) 355. <https://doi.org/10.3390/ma11030355>.

- [107] W.H. Kim, S. Woo, K.P. Kim, S.M. Kwon, D.H. Kim, Efficient TiO<sub>2</sub> Surface Treatment Using Cs<sub>2</sub>CO<sub>3</sub> for Solution-Processed Planar-Type Sb<sub>2</sub>S<sub>3</sub> Solar Cells, *Nanoscale Research Letters* 14 (2019). <https://doi.org/10.1186/s11671-019-2858-5>.
- [108] H. Ning, H. Guo, J. Zhang, X. Wang, X. Jia, J. Qiu, N. Yuan, J. Ding, Enhancing the efficiency of Sb<sub>2</sub>S<sub>3</sub> solar cells using dual-functional potassium doping, *Solar Energy Materials and Solar Cells* 221 (2021). <https://doi.org/10.1016/j.solmat.2020.110816>.
- [109] H. Lei, G. Yang, Y. Guo, L. Xiong, P. Qin, X. Dai, X. Zheng, W. Ke, H. Tao, Z. Chen, B. Li, G. Fang, Efficient planar Sb<sub>2</sub>S<sub>3</sub> solar cells using a low-temperature solution-processed tin oxide electron conductor, *Physical Chemistry Chemical Physics* 18 (2016) 16436–16443. <https://doi.org/10.1039/c6cp02072k>.
- [110] Y. Itzhaik, O. Niitsoo, M. Page, G. Hodes, Sb<sub>2</sub>S<sub>3</sub>-Sensitized Nanoporous TiO<sub>2</sub> Solar Cells, *The Journal of Physical Chemistry C* 113 (2009) 4254–4256. <https://doi.org/10.1021/jp900302b>.
- [111] N. Dematage, E.V.A. Premalal, A. Konno, Employment of CuI on Sb<sub>2</sub>S<sub>3</sub> Extremely Thin Absorber Solar Cell: N719 Molecules as a Dual Role of a Recombination Blocking Agent and an Efficient Hole Shuttle, *International Journal of Electrochemical Science* 9 (2014) 1729–1737. [https://doi.org/10.1016/S1452-3981\(23\)07886-0](https://doi.org/10.1016/S1452-3981(23)07886-0).
- [112] Y. Xiao, C. Li, X. Tan, L. Zhang, Y. Zhong, H. Zhu, Full-Inorganic Thin Film Solar Cell and Photodetector Based on “Graphene-on-Antimony Sulfide” Heterostructure, *Solar RRL* 1 (2017). <https://doi.org/10.1002/solr.201700135>.
- [113] W. Chen, L. Jiang, R. Pathak, F. Wu, Sb<sub>2</sub>S<sub>3</sub>/TiO<sub>2</sub> Heterojunction Solar Cells Based on Carbon Electrode with Higher Photocurrent, *ECS Journal of Solid State Science and Technology* 8 (2019) Q67–Q71. <https://doi.org/10.1149/2.0021904jss>.
- [114] X. Jing, Z. Zhang, T. Chen, J. Luo, Review of Inorganic Hole Transport Materials for Perovskite Solar Cells, *Energy Technology* 11 (2023). <https://doi.org/10.1002/ente.202201005>.
- [115] S. Li, Y.-L. Cao, W.-H. Li, Z.-S. Bo, A brief review of hole transporting materials commonly used in perovskite solar cells, *Rare Metals* 40 (2021) 2712–2729. <https://doi.org/10.1007/s12598-020-01691-z>.
- [116] C. Zhang, K. Wei, J. Hu, X. Cai, G. Du, J. Deng, Z. Luo, X. Zhang, Y. Wang, L. Yang, J. Zhang, A review on organic hole transport materials for perovskite solar cells: Structure, composition and reliability, *Materials Today* 67 (2023) 518–547. <https://doi.org/10.1016/j.mattod.2023.06.009>.
- [117] H.D. Pham, T.C. Yang, S.M. Jain, G.J. Wilson, P. Sonar, Development of Dopant-Free Organic Hole Transporting Materials for Perovskite Solar Cells, *Advanced Energy Materials* 10 (2020). <https://doi.org/10.1002/aenm.201903326>.
- [118] M.L. Petrus, T. Bein, T.J. Dingemans, P. Docampo, A low cost azomethine-based hole transporting material for perovskite photovoltaics, *Journal of Materials Chemistry A* 3 (2015) 12159–12162. <https://doi.org/10.1039/C5TA03046C>.
- [119] L. Zhu, J. Chen, R. Liu, C. Dong, J. Huang, Z. Wan, W. Cao, X. Zhang, C. Ge, M. Wang, Amorphous-conjugated polymer-additive approach to prepare quality Spiro-OMeTAD-based hole transporting material for efficient Sb<sub>2</sub>S<sub>3</sub> solar cells, *Materials Letters* 316 (2022) 132028. <https://doi.org/10.1016/j.matlet.2022.132028>.

- [120] C.-C. Chung, T.-W. Tsai, H.-P. Wu, E.W.-G. Diau, Phosphonic Acid and Lithium Salt as Effective *p*-Dopants to Oxidize Spiro-OMeTAD for Mesoscopic Sb<sub>2</sub>S<sub>3</sub> Solar Cells, *The Journal of Physical Chemistry C* 121 (2017) 18472–18479. <https://doi.org/10.1021/acs.jpcc.7b07958>.
- [121] Y. Xiang, H. Guo, Z. Cai, C. Jiang, C. Zhu, Y. Wu, W.-H. Zhu, T. Chen, Dopant-free hole-transporting materials for stable Sb<sub>2</sub>(S,Se)<sub>3</sub> solar cells, *Chemical Communications* 58 (2022) 4787–4790. <https://doi.org/10.1039/D1CC07041J>.
- [122] C. Jiang, J. Zhou, R. Tang, W. Lian, X. Wang, X. Lei, H. Zeng, C. Zhu, W. Tang, T. Chen, 9.7%-efficient Sb<sub>2</sub>(S,Se)<sub>3</sub> solar cells with a dithieno[3,2-*b*:2',3'-*d*]pyrrole-cored hole transporting material, *Energy & Environmental Science* 14 (2021) 359–364. <https://doi.org/10.1039/D0EE02239J>.
- [123] J.A. Chang, J.H. Rhee, S.H. Im, Y.H. Lee, H. Kim, S. Il Seok, Md.K. Nazeeruddin, M. Gratzel, High-Performance Nanostructured Inorganic–Organic Heterojunction Solar Cells, *Nano Letters* 10 (2010) 2609–2612. <https://doi.org/10.1021/nl101322h>.
- [124] E.L. Gui, A.M. Kang, S.S. Pramana, N. Yantara, N. Mathews, S. Mhaisalkar, Effect of TiO<sub>2</sub> Mesoporous Layer and Surface Treatments in Determining Efficiencies in Antimony Sulfide-(Sb<sub>2</sub>S<sub>3</sub>) Sensitized Solar Cells, *Journal of The Electrochemical Society* 159 (2012) B247–B250. <https://doi.org/10.1149/2.007203jes>.
- [125] C.-S. Lim, S.H. Im, H. Kim, J.A. Chang, Y.H. Lee, S. Il Seok, Enhancing the device performance of Sb<sub>2</sub>S<sub>3</sub>-sensitized heterojunction solar cells by embedding Au nanoparticles in the hole-conducting polymer layer, *Physical Chemistry Chemical Physics* 14 (2012) 3622. <https://doi.org/10.1039/c2cp23650h>.
- [126] C.P. Liu, H.E. Wang, T.W. Ng, Z.H. Chen, W.F. Zhang, C. Yan, Y.B. Tang, I. Bello, L. Martinu, W.J. Zhang, S.K. Jha, Hybrid photovoltaic cells based on ZnO/Sb<sub>2</sub>S<sub>3</sub>/P3HT heterojunctions, *Physica Status Solidi (b)* 249 (2012) 627–633. <https://doi.org/10.1002/pssb.201147393>.
- [127] R.A. Miranda Gamboa, O.A. Jaramillo-Quintero, Y.A. Alarcón Altamirano, M.O. Concha-Guzmán, M.E. Rincón, A novel nanocomposite based on NiOx-incorporated P3HT as hole transport material for Sb<sub>2</sub>S<sub>3</sub> solar cells with enhanced device performance, *Journal of Colloid and Interface Science* 535 (2019) 400–407. <https://doi.org/10.1016/j.jcis.2018.10.015>.
- [128] Spiro-MeOTAD, <https://www.ossila.com/> (accessed September 30, 2024).
- [129] P3HT, <https://www.ossila.com/> (accessed September 30, 2024).
- [130] K. Tsujimoto, D.-C. Nguyen, S. Ito, H. Nishino, H. Matsuyoshi, A. Konno, G.R.A. Kumara, K. Tennakone, TiO<sub>2</sub> Surface Treatment Effects by Mg<sup>2+</sup>, Ba<sup>2+</sup>, and Al<sup>3+</sup> on Sb<sub>2</sub>S<sub>3</sub> Extremely Thin Absorber Solar Cells, *The Journal of Physical Chemistry C* 116 (2012) 13465–13471. <https://doi.org/10.1021/jp208937j>.
- [131] P. Sun, X. Zhang, L. Wang, Y. Wei, C. Wang, Y. Liu, Efficiency enhanced rutile TiO<sub>2</sub> nanowire solar cells based on an Sb<sub>2</sub>S<sub>3</sub> absorber and a CuI hole conductor, *New Journal of Chemistry* 39 (2015) 7243–7250. <https://doi.org/10.1039/C5NJ00299K>.
- [132] L. Bu, Z. Liu, M. Zhang, W. Li, A. Zhu, F. Cai, Z. Zhao, Y. Zhou, Semitransparent Fully Air Processed Perovskite Solar Cells, *ACS Applied Materials and Interfaces* 7 (2015) 17776–17781. <https://doi.org/10.1021/acsami.5b04040>.
- [133] Z. Zhou, Z. Yuan, Z. Yin, Q. Xue, N. Li, F. Huang, Progress of semitransparent emerging photovoltaics for building integrated applications, *Green Energy & Environment* 9 (2024) 992–1015. <https://doi.org/10.1016/j.gee.2023.05.006>.

- [134] S.-J. Lee, S.-J. Sung, K.-J. Yang, J.-K. Kang, J.Y. Kim, Y.S. Do, D.-H. Kim, Approach to Transparent Photovoltaics Based on Wide Band Gap  $\text{Sb}_2\text{S}_3$  Absorber Layers and Optics-Based Device Optimization, *ACS Applied Energy Materials* 3 (2020) 12644–12651. <https://doi.org/10.1021/acsaem.0c02552>.
- [135] Y. Li, X. Guo, Z. Peng, B. Qu, H. Yan, H. Ade, M. Zhang, S.R. Forrest, Color-neutral, semitransparent organic photovoltaics for power window applications, *Proceedings of the National Academy of Sciences* 117 (2020) 21147–21154. <https://doi.org/10.1073/pnas.2007799117>.
- [136] H. Kwon, A. Kim, H. Lee, D. Lee, S. Jeong, J. Moon, Parallelized Nanopillar Perovskites for Semitransparent Solar Cells Using an Anodized Aluminum Oxide Scaffold, *Advanced Energy Materials* 6 (2016). <https://doi.org/10.1002/aenm.201601055>.
- [137] P. Kumar, M. Eriksson, D.S. Kharytonau, S. You, M.M. Natile, A. Vomiero, All-Inorganic Hydrothermally Processed Semitransparent  $\text{Sb}_2\text{S}_3$  Solar Cells with  $\text{CuSCN}$  as the Hole Transport Layer, *ACS Applied Energy Materials* 7 (2024) 1421–1432. <https://doi.org/10.1021/acsaem.3c02492>.
- [138] P. Yan, D. Yang, H. Wang, S. Yang, Z. Ge, Recent advances in dopant-free organic hole-transporting materials for efficient, stable and low-cost perovskite solar cells, *Energy & Environmental Science* 15 (2022) 3630–3669. <https://doi.org/10.1039/D2EE01256A>.
- [139] F. Machui, M. Hösel, N. Li, G.D. Spyropoulos, T. Ameri, R.R. Søndergaard, M. Jørgensen, A. Scheel, D. Gaiser, K. Kreul, D. Lenssen, M. Legros, N. Lemaitre, M. Vilkman, M. Välimäki, S. Nordman, C.J. Brabec, F.C. Krebs, Cost analysis of roll-to-roll fabricated ITO free single and tandem organic solar modules based on data from manufacture, *Energy & Environmental Science* 7 (2014) 2792. <https://doi.org/10.1039/C4EE01222D>.
- [140] S. Daskeviciute, C. Momblona, K. Rakstys, A.A. Sutanto, M. Daskeviciene, V. Jankauskas, A. Gruodis, G. Bubniene, V. Getautis, M.K. Nazeeruddin, Fluorene-based enamines as low-cost and dopant-free hole transporting materials for high performance and stable perovskite solar cells, *Journal of Materials Chemistry A* 9 (2021) 301–309. <https://doi.org/10.1039/D0TA08452B>.
- [141] S. Xu, J. Wu, F. Guo, M. Wu, S. Chen, W. Chen, C. Shi, Self-passivation hole-transporting materials with pyridine-containing cores for antimony chalcogenide solar cells studied under dopant-free conditions, *Sustain Energy Fuels* 7 (2023) 61–65. <https://doi.org/10.1039/D2SE01448C>.
- [142] S.H. Im, C.-S. Lim, J.A. Chang, Y.H. Lee, N. Maiti, H.-J. Kim, Md.K. Nazeeruddin, M. Grätzel, S. Il Seok, Toward Interaction of Sensitizer and Functional Moieties in Hole-Transporting Materials for Efficient Semiconductor-Sensitized Solar Cells, *Nano Letters* 11 (2011) 4789–4793. <https://doi.org/10.1021/nl2026184>.
- [143] T. Malinauskas, D. Tomkute-Luksiene, R. Sens, M. Daskeviciene, R. Send, H. Wonneberger, V. Jankauskas, I. Bruder, V. Getautis, Enhancing Thermal Stability and Lifetime of Solid-State Dye-Sensitized Solar Cells via Molecular Engineering of the Hole-Transporting Material Spiro-OMeTAD, *ACS Applied Materials and Interfaces* 7 (2015) 11107–11116. <https://doi.org/10.1021/am5090385>.
- [144] J. Chen, G. Li, Z. Xu, C. Xu, F. Naveed, B. Liu, Y. Zhang, R. Zhou, C. Chen, M. Wang, J. Xu, L. Li, Recent Advances and Prospects of Solution-Processed Efficient  $\text{Sb}_2\text{S}_3$  Solar Cells, *Advance Functional Materials* (2024). <https://doi.org/10.1002/adfm.202313676>.

## Acknowledgements

I would like to express my sincere gratitude to my supervisors Prof. Dr. Malle Krunks and Prof. Dr. Nicolae Spalatu for their guidance, patience, and generous support throughout my doctoral research. Many thanks to the head of the research group Prof. Dr. Ilona Oja Açıık for giving me the opportunity to work in the lab. I would like to thank the Baltic-Nordic project partners – researchers from Kaunas University of Technology (KTU) in Lithuania, University of Latvia in Latvia and Institute for Energy Technology (IFE) in Norway. Special thanks to Dr. Valdek Mikli of Laboratory of Photovoltaic Materials and staff members of Laboratory for Thin Film Energy Materials. I am also grateful to all co-authors and my colleagues for their generous help throughout my doctoral research. My deepest gratitude goes to my parents and my wife for their constant support.

The study received financial support from Iceland, Liechtenstein and Norway through the EEA Grants. The aim of the project was to develop new approach based on novel materials and structures and production technologies, which are the key to further increase the share, and range of application of PV in areas with sub-average sunlight, including Baltic and Nordic countries. Therefore, development of resource saving, cost-effective and efficient PV devices is a primary challenge of this project. Project contract with the Research Council of Lithuania (LMTLT) No is S-BMT-21-1(LT08-2-LMT-K-01-003). The research was also supported by Estonian Research Council, projects PRG627 “Antimony chalcogenide thin films for next-generation semi-transparent solar cells applicable in electricity producing windows”; European Union’s Horizon 2020 - ERA Chair project 5GSOLAR (grant No. 952509); H2020-WIDESPREAD-01-2016-2017-TeamingPhase2 (grant No. 739508, project CAMART<sup>2</sup>); European Cooperation in Science and Technology (COST) project RENEW-PV (CA21148) and by the Estonian Ministry of Education and Research (project TK210; TK210U8 “Center of Excellence in Sustainable Green Hydrogen and Energy Technologies”).

## Abstract

### Development of semi-transparent $\text{Sb}_2\text{S}_3$ solar cells with fluorene-based compounds as hole transport materials

Photovoltaics (PV) converts sunlight to electricity and is becoming one of the cheapest technologies to produce carbon-free electricity. An emerging generation of PV absorber materials, that are characterized by stability and easy of manufacturing are under investigation in the PV community. These materials, which are both economically and environmentally sustainable, have the potential to significantly enhance the capacity and scalability of sustainable PV solutions and can lead to enhanced social acceptance of the integrated PV solutions. Among these PV materials, antimony chalcogenides are rapidly gaining recognition as viable alternative light-absorbing materials.  $\text{Sb}_2\text{S}_3$  is a promising absorber material for employment in semi-transparent solar cells due to its optoelectronic properties, with an absorption coefficient of  $1.8 \times 10^5 \text{ cm}^{-1}$  at 450 nm and a direct bandgap of ca. 1.7 eV. The constituent elements are non-toxic, earth abundant, and cost-effective. Recently, in the year 2022,  $\text{Sb}_2\text{S}_3$  based solar have reported photoconversion efficiency (PCE) of 8.0%.

$\text{Sb}_2\text{S}_3$  based solar cells utilize the configuration – glass/TCO/ETL/ $\text{Sb}_2\text{S}_3$ /HTM/metal, wherein the Transparent Conducting Oxide (TCO) is the front contact and the metal layers is the back contact while the Electron Transport Layer (ETL) and layer of Hole Transport material (HTM) are transporting the charge carriers.  $\text{TiO}_2$  and CdS are the most widely used ETL materials, while the most popular HTMs are P3HT (poly(3-hexylthiophene) and Spiro-OMeTAD (2,2',7,7'-tetrakis[N,N-di(4-methoxyphenyl)amino]-9,9'-spirobi-fluorene). HTMs are essential components in solar cells as they facilitate effective extraction and transport of photogenerated holes in the absorber layer to the metal contacts. Additionally, they prevent metal diffusion and their direct contact with the absorber, thereby reducing recombination losses at the absorber/HTM/back contact interface. Conventional HTMs have their own set of drawbacks such as high cost and complex synthesis processes, hindering their scalability for commercial applications. P3HT is constrained by its parasitic absorption in the visible spectrum, resulting in reduced overall transmittance of the solar cell device and necessitates post-deposition activation at approximately 170 °C, in vacuum or inert atmosphere. Spiro-OMeTAD requires doping that can cause stability issues. Together, these factors limit the manufacture of large area  $\text{Sb}_2\text{S}_3$ -based solar cells for semi-transparent applications.

The aim of this thesis is to develop semi-transparent  $\text{Sb}_2\text{S}_3$  solar cells with the employment of new fluorene-based HTMs and provide understanding on the impact of HTMs on the efficacy of the charge transport in the solar cell device. These fluorene-based compounds, synthesized by Prof. Vytautas Getautis' group in Kaunas University of Technology, are being applied for the first time in  $\text{Sb}_2\text{S}_3$  solar cells. These HTM compounds are produced in a straightforward condensation reaction from commercially available materials and relatively cheap reagents.

The research emphasizes the systematic characterization, implementation, and validation of novel HTM thin films as alternative charge selective layers in  $\text{Sb}_2\text{S}_3$  thin film solar cells with a focus on understanding their influence on the overall performance of the devices. Three distinct groups of fluorene-based enamines as dopant-free HTMs were employed: 1) fluorene-based molecules with aliphatic chains (V1275, V1235, V1236, V1461); 2) fluorene-based compounds with thiophene end units (V808, V1385,

V1386); and 3) fluorene-based dimers linked with thiophene units (V1422, V1423, V1454, V1455).

Sb<sub>2</sub>S<sub>3</sub> solar cells were fabricated in superstrate configuration with a structure glass/FTO/TiO<sub>2</sub>/Sb<sub>2</sub>S<sub>3</sub>/HTM/Au wherein TiO<sub>2</sub> and Sb<sub>2</sub>S<sub>3</sub> layer were deposited on glass/FTO substrate using ultrasonic spray pyrolysis (USP). All the fluorene-based HTMs and conventionally used P3HT were deposited using spin coating. For the material characterization, techniques like X-ray diffraction (XRD), Raman spectroscopy, Scanning Electron Microscopy (SEM) and ultraviolet-visible spectroscopy (UV-Vis) were used. The characterization of solar cell devices was performed using current-voltage (J-V) and external quantum efficiency (EQE) measurements. To understand the energy levels alignment in solar cell device, Ionization potential (I<sub>p</sub>) of all the functional layers (FTO, TiO<sub>2</sub>, Sb<sub>2</sub>S<sub>3</sub>, HTM) in the solar cell structure was measured using Photoelectron yield spectroscopy (PYS). X-ray photoelectron spectroscopy (XPS) studies were performed to study the Sb<sub>2</sub>S<sub>3</sub>/HTM interface.

A methodology for the preparation of HTMs layers on USP deposited Sb<sub>2</sub>S<sub>3</sub> absorber layer was successfully developed via spin coating technique. Optimal concentrations were identified for each HTM group, by systematically varying the HTM precursor concentration, resulting in thicknesses of 20–25 nm being optimal for the highest performance of USP-Sb<sub>2</sub>S<sub>3</sub> absorber solar cells. The fabricated devices with the optimized concentration of fluorene-based HTMs were then compared with solar cell devices without any HTM and with reference P3HT-based device.

Novel fluorene-based HTMs reveal Highest Occupied Molecular Orbital (HOMO) level at around -5.0 eV (from -4.8 eV to -5.1 eV) and USP Sb<sub>2</sub>S<sub>3</sub> absorber Valence Band Edge (VBE) at -5.1 eV as determined by PYS. According to the solar cell band diagram, the transfer of photogenerated holes from the absorber to the HTM is feasible in case of all fluorene-based molecules used. The band offset between Conduction Band Edge (CBE) of the Sb<sub>2</sub>S<sub>3</sub> absorber (-3.4 eV) and Lowest Unoccupied Molecular Orbital (LUMO) levels in fluorene-based HTM molecules with aliphatic chains (ca. -2.1 eV) and molecules with thiophene end units (from -2.1 to -2.7 eV depending on number of thiophene units in the structure), is big enough to block the transfer of electrons at the back-contact interface.

Compared to devices without any HTM, application of fluorene-based HTMs led to a significant gain in device performance. Solar cell devices incorporated with fluorene-based molecules with aliphatic chains and thiophene end units yielded PCE of up to 4.3 and 4.9%, respectively, which were comparable with cells employing reference HTM – P3HT (3.8 and 4.7%). EQE measurements of the devices with P3HT (E<sub>g</sub> – 1.8 eV) showed parasitic absorption losses in visible range), that are not present in the case of the fluorene-based HTMs with aliphatic chains (V1275, V1235, V1236, V1461, E<sub>g</sub> – ca. 3 eV), and with thiophene end units (V808, V1385, V1386, E<sub>g</sub> from 2.3 to 2.8 eV), due to their larger band gap values. Total transmittance spectra were recorded and average visible transmittance (AVT) values in the range of 400 - 800 nm were calculated for all fabricated solar cells without metal contacts. Solar cell devices with HTMs with aliphatic chains and thiophene end units showed an enhanced AVT of up to 33%, resulting in an overall gain of around 20% in device transparency compared to that obtained with P3HT. Solar cells with dimer-based HTMs with E<sub>g</sub> values of ca. 1.8 eV showed only slightly higher AVT values compared to P3HT counterpart device due to thinner HTM layer applied. XPS studies revealed that the Sb 3d and S 2p peaks of Sb<sub>2</sub>S<sub>3</sub> shift toward lower binding energies, on application of fluorene-based dimers linked with

thiophene units as HTMs, indicating strong interactions between S atoms in thiophene units and Sb atoms in the absorber.

Overall, it was observed that both the thickness of the HTM layer and the structure of the HTM molecule has a direct impact on the device performance. In summary, the study confirms that fluorene-based compounds, particularly those with aliphatic chains (V1275, V1235, V1236 and V1461) and with thiophene end units (V808, V1385 and V1386), are promising candidates for hole-selective contacts in semi-transparent  $\text{Sb}_2\text{S}_3$  solar cells. The study provides new insights, laying a strong foundation for developing high-performance, semi-transparent  $\text{Sb}_2\text{S}_3$  solar cells in the future.

## Lühikokkuvõte

### **Poolläbipaistvate Sb<sub>2</sub>S<sub>3</sub> päikeseptareide arendus: fluoreenipõhised ühendid aukude transportkihi materjalina**

Päikeseenergeetika (PV) on üks odavamaid ja puhtamaid elektrienergia tootmise tehnoloogiaid. PV tulevikutehnoloogiad on seotud absorbermaterjalide ja seadistega mida iseloomustab stabiilsus, valmistamise tehnoloogia lihtsus ning skaleeritavus tootmisesse. Uudsed PV materjalid ja tehnoloogiad, mis on säästlikud nii tootmise kui keskkonna seisukohast, võivad oluliselt suurendada päikeseenergeetika lahenduste suutlikkust ja mastaapsust ning viia integreeritud PV lahenduste laialdasemale rakendamisele. Uudsete PV materjalide perekonnas on antimoni kalkogeniidid tõestanud ennast võimekate valgust neelavate materjalidena. Sb<sub>2</sub>S<sub>3</sub> on perspektiivikas absorbermaterjal kasutamiseks poolläbipaistvates päikeseelementides tänu sellistele optoelektronsetele omadustele nagu valguse neeldumistegur  $1.8 \times 10^5 \text{ cm}^{-1}$  450 nm juures ja otseste üleminekutega keelutsoon laiusega 1,7 eV. Ühend ja tema koostisosad on madala toksilisusega, piisava kättesaadavusega ja suhteliselt odavad. Üsnagi lühikese arendusperioodi jooksul on Sb<sub>2</sub>S<sub>3</sub> päikeseelementide efektiivsus tõusnud 8%-ni.

Sb<sub>2</sub>S<sub>3</sub> päikeseelementide klassikaline struktuur on järgmine: klaas/TCO/ETL/Sb<sub>2</sub>S<sub>3</sub>/HTM/metall, kus TCO on optiliselt läbipaistev elektrit juhtiv metallioksiidi kiht kui esikontakt ja metalli kiht kui tagakontakt. ETL (elektronide transportkiht) ja HTM (aukude transportkiht) kihtide ülesanne on laengukandjate, vastavalt elektronide ja aukude transport välistele elektroodidele. ETL materjalidena kasutakse peamiselt CdS või TiO<sub>2</sub> õhukest kihti, HTM kihi materjalina on põhiliselt kasutusel kas P3HT (poly(3-hexylthiophene) või Spiro-OMeTAD (2,2',7,7'-tetrakis[N,N-di(4-methoxyphenyl)amino]-9,9'-spirobi-fluorene). HTM kiht on oluline päikeseelementi koostisosa, mille ülesandeks on hõlbustada fotogeneereeritud aukude ekstraktsiooni absorberkihist välisele metall-elektroodile, takistada metalli difusiooni ja vähendada rekombinatsioonilisi kadusid absorber/metall piirpinnal. Traditsiooniliselt kasutatavate HTM-de põhilised puudused on nende kõrge hind tingituna sünteesi keerukusest. P3HT keelutsooni väärtus ca. 1,8 eV põhjustab parasiitse valguse neeldumise spektri nähtavas osas, mis põhjustab voolu kadu ja ei võimalda valmistada optiliselt hea läbipaistvusega elemente. Spiro-OmeTAD on laia keelutsooniga (ca 3,0 eV), mis ei põhjusta optilisi kadusid, kuid vajaliku elektrijuhtivuse saavutamiseks tuleb materjali legeerida, mis muudab materjali ebastabiilseks. Loetletud asjaolud piiravad poolläbipaistvate Sb<sub>2</sub>S<sub>3</sub> päikeseelementide arendamist ja osutavad uudsete HTM materjalide väljatöötamise ja rakendamise vajalikkusele.

Antud doktoritöö eesmärk oli poolläbipaistvate päikeseelementide arendus kasutades HTM kihis uusi fluoreeni-põhiseid materjale ja sätestada arusaam uudsete materjalide mõjust laengukandjate transpordi tõhususele ja seadiste väljundparameetritele. Uudsed fluoreenipõhised orgaanilised ühendid sünteesiti prof. Vytautas Getautis uurimisgrupi poolt Kaunase Tehnoloogiaülikoolis kasutades selleks lihtsat sünteesi metodikat ja odavaid reagente.

Uurimistöös keskenduti uudsete HTM materjalide karakteriseerimisele, kasutamisele päikeseelementi struktuuris ja nende sobivuse valideerimisele aukude transportkihina poolläbipaistvates rakendustes. HTM materjalina kasutati kolme erinevat tüüpi fluoreeni-põhiseid molekule: 1) alifaatset rühma sisaldavad fluoreenipõhised ühendid (V1275, V1235, V1236, V1461; 2) tiofeeni rühma sisaldavad fluoreenipõhised ühendid (V808,

V1385, V1386); 3) fluoreenipõhised dimeerid, lingitud läbi tiofeenrühma (V1422, V1423, V1454, V1455).

Päikeseelemendid valmistati superstraat konfiguratsioonis klass/FTO/TiO<sub>2</sub>/Sb<sub>2</sub>S<sub>3</sub>/HTM/Au, kus TiO<sub>2</sub> ja Sb<sub>2</sub>S<sub>3</sub> kihid sadestati klaas/FTO alusele ultraheli pihustuse (USP) meetodil. Kõik HTM kihid valmistati pindvurritamise meetodil. Materjalide iseloomustamiseks kasutati röntgendifraktsioon analüüsi (XRD), Raman spektroskoopia, skaneeriva elektronmikroskoopia (SEM) ja optilise spektroskoopia/(UV-vis) meetodeid. Päikeseelementide karakteriseerimiseks rakendati J-V karakteristikute ning välise kvantefektiivsuse (EQE) mõõtmisi. Seadise energetilise tsooni diagrammi koostamiseks mõõdeti kõigi funktsionaalsete komponentide ionisatsiooni potentsiaal (Ip) fotoelektronide saagise spektroskoopia (PYS) meetodil. Röntgenkiire fotoelektronspektroskoopia (XPS) meetodit kasutati Sb<sub>2</sub>S<sub>3</sub>/HTM piirpinna uurimiseks.

Töötati välja metoodika HTM kihtide sadestamiseks pindvurritamise meetodil Sb<sub>2</sub>S<sub>3</sub> absorberkihtedele. Määrati HTM lahuse optimaalsed kontsentratsioonid iga HTM tüübi jaoks läbi HTM lähtelahuse kontsentratsiooni muutmise. Leiti, et HTM kihi paksus vahemikus 20–25 nm on optimaalne saavutamaks seadise kõrgeimat efektiivsust. Teostati võrdlus päikeseelementidele, kus HTM-na kasutati fluoreenipõhiseid ühendeid, traditsioonilist P3HT või HTM-i ei kasutatud.

Energeetiliste parameetrite mõõtmine näitas, et HOMO nivoo kõigis uuritud uutes HTM-des on ca. –5,0 eV allpool vaakumnivood, ja Sb<sub>2</sub>S<sub>3</sub> valentstsooni lagi (VBE) asetseb –5,1 eV juures. Seega fotogenereeritud aukude liikumine absorberkihist HTM-i on võimalik kõigi uute HTM kasutamisel. Kuna Sb<sub>2</sub>S<sub>3</sub> juhtivustsooni põhi (CBE) asub –3,4 eV juures vaakuumi suhtes ja alifaatseid rühmi sisaldavates HTM molekulides on LUMO nivood –2,1 eV juures ning tiofeeni rühmi sisaldavates molekulides asub LUMO –2,1 kuni –2,7 eV juures sõltuvalt tiofeeni rühmade arvust molekulis, siis energetilise barjäär Sb<sub>2</sub>S<sub>3</sub>/HTM piirpinnal on piisav, et blokeerida elektronide liikumist absorberist HTM kihti.

Uurimistöö näitas, et fluoreenipõhiste HTM-de lisamine päikeseelemendi struktuuri suurendas oluliselt seadiste efektiivsust võrreldes sellega, kus HTM-i kihti ei kasutatud. Alifaatset ahelat ja tiofeenrühma sisaldavate fluoreenipõhiste HTM kihtide kasutamisel saavutati kasutegurid vastavalt 4,3% ja 4,9%, mis on kõrgemad kui P3HT-ga võrdlusobjektidel (vastavalt 3,8 ja 4,7%). EQE mõõtmised kinnitasid parasiitse absorptsiooni puudumist kui HTM-dena kasutati alifaatset ahelat sisaldavaid aineid (V1275, V1235, V1236, V1461, E<sub>g</sub> ca. 3 eV) või tiofeeni rühma sisaldavaid kihte (V808, V1385, V1386, E<sub>g</sub> vahemikus 2,3 kuni 2,8 eV), Mõõdeti päikeseelemendi (ilma Au elektroodita) keskmist optilist läbipaistvust (AVT) spektri nähtavas osas lainepikkuste vahemikus 400–800 nm. Alifaatset ahelat ja tiofeenrühma sisaldavate fluoreenipõhiste HTM kihtide puhul mõõdeti AVT väärtuseks kuni 33%, mis on ca. 20% kõrgem kui P3HT kasutamisel HTM-na. Dimeersed HTM-d, mille E<sub>g</sub> on ca 1,8 eV, ei ole sobiv valik poolläbipaistvate seadiste valmistamiseks, kuigi tänu HTM kihi tunduvalt väiksemale paksusele (ca. 25 nm) võrreldes P3HT-ga (100 nm) mõõdeti AVT väärtuseks kuni 25%.

XPS mõõtmised näitasid, et tiofeeni rühma sisaldava HTM-i kihi sadestamisel Sb<sub>2</sub>S<sub>3</sub> absorberi kihi pinnale toimub interaktsioon tiofeeni rühma kuuluva S aatomi ja absorberi molekuli kuuluva Sb aatomi vahel, mis võib kaasa aidata laengute ülekandmisele Sb-kalkogeniid absorberist HTM-i.

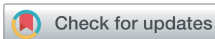
Kokkuvõttes, HTM molekuli struktuur ja HTM kihi paksus omavad olulist mõju päikeseelemendi efektiivsusele. Antud uurimistöös tõestati, et fluoreenipõhised ühendid, mille struktuuris on alifaatsed ahelad (V1275, V1235, V1236 and V1461) või tiofeenrühm (V808, V1385 and V1386) on perspektiivsed aukude transportkihi materjalid poolläbipaistvate Sb<sub>2</sub>S<sub>3</sub> päikeseelementide valmistamiseks.

# Appendix 1

## Publication I

**Nimish Juneja**, Sreekanth Mandati, Atanas Katerski, Nicolae Spalatu, Šarūnė Daškevičiūtė-Gegužienė, Aivars Vembris, Smagul Karazhanov, Vytautas Getautis, Malle Krunks, and Ilona Oja Ačik, “Sb<sub>2</sub>S<sub>3</sub> solar cells with a cost-effective and dopant-free fluorene-based enamine as a hole transport material”, *Sustainable Energy and Fuels* 6, 13, 3220–29, 2022, doi: 10.1039/d2se00356b.




 Cite this: *Sustainable Energy Fuels*, 2022, 6, 3220

## Sb<sub>2</sub>S<sub>3</sub> solar cells with a cost-effective and dopant-free fluorene-based enamine as a hole transport material†

 Nimish Juneja,<sup>a</sup> Sreekanth Mandati,<sup>b</sup> Atanas Katerski,<sup>a</sup> Nicolae Spalatu,<sup>b</sup> Sarune Daskeviciute-Geguziene,<sup>b</sup> Aivars Vembris,<sup>c</sup> Smagul Karazhanov,<sup>d</sup> Vytautas Getautis,<sup>b</sup> Malle Krunks<sup>a</sup> and Ilona Oja Acik<sup>b</sup>

Antimony sulphide (Sb<sub>2</sub>S<sub>3</sub>) is a promising candidate for semi-transparent and tandem solar cells owing to its suitable optoelectronic properties. However, the applications of Sb<sub>2</sub>S<sub>3</sub> solar cells are rather limited by their low power conversion efficiencies (PCEs) and use of expensive hole transport materials (HTMs). Furthermore, HTMs like P3HT exhibit parasitic absorption and hinder overall transparency of the devices. To circumvent these problems, V1236, a fluorene-based enamine is explored for the first time for Sb<sub>2</sub>S<sub>3</sub> solar cells, which is significantly cheaper, transparent, and does not require high temperature activation like P3HT. Solar cells are fabricated in the glass/FTO/TiO<sub>2</sub>/Sb<sub>2</sub>S<sub>3</sub>/HTM/Au configuration wherein TiO<sub>2</sub> and Sb<sub>2</sub>S<sub>3</sub> are deposited using ultrasonic spray pyrolysis and HTMs are spin coated. The concentration of V1236 is systematically varied and its impact on the Sb<sub>2</sub>S<sub>3</sub> device performance is investigated. The J<sub>SC</sub> of the solar cells with V1236 is about 17% higher which is attributed to the better valence band edge alignment compared to P3HT. The EQE measurements show no parasitic absorption with V1236 while the optical studies show a larger bandgap for V1236 (2.6 eV) over P3HT (1.8 eV), indicating negligible loss of transparency. Furthermore, the overall transparency is increased by 20% for V1236 devices in comparison to P3HT devices while yielding better PCEs, demonstrating the efficacy of novel V1236 as an HTM for semi-transparent Sb<sub>2</sub>S<sub>3</sub> solar cells.

 Received 15th March 2022  
 Accepted 15th May 2022

DOI: 10.1039/d2se00356b

[rsc.li/sustainable-energy](http://rsc.li/sustainable-energy)

## 1 Introduction

Antimony chalcogenides are fast emerging as promising alternative light absorbing materials. Among them, Sb<sub>2</sub>S<sub>3</sub> is one of the most promising solar absorbers owing to its superior optoelectronic properties with an absorption coefficient of  $\approx 10^5 \text{ cm}^{-1}$  at 450 nm and a direct bandgap of  $\sim 1.8 \text{ eV}$ .<sup>1,2</sup> With a relatively wide bandgap, Sb<sub>2</sub>S<sub>3</sub> can be used either as an absorber material in single junction solar cells or as a light harvester in tandem cells.<sup>1,2</sup> Furthermore, Sb<sub>2</sub>S<sub>3</sub> solar cells are potential candidates for semi-transparent applications and have been under intense investigation for application in solar windows.<sup>3</sup> The constituent elements are non-toxic, earth abundant and cheaper, which makes the Sb<sub>2</sub>S<sub>3</sub> technology all

the more fascinating.<sup>1,4–6</sup> In recent years, with improvements in deposition techniques and interface engineering, Sb<sub>2</sub>S<sub>3</sub> solar cells have achieved a power conversion efficiency (PCE) of about 7.5%.<sup>7</sup> The deposition of Sb<sub>2</sub>S<sub>3</sub> absorbers by a variety of chemical and physical methods is reasonably well studied. Chemical bath deposition (CBD),<sup>6,7</sup> spin coating,<sup>8,9</sup> atomic layer deposition (ALD)<sup>10,11</sup> and chemical spray pyrolysis (CSP)<sup>5,12</sup> have been widely used for absorber fabrication. Among the low-cost solution-based methods, ultrasonic spray pyrolysis (USP) is a high throughput, area-scalable, and cost-effective deposition process, which is majorly used under ambient conditions. The efficacy of USP has been demonstrated by our group for the fabrication of Sb<sub>2</sub>S<sub>3</sub> thin film absorbers,<sup>3,5</sup> as well as for TiO<sub>2</sub> electron transport layers (ETLs).<sup>13,14</sup> The typical growth of Sb<sub>2</sub>S<sub>3</sub> by USP follows a two-step process involving the spray deposition of amorphous films followed by crystallization at elevated temperatures either in a vacuum or an inert atmosphere.<sup>3,5</sup> Physical methods for the deposition of Sb<sub>2</sub>S<sub>3</sub> absorbers include thermal evaporation,<sup>15,16</sup> magnetron sputtering<sup>1,17</sup> and closed space sublimation,<sup>18,19</sup> which resulted in efficiencies in the range of 3–6%.<sup>20,21</sup>

Conventional planar Sb<sub>2</sub>S<sub>3</sub> solar cells have utilized the glass/TCO/ETL/Sb<sub>2</sub>S<sub>3</sub>/HTM/metal configuration, wherein the transparent conducting oxide (TCO) and metal are the front and back

<sup>a</sup>Laboratory of Thin Film Chemical Technologies, Department of Materials and Environmental Technology, Tallinn University of Technology, Ehitajate tee 5, 19086 Tallinn, Estonia. E-mail: sreekanth.mandati@taltech.ee

<sup>b</sup>Department of Organic Chemistry, Kaunas University of Technology, Kaunas LT-50254, Lithuania

<sup>c</sup>Institute of Solid State Physics, University of Latvia, Kengaraga Str. 8, Riga, Latvia

<sup>d</sup>Institute for Energy Technology (IFE), P. O Box 40, No 2027, Kjeller, Norway

 † Electronic supplementary information (ESI) available: Synthesis procedure of the V1236 HTM, optical microscopy images of Sb<sub>2</sub>S<sub>3</sub>, transmittance and EQE curves. See <https://doi.org/10.1039/d2se00356b>


contacts. The electron transport layer (ETL) and hole transport material (HTMs) ferry the electrons and holes generated in the absorber to the contacts, respectively.<sup>3,5,22–26</sup> Indium tin oxide (ITO) and fluorine doped tin oxide (FTO) are commonly used TCOs.<sup>22,23,27</sup> For HTMs, several organic and inorganic materials are explored.<sup>15,28</sup> HTMs are an integral part of the solar cell structure and serve multiple tasks and are crucial to obtain high PCEs, especially for the semi-transparent device concept. HTMs ensure efficient extraction and transport of photogenerated holes to the contacts, prevent diffusion of metal to avoid direct contact with the absorber and suppress the recombination losses at the absorber–HTM interface.<sup>27</sup> HTMs must also possess high hole mobility, good thermal stability, high solubility in a suitable solvent, and appropriate band edge positions compatible with  $\text{Sb}_2\text{S}_3$ .<sup>27,29</sup> More importantly, they need to be transparent in the visible spectral region when used in semi-transparent solar cells and should be cost-effective. The most popular HTMs explored to date for  $\text{Sb}_2\text{S}_3$  solar cells are the organic-based P3HT (poly(3-hexylthiophene)),<sup>3,5,22,27</sup> spiro-OMeTAD (2,2',7,7'-tetrakis[*N,N*-di(4-methoxyphenyl)amino]-9,9'-spirobi-fluorene),<sup>24,25</sup> PEDOT:PSS (poly(3,4-ethylenedioxythiophene)-poly(styrenesulfonate))<sup>23</sup> and PCPDTBT (poly[2,6-(4,4-bis(2-ethylhexyl)-4*H*-cyclo-penta[2,1-*b*;3,4-*b'*]dithiophene)-*alt*-4,7-(2,1,3-benzothiadiazole)]).<sup>30</sup> Among inorganic materials,  $\text{NiO}_x$ ,<sup>31</sup>  $\text{V}_2\text{O}_5$ ,<sup>32</sup> and  $\text{CuSCN}$ :KSCN<sup>6</sup> have been reported as HTMs. For instance, Kim *et al.* have fabricated planar  $\text{Sb}_2\text{S}_3$  solar cells with spin coated PEDOT:PSS as the HTM wherein  $\text{Sb}_2\text{S}_3$  is deposited using CBD, and have obtained a PCE of 5.8%.<sup>23</sup> Zimmermann *et al.* used CBD for the deposition of the absorber and employed P3HT as the HTM where the impact of P3HT thickness on solar cell performance has been investigated resulting in a PCE of 4.1%.<sup>27</sup> You *et al.* used spin coating for deposition of  $\text{Sb}_2\text{S}_3$  and P3HT to fabricate solar cells with a PCE of 2.3%.<sup>22</sup> On a similar note, spiro-OMeTAD has also been used as an HTM for  $\text{Sb}_2\text{S}_3$  solar cells. Zhang *et al.* have used CBD to deposit  $\text{Sb}_2\text{S}_3$  with spiro-OMeTAD as the HTM and have reported an efficiency of 5.5%.<sup>24</sup> Chen *et al.* have adopted spin coating for  $\text{Sb}_2\text{S}_3$  deposition with spiro-OMeTAD as the HTM and demonstrated a PCE of 5.2%.<sup>25</sup> Choi *et al.* have deposited  $\text{Sb}_2\text{S}_3$  using CBD and have employed a combination of PCPDTBT and PEDOT:PSS as the HTM and fabricated solar cells (FTO/mp-TiO<sub>2</sub>/Sb<sub>2</sub>S<sub>3</sub>/PCPDTBT/PEDOT:PSS/Au) with a PCE of 7.5%, which remains the highest to date.<sup>7</sup> However, despite the successful demonstration of conventionally used HTMs like P3HT, spiro-OMeTAD, PCPDTBT, *etc.*, the high manufacturing costs of these materials coupled with low yields pose limitations on the commercial maturity of  $\text{Sb}_2\text{S}_3$  solar cells.<sup>33</sup> Furthermore, P3HT requires an additional activation step at temperatures around 170 °C.<sup>35</sup> Also, a similar bandgap value of P3HT (1.8 eV)<sup>3</sup> to that of  $\text{Sb}_2\text{S}_3$  (1.7 eV)<sup>5</sup> coupled with the parasitic absorption losses limits the overall transparency of solar cells.<sup>34</sup>

Considering the aforementioned HTM related drawbacks, this study aims to fabricate  $\text{Sb}_2\text{S}_3$  semi-transparent solar cells employing a fluorene-based enamine – V1236 ( $N^2, N^2, N^7, N^7$ -tetrakis[2,2-bis(4-methoxyphenyl)viny]l-9,9-dihexyl-9*H*-fluorene-2,7-diamine) as an HTM for the first time. V1236 has been investigated as a dopant-free HTM in perovskite solar cells

yielding an efficiency of 17.1%.<sup>34</sup> V1236 possesses a band gap of 2.6 eV and a hole mobility of  $\approx 2.6 \times 10^{-4} \text{ cm}^2 \text{ V}^{-1} \text{ s}^{-1}$ .<sup>34</sup> Owing to its largely simplified synthesis process and high yield, the estimated synthesis cost of V1236 is  $\sim 17 \text{ € per g}$  (Table S1†), which is considerably cheaper than those of conventional HTMs like spiro-OMeTAD ( $\sim 92 \text{ € per g}$ )<sup>35</sup> and P3HT ( $\sim 45 \text{ € per g}$ ).<sup>36</sup> The present study focuses on validating the use of cost-effective V1236 as an HTM by demonstrating the successful fabrication of planar  $\text{Sb}_2\text{S}_3$  solar cells (glass/FTO/TiO<sub>2</sub>/Sb<sub>2</sub>S<sub>3</sub>/HTM/Au), wherein TiO<sub>2</sub> and Sb<sub>2</sub>S<sub>3</sub> layers are deposited using ultrasonic spray pyrolysis. For a fair comparison, the conventionally used P3HT is also employed and both the HTMs are spin coated. The solar cell devices with optimized V1236 and P3HT have resulted in similar efficiencies. Insights from band alignment reveal that V1236 serves as a better HTM due to its better LUMO level alignment with the conduction band edge of  $\text{Sb}_2\text{S}_3$  compared to P3HT. Additionally, the device stack from V1236 devoid of metal contact exhibits an increase in average visible transmittance (AVT) in the visible region over P3HT devices, demonstrating the efficacy of V1236 as an HTM in semi-transparent  $\text{Sb}_2\text{S}_3$  solar cells.

## 2 Experimental

### 2.1 Materials

FTO substrate ( $7 \Omega \square^{-1}$ ), titanium(IV) tetraisopropoxide (TTIP) – 99 wt% (Acros Organics), acetylacetone – 99 wt% (Acros Organics), ethanol – 96.6 vol% (Estonian Spirit), methanol – 99.9 vol% (Sigma-Aldrich), antimony trichloride – 99.99 wt% (Sigma-Aldrich), thiourea – 99 wt% (Sigma-Aldrich), chlorobenzene – 99.5 vol% (Sigma-Aldrich), poly(3-hexylthiophene-2,5-diyl) (P3HT) – 100 kDa, >90% regioregular (Sigma-Aldrich) and  $N^2, N^2, N^7, N^7$ -tetrakis[2,2-bis(4-methoxyphenyl)viny]l-9,9-dihexyl-9*H*-fluorene-2,7-diamine (V1236). The materials are used as received. The chemical structures of V1236 and P3HT are shown in Fig. 1.

### 2.2 Methods

**2.2.1 Fabrication of solar cells.** The typical procedure adopted for the fabrication of  $\text{Sb}_2\text{S}_3$  solar cells is shown as a schematic in Fig. 2a and the device configuration is depicted in Fig. 2b. The glass/FTO substrates (25 mm × 25 mm) were rinsed thoroughly with deionized water, ethanol and methanol

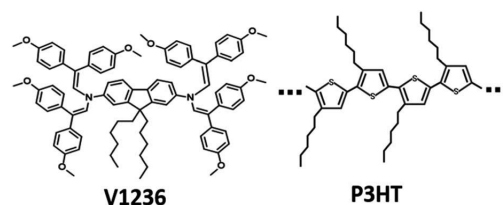


Fig. 1  $N^2, N^2, N^7, N^7$ -Tetrakis[2,2-bis(4-methoxyphenyl)viny]l-9,9-dihexyl-9*H*-fluorene-2,7-diamine (V1236) and poly(3-hexylthiophene-2,5-diyl) (P3HT).



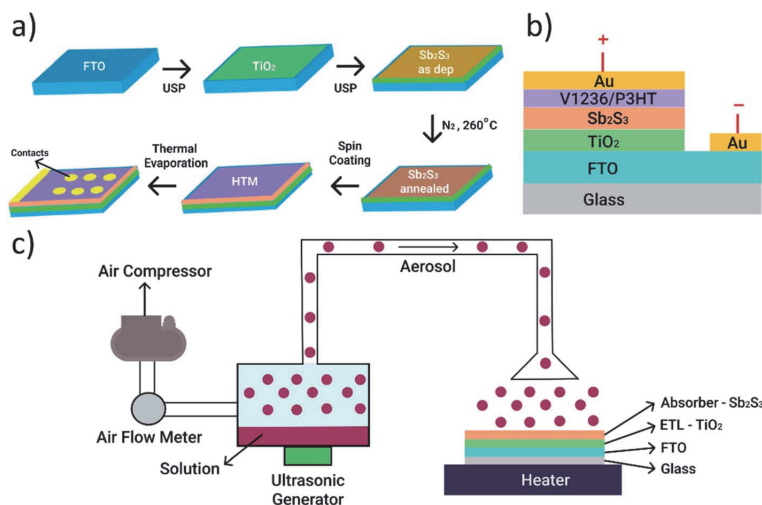


Fig. 2 (a) Schematic of the procedure adopted for the fabrication of Sb<sub>2</sub>S<sub>3</sub> solar cells, (b) Sb<sub>2</sub>S<sub>3</sub> solar cell configuration and (c) schematic of ultrasonic spray pyrolysis (USP) deposition.

followed by cleaning in boiled deionized water for 15 min and were dried with nitrogen prior to deposition. The TiO<sub>2</sub> precursor was prepared by mixing 0.2 M TTIP with 0.2 M acetylacetonate in ethanol. The TiO<sub>2</sub> electron transport layer (ETL) and Sb<sub>2</sub>S<sub>3</sub> absorber were deposited using an indigenously developed and scalable ultrasonic spray pyrolysis technique (USP) as shown in the schematic in Fig. 2c. The USP process is a conventional approach used for the fabrication of semiconducting absorbers. The typical process involves the generation of an aerosol from the precursor solution using an ultrasonic generator, and the aerosol is carried to the substrate surface using a carrier gas, which is compressed air. Furthermore, a director gas, also compressed air, is used to direct the aerosol onto the substrate surface, which is kept on a hot plate. Typically, the director gas nozzle moves in the *x-y* plane which covers the substrate for uniform coating. Each *x* and *y*-directional movement is termed a meander and a set of meanders covering the entire substrate is a cycle. The TiO<sub>2</sub> ETLs were sprayed with 8 meanders and for 75 cycles, which accounted for a sprayed solution of  $\approx 80$  ml and a deposition time of  $\approx 35$  min. A carrier gas flow rate of 7.5 l min<sup>-1</sup> was used, with a spray rate of 2.5 ml min<sup>-1</sup> while the substrate was kept at 340 °C. The as-deposited TiO<sub>2</sub> samples were annealed on a hot plate at 450 °C for 30 min in air. For Sb<sub>2</sub>S<sub>3</sub>, 60 mM of antimony chloride (SbCl<sub>3</sub>) was mixed with 180 mM of thiourea in methanol. A similar USP process was adopted for Sb<sub>2</sub>S<sub>3</sub> where the substrate temperature is 200 °C with the carrier gas flow rate being 2.5 l min<sup>-1</sup>. The same 8-meander approach is followed for a total of 40 cycles utilizing a precursor of  $\approx 60$  ml and a deposition time of  $\approx 30$  min, which resulted in a spray rate of 1.5 ml min<sup>-1</sup>. The as-deposited Sb<sub>2</sub>S<sub>3</sub> thin films on glass/FTO/TiO<sub>2</sub> substrates were then annealed at 250 °C for 5 min in a N<sub>2</sub> atmosphere. To complete the fabrication of solar cells, V1236 and P3HT were spin coated

from their respective precursors dissolved in chlorobenzene. The detailed synthesis process of V1236 is shown in the ESI and the materials are listed in Table S1.† While the concentration of V1236 was systematically varied to obtain the optimal value, the P3HT concentration was 1 wt%, which was conventionally used. It may be noted that after the spin coating of P3HT, the samples were heat treated in a vacuum at 170 °C for 5 min for activation of P3HT whereas no such step was employed for V1236. Finally, Au was thermally evaporated as the top contact with the active area of final solar cells being 7.06 mm<sup>2</sup>.

**2.2.2 Characterization.** The structure and phase constitution of the as-deposited and annealed Sb<sub>2</sub>S<sub>3</sub> films were characterized by X-ray diffraction (XRD) and spectra were collected using a Rigaku Ultima IV instrument with a Cu K<sub>α</sub> source ( $\lambda = 1.5406$  Å) in a  $2\theta$  range of 10–80° at a step size of 0.02°. Micro-Raman spectra were collected at room temperature using a Horiba LabRam HR 800 in the backscattering mode. The He-Ne laser intensity was attenuated to 143  $\mu\text{W } \mu\text{m}^{-2}$  over a focal area of  $\varnothing 5$   $\mu\text{m}$  with a wavelength of 532 nm. Surface and cross-sectional morphologies of the layers were recorded using a Zeiss HR FESEM Ultra 55 (SEM) at an electron beam accelerating voltage of 4 kV. The elemental composition of the films was determined by energy dispersive X-ray spectroscopy (EDX) using a Bruker spectrometer with an ESPRIT 1.8 system at an accelerating voltage of 7 kV. Optical total transmittance and total reflectance spectra of the functional layers (FTO, TiO<sub>2</sub>, Sb<sub>2</sub>S<sub>3</sub>, P3HT and V1236) and the devices were measured in the 250–1100 nm range with reference to air using a Jasco V-670 ultraviolet-visible spectrophotometer (UV-VIS) equipped with a 40 mm integrating sphere.

The work function of Au contacts was measured using a Kelvin probe. To ascertain the band alignment, the ionization potential and electron affinities of the functional layers were



determined by the photoelectron emission spectroscopy method, which measures the dependence of the photoelectron emission current on the photon energy. The electron affinity (LUMO) is calculated as a difference between the ionization energy and photoconductivity threshold energy.<sup>37</sup> Current-voltage ( $I$ - $V$ ) characteristics of the solar cells were measured using a Wavelabs LS-2 LED solar simulator with an AM1.5G (100 mW cm<sup>-2</sup>) light source. External quantum efficiency (EQE) spectra were recorded using a Newport 69911 system with a 300 W Xenon lamp.

### 3 Results and discussion

The as-deposited and annealed Sb<sub>2</sub>S<sub>3</sub> films are characterized to ascertain the quality of films prior to their application in solar cells. XRD patterns of the as-deposited and annealed Sb<sub>2</sub>S<sub>3</sub> films deposited on the glass/FTO/TiO<sub>2</sub> substrate are shown in Fig. 3a. The pattern of the sample with the as-deposited Sb<sub>2</sub>S<sub>3</sub> films shows peaks belonging to FTO and anatase TiO<sub>2</sub> underlayers. In contrast, the annealed films show sharp intense peaks at  $2\theta$  of 15.9, 17.8, 29.2 and 30.5°, which are characteristic of the orthorhombic stibnite structure of Sb<sub>2</sub>S<sub>3</sub> (ICDD PDF 01-075-4013).<sup>3,5</sup> XRD data suggest that the as-deposited films are amorphous in nature and annealing induces crystallization. Additionally, no peaks corresponding to Sb<sub>2</sub>O<sub>3</sub> are detected, which are otherwise present at  $2\theta$  of 13.6 and 27.5°,<sup>3,5</sup> indicating that the annealed Sb<sub>2</sub>S<sub>3</sub> films are of high quality, and devoid of impurities and undesired phases such as oxides. To further

verify the crystallinity and phase of Sb<sub>2</sub>S<sub>3</sub>, the as-deposited and annealed films are characterized using Raman spectroscopy and the recorded spectra are shown in Fig. 3b. As revealed in the spectra, a wide Raman band centred at around 300 cm<sup>-1</sup> is detected in the sample with as-deposited films, which is characteristic of amorphous Sb<sub>2</sub>S<sub>3</sub>.<sup>3</sup> The patterns collected from annealed samples show several sharp peaks characteristic of orthorhombic Sb<sub>2</sub>S<sub>3</sub> at 128, 155, 188, 236, 280, 302, and 312 cm<sup>-1</sup>, which agree with previous reports.<sup>3,5</sup> XRD and Raman analyses corroborate each other to affirm the formation of amorphous and crystalline stibnite phases in as-deposited and annealed Sb<sub>2</sub>S<sub>3</sub> films, respectively, and have further confirmed the presence of single phase Sb<sub>2</sub>S<sub>3</sub> without any secondary phases. The surfaces of the as-deposited and annealed Sb<sub>2</sub>S<sub>3</sub> films are analysed using optical microscopy and the relevant images are shown in Fig. S1†

The images clearly reveal that the surface of the substrates is conformally covered with amorphous Sb<sub>2</sub>S<sub>3</sub> films and the annealed films show a grain structure. Annealing of Sb<sub>2</sub>S<sub>3</sub> films has produced a visual colour change with the as-deposited films turning from orange to dark brown upon annealing (see Fig. S2†). The elemental composition of the as-deposited and annealed Sb<sub>2</sub>S<sub>3</sub> films, determined using energy dispersive X-ray spectroscopy (EDS), shows an atomic ratio of 1.3 for S/Sb. The optical properties of the samples with the as-deposited and annealed Sb<sub>2</sub>S<sub>3</sub> thin films are analysed using UV-Vis-NIR absorption spectroscopy and the corresponding absorbance vs. wavelength curves are shown in Fig. 3c. The spectra reveal

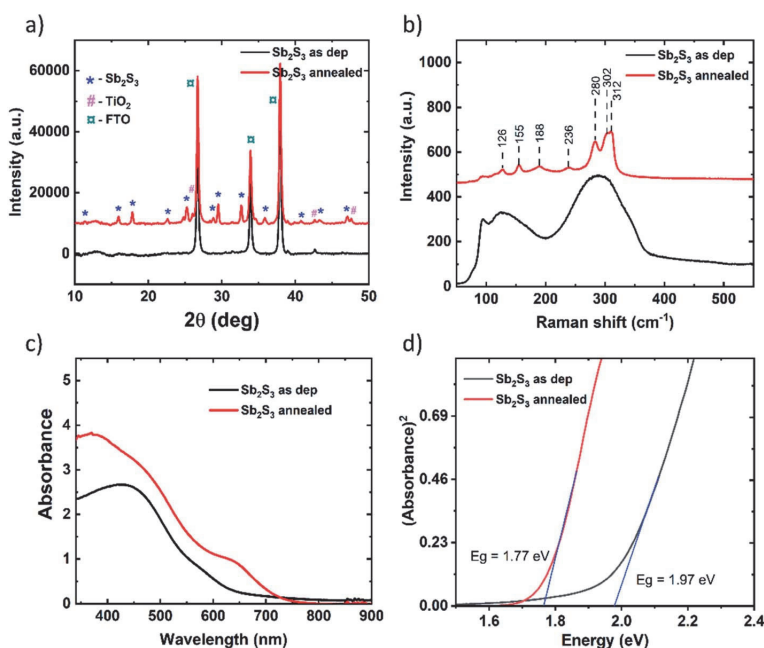


Fig. 3 (a) XRD patterns, (b) Raman spectra, (c) absorption spectra and (d) Tauc plots of as-deposited and annealed Sb<sub>2</sub>S<sub>3</sub> films. Substrate: glass/FTO/TiO<sub>2</sub>.



that the absorption is stronger in annealed  $\text{Sb}_2\text{S}_3$  films with a sharper absorption edge (around 700 nm) compared to amorphous films (around 650 nm). The optical band gap ( $E_g$ ) of amorphous and crystalline  $\text{Sb}_2\text{S}_3$  absorbers is determined using Tauc plots, as shown in Fig. 3d. The allowed band-to-band transitions are considered to be direct in nature while determining the bandgap. The bandgap values of amorphous and crystallized  $\text{Sb}_2\text{S}_3$  absorbers are inferred to be 2.1 and 1.8 eV, respectively, which agree well with previously reported values.<sup>3,5</sup> The morphological, compositional, structural and optical analyses of annealed  $\text{Sb}_2\text{S}_3$  films indicate that the absorber shows conformal coverage on the  $\text{TiO}_2$  layer, a single stibnite phase and a suitable direct bandgap as desired for solar cell applications. On the crystallized  $\text{Sb}_2\text{S}_3$  absorber, V1236 and P3HT are spin coated followed by the thermal evaporation of Au to complete the solar cell fabrication. The detailed synthesis procedure and materials adopted for V1236 are shown in the ESI.† The NMR and mass spectra of intermediate compounds during synthesis and the final V1236 are shown in Fig. S3 and S4,† respectively.

The current density–voltage ( $J$ - $V$ ) characteristics of the devices are measured under one sun illumination (AM 1.5G) and the  $J$ - $V$  curves of the champion cells for each device are shown in Fig. 4 and the corresponding photovoltaic parameters are summarized in Table 1. Primarily, solar cells are prepared using V1236 with a concentration of 15 mM as has been

previously used to fabricate perovskite solar cells.<sup>29</sup> However, the  $\text{Sb}_2\text{S}_3$  solar cells with 15 mM V1236 exhibit a low power conversion efficiency (PCE) of 0.1%, with an open circuit voltage ( $V_{\text{OC}}$ ) of 566 mV, a short-circuit current density ( $J_{\text{SC}}$ ) of  $0.87 \text{ mA cm}^{-2}$ , and a fill factor (FF) of 0.15. While the reasonable  $V_{\text{OC}}$  value indicates the formation of the desired p-n junction, the devices hardly have yielded any  $J_{\text{SC}}$ . The layer thickness of 15 mM V1236 is estimated to be around 140 nm and the resulting series resistance ( $R_s$ ) of the device is estimated to be  $17.2 \Omega \text{ cm}^2$ . The extremely low  $J_{\text{SC}}$  of the solar cell could be attributed to the larger series resistance, which also results in a very low FF. To solve this issue, a series of experiments are carried out where the concentration of V1236 has been systematically reduced ( $4\times$ ,  $8\times$ ,  $16\times$  and  $32\times$ ). The resulting concentrations of 4 mM, 2 mM, 1 mM and 0.5 mM are used for the HTM layer in the fabrication of solar cells. Fig. 4a shows the  $J$ - $V$  characteristics of solar cells with varied V1236 concentrations. As seen from Fig. 4a and Table 1, the concentration dilution has resulted in a considerable increase in PCE particularly arising from significantly higher  $J_{\text{SC}}$  compared to that of the 15 mM case. The highest PCE of 3.9% is obtained for 2 mM V1236 where the  $J_{\text{SC}}$  is  $13.8 \text{ mA cm}^{-2}$ ,  $V_{\text{OC}}$  is 610 mV, and FF is 0.46. However, a further dilution in concentration has decreased the PCE, which is majorly affected by the decrease in  $V_{\text{OC}}$ . This could be attributed to a plausibly very thin V1236 film owing to the low concentration which may not be enough for

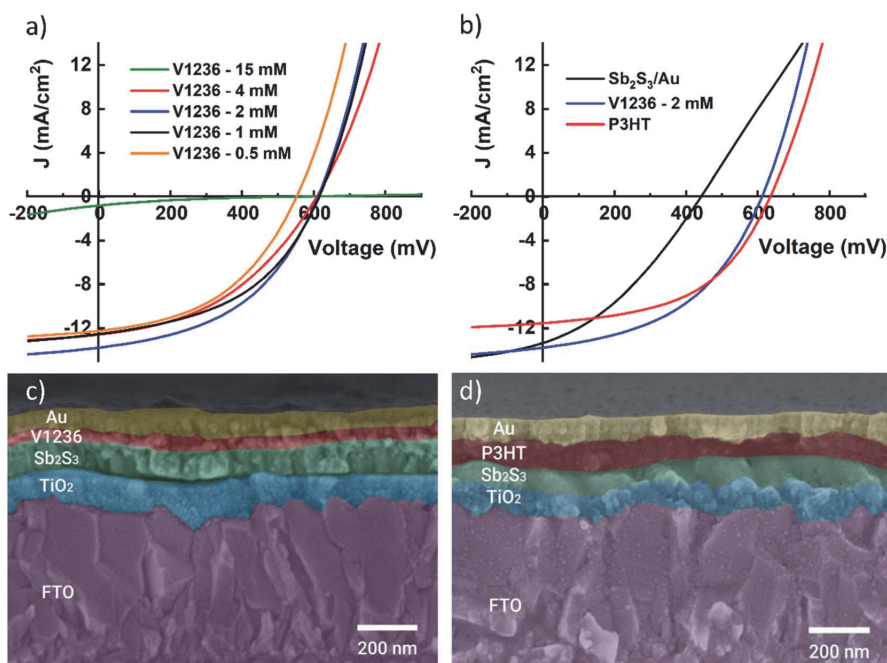


Fig. 4  $J$ - $V$  curves of the champion  $\text{Sb}_2\text{S}_3$  solar cells with (a) different concentrations of V1236 as the HTM. (b) Comparison of cells without an HTM and with optimized V1236 and P3HT. (c) and (d) Cross-sectional images of  $\text{Sb}_2\text{S}_3$  solar cells with optimized V1236 and P3HT as HTMs. Structure: glass/FTO/ $\text{TiO}_2$ / $\text{Sb}_2\text{S}_3$ /HTM/Au.



Table 1 Device parameters of Sb<sub>2</sub>S<sub>3</sub> solar cells without and with V1236 and P3HT HTMs

Sample	HTM conc. (mM)	V <sub>OC</sub> (mV)	J <sub>SC</sub> (mA cm <sup>-2</sup> )	FF (%)	PCE (%)	R <sub>S</sub> (Ω cm <sup>2</sup> )
Sb <sub>2</sub> S <sub>3</sub> /Au	No HTM	440	13.2	34	2.0	4.7
P3HT	1 wt%	634	11.5	50	3.7	3.1
V1236	15	566	0.9	15	0.1	17.2
V1236	4	608	12.5	42	3.2	0.7
V1236	2	612	13.8	46	3.9	0.6
V1236	1	614	12.5	46	3.6	0.5
V1236	0.5	552	12.2	45	3.0	0.4

the complete coverage of the underlying Sb<sub>2</sub>S<sub>3</sub> absorber. The layer thickness measured in the case of V1236 with 2 mM concentration is found to be ≈20 nm. A positive correlation is found between the concentration of V1236 and its thickness. As the concentration of V1236 decreases from 15 mM to 2 mM, the thickness decreases from approximately 140 nm to 20 nm. A decrease in the concentration of V1236, resulting in thinner films, has also led to a decrease in R<sub>S</sub>. Furthermore, for a fair evaluation of V1236 as an HTM, optimized solar cells with 2 mM concentration are compared with the devices made using P3HT as an HTM. The concentration of P3HT (0.5, 1 and 2 wt%) has been optimized as shown in Fig. S5,† which shows that solar cells with 1 wt% P3HT have yielded the highest PCE and are therefore used as the reference. The summarized device parameters from *JV* curves are shown in Table S2.† The *J-V* curves of solar cells with optimized V1236 and P3HT are compared as shown in Fig. 4b, which indicates almost comparable efficiencies, demonstrating the efficacy of V1236 as an HTM for Sb<sub>2</sub>S<sub>3</sub> solar cells. Furthermore, to understand the impact of HTMs as such, reference devices are made without HTMs, and have yielded a PCE of 2.0% with a lower V<sub>OC</sub> and FF. This fact affirms the need for HTMs in Sb<sub>2</sub>S<sub>3</sub> solar cells to obtain a higher V<sub>OC</sub> and hence, efficiency. In addition, to investigate any plausible hysteresis in devices, the forward and reverse *J-V* characteristics of Sb<sub>2</sub>S<sub>3</sub> solar cells with V1236 and P3HT as HTMs are measured and the plots are shown in Fig. S6.† The *J-V* curves in forward and reverse directions are almost identical and the calculated hysteresis index (HI) values in both the cases are <0.05 indicating negligible hysteresis in Sb<sub>2</sub>S<sub>3</sub> solar cells with both HTMs.

Cross-sectional images of solar cell stacks with optimized V1236 and P3HT are shown in Fig. 4c and d, respectively. The thickness of TiO<sub>2</sub> and Sb<sub>2</sub>S<sub>3</sub> is almost identical in both cases (≈90 nm) while V1236 is a considerably thinner layer (≈20 nm) compared to the P3HT layer (≈100 nm). It is important to note that the V1236 and P3HT are independently optimized for Sb<sub>2</sub>S<sub>3</sub> solar cells leading to higher efficiency, which shows that thinner V1236 is sufficient for obtaining similar efficiencies compared to a reasonably thicker P3HT. Therefore, irrespective of their thickness, the optimized V1236- and P3HT-based solar cells are further characterized and compared for band energetics, quantum efficiency, and overall transparency. The reproducibility of semi-transparent solar cells with V1236 and P3HT HTMs is compared with the box plots as shown in Fig. 5. The

spread is not only reasonably small but also almost identical for both the cases and for all the device parameters (V<sub>OC</sub>, J<sub>SC</sub>, FF and PCE), indicating the good reproducibility of solar cells.

Since V1236 is explored as an HTM for Sb<sub>2</sub>S<sub>3</sub> solar cells for the first time, it is imperative to understand the band edge positions of this material with respect to the absorber for a better understanding of device physics. It is well known that photogenerated electrons in the absorber flow towards the ETL (TiO<sub>2</sub>) and the holes towards the HTM. The energy levels at the Sb<sub>2</sub>S<sub>3</sub>/HTM interface have a strong effect on the hole extraction process. A staggered-gap heterointerface can benefit the process greatly and also prevent the electrons from passing to the HTM layer. The typical curves and the estimation of ionization energy for the V1236 HTM are shown in Fig. S7.† Fig. 6 shows the band energy diagram of solar cells with V1236 and P3HT. The energy levels of FTO, TiO<sub>2</sub>, Sb<sub>2</sub>S<sub>3</sub>, P3HT and V1236 are obtained from photoemission spectroscopy and intrinsic photoconductivity measurements. As clearly revealed in the figure, the HOMO of V1236 (-5.0 eV) is in closer proximity than P3HT (-4.6 eV) to the valence band edge of Sb<sub>2</sub>S<sub>3</sub> (-5.1). This could explain the enhanced performance of V1236 over P3HT due to better hole transport at the absorber-V1236 interface. An interesting observation from Table 1 is that devices with V1236 exhibit a slightly lower V<sub>OC</sub> than P3HT despite its deeper HOMO level. It may be noted that the observed difference (≈20 mV) in the present study is not significantly large. It is observed that the thickness of V1236 (≈20 nm) is considerably smaller than that of P3HT (≈100 nm) indicating a difference in the interface across Sb<sub>2</sub>S<sub>3</sub>/HTM/Au, which may also affect the V<sub>OC</sub>. In addition, the V<sub>OC</sub> of the device depends on other parameters like recombination at the absorber-HTM interface, the defects in the absorber, *etc.*, which necessitates deeper analysis like conducting transient photovoltage measurements to analyse the influence of interfacial recombination between the HTM and the absorber layer, which could be investigated further. The LUMO energy level of V1236 (-2.4 eV) is considerably higher than that of P3HT (-2.8 eV) with respect to the conduction band edge (CBE) of Sb<sub>2</sub>S<sub>3</sub> (-3.4 eV). The higher difference between the CBE of Sb<sub>2</sub>S<sub>3</sub> and LUMO of V1236 results in a larger potential barrier (1 eV), which inhibits any chance of electron transport to the Au contact and thus reduces the probability of recombination compared to the P3HT case, which has a smaller energy difference (0.2 eV). The band edge alignment suggests



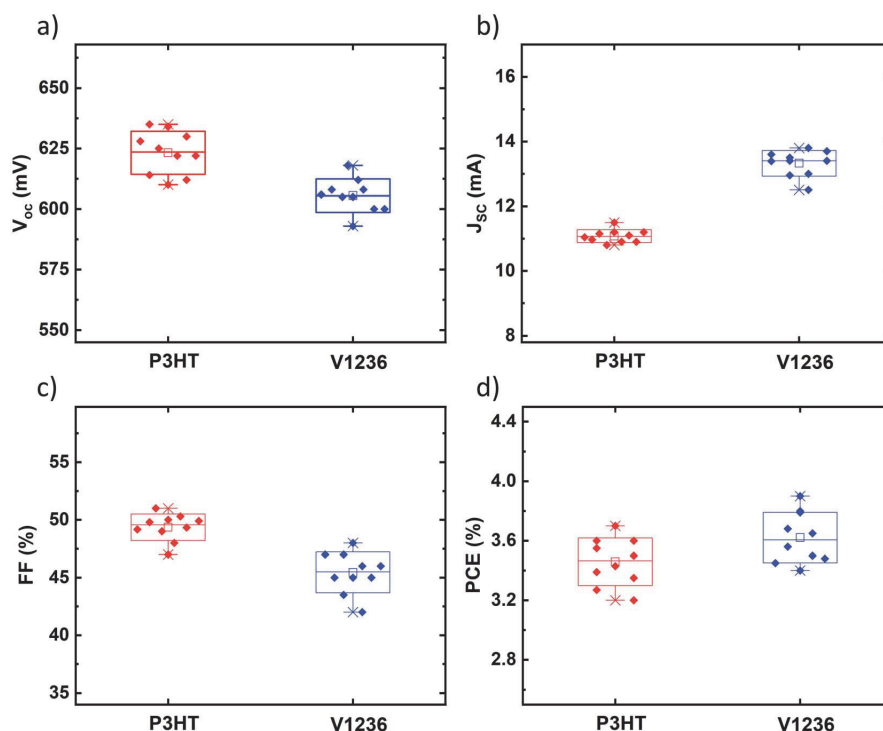


Fig. 5 Box plots showing reproducibility of (a)  $V_{OC}$ , (b)  $J_{SC}$ , (c) FF, and (d) efficiency (PCE) for champion  $Sb_2S_3$  solar cells with V1236 and P3HT as HTMs. Structure: glass/FTO/ $TiO_2$ / $Sb_2S_3$ /HTM/Au.

that V1236 could be a potentially more effective HTM than P3HT for  $Sb_2S_3$  solar cells.

Furthermore, the external quantum efficiencies (EQEs) of the  $Sb_2S_3$  solar cells with P3HT and V1236 are studied and the EQE curves are shown in Fig. 7a. EQE curves of solar cells with varied V1236 concentrations are shown in Fig. S8.† While the plots are amply indicative of the fact that the solar cells with V1236 have exhibited a higher spectral response in the entire wavelength

range, it may also be noted that the dip in EQE observed for P3HT devices in the 500–700 nm range is absent for V1236 devices. Overall, solar cells with V1236 have exhibited an EQE of  $\approx 80\%$  while P3HT devices have yielded 70% in the maximum absorption region, *i.e.*, 400–500 nm. Furthermore, the onset of the absorption edge is situated around 700 nm (1.8 eV), which corresponds to the bandgap of  $Sb_2S_3$  absorbers, corroborating the optical studies. The integrated  $J_{SC}$  values calculated from

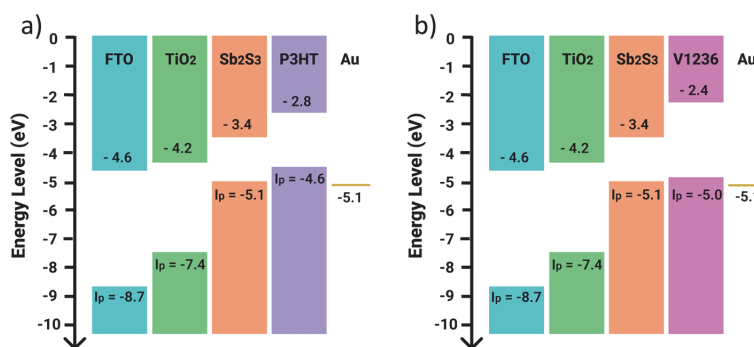


Fig. 6 Energy band diagram of  $Sb_2S_3$  solar cells with (a) P3HT and (b) V1236 as HTMs.



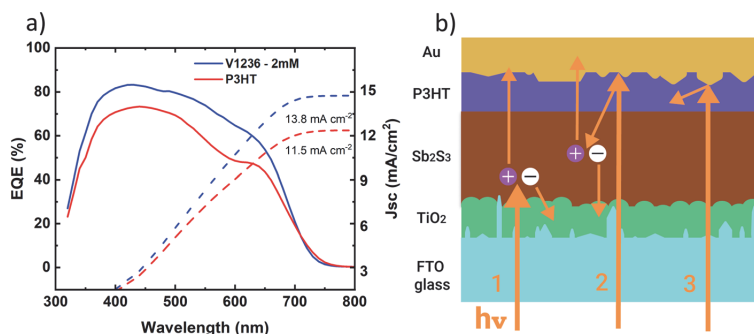


Fig. 7 (a) EQE and integrated  $J_{SC}$  of  $Sb_2S_3$  solar cells with V1236 and P3HT as HTMs and (b) schematic of the spectral response in  $Sb_2S_3$  solar cells. Structure: glass/FTO/TiO<sub>2</sub>/ $Sb_2S_3$ /HTM/Au.

EQE spectra are shown in Fig. 7a and are calculated to be 13.8 and 11.5  $mA\ cm^{-2}$  for V1236 and P3HT, respectively. The values are almost identical to the  $J_{SC}$  values obtained from  $J-V$  characteristics (Fig. 4b). The impact of polymer-based HTMs on EQE was previously explained by Zimmermann *et al.*,<sup>27</sup> wherein three major mechanisms are held responsible. Primarily, the recombination occurs within the exciton diffusion length of the HTM while a weak electronic bonding or an unfavourable band alignment at the HTM-absorber interface also contributes to enhanced recombination and finally, parasitic absorption in the bulk of the HTM. When light traverses through the absorber, the majority of the light gets absorbed depending on the absorption co-efficient and thickness. If the thickness of the absorber is around 100 nm, some of the light transmits through and gets reflected at the HTM-metal interface, which is supposed to be reabsorbed back in the absorber. However, if the HTM is sufficiently thick ( $\approx 100$  nm), the reflected light gets absorbed within the HTM, which is responsible for parasitic absorption.<sup>27</sup> Thus, optimization of layer thicknesses, and interface modifications are key aspects in  $Sb_2S_3$ -polymer devices. The parasitic absorption coupled with the optical spacer effect of P3HT may be responsible for the overall lower EQE.<sup>27</sup> It is also known that P3HT absorbs majorly in the 500–

600 nm region due to its bandgap at 1.8 eV,<sup>3,5</sup> which further corroborates the dip seen in the EQE curve, thus attributing it to the parasitic absorption.<sup>27</sup> Furthermore, the optical spacer effect is dominant when the thickness of the absorber is less than 100 nm, which is the case in the present study. The spectral response in  $Sb_2S_3$  solar cells is schematically demonstrated in Fig. 7b, which shows the direct absorption of sun light contributing to the carrier generation (indicated as 1), the re-absorption of reflected light from the HTM-metal interface, also contributing to photogeneration (2) and the absorption of reflected light within the HTM layer (3). The spectral response in  $Sb_2S_3$  solar cells with P3HT may majorly have the phenomena 1 and 3 while V1236 devices may have 1 and 2 owing to the large difference in the thickness of HTMs, which could be witnessed from the EQE curves wherein V1236 devices displayed a larger response compared to P3HT counterparts.

To further understand the effect of spectral response, optical properties of individual HTMs coated on glass/FTO substrates are analysed and the total transmittance spectra are shown in Fig. 8a, where the reference curve is also included for the glass/FTO substrate. As can be clearly seen, the transmittance spectrum of glass/FTO/V1236 is almost identical to that of the glass/FTO sample indicating the complete transparency of the V1236

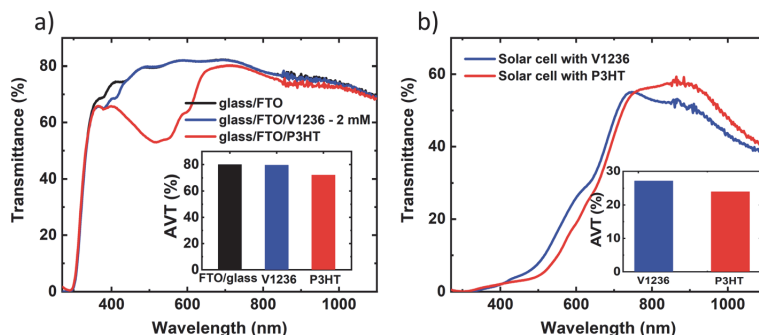


Fig. 8 Total transmission spectra of (a) glass/FTO, glass/FTO/V1236 and glass/FTO/P3HT layers and (b)  $Sb_2S_3$  solar cells with V1236 and P3HT as HTMs devoid of a back contact (insets of a and b: respective average visible transmittance bar charts in the 400–800 nm range).



HTM. P3HT, on the other hand, has exhibited a dip in the transmittance around the 500 nm region, which corresponds to the absorption within P3HT ( $E_g \approx 1.8$  eV). The solar weighted average visible transmittance (AVT) values, calculated in the 400–800 nm region, are compared as shown in the inset of Fig. 8a. The AVT for glass/FTO and glass/FTO/V1236 is almost similar around 80% while that of glass/FTO/P3HT is  $\approx 72\%$ , which further affirms that the optimized V1236 in the present study contributes to more transparency than the P3HT. Furthermore, the total transmittance spectra of V1236 at different concentrations are shown in Fig. S9,† which reveal the transparency of V1236 even for a larger thickness. It may well be noted that the thickness values of P3HT and V1236 compared herein are approximately 100 and 20 nm, respectively, which are optimized for the best efficiency  $\text{Sb}_2\text{S}_3$  in each case. Therefore, for a fair comparison of the optical properties, thinner P3HT deposited on glass/FTO, obtained by diluting the concentration, is compared with V1236 as shown in Fig. S10.† Although the thinner P3HT has exhibited enhanced transparency, the relevant absorption edge is still seen, which is majorly responsible for the reduced overall transparency. On a similar note, the total transmittance spectra are recorded for the solar cell devoid of a top metal contact for V1236 and P3HT devices as shown in Fig. 8b. While both the devices have exhibited AVT over 20%, V1236 devices have shown enhanced transparency (about 20% higher) compared to P3HT devices thereby validating the use of V1236 as an HTM in semi-transparent  $\text{Sb}_2\text{S}_3$  solar cells.

## 4 Conclusions

In conclusion, a cost-effective and transparent fluorene-based enamine (V1236) hole transport material has been successfully demonstrated, for the first time, in the fabrication of semi-transparent  $\text{Sb}_2\text{S}_3$  solar cells yielding a power conversion efficiency of 3.9% with an average visible transmission of 27% in the 400–800 nm spectral range. When compared with conventional P3HT based solar cells, the significantly cheaper V1236 devices have exhibited similar efficiencies and improved transparency. It is observed that the parasitic absorption losses coupled with absorption in the visible range exhibited by P3HT are not present in the case of V1236 thereby validating its efficacy as an HTM for semi-transparent solar cells. Furthermore, the band diagram of solar cells with P3HT and V1236 as HTMs reveals that V1236 is a more effective HTM for the  $\text{Sb}_2\text{S}_3$  absorber owing to its improved band alignment. The study, on a whole, put forward the use of new and significantly cheaper V1236 as an HTM in semi-transparent  $\text{Sb}_2\text{S}_3$  solar cells, which paves the way towards solar window applications.

## Author contributions

Nimish Juneja – conceptualization, data curation, formal analysis, methodology, validation, visualization, and writing – original draft. Sreekanth Mandati – conceptualization, investigation, formal analysis, methodology, validation, visualization, supervision, and writing – review & editing. Atanas Katerski – methodology and validation. Nicolae Spalatu – writing – review

& editing. Sarune Daskeviciute-Geguziene – methodology and writing – review & editing. Aivars Vembris – methodology and writing – review & editing. Smagul Karazhanov – writing – review & editing. Vytautas Getautis – methodology and writing – review & editing. Malle Krunkis – formal analysis, supervision, and writing – review & editing. Ilona Oja Acik – formal analysis, funding acquisition, project administration, resources, supervision, and writing – review & editing.

## Conflicts of interest

There are no conflicts to declare.

## Acknowledgements

The “Development of Semi-Transparent Bifacial Thin Film Solar Cells for Innovative Applications” benefits from a 999372 € grant from Iceland, Liechtenstein and Norway through the EEA Grants. The aim of the project is to develop a new approach based on novel materials and structures and production technologies, which are the key to further increase the share, and range of applications of PV in areas with sub-average sunlight, including Baltic and Nordic countries. Therefore, development of resource saving, cost-effective and efficient PV devices is a primary challenge of this project. Project contract with the Research Council of Lithuania (LMTLT) No is S-BMT-21-1(LT08-2-LMT-K-01-003). The Department of Materials and Environmental Technology, Tallinn University of Technology has received funding from Estonian Research Council project PRG627 “Antimony Chalcogenide Thin Films for Next-Generation Semi-Transparent Solar Cells Applicable in Electricity Producing Windows”, the Estonian Centre of Excellence project TK141 (TAR16016EK) “Advanced Materials and High-Technology Devices for Energy Recuperation Systems”, the European Union's Horizon 2020 programme under the ERA Chair project 5GSOLAR grant agreement No 952509 and PSG689 “Bismuth Chalcogenide Thin-Film Disruptive Green Solar Technology for Next Generation Photovoltaics”. Institute of Solid-State Physics, University of Latvia has received funding from the European Union's Horizon 2020 Framework Programme H2020-WIDESPREAD-01-2016-2017-Teaming Phase 2 under grant agreement No. 739508, project CAMART<sup>2</sup>. The authors thank Dr Tadas Malinauskas and Dr Valdek Mikli for their support in preparation and characterization of the samples.

## Notes and references

- 1 M. Y. Versavel and J. A. Haber, *Thin Solid Films*, 2007, **515**, 7171–7176.
- 2 S. Messina, M. T. S. Nair and P. K. Nair, *Thin Solid Films*, 2007, **515**, 5777–5782.
- 3 J. S. Eensalu, A. Katerski, E. Kärber, L. Weinhardt, M. Blum, C. Heske, W. Yang, I. Oja Acik and M. Krunkis, *Beilstein J. Nanotechnol.*, 2019, **10**, 2396–2409.
- 4 R. Kondrotas, C. Chen and J. Tang, *Joule*, 2018, **2**, 857–878.



- 5 J. S. Eensalu, A. Katerski, E. Kärber, I. Oja Acik, A. Mere and M. Krunk, *Beilstein J. Nanotechnol.*, 2019, **10**, 198–210.
- 6 Y. Itzhaik, O. Niitsoo, M. Page and G. Hodes, *J. Phys. Chem. C*, 2009, **113**, 4254–4256.
- 7 Y. C. Choi, D. U. Lee, J. H. Noh, E. K. Kim and S. il Seok, *Adv. Funct. Mater.*, 2014, **24**, 3587–3592.
- 8 Y. C. Choi and S. il Seok, *Adv. Funct. Mater.*, 2015, **25**, 2892–2898.
- 9 P. Sun, M. Zhang, C. Ai, Z. Wu, S. Lu, X. Zhang, N. Huang, Y. Sun and X. Sun, *J. Power Sources*, 2016, **319**, 219–226.
- 10 H. Wedemeyer, J. Michels, R. Chmielowski, S. Bourdais, T. Muto, M. Sugiura, G. Dennler and J. Bachmann, *Energy Environ. Sci.*, 2013, **6**, 67–71.
- 11 H.-J. Jo, S. H. Kim, J. S. Kim, S.-J. Lee and D.-H. Kim, *J. Korean Phys. Soc.*, 2016, **69**, 541–546.
- 12 R. Parize, A. Katerski, I. Gromyko, L. Rapenne, H. Roussel, E. Kärber, E. Appert, M. Krunk and V. Consonni, *J. Phys. Chem. C*, 2017, **121**, 9672–9680.
- 13 N. Spalatu, R. Krautmann, A. Katerski, E. Karber, R. Josepsson, J. Hiie, I. O. Acik and M. Krunk, *Sol. Energy Mater. Sol. Cells*, 2021, **225**, 111045.
- 14 R. Krautmann, N. Spalatu, R. Gunder, D. Abou-Ras, T. Unold, S. Schorr, M. Krunk and I. Oja Acik, *Sol. Energy*, 2021, **225**, 494–500.
- 15 C. P. Liu, H. E. Wang, T. W. Ng, Z. H. Chen, W. F. Zhang, C. Yan, Y. B. Tang, I. Bello, L. Martinu, W. J. Zhang and S. K. Jha, *Phys. Status Solidi B*, 2012, **249**, 627–633.
- 16 N. Ali, A. Hussain, R. Ahmed, W. N. W. Shamsuri, A. Shaari, N. Ahmad and S. M. Abbas, *Appl. Phys. A: Solids Surf.*, 2016, **122**, 23.
- 17 M. I. Medina-Montes, Z. Montiel-González, N. R. Mathews and X. Mathew, *J. Phys. Chem. Solids*, 2017, **111**, 182–189.
- 18 Y. Zeng, F. Liu, M. Green and X. Hao, in *2018 IEEE 7th World Conference on Photovoltaic Energy Conversion (WCPEC) (A Joint Conference of 45th IEEE PVSC, 28th PVSEC & 34th EU PVSEC)*, IEEE, 2018, pp. 0870–0872.
- 19 L. Guo, B. Zhang, S. Li, Q. Zhang, M. Buettner, L. Li, X. Qian and F. Yan, *APL Mater.*, 2019, **7**, 041105.
- 20 W. Lian, C. Jiang, Y. Yin, R. Tang, G. Li, L. Zhang, B. Che and T. Chen, *Nat. Commun.*, 2021, **12**, 3260.
- 21 C. Lan, G. Liang, H. Lan, H. Peng, Z. Su, D. Zhang, H. Sun, J. Luo and P. Fan, *Phys. Status Solidi RRL*, 2018, **12**, 1800025.
- 22 M. S. You, C.-S. Lim, D. H. Kwon, J. H. Heo, S. H. Im and K. J. Chae, *Org. Electron.*, 2015, **21**, 155–159.
- 23 D.-H. Kim, S.-J. Lee, M. S. Park, J.-K. Kang, J. H. Heo, S. H. Im and S.-J. Sung, *Nanoscale*, 2014, **6**, 14549–14554.
- 24 Y. Zhang, S. Li, R. Tang, X. Wang, C. Chen, W. Lian, C. Zhu and T. Chen, *Energy Technol.*, 2018, **6**, 2126–2131.
- 25 J. Chen, J. Qi, R. Liu, X. Zhu, Z. Wan, Q. Zhao, S. Tao, C. Dong, G. Y. Ashebir, W. Chen, R. Peng, F. Zhang, S. Yang, X. Tian and M. Wang, *Commun. Chem.*, 2019, **2**, 121.
- 26 E. Kärber, A. Katerski, I. Oja Acik, A. Mere, V. Mikli and M. Krunk, *Beilstein J. Nanotechnol.*, 2016, **7**, 1662–1673.
- 27 E. Zimmermann, T. Pfadler, J. Kalb, J. A. Dorman, D. Sommer, G. Hahn, J. Weickert and L. Schmidt-Mende, *Adv. Sci.*, 2015, **2**, 1500059.
- 28 H. Lei, G. Yang, Y. Guo, L. Xiong, P. Qin, X. Dai, X. Zheng, W. Ke, H. Tao, Z. Chen, B. Li and G. Fang, *Phys. Chem. Chem. Phys.*, 2016, **18**, 16436–16443.
- 29 T. Malinauskas, M. Saliba, T. Matsui, M. Daskeviciene, S. Urnikaite, P. Gratia, R. Send, H. Wonneberger, I. Bruder, M. Graetzel, V. Getautis and M. K. Nazeeruddin, *Energy Environ. Sci.*, 2016, **9**, 1681–1686.
- 30 S. H. Im, C.-S. Lim, J. A. Chang, Y. H. Lee, N. Maiti, H.-J. Kim, Md. K. Nazeeruddin, M. Grätzel and S. il Seok, *Nano Lett.*, 2011, **11**, 4789–4793.
- 31 X. Jin, Y. Yuan, C. Jiang, H. Ju, G. Jiang, W. Liu, C. Zhu and T. Chen, *Sol. Energy Mater. Sol. Cells*, 2018, **185**, 542–548.
- 32 L. Zhang, C. Jiang, C. Wu, H. Ju, G. Jiang, W. Liu, C. Zhu and T. Chen, *ACS Appl. Mater. Interfaces*, 2018, **10**, 27098–27105.
- 33 A. Shit, P. Chal and A. K. Nandi, *Phys. Chem. Chem. Phys.*, 2018, **20**, 15890–15900.
- 34 S. Daskeviciute, C. Momblona, K. Rakstys, A. A. Sutanto, M. Daskeviciene, V. Jankauskas, A. Gruodis, G. Bubniene, V. Getautis and M. K. Nazeeruddin, *J. Mater. Chem. A*, 2021, **9**, 301–309.
- 35 M. L. Petrus, T. Bein, T. J. Dingemans and P. Docampo, *J. Mater. Chem. A*, 2015, **3**, 12159–12162.
- 36 F. Machui, M. Hösel, N. Li, G. D. Spyropoulos, T. Ameri, R. R. Søndergaard, M. Jørgensen, A. Scheel, D. Gaiser, K. Kreul, D. Lenssen, M. Legros, N. Lemaitre, M. Vilkmann, M. Välimäki, S. Nordman, C. J. Brabec and F. C. Krebs, *Energy Environ. Sci.*, 2014, **7**, 2792.
- 37 J. Latvels, R. Grzibovskis, K. Pudzs, A. Vembris, D. Blumberga, B. P. Rand, C. Adachi, D. Cheyng and V. van Elsbergen, *J. Mater. Chem. C*, 2014, 91371G.



## Publication II

Sreekanth Mandati, **Nimish Juneja**, Atanas Katerski, Aisté Jegorovè, Raitis Gržibovskis, Aivars Vembris, Tatjana Dedova, Nicolae Spalatu, Artiom Magomedov, Smagul Karazhanov, Vytautas Getautis, Malle Krunks, and Ilona Oja Acik, “4.9 % efficient  $\text{Sb}_2\text{S}_3$  solar cells from semitransparent absorbers with fluorene-based thiophene-terminated hole conductors”, ACS Applied Energy Materials, 6, 3822–33, 2023, doi: 10.1021/acsaem.2c04097.



# 4.9% Efficient $\text{Sb}_2\text{S}_3$ Solar Cells from Semitransparent Absorbers with Fluorene-Based Thiophene-Terminated Hole Conductors

Sreekanth Mandati,\* Nimish Juneja, Atanas Katerski, Aistė Jegorovė, Raitis Grzibovskis, Aivars Vembris, Tatjana Dedova, Nicolae Spalatu, Artiom Magomedov, Smagul Karazhanov, Vytautas Getautis, Malle Krunk, and Ilona Oja Acik\*

Cite This: *ACS Appl. Energy Mater.* 2023, 6, 3822–3833

Read Online

ACCESS |

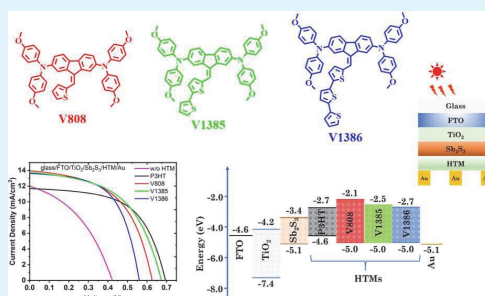
Metrics & More

Article Recommendations

Supporting Information

**ABSTRACT:** Fluorene-based hole transport materials (HTMs) with terminating thiophene units are explored, for the first time, for antimony sulfide ( $\text{Sb}_2\text{S}_3$ ) solar cells. These HTMs possess largely simplified synthesis processes and high yields compared to the conventional expensive hole conductors making them reasonably economical. The thiophene unit-linked HTMs have been successfully demonstrated in ultrasonic spray-deposited  $\text{Sb}_2\text{S}_3$  solar cells resulting in efficiencies in the range of 4.7–4.9% with an average visible transmittance (AVT) of 30–33% (400–800 nm) for the cell stack without metal contact, while the cells fabricated using conventional P3HT have yielded an efficiency of 4.7% with an AVT of 26%. The study puts forward cost-effective and transparent HTMs that avoid a post-coating activation at elevated temperatures like P3HT, devoid of parasitic absorption losses in the visible region and are demonstrated to be well aligned for the band edges of  $\text{Sb}_2\text{S}_3$  thereby ascertaining their suitability for  $\text{Sb}_2\text{S}_3$  solar cells and are potential candidates for semitransparent applications.

**KEYWORDS:** antimony sulfide, solar cells, thiophene, hole transport material, semitransparent



## 1. INTRODUCTION

The energy crisis is among the major problems of the present day's growing world with digitalization and the internet of things. In addition, the limited availability of fossil fuels, the dominant sources of current days' energy and the associated problems of pollutant emissions by burning fossil fuels is a bigger concern. Considering the UNO's policies of net-zero emissions by 2050 coupled with the goals set by many countries worldwide to produce clean energy necessitates the requirement of alternative energy sources that are clean, abundant, and easy to harvest. Renewable energy technologies are the need of the hour to meet these demands and among them, solar photovoltaics (PV) is a technology that has tremendous potential to be a major yet important energy harvesting source. Solar energy is abundantly available and PV is a green technology that facilitates the conversion of sunlight to electricity in a clean manner once the solar panels are in fully operational condition. Furthermore, building-integrated photovoltaics (BIPV) is an emerging technology in PV wherein solar panels could be integrated into buildings that produce energy to meet some portion of energy demand within. Energy-efficient buildings are going to be the future with the growing smart city infrastructure and contribute effectively toward net-zero emissions. Semitransparent solar cells could play an important role in BIPV and could be integrated into

windows. Intense investigations are underway to explore novel materials and device architectures that are suitable for semitransparent solar cells.

Among various emerging materials, antimony sulfide ( $\text{Sb}_2\text{S}_3$ ) is the promising candidate for the photovoltaic community owing to the earth-abundant and environmentally friendly constituent elements alongside appropriate optoelectronic properties such as a desirable band gap of  $\approx 1.7$  eV, large absorption coefficient ( $\approx 10^5 \text{ cm}^{-1}$ ) and long-term stability.<sup>1–3</sup> The Shockley–Queisser limit of the power conversion efficiency (PCE) of the single junction  $\text{Sb}_2\text{S}_3$  solar cells is 28.64%.<sup>1</sup>  $\text{Sb}_2\text{S}_3$  absorbers are potential contenders for semitransparent solar cells due to their relatively wide band gap and the possibility to yield higher PCEs even with very thin absorber layers ( $\approx 100$  nm).<sup>4</sup> Further, the wide band gap of  $\text{Sb}_2\text{S}_3$  also makes them a wiser choice for tandem cell applications.<sup>5–7</sup> The highest reported PCE of  $\text{Sb}_2\text{S}_3$  solar cells

Received: December 21, 2022

Accepted: March 14, 2023

Published: March 23, 2023



**Table 1.** Reported Device Parameters of Sb<sub>2</sub>S<sub>3</sub> Solar Cells with Different HTMs, Device Configurations, Methods of Preparation, and Thicknesses<sup>a</sup>

HTM	device configuration	Sb <sub>2</sub> S <sub>3</sub> (deposition technique)	Sb <sub>2</sub> S <sub>3</sub> thickness (nm)	solar cell parameters				reference
				V <sub>OC</sub> (mV)	J <sub>SC</sub> (mA/cm <sup>2</sup> )	FF (%)	PCE (%)	
P3HT	ITO/ZnO/Sb <sub>2</sub> S <sub>3</sub> /P3HT/Ag	TE	210	450	12.6	42	2.4	21
	ITO/TiO <sub>2</sub> /Sb <sub>2</sub> S <sub>3</sub> /P3HT/Au	CBD	200	630	6.1	35	1.4	22
	ITO/TiO <sub>2</sub> /Sb <sub>2</sub> S <sub>3</sub> /P3HT/Ag	ALD	155	732	9.3	62	4.3	2
	FTO/TiO <sub>2</sub> /Sb <sub>2</sub> S <sub>3</sub> /P3HT/Au	SC		616	8.1	46	2.3	16
	ITO/TiO <sub>2</sub> /Sb <sub>2</sub> S <sub>3</sub> /P3HT/Au	USP	150	618	6.0	51	1.9	23
Spiro-OMeTAD	ITO/TiO <sub>2</sub> /Sb <sub>2</sub> S <sub>3</sub> /Spiro-OMeTAD/Au	CBD	100	693	13.8	58	5.5	6
	FTO/TiO <sub>2</sub> /Sb <sub>2</sub> S <sub>3</sub> /Spiro-OMeTAD/Au	CBD	84	690	13.4	50	4.6	17
	FTO/TiO <sub>2</sub> /Sb <sub>2</sub> S <sub>3</sub> /Spiro-OMeTAD/Au	SC	400	660	13.1	59	5.2	18
	FTO/TiO <sub>2</sub> /Sb <sub>2</sub> S <sub>3</sub> /Spiro-OMeTAD/Au	SC	140	632	12.9	52	4.3	24
	FTO/TiO <sub>2</sub> /Sb <sub>2</sub> S <sub>3</sub> /Spiro-OMeTAD/Ag	TE	300	620	10.7	56	3.8	25
	FTO/TiO <sub>2</sub> /Sb <sub>2</sub> S <sub>3</sub> /Spiro-OMeTAD/Au	SC	162	650	17.7	62	7.1	26
	FTO/TiO <sub>2</sub> /Sb <sub>2</sub> S <sub>3</sub> /Spiro-OMeTAD/Au	SC	146	720	17.2	57	7.1	27
	FTO/CdS/Sb <sub>2</sub> S <sub>3</sub> /Spiro-OMeTAD/Au	HT	300	707	15.2	56	6.0	28
	FTO/CdS/Sb <sub>2</sub> S <sub>3</sub> /Spiro-OMeTAD/Au	TE	200	720	15.9	54	6.2	29
	FTO/TiO <sub>2</sub> /CdS/Sb <sub>2</sub> S <sub>3</sub> /Spiro-OMeTAD/Au	HT	1000	748	15.3	57	6.5	30
P3HT/ PEDOT:PSS	FTO/CdS/Sb <sub>2</sub> S <sub>3</sub> /Spiro-OMeTAD/Au	CBD	214	757	17.4	60.5	8.0	8
	FTO/TiO <sub>2</sub> /ZnS/Sb <sub>2</sub> S <sub>3</sub> /P3HT/ PEDOT:PSS/Au	ALD	75	626	15.7	52	5.1	31
	FTO/TiO <sub>2</sub> /Sb <sub>2</sub> S <sub>3</sub> /P3HT/PEDOT:PSS/ Au	ALD	90	667	14.9	58	5.8	32
V1236	FTO/TiO <sub>2</sub> /Sb <sub>2</sub> S <sub>3</sub> /HTM/Au	USP	90	612	13.8	46	3.9	33

<sup>a</sup>HTM: hole transport material; TE: thermal evaporation; CBD: chemical bath deposition; SC: spin coating; USP: ultrasonic spray pyrolysis; HT: hydrothermal; ALD: atomic layer deposition, V1236: (N<sup>2</sup>,N<sup>2</sup>,N<sup>7</sup>,N<sup>7</sup>-tetrakis[2,2-bis(4-methoxyphenyl)vinyl]-9,9-dihexyl-9H-fluorene-2,7-diamine).

is 8%, achieved recently through a multi-sulfur source approach using the chemical bath deposition method (CBD).<sup>8</sup> The overall efficiencies are rather limited by the deficiencies in open circuit voltage (V<sub>OC</sub>) that are attributed to the self-trapping of carriers due to lattice deformation and/or to the intrinsic defects, which sets the maximum attainable V<sub>OC</sub> to 0.8 V.<sup>9,10</sup> Antimony selenide (Sb<sub>2</sub>Se<sub>3</sub>), another class of antimony chalcogenide, is also a potential candidate for PV applications and is explored extensively.<sup>11–13</sup>

In addition to the considerable challenges in improving the PCEs, the method of Sb<sub>2</sub>S<sub>3</sub> absorber fabrication is critical for upscaling. The high-efficiency Sb<sub>2</sub>S<sub>3</sub> solar cells so far are mostly prepared by spin coating and CBD.<sup>8–15</sup> While the spin coating technique demonstrates excellent control of parameters and reproducibility but is limited to laboratory scale and also has high material wastage (>90%). CBD, on the other hand, has promise for large-scale demonstration but needs longer deposition time at relatively low temperatures (<10 °C) to obtain the desired thickness of the absorbers. Our group has previously demonstrated the fabrication of Sb<sub>2</sub>S<sub>3</sub> solar cells by the ultrasonic spray pyrolysis method, which offers large-area uniformity and is an industrially scalable technique with low capital.<sup>6</sup> Further, the Sb<sub>2</sub>S<sub>3</sub> solar cells are often fabricated in planar superstrate configuration wherein TiO<sub>2</sub> is the most commonly used electron transport layer (ETL) deposited on a transparent conducting oxide followed by the Sb<sub>2</sub>S<sub>3</sub> absorber, hole transport material (HTM), and finally, the back contact, often Au. HTMs are the vital component of planar or mesoscopic Sb<sub>2</sub>S<sub>3</sub> solar cells that drive the transport of photogenerated holes to the back contact and reduce recombination losses.<sup>2</sup> In general, conventional HTMs like poly(3-hexylthiophene) (P3HT),<sup>2,16</sup> 2,2',7,7'-tetrakis[N,N-di(4-methoxyphenyl)amino]-9,9'-spirobifluorene (Spiro-OMe-

TAD),<sup>17,18</sup> poly{4,4-dialkyl-4H-cyclopenta[2,1-b;3,4-b']-dithiophene-2,6-diyl-alt-2,1,3-benzothiadiazole-4,7-diyl} (PCPDTBT),<sup>19,20</sup> etc. are the most commonly employed in the fabrication of Sb<sub>2</sub>S<sub>3</sub> solar cells. The use of these different HTMs in Sb<sub>2</sub>S<sub>3</sub> solar cells where the Sb<sub>2</sub>S<sub>3</sub> absorbers are prepared by different techniques and device architectures are summarized in Table 1 alongside the power conversion efficiencies achieved. It may be noted that only organic HTMs and planar configuration devices are considered for summary.

It may be noted that except for V1236, an economic and transparent hole conductor previously reported by our group,<sup>33</sup> other studies have majorly used conventional P3HT and Spiro-OMeTAD. These hole conductors are very expensive mainly due to their complex, expensive, and time-consuming synthesis processes<sup>34</sup> and are also moisture sensitive, and thereby could be significant barriers to the potential upscale for commercial applications. Further, tailoring HTMs with suitable thickness is also important to obtain high-efficiency solar cells but may hinder the overall transparency of the solar cell stack, an important parameter in semitransparent solar cells. For instance, the commonly employed P3HT exhibits parasitic absorption in the visible spectral region, which induces a loss in the total transmittance of the solar cell.<sup>2,33</sup> In addition, P3HT also requires additional post-coating activation at temperatures around 170 °C either in a vacuum or inert atmosphere.<sup>35</sup> Therefore, it becomes imperative to explore low-cost novel HTMs, which could be easily synthesized using available commercial starting materials while possessing suitable properties like good thermal stability, desired solubility, and hole mobility.

In view of the above, the study herein proposes to fabricate Sb<sub>2</sub>S<sub>3</sub> solar cells by a scalable and industrially benign ultrasonic

spray pyrolysis (USP) method by employing novel, low-cost, and transparent hole conductors from fluorene-based molecules with terminated thiophene units. The 4,4'-dimethoxydiphenylamine-substituted fluorene fragment is used due to its wider application in the organic HTMs, in particular, Spiro-OMeTAD, while thiophene units are added mimicking P3HT HTM. The new materials follow simple synthesis processes with high yields thereby having considerably lower costs than conventional HTMs.  $\text{Sb}_2\text{S}_3$  solar cells with new HTMs are fabricated in the standard superstrate configuration wherein ETL and absorber are deposited by USP while HTMs are spin coated followed by the thermal evaporation of Au. Comprehensive characterization of solar cells through different techniques clearly demonstrates that the cells with new HTMs yield similar or better PCEs compared to the conventional P3HT-based devices and have exhibited enhanced average visible transmittance in the 400–800 nm range. Further, the band energetics show that the new HTMs possess favorable band alignment with the  $\text{Sb}_2\text{S}_3$  absorber thereby validating their efficacy toward semitransparent solar cells.

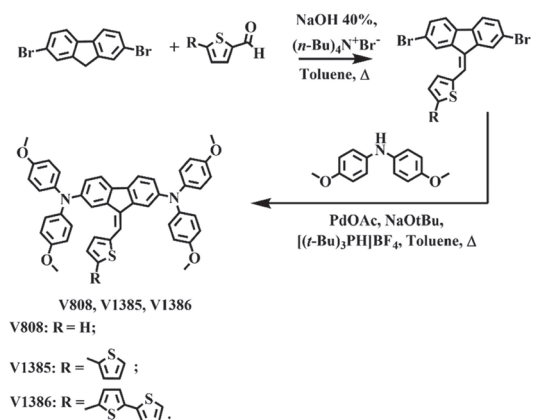
## 2. EXPERIMENTAL SECTION

**2.1. Materials.** The following materials were used: FTO substrate ( $7 \Omega \text{ sq}^{-1}$ ), titanium(IV) tetraisopropoxide (TTIP)—99 wt % (Acros Organics), acetylacetone—99 wt % (Acros Organics), ethanol—96.6 vol % (Estonian Spirit), methanol—99.9 vol % (Sigma-Aldrich), antimony trichloride—99.99 wt % (Sigma-Aldrich), thiourea—99 wt % (Sigma-Aldrich), chlorobenzene—99.5 vol % (Sigma-Aldrich), poly(3-hexyl-thiophene-2,5-diyl) (P3HT)—100 kDa, >90% regioregular (Sigma-Aldrich), and materials related to HTM synthesis as mentioned in the S1. The materials were used as received.

**2.2. Solar Cell Fabrication.** Antimony sulfide ( $\text{Sb}_2\text{S}_3$ ) solar cells were fabricated in superstrate configuration (glass/FTO/ $\text{TiO}_2$ / $\text{TiO}_2$ / $\text{Sb}_2\text{S}_3$ /HTM/Au). The fabrication process started with thorough cleaning of the glass/FTO substrate with DI water, acetone, and IPA in an ultrasonic bath for 10 min each followed by boiling the substrates in DI water and purging with  $\text{N}_2$  gas. The  $\text{TiO}_2$  electron transport layer (ETL) and  $\text{Sb}_2\text{S}_3$  absorbers were deposited by an indigenously made ultrasonic spray deposition system.  $\text{TiO}_2$  was sprayed from a solution mixture of 0.2 M TTIP with 0.2 M acetylacetone in ethanol by using a spray rate of  $\approx 2.5 \text{ mL/min}$  for 30 min on a hot plate maintained at around  $340^\circ\text{C}$ . The sprayed  $\text{TiO}_2$  samples were then annealed at  $450^\circ\text{C}$  for 30 min in air.  $\text{Sb}_2\text{S}_3$  thin films were spray-deposited from a solution mixture of 60 mM  $\text{SbCl}_3$  and 180 mM thiourea in methanol. The films were deposited at a spray rate of 2 mL/min while maintaining a substrate temperature of  $\approx 200^\circ\text{C}$ . The as-deposited  $\text{Sb}_2\text{S}_3$  films were annealed at around  $250\text{--}260^\circ\text{C}$  for 5 min under nitrogen. The hole transport materials (HTM) explored in this study are the fluorene-based molecules with linked thiophene units  $\text{N}^2, \text{N}^2, \text{N}^7, \text{N}^7$ -tetrakis(4-methoxyphenyl)-9-(thiophen-2-ylmethylene)-9H-fluorene-2,7-diamine (V808), 9-([2,2':5',2'-terthiophen]-5-ylmethylene)- $\text{N}^2, \text{N}^2, \text{N}^7, \text{N}^7$ -tetrakis(4-methoxyphenyl)-9H-fluorene-2,7-diamine (V1385), and 9-([2,2'-bithiophen]-5-ylmethylene)- $\text{N}^2, \text{N}^2, \text{N}^7, \text{N}^7$ -tetrakis(4-methoxyphenyl)-9H-fluorene-2,7-diamine (V1386). The detailed synthesis procedure of V808, V1385, and V1386 is described in Section S1 while the synthesis process is presented in Scheme 1. The HTM layers were spin coated on glass/FTO/ $\text{TiO}_2$ / $\text{Sb}_2\text{S}_3$  samples followed by the thermal evaporation of Au contacts. The active area of solar cells was  $7.06 \text{ mm}^2$ .

**2.3. Characterization.** The crystal structure and phase constitution of the as-deposited and annealed  $\text{Sb}_2\text{S}_3$  thin films were examined using a Rigaku Ultima IV X-ray diffractometer with a  $\text{Cu K}\alpha$  source ( $\lambda = 1.5406 \text{ \AA}$ ). In addition, micro-Raman spectroscopy was further used to ascertain the crystalline purity while also detecting the possible presence of the minute antimony oxide phase and micro-Raman spectra were recorded at room temperature using a Horiba Labram HR 800 in backscattering mode with a He Ne laser of 532

## Scheme 1. Synthetic Route to the Novel Hole Transporting Materials V808, V1385, and V1386



nm. A Zeiss HR FESEM was used to analyze the cross-sectional morphologies of the layers. The optical absorption and transmittance measurements were made using a Jasco V-670 ultraviolet–visible spectrophotometer (UV–VIS) in the range of 300–1000 nm. For the band diagram construction, photoelectron emission spectroscopy (PES) and photoconductivity methods were used. For these methods, the measurement system consisted of an ENERGETIQ Laser-Driven Light Source (LDLS EQ-99) as a light source, a Spectral Products DK240 1/4m monochromator, and a Keithley 617 electrometer. The measurements were performed in vacuum at a pressure of  $\sim 10^{-5}$  mbar. Both methods are described in detail in S2. The hole transport materials were characterized comprehensively using thermogravimetric analysis (TGA), differential scanning calorimetric (DSC) analysis, and absorption spectroscopy. The work function of Au contacts was measured using a Kelvin probe. The current–voltage ( $I$ – $V$ ) characteristics of the fabricated solar cells were measured using Wavelabs LS-2 LED solar simulator with an AM1.5G ( $100 \text{ mW cm}^{-2}$ ) light source. A Newport 69911 system with a 300 W Xenon lamp was used to measure the external quantum efficiency (EQE) of the fabricated solar cells.

## 3. RESULTS AND DISCUSSION

The fluorene-based thiophene-linked hole transport materials (HTMs) are explored in this study for the fabrication of  $\text{Sb}_2\text{S}_3$  solar cells. The design of these p-type photoconductors has been inspired by recently published findings that thiophene can coordinate with Sb atoms in  $\text{Sb}_2(\text{S}, \text{Se})_3$  leading to the improvement of the interfacial properties between  $\text{Sb}_2(\text{S}, \text{Se})_3$  and HTM.<sup>36,37</sup> This interaction provides desirable channels for carrier transport, which significantly enhances the open circuit voltage and fill factor. In a single thiophene unit-linked molecule (V808), 4,4-dimethoxydiphenylamine chromophores are symmetrically connected on both sides of the fluorene core, which was easily modified chemically by the thiophene end-group. V808 is synthesized through a simple two-step process (Scheme 1) devoid of expensive/complex materials/steps with considerably good yields thereby resulting in low synthesis costs. On a similar note, to further investigate the possibility of better interaction, the molecules are synthesized by adding 2 and 3 thiophene units to the fluorene core, which are thus named V1385 and V1386, respectively. The detailed synthesis procedure of V808, V1385, and V1386 is described in Section S1 and the cost estimation is given in Tables S1–S3, respectively. It may be observed that the synthesis cost of a

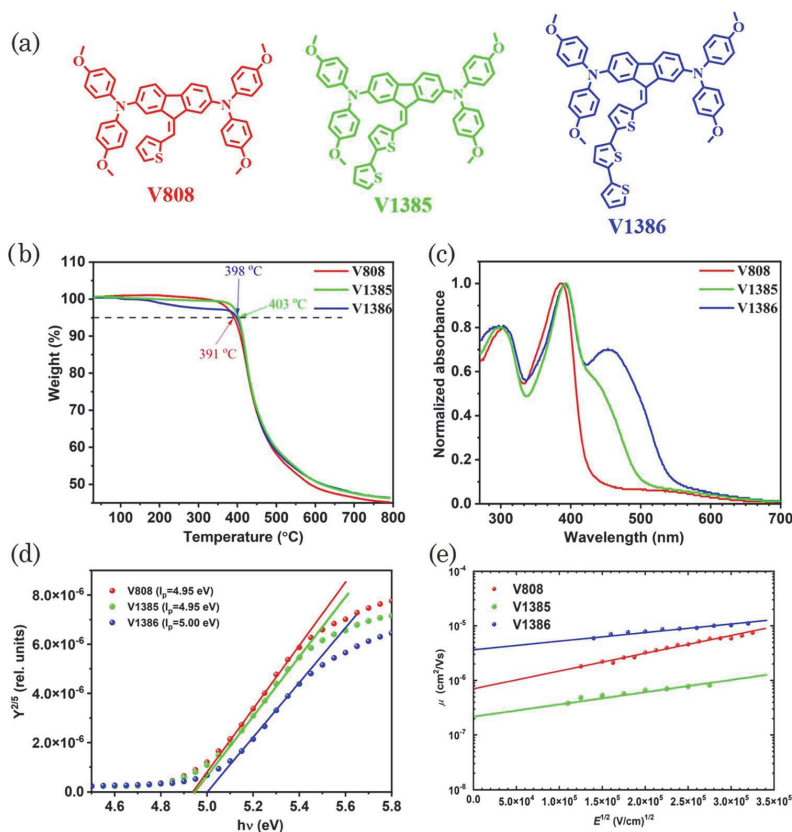


**Figure 1.** (a) Chemical structures of new fluorene-based hole transport materials with terminating thiophene units (V808, V1385, and V1386), (b) thermogravimetric analysis (TGA) data, (c) normalized absorbance spectra of the HTMs deposited on glass, (d) photoemission spectra in air for determining the ionization potential, and (e) electric field dependencies of the hole mobility of V808, V1385, and V1386.

single thiophene linking molecule (V808) is  $\approx 13$  € per gram while those of the ones with 2 and 3 thiophene units are 32 and 177 € per gram, respectively, indicating the increase in cost is majorly owing to the increased price of the starting thiophenecarbaldehyde. However, the cost of single and double thiophene unit-linked molecules (V808 and V1385) is considerably cheaper in comparison to the conventional hole conductors like P3HT and Spiro-OMeTAD. Irrespective of the cost, all three materials are comprehensively characterized and are explored as HTMs in  $\text{Sb}_2\text{S}_3$  solar cells. The typical chemical structures of V808, V1385, and V1386 with 1, 2, and 3 linked thiophene units, respectively, are shown in Figure 1a. Figure 1b shows the thermogravimetric analysis (TGA) curves of V808, V1385, and V1386, and as the plots reveal all three materials start to decompose at temperatures  $>390$  °C, which is far above the temperature for conventional device operation. The differential scanning calorimetric (DSC) curves of new HTMs are shown in Figure S1. All compounds have shown  $T_g$  slightly less than 100 °C (92, 97, and 99 °C for V808, V1385, and V1386, respectively). Comparison of  $T_g$  of new materials reveals that an increase in thiophene fragments in the molecule leads to slightly increased  $T_g$ , and could be attributed to the increased molecular weight. In addition, it is important to note that the melting process is observed just for V808, while other

new synthesized compounds (V1385 and V1386) have shown no endothermic peaks, indicating that they have only an amorphous state, which is an advantage for the formation of homogenous films as it eliminates the possibility of crystallization of films during preparation/operation of devices. The normalized absorbance spectra of the films, deposited on glass, are shown in Figure 1c. As can be seen, the spectra of new compounds display intensive  $\pi-\pi^*$  absorption bands at 270–430 nm, which might be attributed to the 4,4'-dimethoxydiphenylamine-substituted fluorene fragment. In addition, with the increase in the number of thiophene units, the ( $\pi-\pi^*$ ) transition associated with this conjugated part exhibits a strong bathochromic shift. For compound V1386, this results in a band with the absorption maximum at 453 nm, for V1385 it appears as a shoulder to the main peak, while for V808 it overlaps with the main peak. The normalized absorbance spectra of new HTMs are also compared with the conventional P3HT as presented in Figure S2, which shows that P3HT absorbs significantly in the 400–650 nm region while the new HTMs possess much less absorption in the same region thereby demonstrating better visible light transparency.

The solid-state ionization potential ( $I_p$ ) of HTMs is determined using photoelectron emission spectroscopy

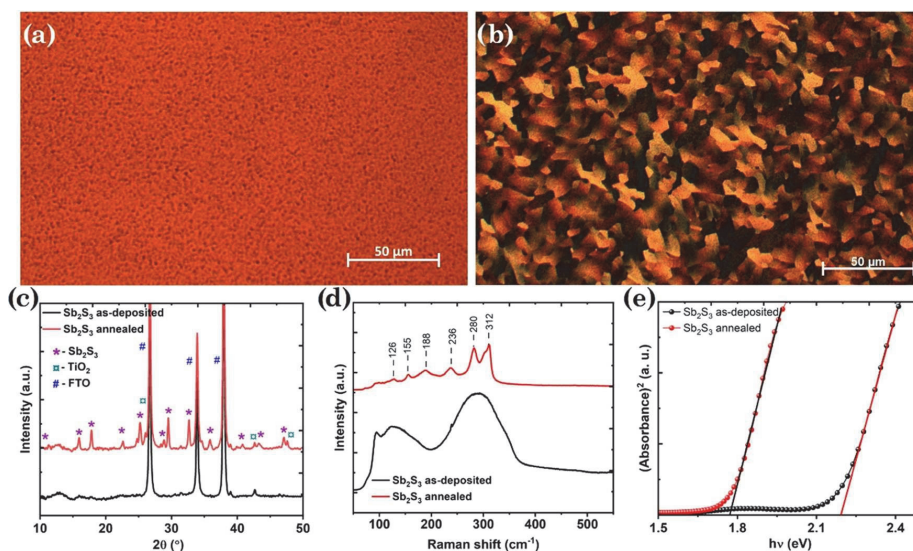


**Figure 2.** Morphological, structural, and optical characteristics of  $\text{Sb}_2\text{S}_3$  thin films deposited by ultrasonic spray pyrolysis: Optical microscopy images of (a) as-deposited and (b) annealed  $\text{Sb}_2\text{S}_3$ , (c) XRD patterns, (d) Raman spectra, and (e) (absorbance)<sup>2</sup> vs  $h\nu$  plots of as-deposited and annealed  $\text{Sb}_2\text{S}_3$ .

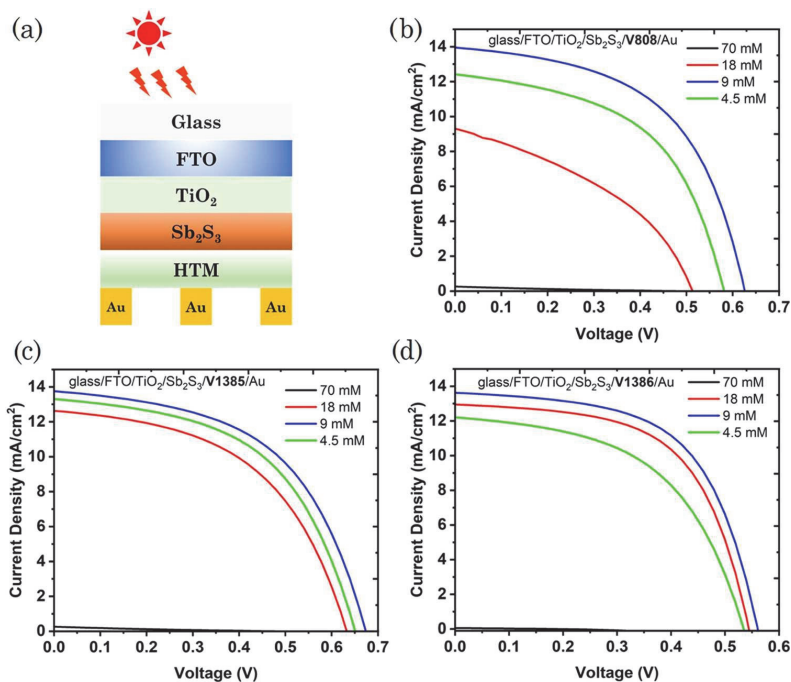


**Figure 3.** (a) Schematic illustration of device configuration (glass/FTO/TiO<sub>2</sub>/Sb<sub>2</sub>S<sub>3</sub>/HTM/Au) of  $\text{Sb}_2\text{S}_3$  solar cells (Note: Not to scale),  $J$ - $V$  characteristics of solar cells with (b) V808, (c) V1385, and (d) V1386 as HTMs with the variation in precursor concentrations from 4.5 to 70 mM in each case.

(PES) of the thin films (Figure 1d), which clearly reveals that the  $I_p$  levels of V808, V1385, and V1386 are determined to be  $-4.95$  eV,  $-4.95$ , and  $-5.00$  eV, respectively. Almost similar  $I_p$

values can be explained by the unfavorable arrangement of thiophene fragments. As can be seen from absorbance spectra, the increase of the conjugated system is very slight with the

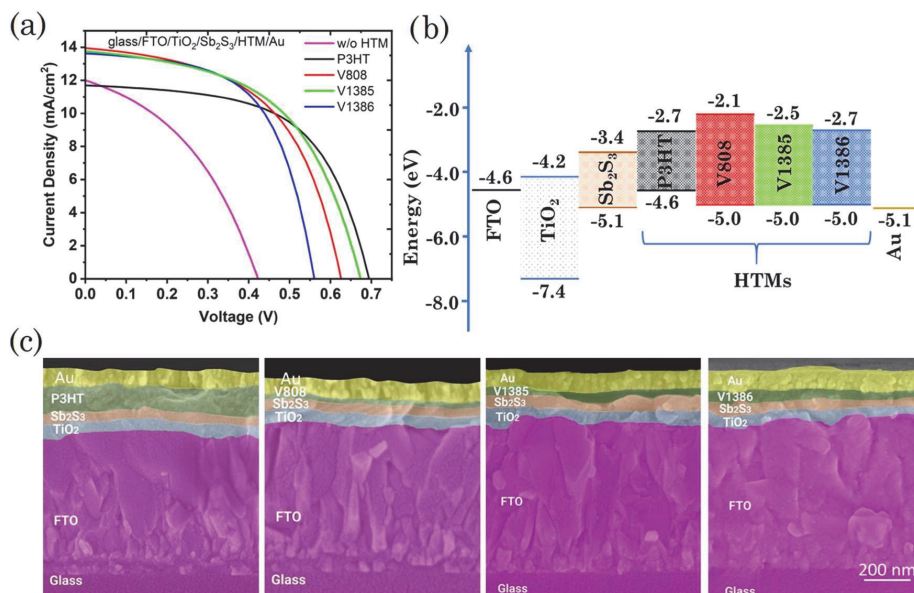


**Figure 4.** (a)  $J$ - $V$  characteristics of champion cells, (b) band energy diagram and (c) cross-sectional images of  $\text{Sb}_2\text{S}_3$  solar cells with P3HT, V808, V1385, and V1386 as HTMs, respectively.

increasing number of thiophene moieties in the molecule, therefore the highest occupied molecular orbital (HOMO) levels can be very similar. Further, hole drift-mobility of HTMs is estimated using the time of flight (ToF) method with Ekspla PL kHz ps tunable laser as a light source and a Tektronix MDO3024 oscilloscope for signal registration. As shown in Figure 1e, the inferred zero-field hole mobilities are  $7.07 \times 10^{-7}$ ,  $2.15 \times 10^{-7}$ , and  $3.68 \times 10^{-6}$  cm<sup>2</sup>/(V·s), for V808, V1385, and V1386, respectively.

$\text{Sb}_2\text{S}_3$  thin films are deposited by the USP process on glass/FTO/ $\text{TiO}_2$  samples. Optical microscopic images are recorded to ascertain the conformal coverage of  $\text{Sb}_2\text{S}_3$  films on  $\text{TiO}_2$  as shown in Figure 2a and as the image, which is recorded for a considerably larger area, unveils that the films are conformally covered devoid of any pin holes or crystallization during the deposition. The crystallization of  $\text{Sb}_2\text{S}_3$  thin films during deposition in the USP process is a commonly observed feature, which is a detrimental process that reduces the quality of films for solar cell applications as this crystallization during deposition is an uncontrollable process and the resulting crystallinity is not the desired form too, which is absent in the present study. Further, the as-deposited films are characterized by XRD and Raman as shown in Figure 2c,d. The XRD pattern shows the sharp peaks pertaining to FTO and  $\text{TiO}_2$  layers while the Raman spectra reveal broad characteristic peaks of  $\text{Sb}_2\text{S}_3$ , confirming that the as-deposited films are amorphous in nature. Upon annealing under a nitrogen atmosphere at 250 °C, the  $\text{Sb}_2\text{S}_3$  films exhibit crystallinity. Optical microscopy images of annealed  $\text{Sb}_2\text{S}_3$  films show a large grain structure as shown in Figure 2b without any voids or pin holes. The XRD patterns of annealed  $\text{Sb}_2\text{S}_3$  show several sharp peaks in addition to the existing FTO and  $\text{TiO}_2$  peaks, which correspond to the orthorhombic stibnite  $\text{Sb}_2\text{S}_3$  phase (ICDD PDF 01-075-4013). On a similar note, the Raman spectra of annealed  $\text{Sb}_2\text{S}_3$  show sharp peaks characteristic of  $\text{Sb}_2\text{S}_3$ ,

thereby corroborating the XRD analysis and confirming the formation of the crystalline stibnite  $\text{Sb}_2\text{S}_3$  phase. Further, the band gap of  $\text{Sb}_2\text{S}_3$  absorbers is inferred from (absorbance)<sup>2</sup> vs  $h\nu$  plots as shown in Figure 2e. The band gap of amorphous  $\text{Sb}_2\text{S}_3$  is determined to be around 2.2 eV while that of crystallized one is 1.7 eV, which agree well with the values reported previously.<sup>33</sup> Therefore, it may be inferred that the crystalline  $\text{Sb}_2\text{S}_3$  absorbers with the desired band gap are successfully fabricated by the area-scalable USP process followed by annealing.

In the next step, the  $\text{Sb}_2\text{S}_3$  solar cells are fabricated in the planar configuration, as shown in Figure 3a, using conventional P3HT and new V808, V1385, and V1386 as HTMs, which are spin coated onto glass/FTO/ $\text{TiO}_2$ / $\text{Sb}_2\text{S}_3$  samples and Au is thermally evaporated. While the concentration of P3HT has been previously optimized for the best efficient  $\text{Sb}_2\text{S}_3$  solar cells,<sup>33</sup> the new HTMs require a similar process. Therefore, prior to comparison with P3HT-based solar cells, the concentration of the precursors in spin coating has been optimized for new HTMs. Figure 3b–d shows the current density–voltage ( $J$ - $V$ ) characteristics of solar cells with concentration variation in each case for V808, V1385, and V1386, respectively. The variation in the associated device parameters with concentration is shown in Figure S3. For an initial concentration of 70 mM V808, the solar cells exhibit very low PCEs, essentially due to the negligible photocurrent. The concentration of V808 is therefore diluted considerably in steps of ca. 4× resulting in 18, 9, and 4.5 mM. As shown in the  $J$ - $V$  curves in Figure 3b, the efficiencies of solar cells for V808 concentrations of 70, 18, 9, and 4.5 mM are 0.1, 2.0, 4.7, and 3.8%, respectively. The device parameters,  $V_{\text{OC}}$ ,  $J_{\text{SC}}$ , and FF have followed an identical trend that the respective values are maximum for 9 mM V808 and are lower on either side (see Figure S3a,b). To identify the plausible reasons, the series resistance ( $R_s$ ) of the devices is determined from the  $J$ - $V$  data

that a very large  $R_s$  ( $>200 \Omega\text{-cm}^2$ ) is observed for the 70 mM **V808** device, which decreased significantly with a decrease in the concentration resulting in considerable improvement in  $J_{SC}$ . The large  $R_s$  may be attributed to the larger thickness of **V808** arising from the large concentration. It may therefore be concluded that 9 mM **V808** is considered optimal resulting in the highest PCE among all. On a similar note, the power conversion efficiencies of the solar cells with 70, 18, 9, and 4.5 mM concentrations of **V1385** are obtained to be 0.2, 4.0, 4.9, and 4.5%, respectively. For the case of **V1386**, the obtained efficiencies are 0.15, 4.1, 4.5, and 3.4% for concentrations of 70, 18, 9, and 4.5 mM. The variation trends in the associated device parameters are also similar as shown in Figure S3c–f. It may therefore be inferred that the 9 mM concentration in each case has resulted in the best device efficiencies of 4.7, 4.9, and 4.5% for solar cells with **V808**, **V1385**, and **V1386** as HTMs, respectively.

While the new molecules **V808**, **V1385**, and **V1386** have demonstrated reasonable efficiencies, it is important to compare them with existing conventional proven HTMs. Therefore, to further validate the efficacy of new molecules as the HTM layer in  $\text{Sb}_2\text{S}_3$  solar cells, they are compared with conventional P3HT-based devices. The  $J$ – $V$  characteristics of champion  $\text{Sb}_2\text{S}_3$  solar cells with P3HT, **V808**, **V1385**, and **V1386** are shown in Figure 4a. In addition, to understand the need for an HTM in devices, solar cells fabricated without the HTM layer are also shown. The device parameters are listed in Table 2. The solar cells without HTM have exhibited a PCE of

**Table 2.** Device Parameters of Champion  $\text{Sb}_2\text{S}_3$  Solar Cells with P3HT, **V808**, **V1385**, and **V1386** HTMs

HTM	$V_{OC}$ (V)	$J_{SC}$ (mA/cm <sup>2</sup> )	FF	PCE (%)	$R_s$ ( $\Omega\text{-cm}^2$ )	$R_{SH}$ ( $\Omega\text{-cm}^2$ )
no HTM	0.43	12.0	0.41	2.12	1.33	167
P3HT	0.69	11.7	0.58	4.68	2.1	1190
<b>V808</b>	0.63	13.9	0.54	4.73	1.01	586
<b>V1385</b>	0.68	13.7	0.53	4.94	2.3	569
<b>V1386</b>	0.56	13.6	0.59	4.50	0.89	844

2.12% with a reasonably low  $V_{OC}$  of 0.43 V, a  $J_{SC}$  of 12.0 mA/cm<sup>2</sup>, and an FF of 0.41. Such characteristics are often classically observed for bare  $\text{Sb}_2\text{S}_3$ -based solar cells devoid of HTM. The band energy positions of different device layers explored in the present study are determined using photoelectron emission spectroscopy and the band energy diagram is presented in Figure 4b. The  $\text{Sb}_2\text{S}_3$  absorber possesses the valence (VBE) and conduction band edges (CBE) at  $-5.1$  and  $-3.4$  eV, respectively, and with Au and  $\text{TiO}_2$  on either side of the absorber in solar cells without HTM, the transport of photogenerated electrons and holes is reasonably smooth owing to the favorable band edge positions. However, with Au being the back contact there is no barrier for electrons from the conduction band of  $\text{Sb}_2\text{S}_3$  at the  $\text{Sb}_2\text{S}_3$ -Au interface thereby leading to recombination often resulting in low  $V_{OC}$  and FF. The devices also exhibit a very low shunt resistance ( $R_{SH}$ ) of  $\approx 167 \Omega\text{-cm}^2$ . On the other hand, the solar cells with conventional P3HT have demonstrated a PCE of 4.68% with a  $V_{OC}$  of 0.69 V, a  $J_{SC}$  of 11.7 mA/cm<sup>2</sup>, and an FF of 0.58. It can be observed that the device parameters are considerably increased, particularly the  $V_{OC}$  and FF. The presence of an HTM contributes in various ways to enhance the conversion efficiency of solar cells as they improve band energetics of the

device for improved transport of photogenerated carriers while reducing recombination losses as they block the electrons by passivating the interface across  $\text{Sb}_2\text{S}_3$ -HTM. As seen from Figure 4b, P3HT possesses the VBE and CBE at  $-4.6$  and  $-2.7$  eV, respectively, that its presence could provide a barrier at the  $\text{Sb}_2\text{S}_3$ -HTM interface for the electrons to travel back and therefore, reduce the recombination losses. The devices have shown a significantly enhanced  $R_{SH} \approx 1.2 \text{ k}\Omega\text{-cm}^2$ , an almost 7-fold increment compared to the bare cells. It may also be observed that the series resistance ( $R_s$ ) of the P3HT-based devices has slightly increased compared to the bare cells and could be due to the additional P3HT layer, which is a reasonably resistive material. However, due to the enhanced charge transport and reduced recombination losses owing to the favorable band alignment, the  $V_{OC}$  is significantly increased and  $J_{SC}$  has not changed hugely despite the higher  $R_s$ .

The solar cells with new HTMs have demonstrated efficiencies of 4.73, 4.94, and 4.50% for **V808**, **V1385**, and **V1386**, respectively. Primarily, it is important to note that the new HTMs have exhibited efficiencies either on par or slightly higher than the conventional P3HT, which clearly demonstrates their validation. Another major observation from Figure 4a and Table 2 is that the solar cells with **V808**, **V1385**, and **V1386** have yielded considerably higher  $J_{SC}$ , almost close to 14 mA/cm<sup>2</sup> over the P3HT devices (11.7 mA/cm<sup>2</sup>). However, the  $V_{OC}$  values of the devices with new HTMs are relatively lower than that of P3HT devices. As can be seen, the  $V_{OC}$  of solar cells with **V808**, **V1385**, and **V1386** are 0.63, 0.68, and 0.56, respectively, while the  $V_{OC}$  of P3HT-based solar cells is 0.69 V. The band edge positions of new HTMs are compared with P3HT alongside other device layers as shown in Figure 4b and it can be observed that all the new HTMs possess the same VBE at  $-5.0$  eV while that of P3HT is  $-4.6$  eV. For the transport of photogenerated holes, the VBE of P3HT is in a favorable position with respect to the  $\text{Sb}_2\text{S}_3$  absorber compared to the new HTMs, however, with the back contact (Au) energy level being  $-5.1$  eV, the relatively smoother transport of holes is feasible in solar cells with new HTMs compared to P3HT. In addition, the CBE positions of new HTMs are  $-2.1$ ,  $-2.5$ , and  $-2.7$  eV for **V808**, **V1385**, and **V1386**, respectively, compared to P3HT ( $-2.7$  eV). As may be observed, the interface barrier at the  $\text{Sb}_2\text{S}_3$ -HTM interface is larger for new HTMs over P3HT, which is responsible for electron blocking at the interface and leads to reduced recombination losses. While the higher  $J_{SC}$  may be ascribed to the favorable band alignment of new HTMs, the lower  $V_{OC}$  values compared to P3HT are not as expected especially considering the larger band gap of new HTMs than P3HT. Particularly, considerably lower  $V_{OC}$  (0.56 V) in solar cells with **V1386** with a deficiency of almost 100 mV or more compared to other solar cells despite its reasonably higher mobility is still a question, although it may be speculated that this is owing to the increase in the number of thiophene units, the coverage might not be as uniform as compared to other layers leading to agglomerated conducting paths that may act as trap centers for photogenerated carriers. On that note, the wettability of new HTMs alongside P3HT in their precursor form is explored on the  $\text{Sb}_2\text{S}_3$  surface. It is observed that all the HTMs including P3HT have shown excellent wettability with close to  $0^\circ$  contact angle for new HTMs and  $2^\circ$  for P3HT. The visual appearance of the samples upon dropping the precursor droplet onto  $\text{Sb}_2\text{S}_3$  indicates that the P3HT drop remains as it is while the new HTM precursor drop spreads quickly in no time, which shows the relatively

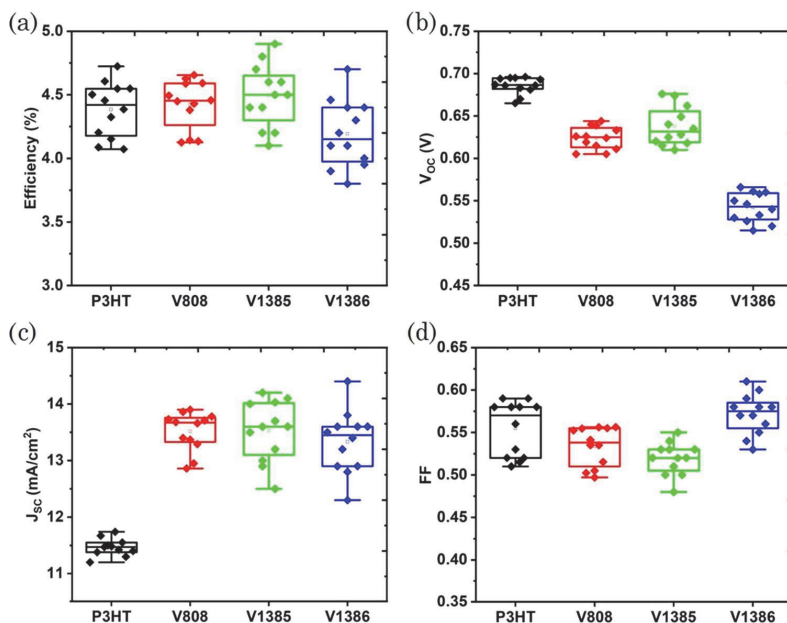


**Figure 5.** Reproducibility box plots of Sb<sub>2</sub>S<sub>3</sub> solar cells with P3HT, V808, V1385, and V1386 as HTMs: (a) Efficiency, (b)  $V_{OC}$ , (c)  $J_{SC}$ , and (d) fill factor (FF).

better wettability of new HTMs on the Sb<sub>2</sub>S<sub>3</sub> surface. Therefore, despite possessing better interaction capability and favorable band edge positions, the solar cells with new HTMs have either marginally achieved similar  $V_{OC}$  as that of the conventional P3HT or have yielded lower values. In addition, it is known that mobility plays a crucial role in the performance of solar cells, but in this study, other factors that influence the PV parameters might be dominant. One of the important PV parameters is  $V_{OC}$  and its variation is generally ascribed to the energy levels, however, as they are quite similar, the other main aspect could be the interfacial recombination at Sb<sub>2</sub>S<sub>3</sub>-HTM. Now, there might be two sources of recombination—one is direct contact between the electrode and absorber layer (microshunts), due to the thinner films (which could explain lower  $V_{OC}$  than P3HT), second—the quality of the interface between the absorber and HTM. Thiophenes, in principle, are introduced for the better interface, for e.g., surface passivation, however, then one would expect the best performance for V1386. So, a further inspection of the Sb<sub>2</sub>S<sub>3</sub>-HTM interface through advanced characterization techniques like deep-level transient spectroscopy may be needed to understand the role of interfacial defects on the performance of solar cells, and can be explored in future studies.

The cross-sectional images of solar cells with P3HT and new HTMs are shown in Figure 4c. While TiO<sub>2</sub> and Sb<sub>2</sub>S<sub>3</sub> have an almost similar thickness in each case, P3HT is reasonably thicker ( $\approx 100$  nm) compared to the new HTMs ( $\approx 25$ – $30$  nm). It may be noted that each individual HTM herein is optimized by its precursor concentration in spin coating to obtain the best efficient solar cells. Apparently, a thick P3HT is needed in order to get an efficiency of  $\approx 4.7\%$  whereas a considerably thinner layer of each of the new HTMs is sufficient to obtain similar or slightly higher efficiencies (4.5–

4.9%). This proves the fact that the new HTMs, particularly V808 and V1385, are not only considerably cheaper but also the required materials consumption is significantly lower, which warrants the plausible fabrication of Sb<sub>2</sub>S<sub>3</sub> solar cells with efficiencies close to 5% at a much cheaper cost. In addition, for the reproducibility of devices, the statistical box plots of efficiency, and the associated device parameters are shown in Figure 5. As Figure 5a unveils, the efficiency spread is almost identical in each case with P3HT and new HTMs. Further, the average efficiencies are also in a similar range in each of the optimized cases, except for the case of V1386, which shows a slightly lower efficiency owing to the low  $V_{OC}$ . Similarly, the trend in  $V_{OC}$ ,  $J_{SC}$ , and FF is almost the same as that for the champion numbers with reasonably identical spreads. The  $V_{OC}$  in V1386-based solar cells is considerably lower while the  $J_{SC}$  in P3HT-solar cells is the lowest and the FFs range from 0.5 to 0.6 in all the cases. As the statistics indicate, the high reproducibility of the results is obtained in the present study.

The normalized external quantum efficiency (EQE) curves of solar cells with P3HT and new HTM layers are shown in Figure 6a. In addition, the integrated photocurrent density ( $J_{integrated}$ ) calculated using EQE spectra is also shown and it can be noted that almost identical  $J_{SC}$  values are obtained from EQE data to the values extracted from  $J$ - $V$  curves. A pertinent aspect to be noted is the dip in EQE for solar cells with P3HT in the range of 500–650 nm, which may be attributed to the parasitic absorption losses.<sup>2</sup> When an absorber is thinner or comparable to the thickness of HTM, the light that gets transmitted through the absorber gets reflected back from the back contact and often, the reflected light could be reabsorbed in the absorber to result in photogenerated carriers. However, if the HTM is sufficiently thick, then the reflected light gets

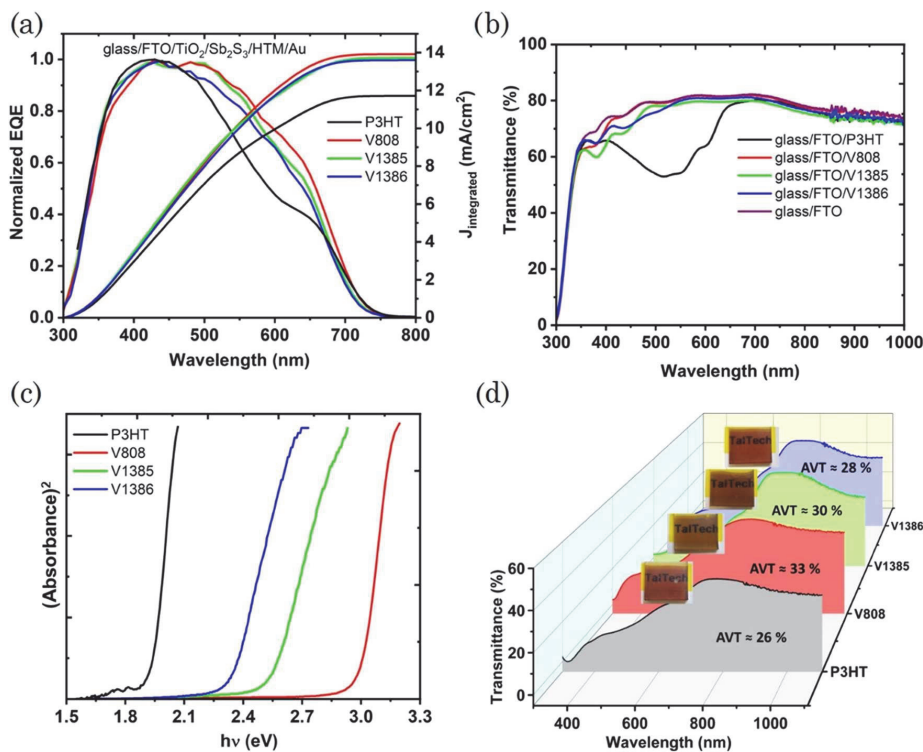


**Figure 6.** (a) Normalized external quantum efficiency (EQE) curves and the integrated  $J_{SC}$  of  $Sb_2S_3$  solar cells with P3HT, V808, V1385, and V1386 as HTMs, (b) transmittance curves of glass/FTO, glass/FTO/P3HT, glass/FTO/V808, glass/FTO/V1385 and glass/FTO/V1386, (c)  $(\text{Absorbance})^2$  vs  $h\nu$  plots of P3HT, V808, V1385, and V1386 for band gap determination, and (d) transmittance curves of the device stack with P3HT, V808, V1385, and V1386 as HTMs without Au (inset: Respective sample photographs captured with a background showing semi-transparency).

absorbed in the HTM layer leading to parasitic absorption. In this study, P3HT is considerably thick and thus exhibits parasitic absorption while the considerably thinner new HTMs (V808, V1385, and V1386) does not show any similar dip in EQE, which could further explain the enhanced  $J_{SC}$  values in the respective solar cells. Optical transmittance studies are performed for bare P3HT and new V808, V1385, and V1386 HTM layers on glass/FTO substrates, as shown in Figure 6b, where the absorption by P3HT is corroborated with EQE results as observed from the dip in transmittance in 400–650 nm region. Further, it may also be observed that the new HTMs exhibit considerable transparency similar to that of the glass/FTO substrate. The band gaps of P3HT, V808, V1385, and V1386 are inferred to be  $\approx 1.9$ , 2.9, 2.5, and 2.3 eV, respectively, from the plots shown in Figure 6c and the absorption coefficient-based Tauc's plots in Figure S4, which ascertains the fact that new HTMs are optically more transparent in the visible region compared to P3HT. Finally, the overall transparency of device stacks without top metal contact is analyzed (see Figure 6d) and the solar weighted average visible transmittance (AVT) (400–800 nm) of devices with P3HT, V808, V1385, and V1386 HTMs are determined to be  $\approx 26$ , 33, 30, and 28%, respectively. In the case of new HTMs, as the thiophene units increased the band gap decreased resulting in slightly reduced transparency as

witnessed from the overall device transmittance. The sample pictures of glass/FTO/ $TiO_2$ / $Sb_2S_3$ /HTM where HTM is P3HT, V808, V1385, and V1386 are shown with a background and it may be observed that all the samples exhibit decent transparency with visibility being the highest for V808. While all device stacks exhibit reasonably good AVT values as required for semitransparent applications, the devices with new HTMs exhibit enhanced transparency, which is due to their increased transmittance over P3HT. The cost-effective fluorene-based thiophene-terminated (V808, V1385, V1386) HTMs are successfully demonstrated in  $Sb_2S_3$  solar cells as potentially suitable candidates for semitransparent applications and efforts are underway to increase the PCE of solar cells and upscaling the devices.

#### 4. CONCLUSIONS

Novel cost-effective and transparent fluorene-based thiophene-terminated hole transport materials (V808, V1385, and V1386) are demonstrated, for the first time, in semitransparent  $Sb_2S_3$  solar cells exhibiting a power conversion efficiency of 4.5–4.9% and an average visible transmittance of 30–33% (without the metal) in the 400–800 nm range. Solar cells with the conventional P3HT as HTM have yielded 4.7% efficiency, however, they have exhibited lower transparency (26%) owing to parasitic absorption losses in P3HT. The band diagram of

solar cells with new HTMs and P3HT are compared, which unveils that new HTMs have exhibited favorable band offset validating them as effective HTMs for  $\text{Sb}_2\text{S}_3$  solar cells. The new HTMs with terminated thiophene units have demonstrated reasonably improved wettability over conventional P3HT that could provide better interaction channels for charge carrier transport thus leading to enhanced current density. However, a closer inspection of  $\text{Sb}_2\text{S}_3$ -HTM needs to be further explored to unravel the interfacial effects as the solar cells with new HTMs have exhibited reasonably lower  $V_{\text{OC}}$  values, particularly in the case of V808 and V1386.

## ■ ASSOCIATED CONTENT

### Supporting Information

The Supporting Information is available free of charge at <https://pubs.acs.org/doi/10.1021/acsaem.2c04097>.

Synthesis procedure, DSC,  $J$ - $V$  characteristics of solar cells, and absorption spectra related data of V808, V1385, and V1386 (PDF)

## ■ AUTHOR INFORMATION

### Corresponding Authors

**Sreekanth Mandati** – Department of Materials and Environmental Technology, Laboratory of Thin Film Chemical Technologies, Tallinn University of Technology, 19086 Tallinn, Estonia; [orcid.org/0000-0002-3317-271X](https://orcid.org/0000-0002-3317-271X); Email: [sreekanth.mandati@taltech.ee](mailto:sreekanth.mandati@taltech.ee)

**Iлона Oja Acik** – Department of Materials and Environmental Technology, Laboratory of Thin Film Chemical Technologies, Tallinn University of Technology, 19086 Tallinn, Estonia; Email: [ilona.oja@taltech.ee](mailto:ilona.oja@taltech.ee)

### Authors

**Nimish Juneja** – Department of Materials and Environmental Technology, Laboratory of Thin Film Chemical Technologies, Tallinn University of Technology, 19086 Tallinn, Estonia

**Atanas Katerski** – Department of Materials and Environmental Technology, Laboratory of Thin Film Chemical Technologies, Tallinn University of Technology, 19086 Tallinn, Estonia

**Aistė Jegorovė** – Department of Organic Chemistry, Kaunas University of Technology, Kaunas LT-50254, Lithuania

**Raitis Grzibovskis** – Institute of Solid State Physics, University of Latvia, Riga LV 1063, Latvia

**Aivars Vembris** – Institute of Solid State Physics, University of Latvia, Riga LV 1063, Latvia

**Tatjana Dedova** – Department of Materials and Environmental Technology, Laboratory of Thin Film Chemical Technologies, Tallinn University of Technology, 19086 Tallinn, Estonia

**Nicolae Spalatu** – Department of Materials and Environmental Technology, Laboratory of Thin Film Chemical Technologies, Tallinn University of Technology, 19086 Tallinn, Estonia; [orcid.org/0000-0003-0234-2170](https://orcid.org/0000-0003-0234-2170)

**Artiom Magomedov** – Department of Organic Chemistry, Kaunas University of Technology, Kaunas LT-50254, Lithuania; [orcid.org/0000-0003-3159-1870](https://orcid.org/0000-0003-3159-1870)

**Smagul Karazhanov** – Institute for Energy Technology (IFE), NO 2027 Kjeller, Norway

**Vytautas Getautis** – Department of Organic Chemistry, Kaunas University of Technology, Kaunas LT-50254, Lithuania; [orcid.org/0000-0001-7695-4677](https://orcid.org/0000-0001-7695-4677)

**Malle Krungs** – Department of Materials and Environmental Technology, Laboratory of Thin Film Chemical Technologies, Tallinn University of Technology, 19086 Tallinn, Estonia; [orcid.org/0000-0003-4658-4403](https://orcid.org/0000-0003-4658-4403)

Complete contact information is available at: <https://pubs.acs.org/doi/10.1021/acsaem.2c04097>

### Author Contributions

S.M. conceptualization, design of experiments, analysis of the results, and manuscript writing; N.J. experiments and contribution to manuscript writing; A.K. and T.D. support in experiments and data acquisition; N.S. and S.K. supported in analysis; A.J., A.M., and V.G. synthesized and characterized new HTMs; R.G. and A.V. performed ionization potential and hole mobility measurements; M.K. and I.O.A. provided support for analysis and finalizing the manuscript draft. All authors have given approval to the final version of the manuscript.

### Funding

EEA Grants—S-BMT-21-1(LT08-2-LMT-K-01-003). Estonian Research Council—PRG627 and PSG689. Archimedes Foundation—TK141 (TAR16016EK). European Union Horizon2020—952509 and 739508.

### Notes

The authors declare no competing financial interest.

## ■ ACKNOWLEDGMENTS

The “Development of Semitransparent Bifacial Thin-Film Solar Cells for Innovative Applications” benefits from a 999372 € grant from Iceland, Liechtenstein, and Norway through the EEA Grants. The aim of the project is to develop a new approach based on novel materials and structures and production technologies, which are the key to further increase the share and range of applications of PV in areas with sub-average sunlight, including Baltic and Nordic countries. Therefore, the development of resource saving, cost-effective, and efficient PV devices is a primary challenge of this project. Project contract with the Research Council of Lithuania (LMTLT) number is S-BMT-21-1(LT08-2-LMT-K-01-003). Department of Materials and Environmental Technology, Tallinn University of Technology has received funding from the Estonian Research Council projects PRG627 “Antimony chalcogenide thin films for next-generation semitransparent solar cells applicable in electricity producing windows” and PSG689 “Bismuth Chalcogenide Thin-Film Disruptive Green Solar Technology for Next-Generation Photovoltaics”, and the Estonian Centre of Excellence project TK141 (TAR16016EK) “Advanced materials and high-technology devices for energy recuperation systems”, the European Union’s Horizon2020 program under the ERA Chair project SGSOLAR grant agreement No 952509. Institute of Solid-State Physics, University of Latvia has received funding from the European Union’s Horizon2020 Framework Programme H2020-WIDE-SPREAD-01-2016-2017-TeamingPhase2 under grant agreement no. 739508, project CAMART<sup>2</sup>. The authors thank Dr. Tadas Malinauskas and Dr. Valdek Mikli for their support in the preparation and characterization of the samples.

## ■ ABBREVIATIONS

HTM, hole transport material

**V808**,  $N^2, N^2, N^7, N^7$ -tetrakis(4-methoxyphenyl)-9-(thiophen-2-ylmethylene)-9H-fluorene-2,7-diamine

**V1385**, 9-([2,2':5',2''-terthiophen]-5-ylmethylene)- $N^2, N^2, N^7, N^7$ -tetrakis(4-methoxyphenyl)-9H-fluorene-2,7-diamine

**V1386**, 9-([2,2'-bithiophen]-5-ylmethylene)- $N^2, N^2, N^7, N^7$ -tetrakis(4-methoxyphenyl)-9H-fluorene-2,7-diamine

P3HT, poly(3-hexylthiophene)

Spiro-OMeTAD, 2,2',7,7'-tetrakis[ $N,N$ -di(4-methoxyphenyl)amino]-9,9'-spirobifluorene

PCPDTBT, poly{4,4-dialkyl-4H-cyclopenta[2,1-*b*;3,4-*b'*]-dithiophene-2,6-diyl-*alt*-2,1,3-benzothiadiazole-4,7-diyl}

AVT, average visible transmittance

DSC, differential scanning calorimetry

TGA, thermal gravimetric analysis

EQE, external quantum efficiency

## ■ REFERENCES

- (1) Kondrotas, R.; Chen, C.; Tang, J. Sb2S3 Solar Cells. *Joule* **2018**, *2*, 857–878.
- (2) Zimmermann, E.; Pfadler, T.; Kalb, J.; Dorman, J. A.; Sommer, D.; Hahn, G.; Weickert, J.; Schmidt-Mende, L. Toward High-Efficiency Solution-Processed Planar Heterojunction Sb2S3 Solar Cells. *Adv. Sci.* **2015**, *2*, No. 1500059.
- (3) Castro, J. R.; Dale, P.; Mahon, M. F.; Molloy, K. C.; Peter, L. M. Deposition of Antimony Sulfide Thin Films from Single-Source Antimony Thiolate Precursors. *Chem. Mater.* **2007**, *19*, 3219–3226.
- (4) Büttner, P.; Scheler, F.; Döhler, D.; Barr, M. K. S.; Bosch, M.; Rey, M.; Yokosawa, T.; Hinz, S.; Maultzsch, J.; Spiecker, E.; Vogel, N.; Mínguez-Bacho, I.; Bachmann, J. Continuous, Crystalline Sb2S3 Ultrathin Light Absorber Coatings in Solar Cells Based on Photonic Concentric p-i-n Heterojunctions. *Nano Energy* **2022**, *103*, No. 107820.
- (5) Shah, U. A.; Chen, S.; Khalaf, G. M. G.; Jin, Z.; Song, H. Wide Bandgap Sb2S3 Solar Cells. *Adv. Funct. Mater.* **2021**, *31*, No. 2100265.
- (6) Eensalu, J. S.; Katerski, A.; Kärber, E.; Weinhardt, L.; Blum, M.; Heske, C.; Yang, W.; Acik, I. O.; Krunks, M. Semitransparent Sb2S3 Thin Film Solar Cells by Ultrasonic Spray Pyrolysis for Use in Solar Windows. *Beilstein J. Nanotechnol.* **2019**, *10*, 2396–2409.
- (7) Lee, S.-J.; Sung, S.-J.; Yang, K.-J.; Kang, J.-K.; Kim, J. Y.; Do, Y. S.; Kim, D.-H. Approach to Transparent Photovoltaics Based on Wide Band Gap Sb2S3 Absorber Layers and Optics-Based Device Optimization. *ACS Appl. Energy Mater.* **2020**, *3*, 12644–12651.
- (8) Wang, S.; Zhao, Y.; Che, B.; Li, C.; Chen, X.; Tang, R.; Gong, J.; Wang, X.; Chen, G.; Chen, T.; Li, J.; Xiao, X. A Novel Multi-Sulfur Source Collaborative Chemical Bath Deposition Technology Enables 8%-Efficiency Sb2S3 Planar Solar Cells. *Adv. Mater.* **2022**, *34*, No. 2206242.
- (9) Yang, Z.; Wang, X.; Chen, Y.; Zheng, Z.; Chen, Z.; Xu, W.; Liu, W.; Yang Michael, Y.; Zhao, J.; Chen, T.; Zhu, H. Ultrafast Self-Trapping of Photoexcited Carriers Sets the Upper Limit on Antimony Trisulfide Photovoltaic Devices. *Nat. Commun.* **2019**, *10*, No. 4540.
- (10) Dong, J.; Liu, Y.; Wang, Z.; Zhang, Y. Boosting VOC of Antimony Chalcogenide Solar Cells: A Review on Interfaces and Defects. *Nano Sel.* **2021**, *2*, 1818–1848.
- (11) Krautmann, R.; Spalatu, N.; Gunder, R.; Abou-Ras, D.; Unold, T.; Schorr, S.; Krunks, M.; Oja Acik, I. Analysis of Grain Orientation and Defects in Sb2Se3 Solar Cells Fabricated by Close-Spaced Sublimation. *Sol. Energy* **2021**, *225*, 494–500.
- (12) Vidal-Fuentes, P.; Placidi, M.; Sánchez, Y.; Becerril-Romero, I.; Andrade-Arvizu, J.; Jehl, Z.; Pérez-Rodríguez, A.; Izquierdo-Roca, V.; Saucedo, E. Efficient Se-Rich Sb2Se3/CdS Planar Heterojunction Solar Cells by Sequential Processing: Control and Influence of Se Content. *Sol. RRL* **2020**, *4*, No. 2000141.
- (13) Hobson, T. D. C.; Phillips, L. J.; Hutter, O. S.; Shiel, H.; Swallow, J. E. N.; Savory, C. N.; Nayak, P. K.; Mariotti, S.; Das, B.; Bowen, L.; Jones, L. A. H.; Featherstone, T. J.; Smiles, M. J.; Farnworth, M. A.; Zoppi, G.; Thakur, P. K.; Lee, T.-L.; Snaith, H. J.; Leighton, C.; Scanlon, D. O.; Dhanak, V. R.; Durose, K.; Veal, T. D.; Major, J. D. Isotype Heterojunction Solar Cells Using N-Type Sb2Se3 Thin Films. *Chem. Mater.* **2020**, *32*, 2621–2630.
- (14) Zhu, L.; Chen, J.; Liu, R.; Dong, C.; Yang, S.; Chen, T.; Chen, C.; Qiao, Q.; Wang, M. Solution-Processed Compact Sb2S3 Thin Films by a Facile One-Step Deposition Method for Efficient Solar Cells. *Sol. RRL* **2021**, *5*, No. 2100666.
- (15) Choi, Y. C.; Lee, D. U.; Noh, J. H.; Kim, E. K.; Seok, S. II. Highly Improved Sb2S3 Sensitized-Inorganic–Organic Heterojunction Solar Cells and Quantification of Traps by Deep-Level Transient Spectroscopy. *Adv. Funct. Mater.* **2014**, *24*, 3587–3592.
- (16) You, M. S.; Lim, C.-S.; Kwon, D. H.; Heo, J. H.; Im, S. H.; Chae, K. J. Oxide-Free Sb2S3 Sensitized Solar Cells Fabricated by Spin and Heat-Treatment of Sb(III)(Thioacetamide)2Cl3. *Org. Electron.* **2015**, *21*, 155–159.
- (17) Zhang, Y.; Li, S.; Tang, R.; Wang, X.; Chen, C.; Lian, W.; Zhu, C.; Chen, T. Phosphotungstic Acid Regulated Chemical Bath Deposition of Sb2S3 for High-Efficiency Planar Heterojunction Solar Cell. *Energy Technol.* **2018**, *6*, 2126–2131.
- (18) Chen, J.; Qi, J.; Liu, R.; Zhu, X.; Wan, Z.; Zhao, Q.; Tao, S.; Dong, C.; Ashebir, G. Y.; Chen, W.; Peng, R.; Zhang, F.; Yang, S.; Tian, X.; Wang, M. Preferentially Oriented Large Antimony Trisulfide Single-Crystalline Cuboids Grown on Polycrystalline Titania Film for Solar Cells. *Commun. Chem.* **2019**, *2*, No. 121.
- (19) Nie, R.; Seok, S. II. Efficient Antimony-Based Solar Cells by Enhanced Charge Transfer. *Small Methods* **2020**, *4*, No. 1900698.
- (20) Nie, R.; Yun, H.; Paik, M.-J.; Mehta, A.; Park, B.; Choi, Y. C.; Seok, S. II. Efficient Solar Cells Based on Light-Harvesting Antimony Sulfoiodide. *Adv. Energy Mater.* **2018**, *8*, No. 1701901.
- (21) Liu, C. P.; Wang, H. E.; Ng, T. W.; Chen, Z. H.; Zhang, W. F.; Yan, C.; Tang, Y. B.; Bello, I.; Martinu, L.; Zhang, W. J.; Jha, S. K. Hybrid Photovoltaic Cells Based on ZnO/Sb2S3/P3HT Heterojunctions. *Phys. Status Solidi B* **2012**, *249*, 627–633.
- (22) Reejajayan, B.; Manthiram, A. Effects of Bifunctional Metal Sulfide Interlayers on Photovoltaic Properties of Organic–Inorganic Hybrid Solar Cells. *RSC Adv.* **2013**, *3*, 5412–5421.
- (23) Kärber, E.; Katerski, A.; Acik, I. O.; Mere, A.; Mikli, V.; Krunks, M. Sb2S3 Grown by Ultrasonic Spray Pyrolysis and Its Application in a Hybrid Solar Cell. *Beilstein J. Nanotechnol.* **2016**, *7*, 1662–1673.
- (24) Wang, X.; Li, J.; Liu, W.; Yang, S.; Zhu, C.; Chen, T. A Fast Chemical Approach towards Sb2S3 Film with a Large Grain Size for High-Performance Planar Heterojunction Solar Cells. *Nanoscale* **2017**, *9*, 3386–3390.
- (25) Lan, C.; Liang, G.; Lan, H.; Peng, H.; Su, Z.; Zhang, D.; Sun, H.; Luo, J.; Fan, P. Microstructural and Optical Properties of Sb2S3 Film Thermally Evaporated from Antimony Pentasulfide and Efficient Planar Solar Cells. *Phys. Status Solidi RRL* **2018**, *12*, No. 1800025.
- (26) Han, J.; Pu, X.; Zhou, H.; Cao, Q.; Wang, S.; He, Z.; Gao, B.; Li, T.; Zhao, J.; Li, X. Synergistic Effect through the Introduction of Inorganic Zinc Halides at the Interface of TiO2 and Sb2S3 for High-Performance Sb2S3 Planar Thin-Film Solar Cells. *ACS Appl. Mater. Interfaces* **2020**, *12*, 44297–44306.
- (27) Han, J.; Wang, S.; Yang, J.; Guo, S.; Cao, Q.; Tang, H.; Pu, X.; Gao, B.; Li, X. Solution-Processed Sb2S3 Planar Thin Film Solar Cells with a Conversion Efficiency of 6.9% at an Open Circuit Voltage of 0.7 V Achieved via Surface Passivation by a SbCl3 Interface Layer. *ACS Appl. Mater. Interfaces* **2020**, *12*, 4970–4979.
- (28) Tang, R.; Wang, X.; Lian, W.; Huang, J.; Wei, Q.; Huang, M.; Yin, Y.; Jiang, C.; Yang, S.; Xing, G.; Chen, S.; Zhu, C.; Hao, X.; Green, M. A.; Chen, T. Hydrothermal Deposition of Antimony Selenosulfide Thin Films Enables Solar Cells with 10% Efficiency. *Nat. Energy* **2020**, *5*, 587–595.
- (29) Lian, W.; Jiang, C.; Yin, Y.; Tang, R.; Li, G.; Zhang, L.; Che, B.; Chen, T. Revealing Composition and Structure Dependent Dep-

Level Defect in Antimony Trisulfide Photovoltaics. *Nat. Commun.* **2021**, *12*, No. 3260.

(30) Ning, H.; Guo, H.; Zhang, J.; Wang, X.; Jia, X.; Qiu, J.; Yuan, N.; Ding, J. Enhancing the Efficiency of Sb<sub>2</sub>S<sub>3</sub> Solar Cells Using Dual-Functional Potassium Doping. *Sol. Energy Mater. Sol. Cells* **2021**, *221*, No. 110816.

(31) Büttner, P.; Scheler, F.; Pointer, C.; Döhler, D.; Yokosawa, T.; Spiecker, E.; Boix, P. P.; Young, E. R.; Mínguez-Bacho, I.; Bachmann, J. ZnS Ultrathin Interfacial Layers for Optimizing Carrier Management in Sb<sub>2</sub>S<sub>3</sub>-Based Photovoltaics. *ACS Appl. Mater. Interfaces* **2021**, *13*, 11861–11868.

(32) Kim, D.-H.; Lee, S.-J.; Park, M. S.; Kang, J.-K.; Heo, J. H.; Im, S. H.; Sung, S.-J. Highly Reproducible Planar Sb<sub>2</sub>S<sub>3</sub>-Sensitized Solar Cells Based on Atomic Layer Deposition. *Nanoscale* **2014**, *6*, 14549–14554.

(33) Juneja, N.; Mandati, S.; Katerski, A.; Spalatu, N.; Daskeviciute-Geguziene, S.; Vembris, A.; Karazhanov, S.; Getautis, V.; Krunks, M.; Oja Acik, I. Sb<sub>2</sub>S<sub>3</sub> Solar Cells with a Cost-Effective and Dopant-Free Fluorene-Based Enamine as a Hole Transport Material. *Sustainable Energy Fuels* **2022**, *6*, 3220–3229.

(34) Petrus, M. L.; Bein, T.; Dingemans, T. J.; Docampo, P. A Low Cost Azomethine-Based Hole Transporting Material for Perovskite Photovoltaics. *J. Mater. Chem. A* **2015**, *3*, 12159–12162.

(35) Eensalu, J. S.; Katerski, A.; Kärber, E.; Acik, I. O.; Mere, A.; Krunks, M. Uniform Sb<sub>2</sub>S<sub>3</sub> Optical Coatings by Chemical Spray Method. *Beilstein J. Nanotechnol.* **2019**, *10*, 198–210.

(36) Jiang, C.; Zhou, J.; Tang, R.; Lian, W.; Wang, X.; Lei, X.; Zeng, H.; Zhu, C.; Tang, W.; Chen, T. 9.7%-Efficient Sb<sub>2</sub>(S,Se)<sub>3</sub> Solar Cells with a Dithieno[3,2-b: 2',3'-d]Pyrrole-Cored Hole Transporting Material. *Energy Environ. Sci.* **2021**, *14*, 359–364.

(37) Xiang, Y.; Guo, H.; Cai, Z.; Jiang, C.; Zhu, C.; Wu, Y.; Zhu, W.-H.; Chen, T. Dopant-Free Hole-Transporting Materials for Stable Sb<sub>2</sub>(S,Se)<sub>3</sub> Solar Cells. *Chem. Commun.* **2022**, *58*, 4787–4790.

### **Publication III**

**Nimish Juneja**, Šarūnė Daškevičiūtė-Gegužienė, Nicolae Spalatu, Sreekanth Mandati, Atanas Katerski, Raitis Gržibovskis, Aivars Vembris, Smagul Karazhanov, Vytautas Getautis, Malle Krunkis, and Ilona Oja Acik, “Employment of dopant-free fluorene-based enamines as innovative hole transport materials to boost the transparency and performance of Sb<sub>2</sub>S<sub>3</sub> based solar cells”, *Materials Science in Semiconductor Processing*, 169, 107934, 2024, doi: 10.1016/j.mssp.2023.107934.





Contents lists available at ScienceDirect

## Materials Science in Semiconductor Processing

journal homepage: [www.elsevier.com/locate/mssp](http://www.elsevier.com/locate/mssp)

# Employment of dopant-free fluorene-based enamines as innovative hole transport materials to boost the transparency and performance of Sb<sub>2</sub>S<sub>3</sub> based solar cells

Nimish Juneja<sup>a</sup>, Sarune Daskeviciute-Geguziene<sup>b</sup>, Nicolae Spalatu<sup>a</sup>, Sreekanth Mandati<sup>a</sup>, Atanas Katerski<sup>a</sup>, Raitis Grzibovskis<sup>c</sup>, Aivars Vembris<sup>c</sup>, Smagul Karazhanov<sup>d</sup>, Vytautas Getautis<sup>b</sup>, Malle Krunkas<sup>a,\*</sup>, Ilona Oja Acik<sup>a</sup>

<sup>a</sup> Department of Materials and Environmental Technology, Tallinn University of Technology, Ehitajate tee 5, Tallinn, 19086, Estonia

<sup>b</sup> Department of Organic Chemistry, Kaunas University of Technology, Kaunas, LT-50254, Lithuania

<sup>c</sup> Institute of Solid State Physics, University of Latvia, Kengaraga Str. 8, Riga, LV-1063, Latvia

<sup>d</sup> Institute for Energy Technology (IFE), P.O. Box 40, Kjeller, NO 2027, Norway

## ARTICLE INFO

## Keywords:

Antimony sulfide  
Hole transport material  
Semitransparent solar cells  
Photovoltaics

## ABSTRACT

Antimony sulfide (Sb<sub>2</sub>S<sub>3</sub>) with bandgap of ca. 1.7 eV is a promising absorber material for indoor and semi-transparent photovoltaic devices. However, the high cost of commonly used hole transport materials (HTMs) may impede the advancement of this technology. In this study, dopant-free fluorene-based enamines with different aliphatic chain length synthesized by a simple chemical method are used for the first time as HTMs in Sb<sub>2</sub>S<sub>3</sub> solar cell. The study investigates impact of HTM type and layer thickness on the performance of Sb<sub>2</sub>S<sub>3</sub> solar cells. The solar cells are fabricated in superstrate configuration with Sb<sub>2</sub>S<sub>3</sub> absorber layer deposited through ultrasonic spray pyrolysis and HTM layer applied via spin-coating. Energy level diagrams, constructed using ionization potential values of cell component layers, indicate agreeable band offsets validating the suitability of new HTMs for Sb<sub>2</sub>S<sub>3</sub> solar cells. Both the aliphatic chain length in HTM and layer thickness influence the power conversion efficiency (PCE) of the device, layer thickness of 20–25 nm is identified as optimal. Solar cells with new HTMs demonstrate higher PCEs (3.9–4.3%) compared to the reference device employing P3HT (3.8%). Moreover, Sb<sub>2</sub>S<sub>3</sub> cells with new HTMs without metal contact exhibit 20% increase in average visible transmittance, underscoring their potential in semi-transparent applications.

## 1. Introduction

Metal chalcogenides like Cadmium Telluride (CdTe), [1,2] Cu(In,Ga)Se<sub>2</sub> (CIGS), [3,4] have been successful as light harvesting materials due their high absorption coefficients and excellent optoelectronic properties. Thin-film solar cells based on CdTe and CIGSse, have reached power conversion efficiencies (PCE) of 22.1% and 23.4%, respectively [5,6]. However, in a long term, the large-scale implementation of some of these established PV technologies might face some barriers related to the availability of expensive In and Ga elements. In addition to traditional inorganic thin film technologies, antimony chalcogenides, such as Sb<sub>2</sub>S<sub>3</sub>, Sb<sub>2</sub>Se<sub>3</sub> and Sb<sub>2</sub>(S<sub>1-x</sub>Se<sub>x</sub>)<sub>3</sub> have demonstrated strong photon harvesting ability, high chemical stability, nontoxicity and benign synthesis and have recently emerged as viable photovoltaic absorbers [7–11]. In a

short period of time the PCEs of Sb<sub>2</sub>S<sub>3</sub>, Sb<sub>2</sub>Se<sub>3</sub> and Sb<sub>2</sub>(S,Se)<sub>3</sub> based solar cells have reached 8.0%, 10.57%, 10.75%, respectively, [12–14] making them promising candidates for next-generation PV in the family of antimony chalcogenides. Sb<sub>2</sub>S<sub>3</sub> possesses a high absorption coefficient of approximately 10<sup>5</sup> cm<sup>-1</sup> at 450 nm and a relatively wide bandgap of 1.7–1.8 eV [11,15–17]. Consequently, it is a suitable absorber material for both single junction solar cells as well as for advanced device concepts, such as tandem devices. Sb<sub>2</sub>S<sub>3</sub> based PV devices could be principally used in wide range of applications such as solar windows in building-integrated photovoltaics (BIPV), [11,17] semitransparent electronics and due to excellent low-light harvesting ability also in standalone indoor PV [10].

Sb<sub>2</sub>S<sub>3</sub> thin films can be deposited using a range of physical and chemical methods, avoiding the formation of secondary phases. The

\* Corresponding author.

E-mail address: [malle.krunkas@taltech.ee](mailto:malle.krunkas@taltech.ee) (M. Krunkas).

<https://doi.org/10.1016/j.mssp.2023.107934>

Received 29 June 2023; Received in revised form 27 September 2023; Accepted 23 October 2023

Available online 31 October 2023

1369-8001/© 2023 The Authors. Published by Elsevier Ltd. This is an open access article under the CC BY-NC-ND license (<http://creativecommons.org/licenses/by-nc-nd/4.0/>).

chemical deposition techniques include mainly chemical bath deposition (CBD), [18,19] ultrasonic-spray pyrolysis (USP), [11,20,21] spin coating, [22,23] and atomic layer deposition (ALD) [16,24]. Different physical deposition techniques are being employed for the preparation of  $\text{Sb}_2\text{S}_3$  absorbers, including sputtering, [25,26] thermal evaporation, [27,28] and closed space sublimation [29,30]. The composition of the  $\text{Sb}_2\text{S}_3$  solar cell stack is similar to perovskite solar cells, encompassing an electron transport layer (ETL), an absorber layer, a hole transport material (HTM), and metal front and back contacts. In a recent study by Wang et al., the utilization of CBD for the deposition of  $\text{Sb}_2\text{S}_3$  has led to fabrication of solar cells yielding a PCE of 8.0% [12]. Eensalu et al., fabricated solar cells using USP for the preparation of  $\text{Sb}_2\text{S}_3$  and obtained the PCE of 5.5% [17]. Han et al., fabricated solar cell devices with spin coating for the deposition of  $\text{Sb}_2\text{S}_3$  and has obtained PCE of 7.1% [31]. Büttner et al., fabricated solar cells with PCE of 5.1% while using ALD for preparation of the absorber  $\text{Sb}_2\text{S}_3$  [32].

To fabricate semi-transparent solar cells based on  $\text{Sb}_2\text{S}_3$ , it is crucial to ensure an absorber thickness of less than 100 nm, and in this perspective, USP and ALD can be employed to deposit semitransparent absorber layer [11,17,33]. USP is a low-cost, area-scalable and a high throughput solution-based technique [11,17]. In previous studies, we have demonstrated that compact  $\text{Sb}_2\text{S}_3$  films can be deposited using a two-step process [11,17,20]. Firstly, amorphous  $\text{Sb}_2\text{S}_3$  films are deposited at relatively low temperature of around 200 °C. This is followed by crystallization of the absorber layer by thermal annealing in vacuum [11,17,20] or in  $\text{N}_2$  at temperature up to 250 °C [20,21] resulting in PCE of 4–6%. Apart from the quality of the absorber in the solar cells, another key component in the solar cell device is the HTM. The presence of HTM aids in effective extraction and the transport of photogenerated holes to the metal back contact. It prevents the diffusion of metal into the absorber, reduces charge recombination losses at the interface between the absorber and HTM, and provides encapsulation for the absorber. The most popular conjugated polymers as HTMs in  $\text{Sb}_2\text{S}_3$  based solar cells are poly(3-hexylthiophene) (P3HT), [11,16,17,34] 2,2',7,7'-tetrakis[N,N-di(4-methoxyphenyl)amino]-9,9'-spirobifluorene (Spiro-OMeTAD), [12,32,35] poly(3,4-ethylenedioxythiophene)poly(styrenesulfonate) [36,37] (PEDOT:PSS) and poly[2,6-(4,4-bis(2-ethylhexyl)-4H-cyclo-penta[2,1-b;3,4-b']dithiophene)-alt-4,7-(2,1,3 benzothiadiazole)] (PCPDTBT) [38,39].

Wang et al., prepared solar cells (FTO/CdS/ $\text{Sb}_2\text{S}_3$ /Spiro-OMeTAD/Au) yielding a PCE of 8.0% using Spiro-OMeTAD as HTM [12]. Eensalu et al., fabricated solar cells using USP for the preparation of  $\text{Sb}_2\text{S}_3$  with P3HT as HTM (ITO/ $\text{TiO}_2$ / $\text{Sb}_2\text{S}_3$ /P3HT/Au) and obtained the PCE of 5.5% [17]. On a similar note, Choi et al. achieved a PCE of 7.5% by using CBD for  $\text{Sb}_2\text{S}_3$  deposition and utilized HTMs - PCPDTBT and PEDOT:PSS in the solar cell configuration of FTO/mp- $\text{TiO}_2$ / $\text{Sb}_2\text{S}_3$ /PCPDTBT/PEDOT:PSS/Au [19]. Furthermore, alternative inorganic materials such as  $\text{NiO}_x$ , [40] CuSCN, [41,42] and  $\text{V}_2\text{O}_5$  [43] have also been employed as HTMs in  $\text{Sb}_2\text{S}_3$  based solar cells. Despite the fact that conventionally employed HTMs such P3HT, Spiro-OMeTAD, PCPDTBT, etc. have been successfully used, their low synthesis yield and high manufacturing cost may limit the viability of  $\text{Sb}_2\text{S}_3$  solar cells. Spiro-OMeTAD is synthesized in a multi-step reaction scheme that requires a low temperature (−78 °C) and sensitive (*n*-butyllithium or Grignard reagents) reagents [44,45]. Additionally, the use of Spiro-OMeTAD in the solar cell requires its doping with Li-based salt to improve its hole transporting capability. This adds to the cost and reduces the stability of the devices as the dopant Lithium bis(trifluoromethylsulphonyl)imide (LiTFSI) is hygroscopic [46]. The band gap of 1.8 eV in P3HT introduces parasitic absorption losses in the device, consequently reducing the transparency of the solar cells [11,17,34]. Moreover, the processing of P3HT necessitates an additional activation step at around 170 °C [11,17]. Considering the limitations listed above, there is an obvious need to search alternative HTMs combining properties such as optical transparency, efficient charge extraction and low cost.

Thus, the objective of this study is to propose new HTMs as alternative options to conventional HTMs like Spiro-OMeTAD and P3HT for

$\text{Sb}_2\text{S}_3$  solar cells, targeting semi-transparency, appropriate band alignment and enhanced solar cell performance. In the present study, fluorene-based enamines are synthesized, characterized, and their potential as an HTM in  $\text{Sb}_2\text{S}_3$  based solar cells is explored. V1275 ( $N^2,N^2,N^7,N^7$ -tetrakis[2,2-bis(4-methoxyphenyl)vinyl]-9H-fluorene-2,7-diamine), V1235 ( $N^2,N^2,N^7,N^7$ -tetrakis[2,2-bis(4-methoxyphenyl)vinyl]-9,9-dipropyl-9H-fluorene-2,7-diamine), and V1461 ( $N^2,N^2,N^7,N^7$ -tetrakis[2,2-bis(4-methoxyphenyl)vinyl]-9,9-dinonyl-9H-fluorene-2,7-diamine) that are belonging to the enamine family with a central fluorene scaffold, differ from each other by the length of aliphatic chain. These compounds can be produced in a straightforward condensation reaction from commercially available and cheap materials. The synthesis cost of V-series HTMs are considerably lower, estimated to be around 10–20 €/g, in contrast to conventional HTMs like Spiro-OMeTAD (approximately 90 €/g) [47] and P3HT (approximately 45 €/g) [48]. The two out of the three proposed HTMs – namely V1275 and V1235 have previously been utilized as dopant-free HTMs in perovskite solar cells, resulting in PCE of 17.1% and 16.6%, respectively [49]. V1461 with its -nonyl chain is a newly synthesized material. In summary, the three materials - V1275, V1235 and V1461 are tested as HTMs for the first time in  $\text{Sb}_2\text{S}_3$  based solar cells.

The solar cell stacks are fabricated in superstrate configuration glass/FTO/ $\text{TiO}_2$ / $\text{Sb}_2\text{S}_3$ /HTM/Au. USP is used for the deposition of  $\text{TiO}_2$  and  $\text{Sb}_2\text{S}_3$  layers, while the HTMs are applied using the spin-coating technique. In order to investigate the influence of HTM layer thickness on the performance of solar cells, a systematic approach is employed, wherein the thickness of the layer is optimized by changing the concentration of the HTM precursor solution. The solar cell performance with V-series HTMs is compared to that of solar cells with reference HTM - P3HT. Combining the different characterization techniques for material and device, new insights are provided on the functionality of the V - series HTMs in correlation with the performance of  $\text{Sb}_2\text{S}_3$  based semi-transparent device.

## 2. Experimental

### 2.1. Materials

The chemicals used for the synthesis of the HTMs -  $N^2,N^2,N^7,N^7$ -tetrakis[2,2-bis(4-methoxyphenyl)vinyl]-9H-fluorene-2,7-diamine (V1275),  $N^2,N^2,N^7,N^7$ -tetrakis[2,2-bis(4-methoxyphenyl)vinyl]-9,9-dipropyl-9H-fluorene-2,7-diamine (V1235), and  $N^2,N^2,N^7,N^7$ -tetrakis[2,2-bis(4-methoxyphenyl)vinyl]-9,9-dinonyl-9H-fluorene-2,7-diamine (V1461) are purchased from Sigma-Aldrich and used as received without further purification. A detailed description of the materials related to HTM synthesis are presented in Supporting Information (SI) file, in Table S1. FTO substrate (7  $\Omega/\text{sq}$ ), Titanium(IV) tetraisopropoxide (TTIP) – Acros Organics (99 wt%), Acetylacetone - Acros Organics (99 wt%), Ethanol - Estonian Spirit (96.6 vol%), Methanol - Sigma-Aldrich (99.9 vol%), Antimony trichloride - Sigma-Aldrich (99.99 wt%), Thiourea - Sigma-Aldrich (99 wt%), Chlorobenzene - Sigma-Aldrich (99.5 vol%), and Poly(3-hexylthiophene-2,5-diyl) (P3HT) Sigma-Aldrich (Regio regular, >90%) are used as received.

### 2.2. Methods

#### 2.2.1. Fabrication of solar cell

Solar cell devices are fabricated using the same experimental procedure as described elsewhere [20,21]. In brief, Fluorinated tin oxide (FTO) coated glass with a sheet resistivity of 7  $\Omega \text{ sq}^{-1}$  is used as a substrate. The device configuration and schematic representation of the standard process used to fabricate  $\text{Sb}_2\text{S}_3$  solar cells is presented in SI, in Fig. S1. The glass/FTO substrates (20 mm × 20 mm) were meticulous cleaned with a procedure, which includes extensive rinsing with deionized water, ethanol, and methanol. This is followed by immersion in boiling deionized water for a duration of 15 min. Finally, the substrates are dried by  $\text{N}_2$  gas. The  $\text{TiO}_2$  precursor solution is prepared by

combining 0.2 M TTIP and 0.2 M acetylacetonate in solvent ethanol. The ETL -  $\text{TiO}_2$ , and the absorber -  $\text{Sb}_2\text{S}_3$  are deposited onto the cleaned glass/FTO substrates using a USP setup. Deposition of films by USP involves spraying the aerosol onto the substrate using compressed air as the carrier gas. During the deposition, the substrates are maintained at a temperature of 340 °C using a hot plate. The as-deposited  $\text{TiO}_2$  samples are then subjected to annealing on a hot plate in air at a temperature of 450 °C for a duration of 30 min. For the preparation of the  $\text{Sb}_2\text{S}_3$  precursor solution, 180 mM of thiourea is dissolved in 60 mM of antimony chloride ( $\text{SbCl}_3$ ) within 120 mL of methanol. Similar to  $\text{TiO}_2$ , the absorber is deposited using USP method, with the substrate maintained at a temperature of 198 °C. After deposition, the amorphous  $\text{Sb}_2\text{S}_3$  thin films underwent annealing at 250 °C for 5 min within a  $\text{N}_2$  atmosphere. Subsequently, the HTMs are applied onto the  $\text{Sb}_2\text{S}_3$  films through spin coating (3000 rpm at 30s), utilizing the respective precursors dissolved in chlorobenzene. The concentrations of the three HTMs - V1275, V1235, and V1461 - are systematically altered. For P3HT, the standard concentration of 1% wt. is used [20,21]. Samples with P3HT need an additional activation step in vacuum at 170 °C for 5 min, whereas no such step is needed for the new HTMs. Sequentially, 80–100 nm of Au back contact is thermally evaporated through a shadow mask under a pressure of about  $10^{-4}$  Pa. The active contact area of the fabricated device is 7.06  $\text{mm}^2$ .

### 2.2.2. Characterization of synthesized HTMs and fabricated solar cells

The structure of the HTMs was confirmed using the  $^1\text{H}$  NMR measurements. Details are introduced in SI, section S2, and the NMR and mass spectroscopy (MS) spectra are presented in Figs. S2–S4. The HTMs were characterized comprehensively using TGA, DSC, and absorption spectroscopy. DSC data is presented in SI, in Fig. S4. Optical absorption and Photoluminescence spectra of the HTMs were measured in THF solution ( $10^{-4}$  M). Details are given in SI, section S1. The hole drift mobility of the novel HTMs was determined using the time of flight (ToF) method on “sandwich” type samples (ITO/HTM/AI) as described in detail in SI, in section S3. Ionization potential of the constituent layers was measured using the photoelectron yield spectroscopy (PYS) method described in detail in SI, in section S4. The total transmittance and total reflectance spectra of the stacks - glass/FTO/HTM and glass/FTO/ $\text{TiO}_2$ / $\text{Sb}_2\text{S}_3$ /HTM, were measured using an ultraviolet-visible (UV-VIS) spectrophotometer within the 250–1100 nm range. In order to

determine the optical bandgap values of the HTMs, the total transmittance spectra of HTM films was utilized to calculate the absorption coefficient ( $\alpha$ ) and derive the corresponding bandgap values ( $E_g$ ) through Tauc plots. Additionally, the work function of the Au metal contacts was measured employing a Kelvin probe.

The electrical characterization of the solar cells was performed by measuring their current-voltage (I–V) characteristics using a Wavelabs LS-2 LED solar simulator ( $\text{AM1.5G}$ ,  $100 \text{ mW cm}^{-2}$ ). To measure the external quantum efficiency (EQE) spectra of the fabricated solar cells, a Newport 69911 system was employed. Furthermore, the surface and cross-sectional morphologies of the fabricated devices were examined using a Zeiss HR FESEM Ultra 55.

## 3. Results and discussion

### 3.1. Synthesis and properties of HTMs

The HTM compounds – V1275, V1235 and V1461 were synthesized using one-pot or two-step reactions performed under ambient conditions. Synthesis route is presented in Fig. 1a. Materials with high yields and purity could be synthesized. Commercially available reagents 2,7-diamino fluorene and 2,2-bis(4-methoxyphenyl) acetaldehyde were used in the presence of camphor sulfonic acid to yield V1275 [49] V1275 on further reaction with alkylating agents bromopropane and bromononane yielded propyl- and nonyl-substituted fluorene enamines V1235 and V1461. The chemical composition of the produced compounds is confirmed by NMR and MS spectroscopy (see details in SI, Figs. S2–S4). The chemical structures of V1275, V1235 and, V1461 is presented in Fig. 1b, c and d, respectively.

To study the thermal stability of the synthesized HTMs, thermogravimetric analysis (TGA) was performed and is presented in Fig. 2a. Thermal and optoelectronic properties V1275 and V1235 have been published in a previous study [49]. Since V1461 is a newly synthesized material with a longer aliphatic chain (nonyl substituted), its properties are compared to V1275 (with no aliphatic chain) and V1235 (propyl substituted). All the three HTM compounds – V1275, V1235 and V1461, decompose at temperatures of around 400 °C. V1275 has the highest thermal stability with a decomposition temperature ( $T_{\text{dec}}$ ) of 403 °C. It should be noted that V1275 and V1235 exist in both the crystalline and amorphous states, in contrast to V1461, which is amorphous. The glass

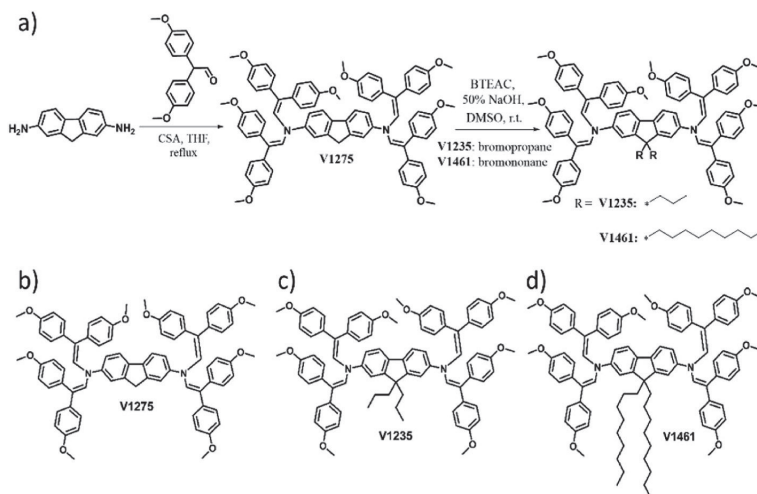


**Fig. 1.** a) Synthetic route to V1275, V1235 and V1461. b) N<sub>2</sub>,N<sub>2</sub>,N<sub>7</sub>,N<sub>7</sub>-tetrakis[2,2-bis(4-methoxyphenyl)vinyl]-9H-fluorene-2,7-diamine (V1275). c) N<sub>2</sub>,N<sub>2</sub>,N<sub>7</sub>,N<sub>7</sub>-tetrakis[2,2-bis(4-methoxyphenyl)vinyl]-9,9-dipropyl-9H-fluorene-2,7-diamine (V1235), d) N<sub>2</sub>,N<sub>2</sub>,N<sub>7</sub>,N<sub>7</sub>-tetrakis[2,2-bis(4-methoxyphenyl)vinyl]-9,9-dinonyl-9H-fluorene-2,7-diamine (V1461).

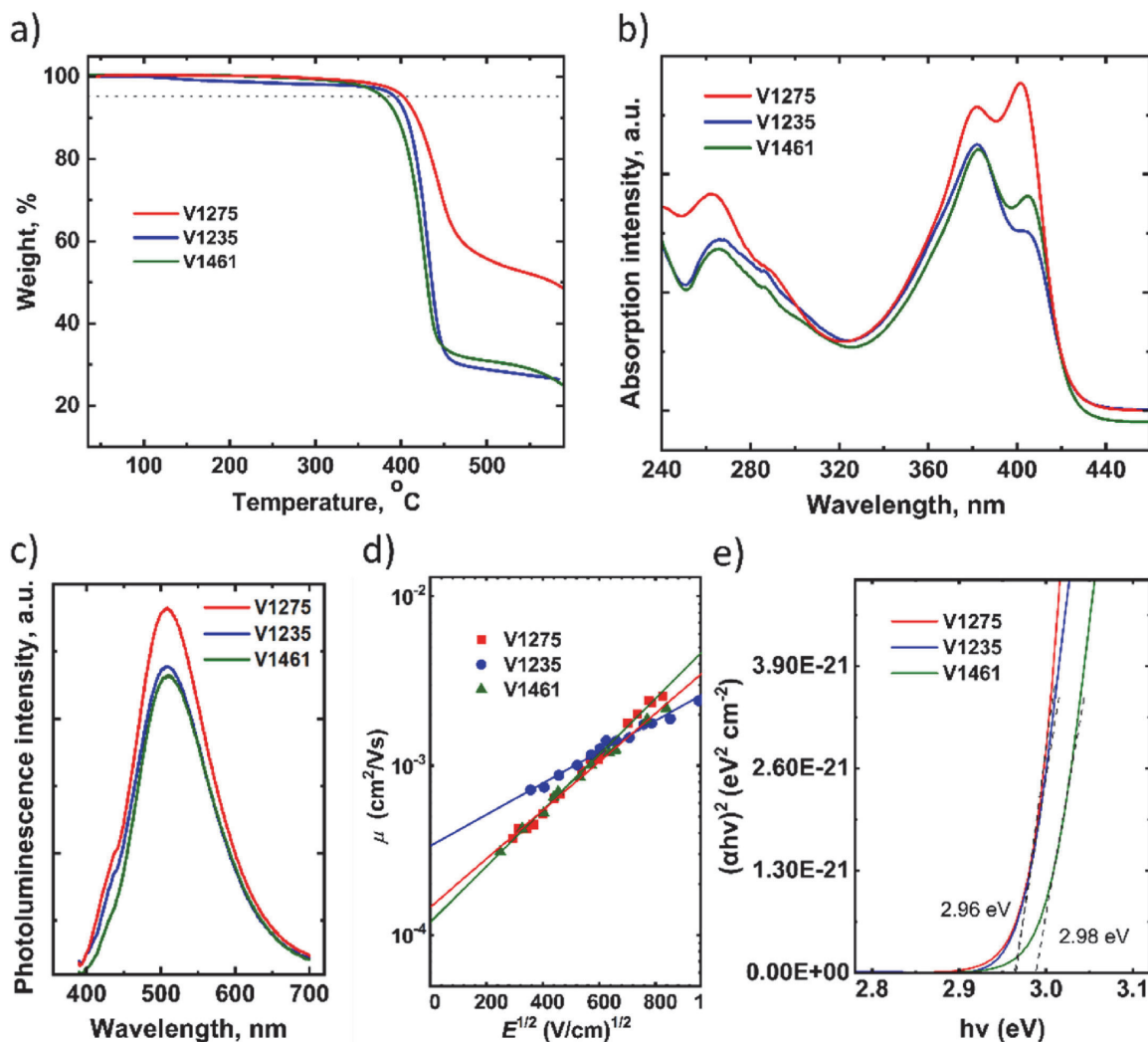


Fig. 2. a) Thermogravimetric analysis (TGA) data (heating rate of 10 °C/min, N<sub>2</sub> atmosphere). b) UV-Vis absorption spectra of V-series HTMs in THF solutions (10<sup>-4</sup> M). c) Photoluminescence spectra of the HTMs in THF solution (10<sup>-4</sup> M). d) Electric field dependencies of the hole-drift mobility in the studied HTMs. e) Tauc's plots of V1275, V1235 and V1461 thin films.

transition temperatures ( $T_g$ ) for V1275 and V1235 are 150 and 120 °C, respectively, indicating stability of the amorphous state of these molecules. The differential scanning calorimetric (DSC) curves of new HTMs are presented in SI, in Fig. S5. The melting ( $T_m$ ), crystallization ( $T_c$ ) and glass transition ( $T_g$ ) temperatures, together with the decomposition temperatures ( $T_{dec}$ ) of HTMs are summarized in Table 1. Next, to characterize the optoelectronic properties of the HTMs, optical absorption and photoluminescence (PL) spectra were recorded for HTMs in THF solution, and are presented in Fig. 2b and c, respectively. All the three HTMs exhibit two main absorption peaks at about 260 nm and 400 nm. The absorption peak at shorter wavelength of 260 nm corresponds to the localized  $\pi$ - $\pi^*$  transitions. The less intense absorption peak at the shorter wave-length corresponds to localized  $\pi$ - $\pi^*$  transitions while the longer wavelength absorption arises from more intensive delocalisation from the conjugated scaffold and is assigned to n- $p^*$  transitions [49]. The conjugation has not been affected by modifications to the different

Table 1  
Thermal, optical and electrical properties of HTMs - V1275, V1235 and V1461.

HTM	$T_m$ [°C]	$T_c$ [°C]	$T_g$ [°C]	$T_{dec}$ [°C]	$\lambda_{abs}$ [nm]	$\lambda_{em}$ [nm]	$\mu_0$ [cm <sup>2</sup> V <sup>-1</sup> s <sup>-1</sup> ]	$E_g$ [eV]
V1275	255	-	150	403	262, 381, 401	508	$1.2 \times 10^{-4}$	2.96
V1235	273	159	120	399	266, 382, 404	509	$3.3 \times 10^{-4}$	2.96
V1461	-	-	99	370	265, 382, 405	511	$1.5 \times 10^{-4}$	2.98

aliphatic chain length, and thus the spectra of all molecules are nearly the same. As seen in Fig. 2c, the PL spectra of all the three synthesized HTM molecules have a peak at 510 nm. The compounds have absorption peaks at 400 nm and emission peak at 510 nm, which depicts large Stokes shifts of approximately 100 nm for all the molecules [49].

Melting ( $T_m$ ), crystallization ( $T_c$ ), glass transition ( $T_g$ ) and decomposition ( $T_{dec}$ ) temperatures observed from DSC and TGA, respectively (10 °C/min,  $N_2$  atmosphere). Optical absorption ( $\lambda_{abs}$ ) and optical emission ( $\lambda_{em}$ ) peak positions in spectra as measured in THF solution ( $10^{-4}$  M). Hole drift mobility ( $\mu_0$ ) value at zero field strength and the bandgap ( $E_g$ ) estimated using the Tauc plot.

Additionally, to study the hole-mobility of the HTMs, time of flight (TOF) technique is used. High hole mobility is required in HTM for the efficient transport of the holes to the back contact [49]. Fig. 2d shows how the mobility of a hole is dependent on the strength of the electric field. When compared to the other members of the fluorene series, the propyl substituted V1235 has the highest zero-field hole mobility ( $\mu_0$ ) of  $3.3 \times 10^{-4} \text{ cm}^2 \text{ V}^{-1} \text{ s}^{-1}$ . The zero-field hole drift mobility for V1275 and V1461 was found to be at  $1.2 \times 10^{-4} \text{ cm}^2 \text{ V}^{-1} \text{ s}^{-1}$  and  $1.5 \times 10^{-4} \text{ cm}^2 \text{ V}^{-1} \text{ s}^{-1}$ . The V-series HTMs have hole mobility values comparable to those of P3HT ( $\mu_0 = 2 \times 10^{-4} \text{ cm}^2 \text{ V}^{-1} \text{ s}^{-1}$ ) [50] and Spiro-OMeTAD ( $\mu_0 = 1.3 \times 10^{-4} \text{ cm}^2 \text{ V}^{-1} \text{ s}^{-1}$ ) [49]. The incorporation of longer chains into the molecular structure is risky as the mobility of charge carriers can decrease due to the decreasing concentration of photoconductive chromophores [49]. However, the opposite situation is possible when molecules are ordered more due to the presence of the chains and in this case the mobility of charge carriers increases. For example, hole mobility in V1235 at weak field is better than that in V1275, though the concentration of chromophores is the highest in the latter HTM. It can be assumed, that the chains make steric orientation of the molecules more ordered and the obtained layers are of better quality (without pin-holes) [49]. Also, the drift mobility in V1461 is lower due to the presence of long chains, which significantly decrease concentration of chromophores. Thus, there is a correlation between the chain length and HTM performance. The  $E_g$  values were determined from the Tauc plots as

presented in Fig. 2e for V1275 and V1235 were similar, 2.96 eV, and for nonyl substituted V1461,  $E_g$  was 2.98 eV.

### 3.2. Application of HTMs in solar cells

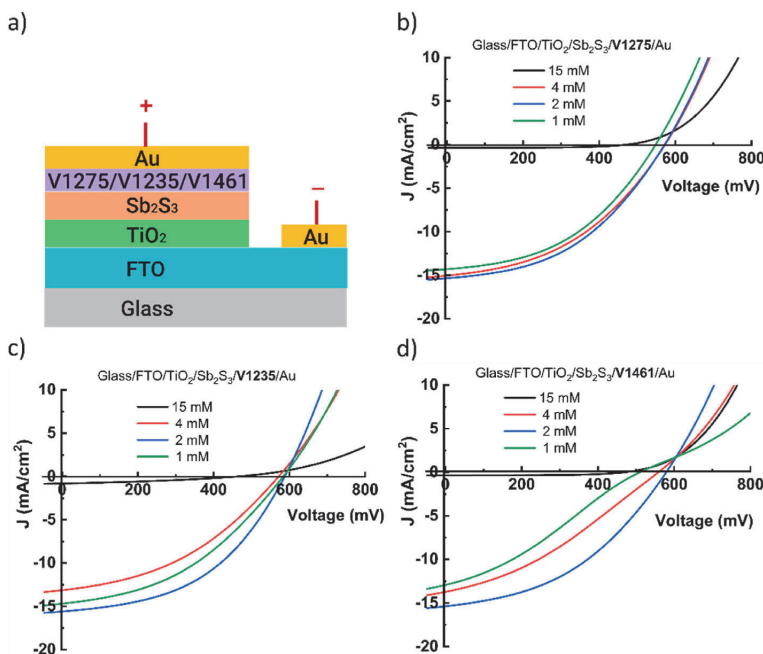
Thin film  $\text{Sb}_2\text{S}_3$  based solar cells were fabricated in the superstrate configuration (glass/FTO/ $\text{TiO}_2$ / $\text{Sb}_2\text{S}_3$ /HTM/Au) as presented in Fig. 3a. The HTMs – V1275, V1235, V1461, and P3HT are spin coated. From our previous study, we observed that P3HT – 1% wt. gives the thickness of 80 nm, which is an optimal value for the most efficient solar cell stack [11,17]. As the V-series HTMs are being used in  $\text{Sb}_2\text{S}_3$  based solar cells for the first time, therefore the conditions for obtaining a layer of suitable thickness for efficient solar cell must be determined. The layer thickness was changed by varying the HTM concentration in the solution.

Fig. 3b, c and d show the current density-voltage (J-V) characteristics of solar cells with concentration variation for the HTMs - V1275, V1235 and V1461. Initially, a concentration of 15 mM of HTM precursor solution was used to fabricate solar cells as this concentration has been previously employed for the successful production of efficient perovskite solar cells [49]. As seen from J-V characteristics, the cell performances are low using 15 mM HTM solutions, yet the dilution of solutions allows to obtain higher  $J_{SC}$  and  $V_{OC}$  for all the devices. For example,  $V_{OC}$  increased from 490 mV to 570 mV,  $J_{SC}$  increased from 0.8 to 12.5  $\text{mA}/\text{cm}^2$  and PCE from 0.8 to 3.0% when reducing V1235 concentration

**Table 2**

Effect of HTM V1235 solution concentration on solar cell output characteristics.

V1235 conc. [mM]	$V_{OC}$ [mV]	$J_{SC}$ [ $\text{mA}/\text{cm}^2$ ]	FF [%]	PCE [%]	$R_s$ [ $\Omega \cdot \text{cm}^2$ ]
15	490	0.8	21	0.8	23
4	570	12.5	42	3.0	2.1
2	587	15.5	47	4.3	1.3
1	582	14.1	45	3.7	1.0



**Fig. 3.** a)  $\text{Sb}_2\text{S}_3$  solar cell configuration and J-V curves of  $\text{Sb}_2\text{S}_3$  solar cells with HTMs, b) V1275, c) V1235, and d) V1461.

from 15 to 4 mM (Fig. 3c, Table 2). Further dilution to 2 mM results in a solar cell demonstrating  $V_{OC}$  of 587 mV,  $J_{SC}$  of 15.5 mA/cm<sup>2</sup> and PCE of 4.3%. Following dilution to 1 mM resulted in a drop in  $J_{SC}$  to 14.1 mA/cm<sup>2</sup> accompanied by a slight drop in  $V_{OC}$  to 582 mV, and a decrease in PCE to 3.7%. Very similar trend of the solution concentration on solar cell output characteristics was recorded using V1461 as HTM (Fig. 3d). In case of V1275, the effect HTM solution concentration on cell output characteristics was less pronounced although some drop in  $V_{OC}$  and  $J_{SC}$  were also recorded when using 1 mM solution (Fig. 3b). The highest PCE values were recorded for the cells with hole transport layers obtained from 2 mM solution of all V-series HTMs (Fig. 3b, c, d).

SEM cross-sectional images of solar cells incorporating HTM layers derived from V1235 at different precursor concentrations are shown in SI, in Fig. 4. As expected, the HTM layer thicknesses decrease when the solution concentration is reduced, for example, V1235 – 15 mM gave a thickness of ca. 120 nm, 2 mM of ca. 25 nm and 1 mM of ca. 15 nm. Thus, a drop in  $R_S$  from 23 to 1.0  $\Omega$  cm<sup>2</sup> correlates with a decrease in HTM layer thickness from 120 nm to 15 nm while reducing solution concentration from 15 to 1 mM (Table 2). According to J-V curves (Fig. 3b–d), the  $V_{OC}$ ,  $J_{SC}$  and FF are lowered when HTM layer from heavily diluted 1 mM solutions is applied, resulting in a decrease of solar cells performances as also observed in a previous study using N<sup>2</sup>,N<sup>2</sup>,N<sup>7</sup>,N<sup>7</sup>-tetrakis[2,2-bis(4-methoxyphenyl)vinyl]-9,9-dihexyl-9H-fluorene-2,7-diamine (V1236) as HTM on Sb<sub>2</sub>S<sub>3</sub> absorber [20]. It is likely that HTM layers with thickness of around 15–20 nm do not cover the absorber layer uniformly and may contain pinholes allowing direct contact of the gold electrode to the active layer. It has been also reported that poor layer formation could be controlled by the HTM molecular structure [51]. In our study, the cell with V1275 that has no aliphatic chain in its structure showed the smallest decline of output parameters at HTM layer low thicknesses (Fig. 3).

In order to understand the energy levels alignment of the studied HTMs (V1275, V1235 and V1461) with that of the absorber material Sb<sub>2</sub>S<sub>3</sub> and metal back contact Au, photoemission spectroscopy was used to measure the ionization potential ( $I_p$ ) of the constituent layers within the solar cell stack, namely FTO, TiO<sub>2</sub>, Sb<sub>2</sub>S<sub>3</sub> and the HTMs. Experimental data for  $I_p$  determination for HTMs - V1275, V1235, V1461 are presented in Fig. 5a, b, and c, respectively. The  $I_p$  values (HOMO levels) for V1275, V1235 and V1461, were found to be at -4.92, -4.80, and -4.94 eV, respectively, that are close to the HOMO levels reported for HTMs such as Spiro-OMeTAD (-5.2 eV) and PCPDTBT (-5.2 eV) [10].  $I_p$  values for P3HT, TiO<sub>2</sub> and Sb<sub>2</sub>S<sub>3</sub> were measured in our previous study [20] and were -4.60 eV, -7.40 eV and -5.10 eV, respectively. Taking

into account the band gap energies measured for V1275, V1235, V1461 (Table 1), the LUMO levels of V-series HTMs are at -2.8 eV, -2.1 eV, -2.0 eV, and -2.1 eV, respectively. The band energy diagram is presented in Fig. 5d.

In order to ensure a comprehensive evaluation, solar cells utilizing V1275 – 2 mM, V1235 – 2 mM, V1461 – 2 mM, and the commonly used HTM - P3HT were fabricated within the same experimental batch. Additionally, to comprehend the influence of HTMs, control solar cell devices were fabricated devoid of any HTM, following the stack configuration of glass/FTO/TiO<sub>2</sub>/Sb<sub>2</sub>S<sub>3</sub>/Au. The J-V characteristics of champion cells with no HTM and HTMs - P3HT – 1% wt., V1275 – 2 mM, V1235 – 2 mM and V1461 – 2 mM are presented in Fig. 6a. The solar cell results are shown in Table 3. The reference device fabricated without an HTM exhibited a  $V_{OC}$  of 450 mV,  $J_{SC}$  of 12.8 mA/cm<sup>2</sup>, FF of 0.4 and a PCE of 2.1%. Application of HTMs significantly increases the  $V_{OC}$  value compared to the reference device. For example,  $V_{OC}$  of 650 mV was recorded for a solar cell with P3HT as HTM, and  $V_{OC}$  at around 580 mV was recorded for solar cells with V-series HTMs being in correlation with enhanced shunt resistance ( $R_{SH}$ ) of the devices (Table 3). As Sb<sub>2</sub>S<sub>3</sub> absorber exhibits the valence band edge (VBE) at -5.1 eV and the conduction band edge (CBE) at -3.4 eV, then in a device without HTM (TiO<sub>2</sub>/Sb<sub>2</sub>S<sub>3</sub>/Au), there is no barrier for electrons to flow from the conduction band of Sb<sub>2</sub>S<sub>3</sub> to the Au back contact (Work function of Au -5.1 eV). This enables the recombination resulting in lower  $V_{OC}$  and FF.

Applying an HTM reduces the recombination losses as electron affinity values of the HTM molecules (-2.0 or -2.1 eV, Fig. 5d) are smaller than the CBE of Sb<sub>2</sub>S<sub>3</sub> at -3.4 eV. Therefore, the electron transfer from the absorber to the HTMs is effectively blocked. According to the VBE of Sb<sub>2</sub>S<sub>3</sub> at -5.1 eV and that of V-series HTMs at -4.9 eV, the transfer of photogenerated holes from the absorber - Sb<sub>2</sub>S<sub>3</sub> to HTM is feasible, although HTMs with higher HOMO levels are expected to perform better. The PCE obtained for the optimized concentrations of V1275 and V1461 were 3.9% and 3.7%, respectively, comparable to the cell with P3HT (3.8%), however, the highest PCE of 4.3% was recorded for solar cell device with HTM - V1235. Next, the external quantum efficiency (EQE) response of the devices were performed and the plot is presented in Fig. 6b. Solar cells incorporating the V-series HTMs demonstrated a higher EQE spectral response than cells with P3HT across the entire wavelength range. The EQE response of the solar cell with P3HT exhibits a concavity within the 500–700 nm range, whereas this drop in response is absent in the solar cells incorporating V-series HTMs. Significant EQE response drop in the long wavelength range of P3HT device was observed in previous studies [20,21] and ascribed to

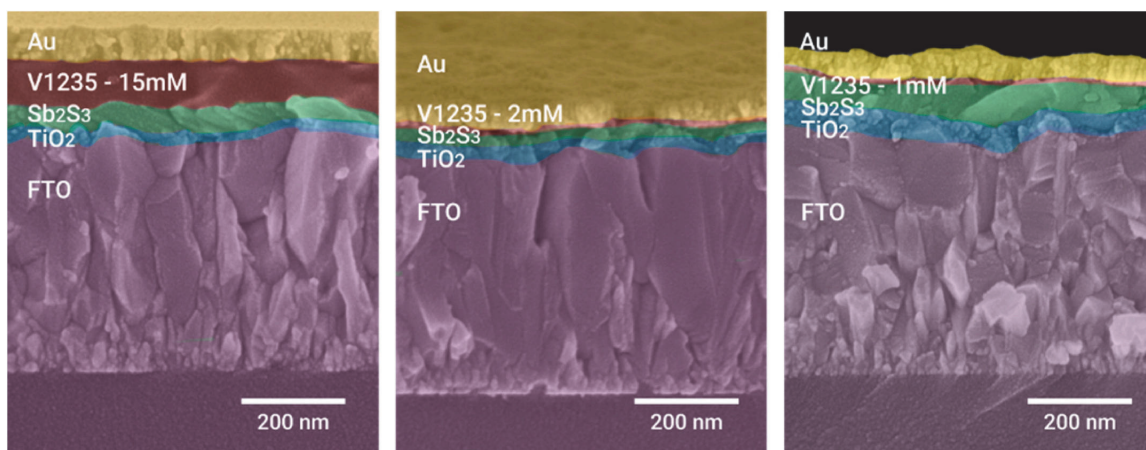


Fig. 4. SEM cross-sectional images of solar cells with HTM V1235 concentrations of 15 mM, 2 mM and 1 mM.

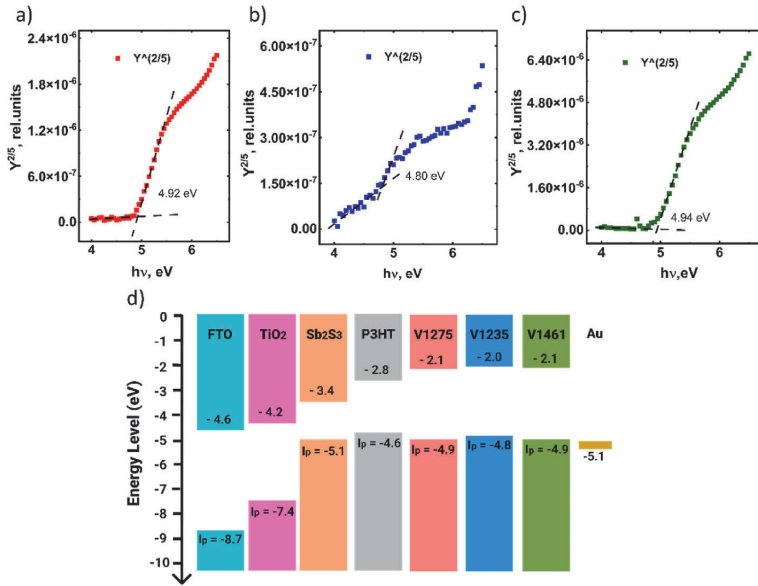


Fig. 5. Ionization potential of HTMs – a) V1275, b) V1235, c) V1461 as measured by the photoelectron yield spectroscopy method. d) Energy band diagram of  $Sb_2S_3$  solar cells with all the constituent layers.

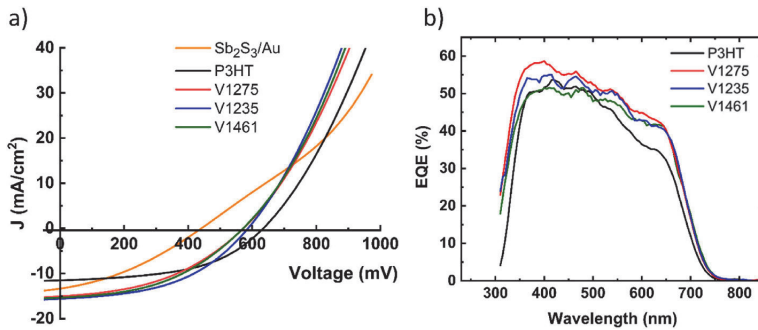


Fig. 6. a) J-V characteristics of champion  $Sb_2S_3$  solar cells without an HTM and with optimized HTMs thicknesses for cells with P3HT, V1275, V1235, and V1461. b) EQE curves of  $Sb_2S_3$  solar cells with different HTMs.

**Table 3**  
Solar cell performance parameters of champion  $Sb_2S_3$  solar cells fabricated without an HTM and with HTMs - P3HT, V1275, V1235 and V1461.

HTM	HTM conc. [mM]	$V_{OC}$ [mV]	$J_{SC}$ [mA/cm <sup>2</sup> ]	FF [%]	PCE [%]	$R_S$ [ $\Omega$ , cm <sup>2</sup> ]	$R_{SH}$ [ $\Omega$ , cm <sup>2</sup> ]
No HTM	-	450	12.8	40	2.1	3.2	210
P3HT	1 wt%	650	11.2	50	3.8	3.5	650
V1275	2	572	15.3	44	3.9	1.2	390
V1235	2	587	15.5	47	4.3	1.3	444
V1461	2	573	15.0	43	3.7	1.8	373

the parasitic absorption of ca. 100 nm thick P3HT layer ( $E_g$  of P3HT is ca. 1.8 eV). Also, a thicker P3HT layer prevents the reflection of incident light from the Au back contact which would otherwise double the optical path and increase its chance of absorption in the  $Sb_2S_3$  layer [20, 21]. Such a concavity is missing in EQE spectra of solar cells using

thinner layers of V-series HTMs. The absorption edge can be detected at around 700 nm, that is in line with the calculated bandgap value of  $Sb_2S_3$  absorber ( $E_g = 1.75$  eV). The calculated bandgap of  $Sb_2S_3$  from the EQE curve with HTM V1235 is presented in SI, in Fig. S6.

Solar cells with no HTM, and with HTMs – P3HT, V1275, V1235, V1461, are fabricated to check for the reproducibility. The resulting box plots of solar cell performance parameters ( $V_{OC}$ ,  $J_{SC}$ , FF and PCE) are presented in Fig. 7. It can be seen that the  $J_{SC}$  values of the cells with new HTMs - V1275, V1235 and V1461 are higher, at around 15 mA/cm<sup>2</sup>, compared to the cells with P3HT showing  $J_{SC}$  values of around 11–12 mA/cm<sup>2</sup>. Higher current densities of solar cells with V-series HTMs are probably due to lower layer thicknesses and absence of parasitic absorption characteristic of P3HT. Nevertheless, the  $V_{OC}$  values of cells with new HTMs are lower (at around 570–580 mV) compared to the cells with P3HT presenting  $V_{OC}$  at around 620–630 mV. Higher  $V_{OC}$  values in P3HT-based devices may result from favorable chemical interactions between thiophene and Sb atoms at the  $Sb_2S_3$ /P3HT interface, enhancing carrier collection and suppressing charge recombination.

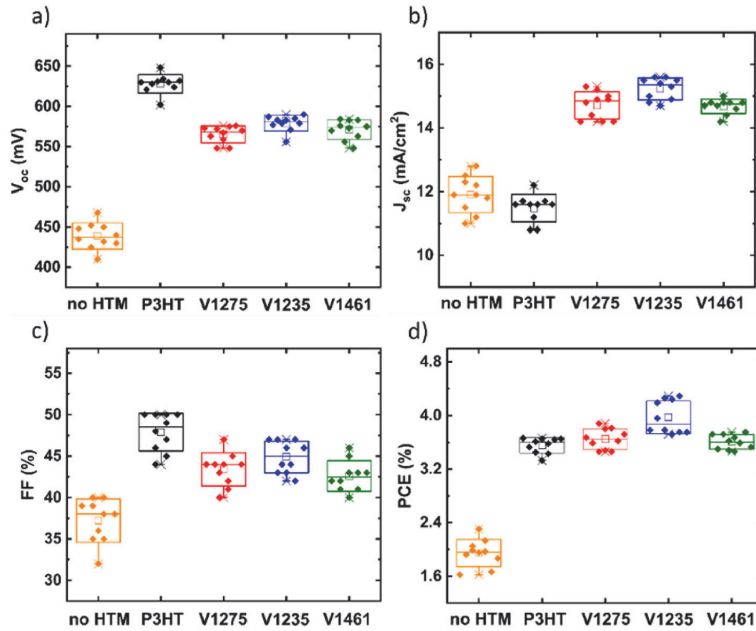


Fig. 7. Box-plot diagrams of performance parameters of the fabricated solar cell devices without any HTM and incorporating various HTMs (P3HT, V1275, V1235, and V1461).

Additionally, V-series HTMs with a 15–20 nm thickness may enable direct Au contact with the absorber at some points, unlike P3HT (ca. 100 nm). Intriguingly, lower  $V_{OC}$  values were observed in perovskite cells using V-series HTMs with larger layer thickness (120–150 nm) compared to Spiro-OMeTAD [49]. Thus, substituting traditional HTMs with V-series HTMs yields lower  $V_{OC}$  values in both perovskite and  $Sb_2S_3$  solar cells. The PCEs of solar cells using V1275 and V1235 as HTMs outperform the PCEs of P3HT based cells. It should be noted that the spread of all the device parameters ( $V_{OC}$ ,  $J_{SC}$ , FF and PCE) is reasonably small, demonstrating a good reproducibility of the fabricated solar cells. The long-term stability of unencapsulated solar cell devices with various HTMs was assessed, the aged solar cell efficiencies are compared to that of as-prepared devices (Table S2, in SI). It appears that devices with V1275 and V1235 show better stability compared to that with P3HT, but the device with V1461, which has the longest aliphatic chain in its structure, is the most unstable.

The measured transmittance spectra of the HTM layers (P3HT,

V1275, V1235, and V1461) deposited on a glass/FTO substrate are shown in Fig. 8a. Parasitic absorption can be seen in case of P3HT in range of 400–650 nm which is missing from the V-series HTMs. In order to gain a better understanding of the impact of investigated HTMs on the spectral response, the total transmission spectra measurements of the fabricated solar cell devices were performed as well and are provided in SI in Fig. S7. Values of average visible transmittance (AVT), are calculated in the 400–800 nm region, for all the fabricated solar cell devices (glass/FTO/ $Sb_2S_3$ /HTM/Au) and is presented in Fig. 8b.

While the devices with P3HT and the investigated HTMs, exhibit AVT values exceeding 20%, it is observed that devices with V-series HTMs have shown enhanced transparency, with approximately 20% higher AVT compared to devices with P3HT. Here, it is important to highlight that the thickness values of the HTM films compared herein for P3HT and V1275, V1235 and V1461 are ca. 100 and 25 nm, respectively. These thicknesses have been optimized for achieving the highest efficiency in  $Sb_2S_3$  based solar cells in each respective case. The

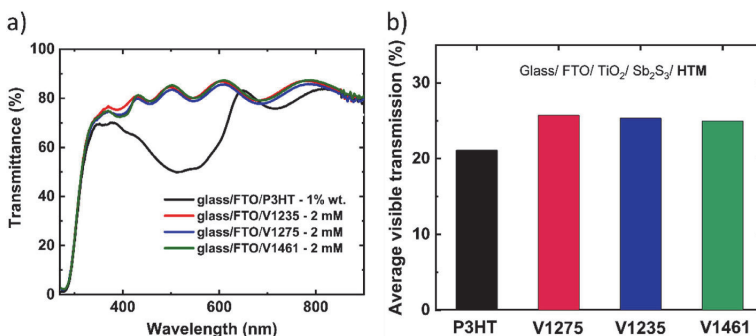


Fig. 8. a) Transmittance spectra of HTM layers (P3HT, V1275, V1235, and V1461) deposited on glass/FTO substrate, and b) calculated average visible transmittance values of solar cell devices in the range 400–800 nm incorporating different HTM layers (P3HT, V1275, V1235, and V1461).

observed improvement in transparency at the device level further validates the use of V-series HTMs in  $\text{Sb}_2\text{S}_3$  solar cells for semi-transparent applications.

#### 4. Conclusions

In our study, we have successfully demonstrated, for the first time, the utilization of cost-effective and transparent fluorene-based enamines - V1275, V1235 and V1461, as efficient hole transport layers in semi-transparent  $\text{Sb}_2\text{S}_3$  based solar cells. It was demonstrated that the new V-series HTMs can boost both, the PCE as well as the average visible transmittance of USP  $\text{Sb}_2\text{S}_3$  based devices, compared to traditional P3HT-based solar cells. While the solar cells with the conventional P3HT as HTM have yielded 3.8% efficiency and an AVT of 21%, the devices with optimized V1275, V1235, and V1461 HTM thicknesses yielded efficiencies of 3.9%, 4.3%, and 3.7%, respectively and an AVT of 25% in the spectral region 400–800 nm. The increase in the solar cell performance with new HTMs was mainly determined by substantial enhancement in the current densities of the cells. Energy level diagrams compiled using the ionization potential values measured for the cell component layers in the structure FTO/ $\text{TiO}_2$ / $\text{Sb}_2\text{S}_3$ /HTM/Au, reveal that the new HTMs show agreeable band offsets, validating them as efficient HTMs for  $\text{Sb}_2\text{S}_3$  solar cells. The improvement in the PCE of the cells was explained in correlation with the band alignment between HTM layer and  $\text{Sb}_2\text{S}_3$  absorber, the length of the HTM aliphatic chain and its resulting carrier mobility in HTM and the passivation effect at the HTM - absorber back interface. These results provide new knowledge on the development of semi-transparent  $\text{Sb}_2\text{S}_3$  based solar cells incorporating alternative HTMs, opening new opportunities to expand the application range of semi-transparent devices (such as solar windows) as well as offering broader possibilities to implement the developed processes in other emerging inorganic PV materials and device concepts.

#### CRedit authorship contribution statement

**Nimish Juneja:** Writing – original draft, Visualization, Validation, Methodology, Data curation, Conceptualization. **Sarune Daskeviciute-Geguziene:** Writing – review & editing, Validation, Methodology. **Nicolae Spalatu:** Writing – review & editing, Visualization, Supervision, Methodology, Formal analysis. **Sreekanth Mandati:** Writing – review & editing, Conceptualization. **Atanas Katerski:** Validation, Methodology. **Raitis Grzibovskis:** Writing – review & editing, Validation, Methodology. **Aivars Vembris:** Writing – review & editing, Methodology. **Smagul Karazhanov:** Writing – review & editing. **Vytautas Getautis:** Writing – review & editing, Validation, Methodology, Conceptualization. **Malle Krunks:** Writing – review & editing, Supervision, Methodology, Conceptualization. **Iлона Oja Acik:** Writing – review & editing, Project administration, Funding acquisition, Conceptualization.

#### Declaration of competing interest

The authors declare that they have no known competing financial interests or personal relationships that could have appeared to influence the work reported in this paper.

#### Data availability

Data will be made available on request.

#### Acknowledgments

The “Development of Semi-Transparent Bifacial Thin Film Solar Cells for Innovative Applications” benefits from a 999372 € grant from Iceland, Liechtenstein and Norway through the EEA Grants. The aim of the project is to develop new approach based on novel materials and

structures and production technologies, which are the key to further increase the share, and range of application of PV in areas with sub-average sunlight, including Baltic and Nordic countries. Therefore, development of resource saving, cost-effective and efficient PV devices is a primary challenge of this project. Project contract with the Research Council of Lithuania (LMTLT) No is S-BMT-21-1(LT08-2-LMT-K-01-003). Department of Materials and Environmental Technology, Tallinn University of Technology has received funding from the Estonian Research Council, projects PRG627 “Antimony chalcogenide thin films for next-generation semi-transparent solar cells applicable in electricity producing windows” and PSG689 “Bismuth Chalcogenide Thin-Film Disruptive Green Solar Technology for Next Generation Photovoltaics”. The research was partially funded by the Estonian Centre of Excellence project TK141 (TAR16016EK) “Advanced materials and high-technology devices for energy recuperation systems”, the European Union’s Horizon 2020 ERA Chair project 5GSOLAR (grant agreement No. 952509). Institute of Solid-State Physics, University of Latvia has received funding from the European Union’s Horizon 2020 Framework Programme H2020-WIDESPREAD-01-2016-2017-TeamingPhase2 under grant agreement No. 739508, project CAMART<sup>2</sup>. The article is also based upon work from COST Action “Research and International Networking on Emerging Inorganic Chalcogenides for Photovoltaics (RENEW-PV)”, CA21148, supported by COST (European Cooperation in Science and Technology). The authors thank Dr. Tadas Malinauskas and Dr. Valdek Mikli for their support in preparation and characterization of the samples.

#### Appendix A. Supplementary data

Supplementary data to this article can be found online at <https://doi.org/10.1016/j.mssp.2023.107934>.

#### References

- [1] T.D. Lee, A.U. Ebong, A review of thin film solar cell technologies and challenges, *Renew. Sustain. Energy Rev.* 70 (2017) 1286–1297, <https://doi.org/10.1016/j.rser.2016.12.028>.
- [2] J. Ramanujam, D.M. Bishop, T.K. Todorov, O. Gunawan, J. Rath, R. Nekovej, E. Artagiani, A. Romeo, Flexible CIGS, CdTe and a-Si:H based thin film solar cells: a review, *Prog. Mater. Sci.* 110 (2020), 100619, <https://doi.org/10.1016/j.pmatsci.2019.100619>.
- [3] N. Mufti, T. Amrillah, A. Taufiq, Aripriharta Sunaryono, M. Diantoro, Zulhadjri, H. Nur, Review of CIGS-based solar cells manufacturing by structural engineering, *Sol. Energy* 207 (2020) 1146–1157, <https://doi.org/10.1016/j.solener.2020.07.065>.
- [4] J. Ramanujam, U.P. Singh, Copper indium gallium selenide based solar cells – a review, *Energy Environ. Sci.* 10 (2017) 1306–1319, <https://doi.org/10.1039/C7EE00826K>.
- [5] L. El Chaar, L.A. lamont, N. El Zein, Review of photovoltaic technologies, *Renew. Sustain. Energy Rev.* 15 (2011) 2165–2175, <https://doi.org/10.1016/j.rser.2011.01.004>.
- [6] S. Philipps, F. Ise, W. Warmuth, P. Projects GmbH, Photovoltaics report, n.d., [www.ise.fraunhofer.de](http://www.ise.fraunhofer.de).
- [7] T.D.C. Hobson, H. Shiel, C.N. Savory, J.E.N. Swallow, L.A.H. Jones, T. J. Featherstone, M.J. Smiles, P.K. Thakur, T.-L. Lee, B. Das, C. Leighton, G. Zoppi, V.R. Dhanak, D.O. Scanlon, T.D. Veal, K. Durose, J.D. Major, P-type conductivity in Sn-doped  $\text{Sb}_2\text{Se}_3$ , *J. Phys.: Energy* 4 (2022), 045006, <https://doi.org/10.1088/2515-7655/ac91a6>.
- [8] R. Krautmann, N. Spalatu, R. Josepson, R. Nedzinskas, R. Kondrotas, R. Grzibovskis, A. Vembris, M. Krunks, I. Oja Acik, Low processing temperatures explored in  $\text{Sb}_2\text{S}_3$  solar cells by close-spaced sublimation and analysis of bulk and interface related defects, *Sol. Energy Mater. Sol. Cell.* 251 (2023), 112139, <https://doi.org/10.1016/j.solmat.2022.112139>.
- [9] M. Koltsov, R. Krautmann, A. Katerski, N. Maticiu, M. Krunks, I. Oja Acik, N. Spalatu, A post-deposition annealing approach for organic residue control in  $\text{TiO}_2$  and its impact on  $\text{Sb}_2\text{Se}_3/\text{TiO}_2$  device performance, *Faraday Discuss* 239 (2022) 273–286, <https://doi.org/10.1039/D2FD00064D>.
- [10] S. Barthwal, R. Kumar, S. Pathak, Present status and future perspective of antimony chalcogenide ( $\text{Sb}_2\text{X}_3$ ) photovoltaics, *ACS Appl. Energy Mater.* 5 (2022) 6545–6585, <https://doi.org/10.1021/acs.aem.2c00420>.
- [11] J.S. Eensalu, A. Katerski, E. Kärber, I. Oja Acik, A. Mere, M. Krunks, Uniform  $\text{Sb}_2\text{S}_3$  optical coatings by chemical spray method, *Beilstein J. Nanotechnol.* 10 (2019) 198–210, <https://doi.org/10.3762/bjnano.10.18>.
- [12] S. Wang, Y. Zhao, B. Che, C. Li, X. Chen, R. Tang, J. Gong, X. Wang, G. Chen, T. Chen, J. Li, X. Xiao, A novel multi-sulfur source collaborative chemical bath

- deposition technology enables 8%-efficiency  $\text{Sb}_2\text{S}_3$  planar solar cells, *Adv. Mater.* 34 (2022), 2206242, <https://doi.org/10.1002/adma.202206242>.
- [13] Y. Zhao, S. Wang, C. Jiang, C. Li, P. Xiao, R. Tang, J. Gong, G. Chen, T. Chen, J. Li, X. Xiao, Regulating energy band alignment via alkaline metal fluoride assisted solution post-treatment enabling  $\text{Sb}_2(\text{S,Se})_3$  solar cells with 10.7% efficiency, *Adv. Energy Mater.* 12 (2022), <https://doi.org/10.1002/aenm.202103015>.
- [14] Y. Zhao, S. Wang, C. Li, B. Che, X. Chen, H. Chen, R. Tang, X. Wang, G. Chen, T. Wang, J. Gong, T. Chen, X. Xiao, J. Li, Regulating deposition kinetics via a novel additive-assisted chemical bath deposition technology enables fabrication of 10.57%-efficiency  $\text{Sb}_2\text{Se}_3$  solar cells, *Energy Environ. Sci.* 15 (2022) 5118–5128, <https://doi.org/10.1039/D2EE02261C>.
- [15] C. Lan, J. Luo, H. Lan, B. Fan, H. Peng, J. Zhao, H. Sun, Z. Zheng, G. Liang, P. Fan, Enhanced charge extraction of Li-doped  $\text{TiO}_2$  for efficient thermal-evaporated  $\text{Sb}_2\text{S}_3$  thin film solar cells, *Materials* 11 (2018) 355, <https://doi.org/10.3390/ma11030355>.
- [16] P. Büttner, F. Scheler, C. Pointer, D. Döhler, M.K.S. Barr, A. Koroleva, D. Pankin, R. Hatada, S. Flege, A. Manshina, E.R. Young, I. Mínguez-Bacho, J. Bachmann, Adjusting interfacial chemistry and electronic properties of photovoltaics based on a highly pure  $\text{Sb}_2\text{S}_3$  absorber by atomic layer deposition, *ACS Appl. Energy Mater.* 2 (2019) 8747–8756, <https://doi.org/10.1021/acsaem.9b01721>.
- [17] J.S. Eensalu, A. Katerski, E. Kärber, L. Weinhardt, M. Blum, C. Heske, W. Yang, I. Oja Acik, M. Krunkas, Semitransparent  $\text{Sb}_2\text{S}_3$  thin film solar cells by ultrasonic spray pyrolysis for use in solar windows, *Beilstein J. Nanotechnol.* 10 (2019) 2396–2409, <https://doi.org/10.3762/bjnano.10.230>.
- [18] S. Wang, Y. Zhao, B. Che, C. Li, X. Chen, R. Tang, J. Gong, X. Wang, G. Chen, T. Chen, J. Li, X. Xiao, A novel multi-sulfur source collaborative chemical bath deposition technology enables 8%-efficiency  $\text{Sb}_2\text{S}_3$  planar solar cells, *Adv. Mater.* 34 (2022), 2206242, <https://doi.org/10.1002/adma.202206242>.
- [19] Y.C. Choi, D.U. Lee, J.H. Noh, E.K. Kim, S. Il Seok, Highly improved  $\text{Sb}_2\text{S}_3$  sensitized-inorganic-organic heterojunction solar cells and quantification of traps by deep-level transient spectroscopy, *Adv. Funct. Mater.* 24 (2014) 3587–3592, <https://doi.org/10.1002/adfm.201304238>.
- [20] N. Juneja, S. Mandati, A. Katerski, N. Spalatu, S. Daskeviciute-Geguziene, A. Vembris, S. Karazhanov, V. Getautis, M. Krunkas, I. Oja Acik,  $\text{Sb}_2\text{S}_3$  solar cells with a cost-effective and dopant-free fluorene-based enamine as a hole transport material, *Sustain. Energy Fuels* 6 (2022) 3220–3229, <https://doi.org/10.1039/D2SE00356B>.
- [21] S. Mandati, N. Juneja, A. Katerski, A. Jegorová, R. Grzibovskis, A. Vembris, T. Dedova, N. Spalatu, A. Magomedov, S. Karazhanov, V. Getautis, M. Krunkas, I. Oja Acik, 4.9% efficient  $\text{Sb}_2\text{S}_3$  solar cells from semitransparent absorbers with fluorene-based thiophene-terminated hole conductors, *ACS Appl. Energy Mater.* (2023), <https://doi.org/10.1021/acsaem.2c04097>.
- [22] E. Moustafa, J.G. Sánchez, L.F. Marsal, J. Pallarès, Stability enhancement of high-performance inverted polymer solar cells using  $\text{ZnO}$  electron interfacial layer deposited by intermittent spray pyrolysis approach, *ACS Appl. Energy Mater.* 4 (2021) 4099–4111, <https://doi.org/10.1021/acsaem.1c00455>.
- [23] J. Han, X. Pu, H. Zhou, Q. Cao, S. Wang, Z. He, B. Gao, T. Li, J. Zhao, X. Li, Synergistic effect through the introduction of inorganic zinc halides at the interface of  $\text{TiO}_2$  and  $\text{Sb}_2\text{S}_3$  for high-performance  $\text{Sb}_2\text{S}_3$  planar thin-film solar cells, *ACS Appl. Mater. Interfaces* 12 (2020) 44297–44306, <https://doi.org/10.1021/acsaem.1c011550>.
- [24] H.-J. Jo, S.H. Kim, J.S. Kim, S.-J. Lee, D.-H. Kim, Time-resolved photocurrent of an organic-inorganic hybrid solar cell based on  $\text{Sb}_2\text{S}_3$ , *J. Kor. Phys. Soc.* 69 (2016) 541–546, <https://doi.org/10.3938/jkps.69.541>.
- [25] J. Luo, W. Xiong, G. Liang, Y. Liu, H. Yang, Z. Zheng, X. Zhang, P. Fan, S. Chen, Fabrication of  $\text{Sb}_2\text{S}_3$  thin films by magnetron sputtering and post-sulfurization/selenization for substrate structured solar cells, *J. Alloys Compd.* 826 (2020), 154235, <https://doi.org/10.1016/j.jallcom.2020.154235>.
- [26] M.Y. Versavel, J.A. Haber, Structural and optical properties of amorphous and crystalline antimony sulfide thin-films, *Thin Solid Films* 515 (2007) 7171–7176, <https://doi.org/10.1016/j.tsf.2007.03.043>.
- [27] E. Gnenna, N. Khemiri, M. Kong, M. Isabel Alonso, M. Kanzari, Effect of vacuum annealing on the properties of one step thermally evaporated  $\text{Sb}_2\text{S}_3$  thin films for photovoltaic applications, *Eur. Phys. J. Appl. Phys.* 96 (2021), 20301, <https://doi.org/10.1051/epjap/2021210101>.
- [28] C.P. Liu, H.E. Wang, T.W. Ng, Z.H. Chen, W.F. Zhang, C. Yan, Y.B. Tang, I. Bello, L. Martinu, W.J. Zhang, S.K. Jha, Hybrid photovoltaic cells based on  $\text{ZnO}/\text{Sb}_2\text{S}_3/\text{P3HT}$  heterojunctions, *Phys. Status Solidi* 249 (2012) 627–633, <https://doi.org/10.1002/psbb.201147393>.
- [29] L. Guo, B. Zhang, S. Li, Q. Zhang, M. Buettner, L. Li, X. Qian, F. Yan, Scalable and efficient  $\text{Sb}_2\text{S}_3$  thin-film solar cells fabricated by close space sublimation, *Appl. Mater.* 7 (2019), 041105, <https://doi.org/10.1063/1.5090773>.
- [30] Y. Zeng, F. Liu, M. Green, X. Hao, Fabrication of  $\text{Sb}_2\text{S}_3$  planar thin film solar cells with closed-space sublimation method, in: 2018 IEEE 7th World Conference on Photovoltaic Energy Conversion (WCPEC) (A Joint Conference of 45th IEEE PVSC, 28th PVSEC & 34th EU PVSEC), IEEE, 2018, <https://doi.org/10.1109/PVSC.2018.8547305>, 0870–0872.
- [31] J. Han, S. Wang, J. Yang, S. Guo, Q. Cao, H. Tang, X. Pu, B. Gao, X. Li, Solution-Processed  $\text{Sb}_2\text{S}_3$  planar thin film solar cells with a conversion efficiency of 6.9% at an open circuit voltage of 0.7 V achieved via surface passivation by a  $\text{SbCl}_3$  interface layer, *ACS Appl. Mater. Interfaces* 12 (2020) 4970–4979, <https://doi.org/10.1021/acsaem.9b15148>.
- [32] P. Büttner, F. Scheler, C. Pointer, D. Döhler, T. Yokosawa, E. Spiecker, P.P. Boix, E. R. Young, I. Mínguez-Bacho, J. Bachmann,  $\text{ZnS}$  ultrathin interfacial layers for optimizing carrier management in  $\text{Sb}_2\text{S}_3$ -based photovoltaics, *ACS Appl. Mater. Interfaces* 13 (2021) 11861–11868, <https://doi.org/10.1021/acsaem.0c21365>.
- [33] S.-J. Lee, S.-J. Sung, K.-J. Yang, J.-K. Kang, J.Y. Kim, Y.S. Do, D.-H. Kim, Approach to transparent photovoltaics based on wide band gap  $\text{Sb}_2\text{S}_3$  absorber layers and optics-based device optimization, *ACS Appl. Energy Mater.* 3 (2020) 12644–12651, <https://doi.org/10.1021/acsaem.0c02552>.
- [34] E. Zimmermann, T. Pfadler, J. Kalb, J.A. Dorman, D. Sommer, G. Hahn, J. Weickert, L. Schmidt-Mende, Toward high-efficiency solution-processed planar heterojunction  $\text{Sb}_2\text{S}_3$  solar cells, *Adv. Sci.* 2 (2015), 1500059, <https://doi.org/10.1002/advs.201500059>.
- [35] H. Ning, H. Guo, J. Zhang, X. Wang, X. Jia, J. Qiu, N. Yuan, J. Ding, Enhancing the efficiency of  $\text{Sb}_2\text{S}_3$  solar cells using dual-functional potassium doping, *Sol. Energy Mater. Sol. Cells* 221 (2021), 110816, <https://doi.org/10.1016/j.solmat.2020.110816>.
- [36] D.-H. Kim, S.-J. Lee, M.S. Park, J.-K. Kang, J.H. Heo, S.H. Im, S.-J. Sung, Highly reproducible planar  $\text{Sb}_2\text{S}_3$ -sensitized solar cells based on atomic layer deposition, *Nanoscale* 6 (2014) 14549–14554, <https://doi.org/10.1039/C4NR04148H>.
- [37] J. Zhong, X. Zhang, Y. Zheng, M. Zheng, M. Wen, S. Wu, J. Gao, X. Gao, J.-M. Liu, H. Zhao, High efficiency solar cells as fabricated by  $\text{Sb}_2\text{S}_3$ -modified  $\text{TiO}_2$  nanofibrous networks, *ACS Appl. Mater. Interfaces* 5 (2013) 8345–8350, <https://doi.org/10.1021/am401273r>.
- [38] R. Nie, S. Il Seok, Efficient antimony-based solar cells by enhanced charge transfer, *Small Methods* 4 (2020), 1900698, <https://doi.org/10.1002/smdt.201900698>.
- [39] J.A. Chang, S.H. Im, Y.H. Lee, H. Kim, C.-S. Lim, J.H. Heo, S. Il Seok, Panchromatic photon-harvesting by hole-conducting materials in inorganic-organic heterojunction sensitized solar cell through the formation of nanostructured electron channels, *Nano Lett.* 12 (2012) 1863–1867, <https://doi.org/10.1021/nl204224v>.
- [40] X. Jin, Y. Yuan, C. Jiang, H. Ju, G. Jiang, W. Liu, C. Zhu, T. Chen, Solution processed NiOx hole-transporting material for all-inorganic planar heterojunction  $\text{Sb}_2\text{S}_3$  solar cells, *Sol. Energy Mater. Sol. Cells* 185 (2018) 542–548, <https://doi.org/10.1016/j.solmat.2018.06.017>.
- [41] Y. Itzhak, O. Niitsoo, M. Page, G. Hodes,  $\text{Sb}_2\text{S}_3$ -sensitized nanoporous  $\text{TiO}_2$  solar cells, *J. Phys. Chem. C* 113 (2009) 4254–4256, <https://doi.org/10.1021/jp900302b>.
- [42] J.A. Christians, P.V. Kamat, Trap and transfer. Two-step hole injection across the  $\text{Sb}_2\text{S}_3/\text{CuSCN}$  interface in solid-state solar cells, *ACS Nano* 7 (2013) 7967–7974, <https://doi.org/10.1021/nn403058f>.
- [43] L. Zhang, C. Jiang, C. Wu, H. Ju, G. Jiang, W. Liu, C. Zhu, T. Chen,  $\text{V}_2\text{O}_5$  as hole transporting material for efficient all inorganic  $\text{Sb}_2\text{S}_3$  solar cells, *ACS Appl. Mater. Interfaces* 10 (2018) 27098–27105, <https://doi.org/10.1021/acsaem.8b09843>.
- [44] T.P.I. Saragi, T. Spehr, A. Siebert, T. Fuhrmann-Lieker, J. Salbeck, Spiro compounds for organic optoelectronics, *Chem. Rev.* 107 (2007) 1011–1065, <https://doi.org/10.1021/cr0501341>.
- [45] J.P. Chen, H. Tanabe, X.-C. Li, T. Thoms, Y. Okamura, K. Ueno, Novel organic hole transport material with very high  $T_g$  for light-emitting diodes, *Synth. Met.* 132 (2003) 173–176, [https://doi.org/10.1016/S0379-6779\(02\)00203-5](https://doi.org/10.1016/S0379-6779(02)00203-5).
- [46] Y. Xiang, H. Guo, Z. Cai, C. Jiang, C. Zhu, Y. Wu, W.-H. Zhu, T. Chen, Dopant-free hole-transporting materials for stable  $\text{Sb}_2(\text{S,Se})_3$  solar cells, *Chem. Commun.* 58 (2022) 4787–4790, <https://doi.org/10.1039/D1CC007041J>.
- [47] M.L. Petrus, T. Bein, T.J. Dingemans, P. Docampo, A low cost azomethine-based hole transporting material for perovskite photovoltaics, *J. Mater. Chem. A Mater.* 3 (2015) 12159–12162, <https://doi.org/10.1039/C5TA03046C>.
- [48] F. Machui, M. Hösel, N. Li, G.D. Spyropoulos, T. Ameri, R.R. Sondergaard, M. Jørgensen, A. Scheel, D. Gaiser, K. Kreul, D. Lennsen, M. Legros, N. Lemaitre, M. Vilkmann, M. Välimäki, S. Nordman, C.J. Brabec, F.C. Krebs, Cost analysis of roll-to-roll fabricated ITO free single and tandem organic solar modules based on data from manufacture, *Energy Environ. Sci.* 7 (2014) 2792, <https://doi.org/10.1039/C4EE01222D>.
- [49] S. Daskeviciute, C. Mombona, K. Raktys, A.A. Sutanto, M. Daskeviciene, V. Jankauskas, A. Grudis, G. Bubiene, V. Getautis, M.K. Nazeeruddin, Fluorene-based enamines as low-cost and dopant-free hole transporting materials for high performance and stable perovskite solar cells, *J. Mater. Chem. A Mater.* 9 (2021) 301–309, <https://doi.org/10.1039/D0A08452B>.
- [50] F. Laquai, D. Andrienko, R. Mauer, P.W.M. Blom, Charge carrier transport and photogeneration in P3HT:PCBM photovoltaic blends, *Macromol. Rapid Commun.* 36 (2015) 1001–1025, <https://doi.org/10.1002/marc.201500047>.
- [51] J. Santos, J. Calbo, R. Sandoval-Torrientes, I. Garcia-Benito, H. Kanda, I. Zimmermann, J. Aragón, M.K. Nazeeruddin, E. Ortí, N. Martín, Hole-transporting materials for perovskite solar cells employing an anthradithiophene core, *ACS Appl. Mater. Interfaces* 13 (2021) 28214–28221, <https://doi.org/10.1021/acsaem.1c05890>.

#### **Publication IV**

**Nimish Juneja**, Aisté Jegorovė, Raitis Grzibovskis, Atanas Katerski, Maryte Daskeviciene, Tadas Malinauskas, Aivars Vembris, Smagul Karazhanov, Nicolae Spalatu, Vytautas Getautis, Malle Krunks and Ilona Oja Acik, “Dopant-free fluorene based dimers linked with thiophene units as prospective hole transport materials for  $\text{Sb}_2\text{S}_3$  solar cells”, *Sustainable Energy and Fuels*, 8, 4324–4334, 2024, doi: 10.1039/D4SE00472H.





Cite this: DOI: 10.1039/d4se00472h

## Dopant-free fluorene based dimers linked with thiophene units as prospective hole transport materials for $\text{Sb}_2\text{S}_3$ solar cells†

Nimish Juneja,<sup>a</sup> Aistė Jegorovė,<sup>b</sup> Raitis Grzibovskis,<sup>c</sup> Atanas Katerski,<sup>a</sup> Maryte Daskeviciene,<sup>b</sup> Tadas Malinauskas,<sup>b</sup> Aivars Vembris,<sup>c</sup> Smagul Karazhanov,<sup>d</sup> Nicolae Spalatu,<sup>a</sup> Vytautas Getautis,<sup>b</sup> Malle Krunks<sup>\*a</sup> and Ilona Oja Acik<sup>a</sup>

Novel dopant-free dimers comprising methoxydiphenylamine substituted fluorene derivatives and connected by central cores consisting of different numbers of thiophene moieties were synthesized and explored as hole transport materials (HTMs) in  $\text{Sb}_2\text{S}_3$  absorber solar cells. Energy level diagrams show agreeable band offsets validating the compatibility of novel HTMs for the FTO/ $\text{TiO}_2$ / $\text{Sb}_2\text{S}_3$ /HTM/Au solar cell with  $\text{TiO}_2$  and  $\text{Sb}_2\text{S}_3$  layers deposited by ultrasonic spray. X-ray photoelectron spectroscopy (XPS) study reveals the Sb 3d core level peak shift upon applying any of the HTMs on  $\text{Sb}_2\text{S}_3$  indicating an increased electron density surrounding Sb atoms which refers to the interaction of S from electron-rich thiophene units with Sb in the absorber at the  $\text{Sb}_2\text{S}_3$ /HTM interface. It is demonstrated that application of HTMs containing diphenylamine units in their side fragments increases the cell open circuit voltage from 478 mV to 673 mV, fill factor from 46% to 56% and conversion efficiency from 1.9% to 4.5% as compared to the device without any HTM and the observed improvement can be explained by the passivation of the interfacial states. In contrast, no enhancement in device performance has been observed when applying HTMs containing triphenylamine units although strong Sb–S interaction has been detected at the  $\text{Sb}_2\text{S}_3$ /HTM interface. Quantum chemical simulation results suggest that to achieve enhanced charge selectivity by the organic HTM layer, the HOMO of the HTMs should be formed by the thiophene groups. Possible phenomena occurring at the  $\text{Sb}_2\text{S}_3$ /HTM interface are discussed providing new insights towards understanding the charge transfer at the  $\text{Sb}_2\text{S}_3$ /HTM interface.

Received 8th April 2024  
Accepted 16th July 2024

DOI: 10.1039/d4se00472h  
rsc.li/sustainable-energy

## 1. Introduction

The need for resource saving energy applications in society requires accelerated development and design of materials and solar cell devices with a wide set of properties which would allow an extended application range beyond Si photovoltaics (PVs). At this scale, for a new PV technology, it is insufficient to be only competitive with the current established c-Si or CdTe thin film technologies regarding the performance and stability but it should also be environmentally friendly and comprise earth abundant chemical elements. An emerging family of

promising cost-efficient PV materials, such as antimony and bismuth-based chalcogenides<sup>1–3</sup> and lead-free chalcogenide perovskites<sup>4</sup> are currently under investigation in the PV community. Among these materials, antimony chalcogenides such as  $\text{Sb}_2\text{S}_3$ ,  $\text{Sb}_2\text{Se}_3$  and  $\text{Sb}_2(\text{S},\text{Se})_3$  showed a nascent track record of rapid performance development, reaching power conversion efficiencies (PCEs) of 8.0%, 10.57% and 10.75%, respectively.<sup>5–7</sup> These materials have garnered substantial R&D efforts within the PV community due to their compelling attributes such as their abundance in nature, environmentally benign elemental constituents, as well as commendable optoelectronic characteristics and stability.<sup>2,8,9</sup> In particular, the utility of  $\text{Sb}_2\text{S}_3$  absorbers makes them viable for employment in semi-transparent solar cells, owing to their band gap of 1.7 eV, and a high absorption coefficient ( $10^3 \text{ cm}^{-1}$  at 450 nm). These advantageous attributes make them particularly well-suited for integration within tandem cell device configurations and as solar windows.

In many solar cells, including antimony chalcogenide-based solar cells, a hole transporting layer (HTL) is utilized to extract and transport photogenerated charge carriers from the

<sup>a</sup>Department of Materials and Environmental Technology, Tallinn University of Technology, Ehitajate tee 5, Tallinn, 19086, Estonia. E-mail: malle.krunks@ttu.ee

<sup>b</sup>Department of Organic Chemistry, Kaunas University of Technology, Kaunas, LT-50254, Lithuania

<sup>c</sup>Institute of Solid State Physics, University of Latvia, Kengaraga Str. 8, Riga, LV-1063, Latvia

<sup>d</sup>Institute for Energy Technology (IFE), P.O. Box 40, Kjeller, NO 2027, Norway

† Electronic supplementary information (ESI) available. See DOI: <https://doi.org/10.1039/d4se00472h>



absorber layer to the electrode. The HTL also serves as a barrier layer for electron leakage and as a protective layer to screen the active layer from oxygen and moisture. The HTL can be made of inorganic and organic materials. An ideal material for the HTL should have an excess of holes, high hole mobility, good thermal stability, low density of defects, high solubility in a suitable solvent, simple synthesis process and appropriate band energy alignment with the absorber.<sup>10,11</sup> In general, organic hole transporting materials (HTMs) like poly(3-hexylthiophene) (P3HT)<sup>11–13</sup> and 2,2',7,7'-tetrakis[*N,N*-di(4-methoxyphenyl)amino]-9,9'-spirobifluorene (Spiro-OMeTAD)<sup>5,14,15</sup> or a combination of them<sup>16</sup> are the most commonly employed to fabricate efficient Sb chalcogenide solar cells, although Spiro-OMeTAD is the most efficient one to date delivering a PCE of around 10%.<sup>7,17,18</sup> However, both these HTMs possess serious drawbacks for large-scale applications. P3HT and Spiro-OMeTAD are expensive due to their complex and time-consuming synthesis processes.<sup>19</sup> In addition, P3HT exhibits parasitic absorption of light in the visible spectral region, leading to a decrease in the overall optical transmittance of the solar cell<sup>13,20–22</sup> while Spiro-OMeTAD exhibits low values of conductivity and hole mobility.<sup>23</sup> Common additives such as lithium bis(trifluoromethanesulfonyl)imide (LiTFSI) and 4-*tert*-butylpyridine (TBP) are used to improve the electrical properties of Spiro-OMeTAD films,<sup>24</sup> which, in turn, seriously worsen the stability of the devices. Therefore, the exploration and advancement of easily synthesizable and dopant-free HTMs is a challenging task.

It has been demonstrated that fluorene-based enamines synthesized by a facile condensation reaction are efficient dopant-free HTMs for high performance perovskite solar cells yielding a PCE of 17.1% that outperforms the device with undoped Spiro-OMeTAD exhibiting a PCE of 10.4%.<sup>25</sup> Fluorene-based enamines were recently explored as dopant-free HTMs in Sb<sub>2</sub>S<sub>3</sub> solar cells.<sup>20,21</sup> The devices with new transparent HTMs exhibited higher PCEs, up to 4.3% compared to 3.8% by the reference device with P3HT, and *ca.* 20% higher optical transparency.<sup>21</sup>

Novel transparent HTM molecules comprising 4,4'-dimethoxydiphenylamine-substituted fluorene fragments, widely used in organic HTMs, including Spiro-OMeTAD,<sup>26</sup> and thiophene units mimicking P3HT, were synthesized by a simple and high yield synthesis process.<sup>22</sup> Thiophene units were added into the molecule targeting application in antimony chalcogenide active layer solar cells, as the thiophene could interact with Sb atoms at the absorber/HTM interface and an improvement in interfacial properties is expected.<sup>27–29</sup> In our previous study, HTMs from fluorene-based molecules with terminated thiophene units proved their applicability in Sb<sub>2</sub>S<sub>3</sub> solar cells, the devices demonstrate PCEs of 4.7–4.9% and an average optical transparency in the visible spectral range of *ca.* 30%, outperforming the parameters of the P3HT-based device.<sup>22</sup>

In this study four new dopant-free HTMs (V1422, V1423, V1454 and V1455) were synthesized, characterized and explored in Sb<sub>2</sub>S<sub>3</sub> solar cells. The novelty of the study lies in development and optimization of new HTMs and their evaluation as prospective charge transport materials in Sb<sub>2</sub>S<sub>3</sub> thin film

devices. The synthesized molecules are dimers containing diphenylamine units (V1422 and V1423) and triphenylamine units (V1454 and V1455) in their side fragments. The common structural feature of all molecules is that the central core consists of different numbers of thiophene moieties. The properties of the novel HTMs are thoroughly studied; quantum chemical calculations are employed to analyze HTM molecular geometry and determine the Highest Occupied Molecular Orbital (HOMO) and Lowest Unoccupied Molecular Orbital (LUMO) positions. The suitability of the synthesized materials as HTMs in planar Sb<sub>2</sub>S<sub>3</sub>-based solar cells is examined. The solar cell stack comprises glass/FTO/TiO<sub>2</sub>/Sb<sub>2</sub>S<sub>3</sub>/HTM/Au, with TiO<sub>2</sub> and the absorber layer deposited through ultrasonic spray deposition and the HTM layer *via* spin coating. Various characterization methods applied to the materials, interfaces and devices provide insights on the functionality of this new family of dopant-free HTMs for Sb-chalcogenide-based solar cells.

## 2. Experimental

### 2.1. Materials

Chemicals required for the synthesis of the HTMs were purchased from Sigma-Aldrich and TCI Europe and used without any additional purification. Comprehensive information on the synthetic procedures of HTMs is detailed in the ESI.† For the fabrication of solar cells, the following substances were used as received: FTO substrate (10 Ω sq<sup>-1</sup>), titanium(IV) tetraisopropoxide (TTIP) from Acros Organics (99 wt%), acetylacetone from Acros Organics (99 wt%), ethanol from Estonian Spirit (96.6 vol%), methanol from Sigma-Aldrich (99.9 vol%), antimony trichloride from Sigma-Aldrich (99.99 wt%), thiourea from Sigma-Aldrich (99 wt%), chlorobenzene from Sigma-Aldrich (99.5 vol%), and poly(3-hexylthiophene-2,5-diyl) (P3HT) from Sigma-Aldrich (regio regular, >90%).

### 2.2. Methods

**2.2.1. Fabrication of the solar cell.** Solar cell devices are fabricated in superstrate configuration (glass/FTO/TiO<sub>2</sub>/Sb<sub>2</sub>S<sub>3</sub>/HTM/Au) using a similar experimental procedure to that outlined in our previous investigations.<sup>20–22</sup> A fluorine-doped tin oxide (FTO)-coated glass substrate with a sheet resistivity of 10 Ω sq<sup>-1</sup> is subjected to a cleaning process, with steps involving rinsing and boiling in deionized water, followed by drying with N<sub>2</sub>. TiO<sub>2</sub> is deposited using ultrasonic spray pyrolysis (USP) with substrate temperature maintained at 340 °C and then annealed (450 °C, 30 min) on a hot plate in air. Similarly, the absorber Sb<sub>2</sub>S<sub>3</sub> is deposited using USP (198 °C) and annealed (250 °C, 5 min) in a N<sub>2</sub> environment. The HTM powders were dissolved in chlorobenzene. The V-series HTM solutions in concentrations of 4, 2, 1 and 0.6 mM were spin-coated (3000 rpm, 30 s) on the absorber at room temperature. For P3HT, 1% wt concentration is utilized, followed by spin coating (3000 rpm, 30 s). The P3HT samples undergo an additional activation step at 170 °C for 5 minutes in a nitrogen environment after spin coating. Subsequently, a thermal evaporation process is employed to deposit



an 80–100 nm thick gold (Au) back contact using a shadow mask (contact area – 7.06 mm<sup>2</sup>).

**2.2.2. Characterization of synthesized HTMs and fabricated solar cells.** Chemical compositions of the synthesised HTMs were studied by NMR and MS spectroscopy. <sup>1</sup>H NMR and <sup>13</sup>C NMR spectra were collected at 400 and 101 MHz, respectively on a Bruker Avance III spectrometer. The chemical shifts, expressed in ppm, were relative to tetramethylsilane (TMS). All the experiments were performed at 25 °C. Reactions were monitored by thin-layer chromatography on ALUGRAM SIL G/UV254 plates and developed with UV light. Silica gel (grade 9385, 230–400 mesh, 60 Å, Aldrich) was used for column chromatography. Elemental analysis was performed with an Exeter Analytical CE-440 elemental analyser, Model 440 C/H/N. Thermogravimetric analysis (TGA) was performed on a Q50 thermogravimetric analyser (TA Instruments) at a scan rate of 10 °C min<sup>-1</sup> under a nitrogen atmosphere. The values are given for a weight-loss of 5% (*T*<sub>45</sub>). Differential scanning calorimetry (DSC) was performed on a TA Instruments Q2000 differential scanning calorimeter under a nitrogen atmosphere. The heating and cooling rate was 10 °C min<sup>-1</sup>. The UV-vis spectral analysis of the sample in solution (THF, 10<sup>-4</sup> mol L<sup>-1</sup>) was performed on a PerkinElmer Lambda 35 UV/VIS spectrophotometer. The layer thickness of the solution is *d* = 1 mm and the diffraction grating crack width is 2 nm.

The ionization potential (*I*<sub>p</sub>) values of all the functional layers were measured by the photoelectron yield spectroscopy (PYS) method. The optical band gap values (*E*<sub>g</sub>) of the absorber and HTM films were calculated from the absorption spectra using Tauc plots. Additionally, the work function of the Au metal contacts was measured through a Kelvin probe. The hole drift mobility of the HTMs was measured utilizing the time-of-flight (ToF) method. The X-ray diffraction (XRD) pattern of the glass/FTO/TiO<sub>2</sub>/Sb<sub>2</sub>S<sub>3</sub> stack was measured using a Rigaku Ultima-IV with a Cu K<sub>α</sub> source ( $\lambda = 1.5406 \text{ \AA}$ ) in the  $2\theta$  range of 10–80°. Micro-Raman spectra were measured at room temperature using a Horiba Labram HR 800 instrument. The He–Ne laser intensity was attenuated to 143 mW mm<sup>2</sup> with a focal area of  $\varnothing$  5 mm. Scanning electron microscopy (SEM) was used to measure the thickness of the absorber and HTM layers. The instrument used was a Zeiss HR FESEM Ultra 55 with an electron beam accelerating voltage of 4 kV.

X-ray photoelectron spectroscopy (XPS) was conducted on a Thermo Fisher ESCALAB Xi system with a monochromatic Al K<sub>α</sub> (1486.7 eV) X-ray source, and the studied area had a diameter of 650 μm. The total transmittance and total reflectance spectra of the two cell stacks – glass/HTM and glass/FTO/TiO<sub>2</sub>/Sb<sub>2</sub>S<sub>3</sub>/HTM were recorded on an ultraviolet-visible (UV-VIS) spectrophotometer in the range of 300–1100 nm. The Average Visible Transmittance (AVT) values for the glass/HTM and glass/FTO/TiO<sub>2</sub>/Sb<sub>2</sub>S<sub>3</sub>/HTM samples were calculated from the total transmittance spectra in the range of 400–800 nm. The current-voltage (*J*–*V*) characteristics were acquired from a Wavelabs LS-2 LED solar simulator under standard AM1.5G conditions at an irradiance of 100 mW cm<sup>-2</sup>. The measurements were performed at room temperature. The external quantum efficiency (EQE) spectra were measured using a Newport 69911 system.

Density Functional Theory (DFT) calculations were performed using B3LYP functional and the 6-31G(d,p) basis set. The highest occupied and lowest unoccupied molecular orbitals of the molecules were calculated for the optimized molecule geometry of the ground state. All calculations were carried out with the Gaussian 09W program and graphical representation was done using the Avogadro program.<sup>30</sup>

### 3. Results and discussion

The investigated HTMs can be classified into two distinct groups, as depicted in Fig. 1a: molecules featuring diphenylamine units in their side fragments (V1422 and V1423) and molecules containing triphenylamine units (V1454 and V1455). The common structural feature of both groups is that the central core consists of different numbers of thiophene moieties. The thermal stability of the HTMs was investigated with the help of thermogravimetric analysis (TGA) and differential scanning calorimetry (DSC). The data from TGA suggest that the HTMs decompose in the range of 430–445 °C (Fig. S1, in the ESI<sup>†</sup>), exceeding the temperature necessary for both the device preparation and operation.<sup>31</sup> Consequently, thiophene linked fluorene-based dimers with a higher molecular mass and therefore stronger intramolecular interaction possess higher decomposition temperatures compared to their monomeric analogues (391–403 °C).<sup>22</sup>

DSC measurements indicate that thiophene linked fluorene-based dimers are molecular glasses, exhibiting glass transition temperatures (*T*<sub>g</sub>) ranging from 148 °C to 175 °C (Fig. S2<sup>†</sup>), exceeding that of Spiro-OMeTAD (124 °C)<sup>26</sup> as well as of their monomeric analogues.<sup>22</sup> The thermal characteristics of the analysed HTMs are presented in Table 1. Comparing the *T*<sub>g</sub> of new HTMs has revealed that the inclusion of triphenylamine units in HTMs' side fragments (V1454 and V1455) results in an elevated *T*<sub>g</sub>. This increase could be attributed to the higher molecular mass associated with the additional triphenylamine units. It is noteworthy that V1455, with a central trithiophene-based unit and triphenylamine as side fragments, exhibits no endothermic peaks, suggesting an entirely amorphous state (Fig. S2<sup>†</sup>). This property is advantageous for the formation of homogeneous films, eliminating the potential for film crystallization during either device preparation or operation. The ultraviolet-visible (UV-Vis) absorption spectra of the HTMs (Fig. S3<sup>†</sup>) present two prominent absorption peaks at wavelengths of 300 and 375 nm, corresponding to the  $\pi$ – $\pi^*$  transitions of the side chromophores. Notably, the spectra exhibit an additional peak in the 425–550 nm range, which corresponds to  $\pi$ – $\pi^*$  transitions, and is attributed to the electron-rich thiophene  $\pi$  systems. Comparison of the absorption curves of molecules featuring diphenylamine units in their side fragments (V1422 and V1423) and molecules containing triphenylamine units (V1454 and V1455) has revealed that the latter show higher absorption. It can be assumed that this is due to the presence of an additional phenyl fragment in these compounds. Moreover, comparison of the absorption spectra presented in Fig. S3<sup>†</sup> with those reported for monomeric analogues in the previous study<sup>22</sup> revealed that the number and positions of



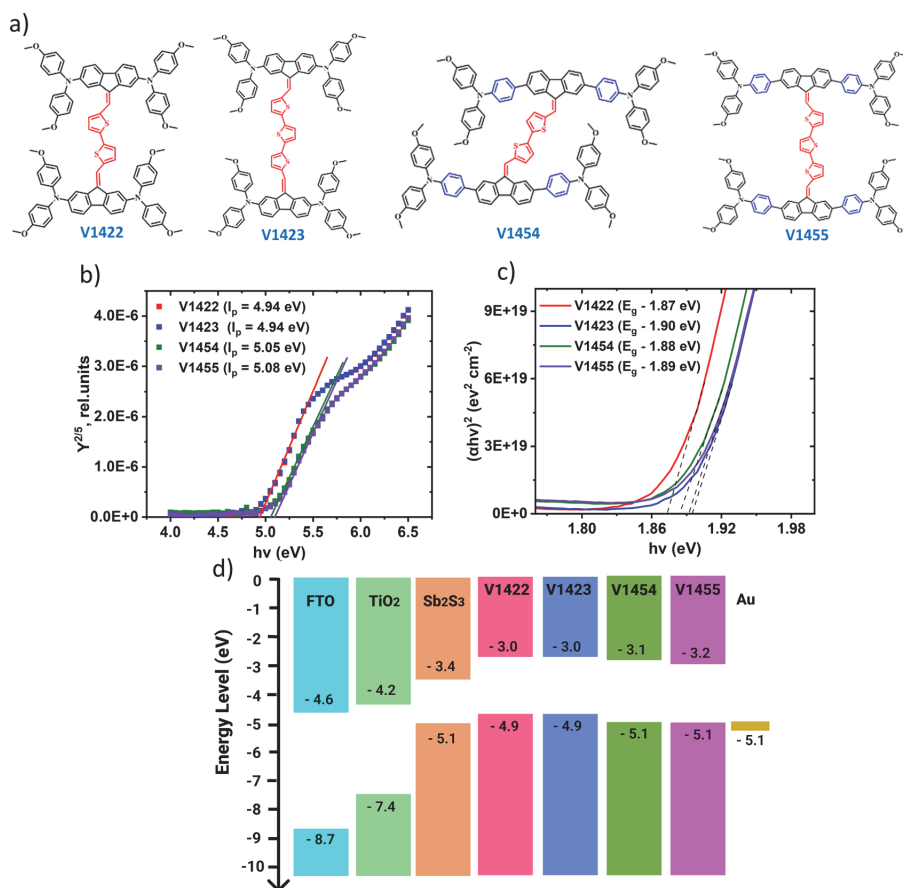


Fig. 1 (a) Chemical structures of synthesised HTMs – V1422, V1423, V1454 and V1455, (b) ionization potential ( $I_p$ ), and (c) band gap ( $E_g$ ) values calculated from the absorption spectra using Tauc plots for V1422, V1423, V1454 and V1455 thin films deposited on glass substrates, and (d) energy band diagram of constituent layers of the solar cell.

absorption peaks remain nearly unchanged, indicating that the conjugated system of the thiophene linked fluorene-based dimers is basically unaffected. As presented in Table 1, the inferred zero-field hole mobilities are  $9.86 \times 10^{-7}$ ,  $1.29 \times 10^{-6}$ ,  $3.38 \times 10^{-6}$ , and  $1.85 \times 10^{-6} \text{ cm}^2 \text{ V}^{-1} \text{ s}^{-1}$  for V1422, V1423, V1454, and V1455, respectively. Therefore, it can be concluded that the presence of the additional phenyl ring in the side diphenyl units of V1454 and V1455 slightly increased the hole drift mobility.

To understand the energy level alignment of the synthesized HTMs with that of  $\text{Sb}_2\text{S}_3$  and the metal back contact, a Photoelectron Yield Spectroscopy (PYS) technique was employed for measuring the ionization potential ( $I_p$ ) (see Fig. 1b). The HOMO levels of V1422, V1423, V1454 and V1455 are found to be at  $-4.94$ ,  $-4.94$ ,  $-5.05$  and  $-5.08$  eV relative to the vacuum level, respectively. Thus, HTMs bearing triphenylamine units (instead of diphenylamine units) exhibit slightly lower HOMO levels. The calculated band gap ( $E_g$ ) values for HTMs V1422, V1423,

Table 1 Properties of the synthesized HTMs – V1422, V1423, V1454 and V1455: glass transition temperature ( $T_g$ ), melting temperature ( $T_m$ ), 5% weight loss temperature ( $T_{d5}$ ), optical absorption peak position ( $\lambda_{\text{abs}}$ ), hole drift mobility ( $\mu_0$ ), band gap energy ( $E_g$ ) and ionization potential ( $I_p$ )

HTM	$T_g$ (°C)	$T_m$ (°C)	$T_{d5}$ (°C)	$\lambda_{\text{abs}}$ (nm)	$\mu_0$ ( $\text{cm}^2 \text{ V}^{-1} \text{ s}^{-1}$ )	$E_g$ (eV)	$I_p$ (eV)
V1422	148	276	430	293, 383, 468	$9.86 \times 10^{-7}$	1.87	4.94
V1423	153	—	435	300, 383, 479	$1.29 \times 10^{-6}$	1.90	4.94
V1454	175	307	445	285, 377, 467	$3.38 \times 10^{-6}$	1.88	5.05
V1455	172	—	444	286, 377, 480	$1.85 \times 10^{-6}$	1.89	5.08



V1454 and V1455 thin films are 1.87, 1.90, 1.88 and 1.89 eV, respectively (see Fig. 1c). The energy band diagram is presented in Fig. 1d and reveals agreeable band offsets conducive to the photogenerated carrier transport from the absorber to the metal back contact.

The  $\text{Sb}_2\text{S}_3$  absorber layer was characterized using XRD and Raman spectroscopy. Data are presented in Fig. S4, in the ESI.† The XRD results confirmed the presence of a single phase of orthorhombic  $\text{Sb}_2\text{S}_3$  (ICDD PDF 01-075-4013) without any secondary phase.<sup>9,13,20,22</sup> The Raman spectrum shows sharp peaks at 128, 155, 188, 236, 280, 302, and 312  $\text{cm}^{-1}$ , which are characteristic of the crystalline  $\text{Sb}_2\text{S}_3$  layer.<sup>9,13,20,22</sup> The band gap of the  $\text{Sb}_2\text{S}_3$  film was 1.78 eV, as calculated from the absorption spectra using the Tauc plot (Fig. S4†), which is in line with the values previously reported for sprayed  $\text{Sb}_2\text{S}_3$  films.<sup>9,13,20,21</sup> The SEM cross-sectional images of solar cells with two HTMs, V1423 and V1454, both deposited from 2 mM solutions, are presented in Fig. S5, in the ESI.† The thickness of the  $\text{Sb}_2\text{S}_3$  absorber layer was approximately 80 nm.

To study a possible chemical interaction at the  $\text{Sb}_2\text{S}_3$ /HTM interface, XPS studies were performed for HTMs on a glass substrate and  $\text{Sb}_2\text{S}_3$  solar cell stacks without and with an HTM. The XPS spectra of  $\text{Sb}_2\text{S}_3$ /HTM (V1422, V1423, V1454 and V1455) samples in the Sb 3d region and S 2p region are shown in the ESI, in Fig. S6 and S7,† respectively. The Sb 3d spectra for  $\text{Sb}_2\text{S}_3$  films and  $\text{Sb}_2\text{S}_3$  covered with a thin layer of V1423 and V1454, are shown in Fig. 2a and b, respectively. The binding energies (BEs) of Sb 3d core level peaks in the  $\text{Sb}_2\text{S}_3$  sample are located at 539.7 eV for Sb 3d<sub>3/2</sub> and 530.3 eV for Sb 3d<sub>5/2</sub>. For the samples

of  $\text{Sb}_2\text{S}_3$  with V1423, the BE peak positions are shifted to lower energy values, to 539.2 eV for Sb 3d<sub>3/2</sub> and to 529.9 eV for Sb 3d<sub>5/2</sub>.

A similar shift in Sb 3d core level peak positions to lower BE values is also observed for the sample with V1454 as the HTM (Fig. 2b). The noted shift towards lower binding energy values, in comparison to pristine  $\text{Sb}_2\text{S}_3$ , indicates an increased electron density around the Sb atoms in the absorber. A similar shift in the Sb 3d core level peak was observed when a dithieno[3,2-*b*:20,30-*d'*]pyrrole-cored small molecule (DTPThMe-ThTPA)<sup>32</sup> and thiophene-modified quinoxaline core small molecules<sup>27</sup> were applied onto the  $\text{Sb}_2(\text{S,Se})_3$  film.

S 2p core level spectra for  $\text{Sb}_2\text{S}_3$  films, HTMs (V1423, V1454) and  $\text{Sb}_2\text{S}_3$ /HTM samples are shown in Fig. 2c and d. S 2p<sub>3/2</sub> peaks for  $\text{Sb}_2\text{S}_3$  and  $\text{Sb}_2\text{S}_3$ /V1423 samples are positioned at BEs of 162.0 and 161.5 eV, respectively (see Fig. 2c). A similar shift of the S 2p<sub>3/2</sub> peak towards the lower BE region is observed when V1454 is applied onto  $\text{Sb}_2\text{S}_3$  (Fig. 2d). V1454 deposited onto a glass substrate shows the S 2p<sub>3/2</sub> peak at 162.4 eV, but after deposition of V1454 onto  $\text{Sb}_2\text{S}_3$ , the S 2p peak of V1454 shifted to a higher energy region and peaked at a BE of 164.2 eV (see Fig. 2d and Fig. S7 in the ESI†).

A similar shift of the S 2p peak of thiophene-modified quinoxaline core small molecules to higher energies has been detected when applied to the  $\text{Sb}_2(\text{S,Se})_3$  layer.<sup>27</sup> Interestingly, we did not detect S 2p peaks characteristic of V1423 in the spectrum of the  $\text{Sb}_2\text{S}_3$ /V1423 stack (Fig. 2c), although the shifts in the positions of S 2p peak and Sb 3d peak of the  $\text{Sb}_2\text{S}_3$  were clearly detected upon application of V1423 onto  $\text{Sb}_2\text{S}_3$ . The

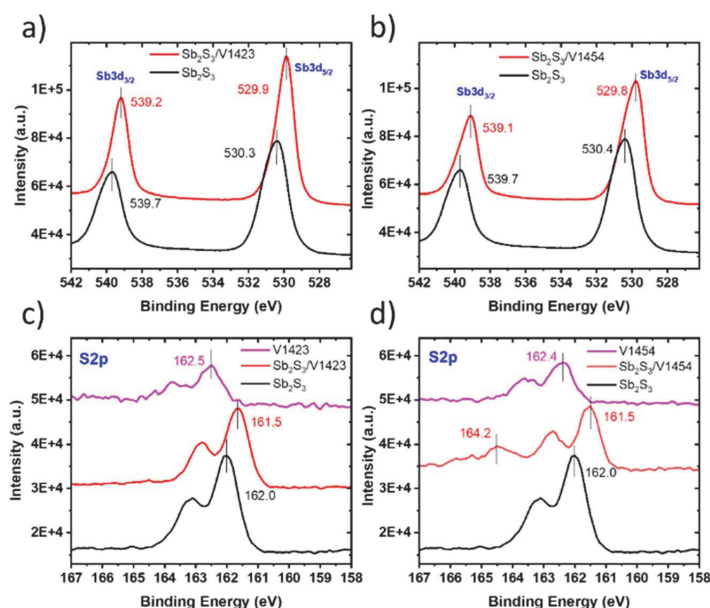


Fig. 2 XPS core level spectra (a) Sb 3d for  $\text{Sb}_2\text{S}_3$  and  $\text{Sb}_2\text{S}_3$ /V1423, (b) Sb 3d for  $\text{Sb}_2\text{S}_3$  and  $\text{Sb}_2\text{S}_3$ /V1454, (c) S 2p for  $\text{Sb}_2\text{S}_3$ , V1423 and  $\text{Sb}_2\text{S}_3$ /V1423, and (d) S 2p for  $\text{Sb}_2\text{S}_3$ , V1454 and  $\text{Sb}_2\text{S}_3$ /V1454.



shifts observed in Sb 3d and S 2p peak positions of  $\text{Sb}_2\text{S}_3$  as well as in S 2p peak positions of HTMS refer to the interaction between S atoms from electron-rich thiophene units and Sb atoms from the Sb-chalcogenide compound which is expected to improve the interfacial carrier extraction ability.

Solar cells based on  $\text{Sb}_2\text{S}_3$  were prepared in the superstrate configuration glass/FTO/ $\text{TiO}_2$ / $\text{Sb}_2\text{S}_3$ /HTM/Au (see the sketch in Fig. 3a and SEM images in Fig. S5, in the ESI†). The systematic change in the concentration of V-series HTM solutions (4, 2, 1, 0.6 mM) was studied. The resulting output parameters are presented in Table S1, in the ESI.† Solar cells fabricated with 2 mM solutions showed the highest performance, independent of the HTM used. The current–voltage ( $J$ - $V$ ) characteristics of the best performing devices using 2 mM HTM solutions are presented in Fig. 3b, and the cell output parameters are summarized in Table 2. The reference device, lacking an HTM, yielded a  $V_{\text{OC}}$  of 478 mV,  $J_{\text{SC}}$  of  $8.7 \text{ mA cm}^{-2}$ , FF of 0.46, and a PCE of 1.9%. Introduction of V1422 and V1423 as HTMs resulted in open circuit voltages of 656 and 673 mV, respectively. On application of HTMs, also other solar cell parameters improved

as compared to the cells without an HTM. In the case of the cell with V1423,  $J_{\text{SC}}$  improved from 9.0 to  $12.1 \text{ mA cm}^{-2}$ , FF from 0.46 to 0.56 and PCE from 1.9 to 4.5%. Therefore, the utilization of HTMs – V1422 and V1423 substantially mitigates carrier recombination at the back interface, leading to improved carrier collection. Notably, the device with the HTM – V1423 yielded device output characteristics comparable to those employing P3HT. In contrast, solar cell devices with V1454 and V1455, having triphenylamine side fragments, yielded  $V_{\text{OC}}$  values of 439 and 437 mV, respectively. As compared to the solar cell without any HTM, there was no improvement in  $V_{\text{OC}}$  values. In addition, an increase in series resistance ( $R_s$ ) values and a decrease in  $J_{\text{SC}}$ , FF and overall PCE was recorded (Fig. 3b and Table 2). High  $R_s$  values up to *ca.*  $5 \Omega \text{ cm}^2$  in solar cells could result from an excessively thick layer. For the purpose of reducing the HTM layer thickness, solar cells were fabricated with diluted HTM solutions. The concentration of HTM solutions was decreased from 2 mM to 0.6 mM. However, no notable improvement in solar cell parameters was observed, as detailed in the ESI, Table S1.† The external quantum efficiency (EQE)

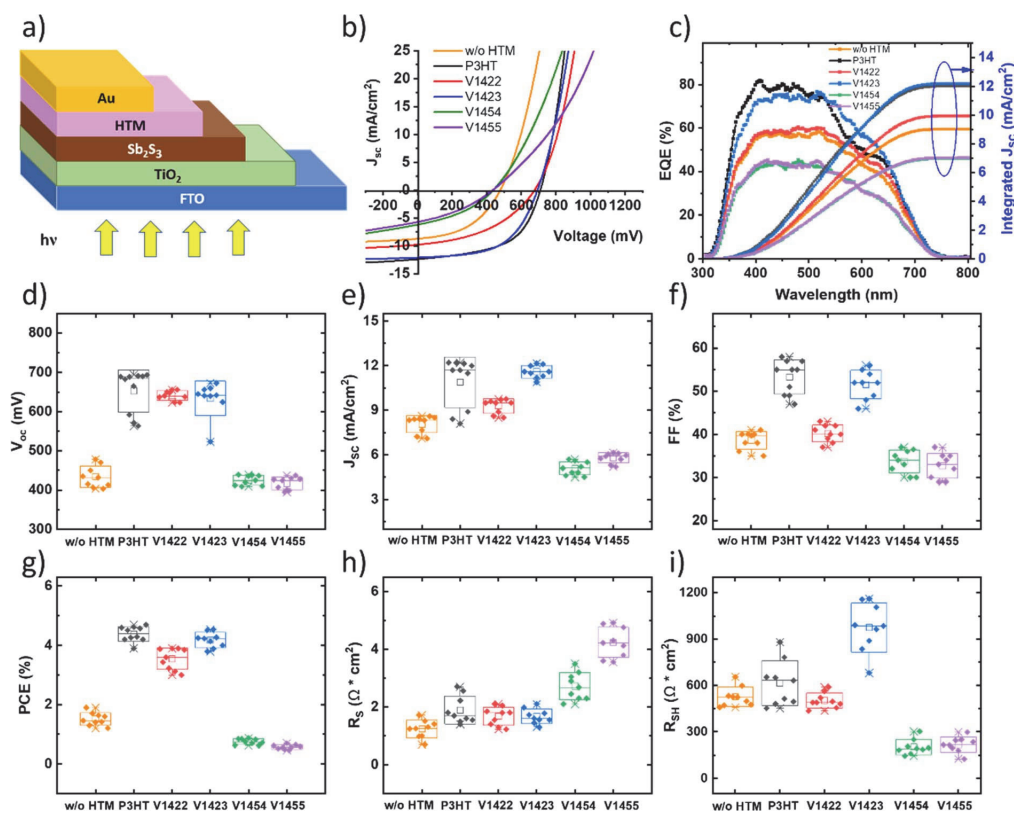


Fig. 3 (a) Schematic of the  $\text{Sb}_2\text{S}_3$  absorber solar cell (glass/FTO/ $\text{TiO}_2$ / $\text{Sb}_2\text{S}_3$ /HTM/Au) fabricated in the superstrate configuration, (b)  $J$ - $V$  characteristics, (c) external quantum efficiency (EQE) curves with the calculated integrated  $J_{\text{SC}}$  curves of the champion solar cells without (w/o) the HTM and with different HTMs (P3HT, V1422, V1423, V1454 and V1455). Box plots of  $\text{Sb}_2\text{S}_3$  solar cells without any HTM ( $\text{Sb}_2\text{S}_3$ /Au) and with P3HT, V1422, V1423, V1454 and V1455 as HTMs: (d)  $V_{\text{OC}}$ , (e)  $J_{\text{SC}}$ , (f) fill factor (FF), (g) PCE, (h) series resistance ( $R_s$ ), and (i) shunt resistance ( $R_{\text{SH}}$ ).



Table 2 Key performance metrics of champion  $\text{Sb}_2\text{S}_3$  solar cells without (w/o) any HTM and with HTMs (V1422, V1423, V1454, V1455 and P3HT)

HTM	HTM conc. ( $\text{mg mL}^{-1}$ )	$V_{\text{OC}}$ (mV)	$J_{\text{SC}}$ ( $\text{mA cm}^{-2}$ )	Integrated $J_{\text{SC}}$ ( $\text{mA cm}^{-2}$ )	FF (%)	PCE (%)	$R_{\text{S}}$ ( $\Omega \text{ cm}^2$ )	$R_{\text{SH}}$ ( $\Omega \text{ cm}^2$ )
w/o	—	478	8.7	9.0	46	1.9	1.1	514
V1422	2 mM	656	9.7	9.9	43	3.9	1.7	436
V1423	2 mM	673	12.1	12.0	56	4.5	1.3	1005
V1454	2 mM	439	5.7	6.8	35	0.8	2.7	192
V1455	2 mM	437	6.1	7.1	33	0.7	4.9	198
P3HT	1 wt%	689	12.2	12.2	55	4.7	1.8	526

graphs of the champion devices without any HTM and with different HTM layers are presented in Fig. 3c. It should be noted that the integrated  $J_{\text{SC}}$ , calculated based on EQE spectra, closely correspond to the values obtained from the  $J$ - $V$  curves (see Table 2). A dip in the spectral response in the case of the device with P3HT can be seen in the range of 550–650 nm, which is attributed to its parasitic absorption losses.<sup>20,22</sup> Normalized EQE curves of the devices with investigated HTMs are presented in the ESI, in Fig. S9.† The concavity in the EQE curve is less pronounced in the case of samples with V-series HTMs. All investigated HTMs have a similar band gap, within the range of 1.8–1.9 eV. However, the V-series HTM layers were considerably thinner, approximately 20–25 nm, in contrast to P3HT, with a thickness of about 80–100 nm. Thus, devices with V-series HTMs show an average visible transmittance (AVT) of 24–26% compared to 21% by the P3HT-based device (see Fig. S10 in the ESI†). A statistical representation (*i.e.*, box plots) of solar cell parameters of the fabricated cells without any HTM and with investigated HTMs (Fig. 3d–i) refers to high reproducibility of the results.

Although the interaction between the S atom from the thiophene unit and Sb from  $\text{Sb}_2\text{S}_3$  has been noted in all interfaces with V-series HTMs, only the use of V1422 and V1423 as HTMs led to an increase in the open-circuit voltage ( $V_{\text{OC}}$ ) of up to 650–670 mV. Furthermore, only the application of V1423 in the solar cell structure resulted in fill factor values of up to 56%, leading to conversion efficiencies exceeding 4% (see box-plot, in Fig. 3), which is very close to that obtained using P3HT as the HTM. Our results show that V1423, a dimer molecule with three thiophene units in its structure is the most efficient one in this family of novel HTMs. The application of V1454 and V1455 as HTM layers did not reduce the interface recombination or improve the carrier collection.  $V_{\text{OC}}$  remains on the level of 400 mV comparable to the cells without the HTM, fill factor values are low and vary in the region 30–35%. The current density is *ca.* two times lower as compared to the cell with V1423 and the solar cell exhibits a high  $R_{\text{S}}$  value of *ca.* 5  $\Omega \text{ cm}^2$  (Fig. 3d–i). Consequently, the solar cell conversion efficiencies are below 1%, that is two times lower than that recorded for the cells without any HTM.

As stated above, the interaction of S from the thiophene unit with Sb from  $\text{Sb}_2\text{S}_3$  at the absorber surface may explain the improvement of the  $V_{\text{OC}}$  and overall solar cell parameters *via* passivation of the interfacial states. Although such a mechanism is validated by the enhanced  $V_{\text{OC}}$  in V1422 and V1423-

based devices, the abrupt decrease in the  $V_{\text{OC}}$  and overall performance of V1454 and V1455-based cells indicate that there might be another concomitant phenomenon which prevails or compensates the benefit of thiophene-based interactions. A possible explanation for the low  $V_{\text{OC}}$  and PCE of V1454 and V1455-based cells, can be linked to the dipole effects at the absorber/HTM interface. As demonstrated in organic solar cells, insertion of organic materials between the photoactive absorber layer and electrodes can be an efficient approach for manipulation of the electric potential distribution by dipole moments at the electrode surface.<sup>33–35</sup> Several experimental and numerical simulation studies reported that the dipoles at the back/front interfaces have to be aligned in such a way that it allows accumulation of high hole concentration at the vicinity of hole contact and high electron density at the vicinity of electron contact.<sup>33,36</sup> The efficiency of photogenerated charge carrier separation (and thus, improved charge selectivity) is influenced by the specific arrangement of the molecules and the orientation of the permanent dipole moment. Thus, in some cases, depending on the angular configuration and molecular arrangement, the organic molecules can act as hole or electron selective layers. For example, Kippelen *et al.*, demonstrated that the HTM – PEDOT:PSS can be easily altered to a well-functionalized electron transport layer by complexation with poly-ethylenimine ethoxylated (PEIE) molecules.<sup>37</sup>

Considering these approaches, it can be assumed that in V1454 and V1455 based solar cell devices, the additional phenyl fragment in the HTMs reconfigured the angular and molecular arrangement resulting in unsuitable alignment in the orientation of the dipoles at the back interface. As a consequence, this imposes an increase of an “incorrect” type of charge carrier concentration in the vicinity of the metal back contact (*i.e.*, electron proximity of the Hall contact), decreasing the  $V_{\text{OC}}$  and deteriorating the overall device performance. Validation of this hypothesis can be assured by in-depth analysis of the changes in the work function of the contact electrode in proximity of the HTM. This approach would imply complex correlative measurements of Kelvin-probe AFM and UPS combined with numerical simulations which has been applied in organic solar cells<sup>33</sup> and remains a great challenge for the emerging  $\text{Sb}_2\text{S}_3/\text{HTM}$  interface.

The anomalous low performance of V1454 and V1455-based cells can be approached from a different angle – by analysing the molecular geometry and orbitals and correspondingly, the positions of the Highest Occupied Molecular Orbital (HOMO)



and Lowest Unoccupied Molecular Orbital (LUMO) of V1422 (a representative of molecules with diphenylamine units in their structures) and V1454 (a representative of molecules with triphenylamine units in their structures) from quantum chemical simulation. Fig. 4 presents the optimized geometry of HTM compound molecules of V1422 and V1454, and their HOMO and LUMO.

The result of the simulation shows that HOMO levels of both V1454 and V1422 are formed by fluorene and benzene rings, while LUMO is primarily located on the thiophene groups. In addition to this HOMO–LUMO configuration, compared to V1422 (having a nonplanar orientation of fluorene in relation to the thiophene groups), V1454 exhibits more planar

arrangement of fluorene groups relative to the thiophene groups. The latter effect allows a greater accessibility of the thiophene moieties in V1454 and consequently, a stronger interaction between S atoms in the thiophene group and Sb from  $\text{Sb}_2\text{S}_3$ . This strong interaction is highlighted by the observed shift of the V1454 S  $2p_{3/2}$  peak towards the higher BE region when applied onto  $\text{Sb}_2\text{S}_3$  (Fig. 2d, XPS analysis). However, this strong interaction does not result in an improved charge carrier transport through the interface since the HOMO level is not located on thiophene moieties and thus the condition for the accumulation of the “right” type of charge carrier (*i.e.*, holes) at the back interface is not satisfied. Thus, the quantum chemical simulation results suggest that to achieve

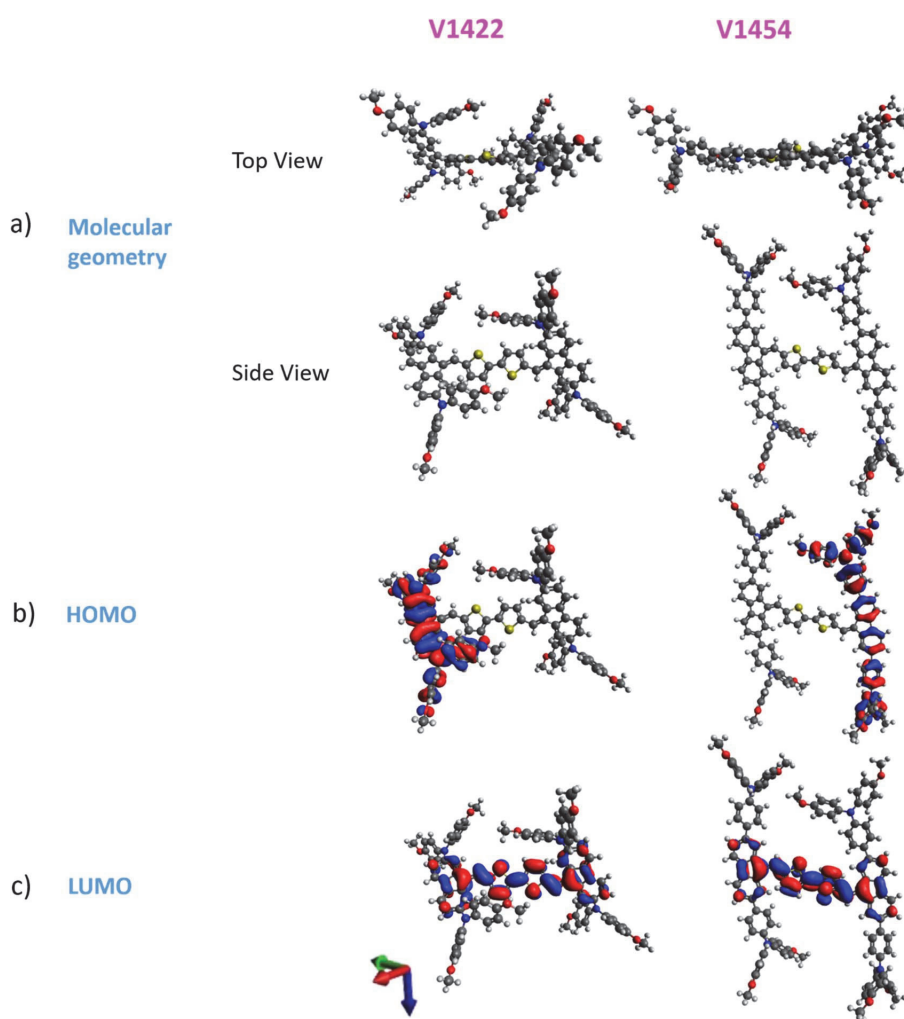


Fig. 4 (a) Optimized geometry of HTM molecules – V1422 and V1454 in top and side views, (b) highest occupied molecular orbital (HOMO) in HTMs – V1422 (left) and V1454 (right), (c) lowest unoccupied molecular orbital (LUMO) in HTMs – V1422 (left) and V1454 (right). Colors used for atoms: gray – C, white – H, yellow – S, red – O and blue – N.



higher efficiency of photogenerated charge carrier separation and improved charge selectivity by an organic HTM layer, the HOMO of the HTMs should be formed by the thiophene groups. Although this hypothesis may interfere with other requirements for the alignment of the electronic states at the organic/inorganic interfaces, these results lay a solid foundation for further investigations and understanding the charge transfer kinetics at the  $\text{Sb}_2\text{S}_3/\text{HTM}$  interface.

## 4. Conclusion

Four dopant-free dimers (V1422, V1423, V1454, V1455) comprising methoxydiphenylamine substituted fluorene derivatives and connected by central cores consisting of different numbers of thiophene moieties were synthesized by a solution chemical route. Synthesized organic semiconductors are molecular glasses, exhibiting glass transition and thermal decomposition temperatures of 148–175 °C and 430–445 °C, respectively and having an energy band gap of 1.9 eV and ionization potential of 4.9–5.1 eV. Synthesized organic semiconductors were explored, for the first time, as HTMs in superstrate configuration FTO/ $\text{TiO}_2/\text{Sb}_2\text{S}_3/\text{HTM}/\text{Au}$  solar cells in which the  $\text{Sb}_2\text{S}_3$  absorber and  $\text{TiO}_2$  layers were deposited by the ultrasonic spray method while HTM layers were obtained by spin-coating. Energy level diagrams demonstrate agreeable band offsets validating the applicability of the synthesized materials as efficient HTMs in an FTO/ $\text{TiO}_2/\text{Sb}_2\text{S}_3/\text{HTM}/\text{Au}$  device. It has been shown that application of the HTM layer on top of the  $\text{Sb}_2\text{S}_3$  layer induces a shift in the Sb 3d core level peak to lower binding energies, indicating increased electron density surrounding the Sb atoms. Such a shift confirms the interaction between S atoms from thiophene units and Sb atoms from the absorber occurring at the  $\text{Sb}_2\text{S}_3/\text{HTM}$  interface. By introducing HTMs comprising diphenylamine units in their structures (V1422, V1423) into the solar cell structure, an increase in the device output characteristics compared to the device without an HTM layer was observed. The highest boost in device performance was observed for V1423-based cells, exhibiting an increase of the  $V_{\text{OC}}$  from 478 mV to 673 mV, fill factor from 46% to 56%, and PCE from 1.9% to 4.5%.

Thus, it can be concluded that this type of HTM effectively mitigates carrier recombination at the back interface, and contributes to better collection of carriers. The application of V1454 and V1455 (molecules with triphenylamine units in their structures) as HTM layers did not improve the device parameters as the  $V_{\text{OC}}$  remained on the level of 430 mV (comparable to the cells without HTMs) while the fill factor values reached the lowest level of 30–35%. For the same cells, the  $J_{\text{SC}}$  values were two times lower compared to the cells with V1423 and the PCEs of solar cells were below 1% – two times lower than those recorded for the cells without any HTM. The abrupt decrease in the  $V_{\text{OC}}, J_{\text{SC}}$  and overall performance of V1454 and V1455-based cells indicates the presence of a concomitant phenomenon which prevails or compensates the benefit of thiophene-based interactions. Possible phenomena occurring at the  $\text{Sb}_2\text{S}_3/\text{HTM}$  interface were discussed through the prism of correlation between the efficiency of the charge transfer/charger selectivity

and final device performance, including possible impacts of the dipole effect as well as a prospective analysis from the quantum chemical simulation side. The results of quantum chemical simulation suggest that to achieve higher efficiency of photogenerated charge carrier separation and improved charge selectivity by the organic HTM layer, the HOMO of the HTMs should be configured by the thiophene groups. So far, the results of this study provide new perspectives on the chemical and physical understanding of  $\text{Sb}_2\text{S}_3/\text{HTM}$  organic/inorganic interfaces towards the identification of suitable innovative HTMs which would allow a significant boost in the efficiency of the emerging Sb-chalcogenide thin film PV technology.

## Data availability

The data that support the findings of this study will be made available by the corresponding author upon request.

## Author contributions

Nimish Juneja – conceptualization, methodology, validation, data curation, writing – original draft. Aistė Jegorovė – conceptualization, methodology, validation, writing – review & editing. Raitis Grzibovskis – methodology, validation, writing – review & editing. Atanas Katerski – methodology, validation. Maryte Daskeviciene – writing – review & editing. Tadas Malinauskas – writing – review & editing. Aivars Vembris – conceptualization, methodology, validation, writing – review & editing. Smagul Karazhanov – writing – review & editing. Nicolae Spalatu – methodology, formal analysis, visualization, supervision, writing – review & editing. Vytautas Getautis – conceptualization, methodology, validation, writing – review & editing. Malle Krunks – conceptualization, methodology, validation, supervision, writing – review & editing. Ilona Oja Acik – conceptualization, funding acquisition, project administration, writing – review & editing.

## Conflicts of interest

There are no conflicts to declare.

## Acknowledgements

The “Development of Semi-Transparent Bifacial Thin Film Solar Cells for Innovative Applications” benefits from a 999372 € grant from Iceland, Liechtenstein and Norway through the EEA Grants. The aim of the project is to develop a new approach based on novel materials and structures and production technologies, which are the key to further increasing the share, and range of application of PV in areas with sub-average sunlight, including Baltic and Nordic countries. Therefore, development of resource saving, cost-effective and efficient PV devices is a primary challenge of this project. The project contract no. with the Research Council of Lithuania (LMTLT) is S-BMT-21-1 (LT08-2-LMT-K-01-003). Department of Materials and Environmental Technology, Tallinn University of Technology has received funding from the Estonian Research Council, projects



PRG627 “Antimony Chalcogenide Thin films for Next-Generation Semi-transparent Solar Cells Applicable in Electricity Producing Windows” and PSG689 “Bismuth Chalcogenide Thin-Film Disruptive Green Solar Technology for Next Generation Photovoltaics”. The research was partially funded by the European Union’s Horizon 2020 ERA Chair project 5GSOLAR (grant agreement no. 952509). The research was supported by the European Cooperation in Science and Technology (COST) project RENEW-PV (CA21148) and by the Estonian Ministry of Education and Research (project TK210; TK210U8 “Center of Excellence in Sustainable Green Hydrogen and Energy Technologies”). Institute of Solid-State Physics, University of Latvia has received funding from the European Union’s Horizon 2020 Framework Programme H2020-WIDESPREAD-01-2016-2017-TeamingPhase2 under grant agreement no. 739508, project CAMART<sup>2</sup>.

## Notes and references

- N. Cates and M. Bernechea, *APL Mater.*, 2018, **6**, 084503.
- S. Barthwal, R. Kumar and S. Pathak, *ACS Appl. Energy Mater.*, 2022, **5**, 6545–6585.
- M. Koltsov, S. V. Gopi, T. Raadik, J. Krustok, R. Josepson, R. Grzibovskis, A. Vembris and N. Spalatu, *Sol. Energy Mater. Sol. Cells*, 2023, **254**, 112292.
- C. Comparotto, P. Ström, O. Donzel-Gargand, T. Kubart and J. J. S. Scragg, *ACS Appl. Energy Mater.*, 2022, **5**, 6335–6343.
- S. Wang, Y. Zhao, B. Che, C. Li, X. Chen, R. Tang, J. Gong, X. Wang, G. Chen, T. Chen, J. Li and X. Xiao, *Adv. Mater.*, 2022, **34**, 2206242.
- Y. Zhao, S. Wang, C. Li, B. Che, X. Chen, H. Chen, R. Tang, X. Wang, G. Chen, T. Wang, J. Gong, T. Chen, X. Xiao and J. Li, *Energy Environ. Sci.*, 2022, **15**, 5118–5128.
- Y. Zhao, S. Wang, C. Jiang, C. Li, P. Xiao, R. Tang, J. Gong, G. Chen, T. Chen, J. Li and X. Xiao, *Adv. Energy Mater.*, 2022, **12**, 2103015.
- A. A. F. Husain, W. Z. W. Hasan, S. Shafie, M. N. Hamidon and S. S. Pandey, *Renewable Sustainable Energy Rev.*, 2018, **94**, 779–791.
- J. S. Eensalu, A. Katerski, E. Kärber, L. Weinhardt, M. Blum, C. Heske, W. Yang, I. Oja Acik and M. Krunk, *Beilstein J. Nanotechnol.*, 2019, **10**, 2396–2409.
- V. K. H. Bui and T. P. Nguyen, *Polymers*, 2023, **15**, 4443.
- E. Zimmermann, T. Pfadler, J. Kalb, J. A. Dorman, D. Sommer, G. Hahn, J. Weickert and L. Schmidt-Mende, *Adv. Sci.*, 2015, **2**, 1500059.
- M. S. You, C.-S. Lim, D. H. Kwon, J. H. Heo, S. H. Im and K. J. Chae, *Org. Electron.*, 2015, **21**, 155–159.
- J. S. Eensalu, A. Katerski, E. Kärber, I. Oja Acik, A. Mere and M. Krunk, *Beilstein J. Nanotechnol.*, 2019, **10**, 198–210.
- J. Chen, J. Qi, R. Liu, X. Zhu, Z. Wan, Q. Zhao, S. Tao, C. Dong, G. Y. Ashebir, W. Chen, R. Peng, F. Zhang, S. Yang, X. Tian and M. Wang, *Commun. Chem.*, 2019, **2**, 121.
- Y. Zhang, S. Li, R. Tang, X. Wang, C. Chen, W. Lian, C. Zhu and T. Chen, *Energy Technol.*, 2018, **6**, 2126–2131.
- Y. Yang, C. Shi, K. Lv, Q. Wang, X. Sun and W. Chen, *New J. Chem.*, 2021, **45**, 10357–10361.
- X. Jin, Y. Fang, T. Salim, M. Feng, Z. Yuan, S. Hadke, T. C. Sum and L. H. Wong, *Adv. Mater.*, 2021, **33**, 2104346.
- R. Tang, X. Wang, W. Lian, J. Huang, Q. Wei, M. Huang, Y. Yin, C. Jiang, S. Yang, G. Xing, S. Chen, C. Zhu, X. Hao, M. A. Green and T. Chen, *Nat. Energy*, 2020, **5**, 587–595.
- M. L. Petrus, T. Bein, T. J. Dingemans and P. Docampo, *J. Mater. Chem. A*, 2015, **3**, 12159–12162.
- N. Juneja, S. Mandati, A. Katerski, N. Spalatu, S. Daskeviciute-Geguziene, A. Vembris, S. Karazhanov, V. Getautis, M. Krunk and I. Oja Acik, *Sustainable Energy Fuels*, 2022, **6**, 3220–3229.
- N. Juneja, S. Daskeviciute-Geguziene, N. Spalatu, S. Mandati, A. Katerski, R. Grzibovskis, A. Vembris, S. Karazhanov, V. Getautis, M. Krunk and I. Oja Acik, *Mater. Sci. Semicond. Process.*, 2024, **169**, 107934.
- S. Mandati, N. Juneja, A. Katerski, A. Jegorovė, R. Grzibovskis, A. Vembris, T. Dedova, N. Spalatu, A. Magomedov, S. Karazhanov, V. Getautis, M. Krunk and I. Oja Acik, *ACS Appl. Energy Mater.*, 2023, **6**, 3822–3833.
- D. Poplavskyy and J. Nelson, *J. Appl. Phys.*, 2003, **93**, 341–346.
- S.-J. Moon, Y. Itzhaik, J.-H. Yum, S. M. Zakeeruddin, G. Hodes and M. Grätzel, *J. Phys. Chem. Lett.*, 2010, **1**, 1524–1527.
- S. Daskeviciute, C. Momblona, K. Rakstys, A. A. Sutanto, M. Daskeviciene, V. Jankauskas, A. Gruodis, G. Bubniene, V. Getautis and M. K. Nazeeruddin, *J. Mater. Chem. A*, 2021, **9**, 301–309.
- T. Malinauskas, D. Tomkute-Luksiene, R. Sens, M. Daskeviciene, R. Send, H. Wonneberger, V. Jankauskas, I. Bruder and V. Getautis, *ACS Appl. Mater. Interfaces*, 2015, **7**, 11107–11116.
- Y. Xiang, H. Guo, Z. Cai, C. Jiang, C. Zhu, Y. Wu, W.-H. Zhu and T. Chen, *Chem. Commun.*, 2022, **58**, 4787–4790.
- S. Xu, J. Wu, F. Guo, M. Wu, S. Chen, W. Chen and C. Shi, *Sustainable Energy Fuels*, 2023, **7**, 61–65.
- S. H. Im, C.-S. Lim, J. A. Chang, Y. H. Lee, N. Maiti, H.-J. Kim, M. K. Nazeeruddin, M. Grätzel and S. Il Seok, *Nano Lett.*, 2011, **11**, 4789–4793.
- M. J. Frisch, G. W. Trucks, H. B. Schlegel, G. E. Scuseria, M. A. Robb, J. R. Cheeseman, G. Scalmani, V. Barone, G. A. Petersson and H. Nakatsuji, *Gaussian 09, Revision A.02*, Gaussian Inc., Wallingford CT, 2016.
- M. V. Khenkin, E. A. Katz, A. Abate, G. Bardizza, J. J. Berry, C. Brabec, F. Brunetti, V. Bulović, Q. Burlingame, A. Di Carlo, R. Cheacharoen, Y.-B. Cheng, A. Colmann, S. Cros, K. Domanski, M. Duszka, C. J. Fell, S. R. Forrest, Y. Galagan, D. Di Girolamo, M. Grätzel, A. Hagfeldt, E. von Hauff, H. Hoppe, J. Kettle, H. Köbler, M. S. Leite, S. Liu, Y.-L. Loo, J. M. Luther, C.-Q. Ma, M. Madsen, M. Manca, M. Matheron, M. McGehee, R. Meitzner, M. K. Nazeeruddin, A. F. Nogueira, Ç. Odabaşı, A. Osherov, N.-G. Park, M. O. Reese, F. De Rossi, M. Saliba, U. S. Schubert, H. J. Snaith, S. D. Stranks, W. Tress, P. A. Troshin, V. Turkovic, S. Veestra, I. Visoly-Fisher, A. Walsh, T. Watson, H. Xie, R. Yildirim, S. M. Zakeeruddin, K. Zhu and M. Lira-Cantu, *Nat. Energy*, 2020, **5**, 35–49.



- 32 C. Jiang, J. Zhou, R. Tang, W. Lian, X. Wang, X. Lei, H. Zeng, C. Zhu, W. Tang and T. Chen, *Energy Environ. Sci.*, 2021, **14**, 359–364.
- 33 U. Würfel, M. Sefßler, M. Unmüssig, N. Hofmann, M. List, E. Mankel, T. Mayer, G. Reiter, J. Bubendorff, L. Simon and M. Kohlstädt, *Adv. Energy Mater.*, 2016, 1600594.
- 34 J. Kesters, T. Ghooos, H. Penxten, J. Drijkoningen, T. Vangerven, D. M. Lyons, B. Verreet, T. Aernouts, L. Lutsen, D. Vanderzande, J. Manca and W. Maes, *Adv. Energy Mater.*, 2013, **3**, 1180–1185.
- 35 F. A. Nüesch, *Chimia*, 2013, **67**, 388–392.
- 36 C. F. N. Marchiori and M. Koehler, *J. Phys. D Appl. Phys.*, 2014, **47**, 215104.
- 37 Y. Zhou, C. Fuentes-Hernandez, J. Shim, J. Meyer, A. J. Giordano, H. Li, P. Winget, T. Papadopoulos, H. Cheun, J. Kim, M. Fenoll, A. Dindar, W. Haske, E. Najafabadi, T. M. Khan, H. Sojoudi, S. Barlow, S. Graham, J.-L. Brédas, S. R. Marder, A. Kahn and B. Kippelen, *Science*, 2012, **336**, 327–332.





## Appendix 2

### Synthesis of fluorene-based compounds:

The synthesis of the fluorene-based compounds was performed by Prof. Vytautis Getautis' group in Kaunas University of Technology in Lithuania and the results are published in [140], I–IV. Fluorene-based compounds with aliphatic chains (V1275, V1235, V1236 and V1461) were synthesized with high yields and purity using a simple route (Fig. S1). V1275 was produced through a one-pot reaction of 2,7-diaminofluorene and 2,2-bis(4-methoxyphenyl)acetaldehyde with camphor sulfonic acid, under ambient conditions. Water, the only by-product, was removed using a Dean-Stark trap, streamlining the process and reducing reaction time. The method avoids the need for column chromatography or vacuum sublimation, minimizing batch variations. V1275 was further reacted with alkylating agents to yield the final compounds – V1235, V1236, and V1461 (Fig. S1).

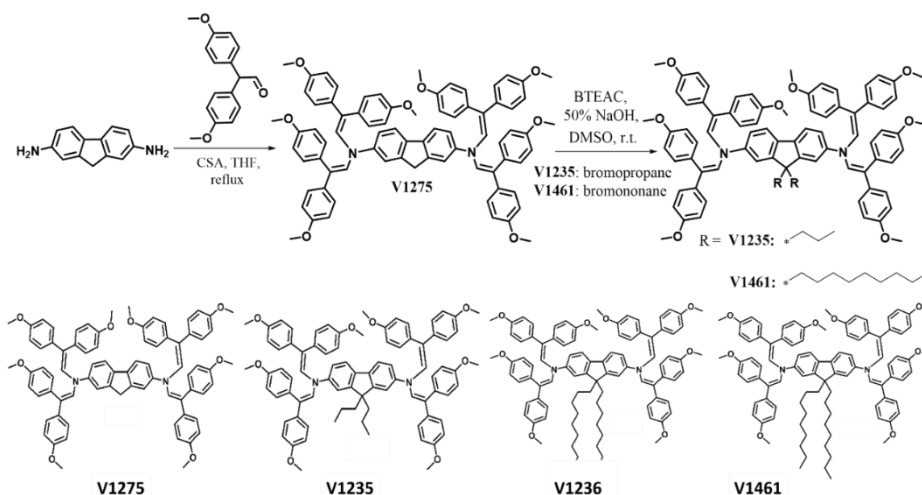


Figure S1. Synthesis route to fluorene-based molecules with aliphatic chains and their chemical structures – N2,N2,N7,N7-tetrakis[2,2-bis(4-methoxyphenyl)viny]-9H-fluorene-2,7-diamine (V1275), N2,N2,N7, N7-tetrakis[2,2-bis(4-methoxyphenyl)viny]-9,9-dipropyl-9H-fluorene-2,7-diamine (V1235), N2,N2,N7,N7-Tetrakis[2,2-bis(4-methoxyphenyl)viny]-9,9-dihexyl-9H-fluorene-2,7-diamine (V1236) and N2,N2,N7,N7-tetrakis[2,2-bis(4-methoxyphenyl)viny]-9,9-dinonyl-9H-fluorene-2,7-diamine (V1461).

Fluorene based compounds with thiophene end units (V808, V1385 and V1386) are synthesized through a simple two-step process (Fig. S2). V808 - the single thiophene unit-linked molecule has 4,4-dimethoxydiphenylamine chromophores symmetrically attached to both sides of the fluorene core, which can be easily chemically modified by the thiophene end group. V808 is produced through a straightforward synthesis and is devoid of complex starting materials with considerably good yields. Similarly, two and three thiophene units were added to the fluorene core, resulting in the synthesis of V1385 and V1386, respectively.

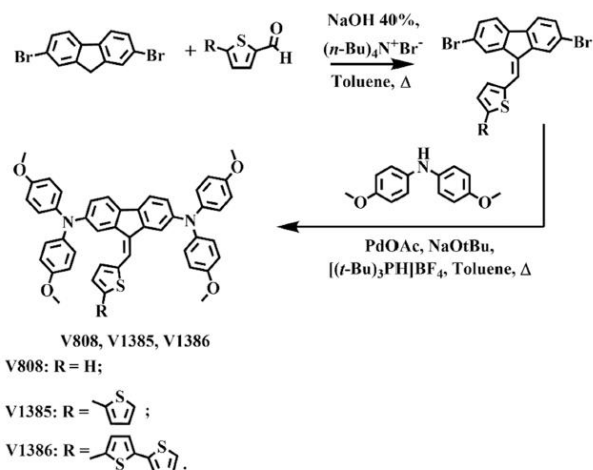


Figure S2. Synthesis route to fluorene-based molecules with thiophene end units and their chemical structures - *N*,*N*,*N*,*N*-tetrakis(4-methoxyphenyl)-9-(thiophen-2-ylmethylene)-9*H*-fluorene-2,7-diamine (V808), 9-([2,2':5',2''-terthiophen]-5-ylmethylene)-*N*,*N*,*N*,*N*-tetrakis(4-methoxyphenyl)-9*H*-fluorene-2,7-diamine (V1385), and 9-([2,2'-bithiophen]-5-ylmethylene)-*N*,*N*,*N*,*N*-tetrakis(4-methoxyphenyl)-9*H*-fluorene-2,7-diamine (V1386).

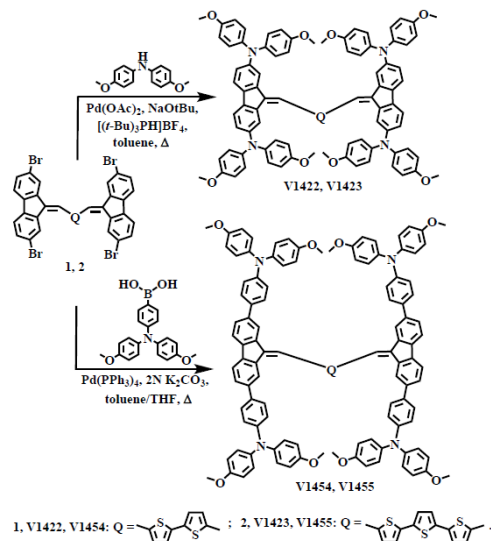


Figure S3. Synthesis route to fluorene-based molecules with dimers linked with thiophene units and their chemical structures - 9,9'-([2,2'-Bithiophene]-5,5'-diylbis(methanylylidene))bis[*N*,*N*,*N*,*N*-tetrakis(4-methoxyphenyl)-9*H*-fluorene-2,7-diamine] (V1422), 9,9'-([2,2':5',2''-Terthiophene]-5,5'-diylbis(methanylylidene))bis[*N*,*N*,*N*,*N*-tetrakis(4-methoxyphenyl)-9*H*-fluorene-2,7-diamine] (V1423), 4,4',4'',4'''-([2,2'-bithiophene]-5,5'-diylbis(methanylylidene))bis(9*H*-fluorene-2,7-diyl-9-ylidene)tetrakis(*N*, *N*-bis(4-methoxyphenyl)aniline) (V1454) and 4,4',4'',4'''-([2,2':5',2''-terthiophene]-5,5''-diylbis(methanylylidene))bis(9*H*-fluorene-2,7-diyl-9-ylidene)tetrakis(*N*, *N*-bis(4-methoxyphenyl)aniline) (V1455).

Fluorene-based HTMs with dimers linked with thiophene units V1422 and V1423 containing diphenylamine chromophores were obtained through palladium cross coupling reactions connecting the central dithiophene or trithiophene-based fluorenylidene-terminated unit with 4,4'-dimethoxydiphenylamine (Fig. S3). V1454 and V1455 with triphenylamine side fragments were obtained under Suzuki coupling reaction conditions. The properties of the studied fluorene-based compounds utilized as HTMs in Sb<sub>2</sub>S<sub>3</sub>-based solar cells are summarized in Table S1.

#### **Characterization of synthesized fluorene-based compounds**

The chemical composition of the synthesized compounds was analyzed using NMR and MS spectroscopy. <sup>1</sup>H NMR and <sup>13</sup>C NMR spectra were collected at 400 and 101 MHz, respectively on a Bruker Avance III spectrometer, with chemical shifts reported in ppm relative to tetramethylsilane (TMS) ([140], **I**, **II**, **III**). All experiments were conducted at 25 °C. Reaction progress was monitored via thin-layer chromatography using ALUGRAM SIL G/UV254 plates and developed with UV light. Silica gel (grade 9385, 230–400 mesh, 60 Å, Aldrich) was used for column chromatography. Elemental analysis was conducted using an Exeter Analytical CE-440 elemental analyzer (**I**, **III**). Thermogravimetric analysis (TGA) was carried out using a Q50 thermogravimetric analyzer (TA Instruments) at a heating rate of 10 °C/min under a nitrogen atmosphere, with decomposition temperatures reported at 5% weight loss (T<sub>d5</sub>). Differential scanning calorimetry (DSC) was performed on a TA Instruments Q2000 under a nitrogen atmosphere, with heating and cooling rates set to 10 °C/min. The hole drift mobility of the studied compounds was determined using the time-of-flight (ToF) method, where “sandwich” type samples (ITO/HTM/Al) were used (**I–IV**). UV-vis spectral analysis was done for synthesized compounds in solution (THF, 10<sup>-4</sup> mol L<sup>-1</sup>) using a PerkinElmer Lambda 35 UV/VIS spectrophotometer, with a solution layer thickness of 1 mm and a diffraction grating width of 2 nm (**II–IV**).

Table S1. Thermal, optical and electrical properties of the studied fluorene-based compounds utilized as HTMs in Sb<sub>2</sub>S<sub>3</sub>-based solar cells.

HTM group	HTM	T <sub>m</sub> [°C]	T <sub>c</sub> [°C]	T <sub>g</sub> [°C]	T <sub>dec</sub> [°C]	λ <sub>abs</sub> [nm]	μ <sub>0</sub> [cm <sup>2</sup> V <sup>-1</sup> s <sup>-1</sup> ]	I <sub>p</sub> [eV]	E <sub>g</sub> [eV]	HTM synthesis and characterization published in Ref.	Solar cell results incorporating HTMs published in Ref.
Fluorene-based compounds with aliphatic chains	V1275	255	-	150	403	262, 381, 401	1.20 x 10 <sup>-4</sup>	4.92	2.96	[142], III	III
	V1235	273	159	120	399	266, 382, 404	3.30 x 10 <sup>-4</sup>	4.80	2.96	[142], III	III
	V1236	173, 195	-	90	393	265, 383, 404	2.60 x 10 <sup>-4</sup>	5.00	2.80	[142]	I
	V1461	-	-	99	370	265, 382, 405	1.50 x 10 <sup>-4</sup>	4.94	2.98	III	III
Fluorene-based compounds with thiophene end units	V808	185	-	92	391	303, 386	7.07 x 10 <sup>-7</sup>	4.95	2.80	II	II
	V1385	-	-	97	403	299, 293, 438	2.15 x 10 <sup>-7</sup>	4.95	2.50	II	II
	V1386	-	-	99	398	293, 392, 449	3.68 x 10 <sup>-7</sup>	5.00	2.30	II	II
Fluorene based compounds with dimers linked with thiophene units	V1422	276	-	148	430	293, 383, 468	9.86 x 10 <sup>-7</sup>	4.94	1.87	IV	IV
	V1423	157	-	153	435	300, 383, 479	1.29 x 10 <sup>-6</sup>	4.94	1.90	IV	IV
	V1454	175, 307	229	175	445	285, 377, 467	3.38 x 10 <sup>-6</sup>	5.05	1.88	IV	IV
	V1455	-	-	172	444	286, 377, 480	1.85 x 10 <sup>-6</sup>	5.08	1.89	IV	IV

Melting (T<sub>m</sub>), crystallization (T<sub>c</sub>), glass transition (T<sub>g</sub>) and decomposition (T<sub>dec</sub>) temperatures observed from DSC and TGA, respectively (10 °C/min, N<sub>2</sub> atmosphere). Optical absorption (λ<sub>abs</sub>) peak positions in spectra as measured in THF solution (10<sup>-4</sup> M). Hole drift mobility (μ<sub>0</sub>) value at zero field strength. Ionization potential (I<sub>p</sub>) of HTM films deposited on glass/FTO substrate was measured using PYS technique. The bandgap (E<sub>g</sub>) of the HTM films was estimated from the absorption spectra using the Tauc plots.

# Curriculum vitae

## Personal data

Name: Nimish Juneja  
Date of birth: 07.03.1991  
Place of birth: Kanpur, India  
Citizenship: Indian

## Contact data

E-mail: nimish.juneja@taltech.ee

## Education

2020–2024 Tallinn University of Technology, Estonia, Materials and Environmental Technology – PhD  
2016–2019 University of Freiburg, Germany, Sustainable Systems and Engineering – MSc  
2010–2014 Sardar Vallabhbhai National Institute of Technology, India, Electrical Engineering – B. Tech  
2004–2009 Dr. Virendra Swarup 21<sup>st</sup> Century School, India

## Language competence

Hindi native speaker  
English fluent  
German intermediate

## Professional employment

2014–2015 Signode India, Engineer

## Defended dissertations

Master's Degree, 2019, Development of transparent conductive oxide films for passivating contacts, University of Freiburg and Fraunhofer ISE, Freiburg, Germany. Supervisors: Dr. Stefan Glunz; Dr. Jürgen Wöllenstein

## Involvement in research projects

PRG627 "Antimony chalcogenide thin films for next-generation semi-transparent solar cells applicable in electricity producing windows (01.01.2020–31.12.2024)", Founder: Estonian Research Council.

ETAG21014 "Development of semi-transparent bifacial thin film solar cells for innovative applications (01.01.2021–31.12.2023)", Founder: Research Council of Lithuania.

TK210U8 "Center of Excellence in Sustainable Green Hydrogen and Energy Technologies GREENTECH (01.01.2024–31.12.2030)", Founder: Ministry of Education and Research.

CA21148 "Research and International Networking on Emerging Inorganic Chalcogenides for Photovoltaics (06.10.2022–05.10.2026)", Founder: European Commission.

## Participation in conferences

2021 Attendance with an oral presentation at "International School on Hybrid, Organic and Perovskite Photovoltaics (HOPE-PV 2021)", November 25-27, Virtual  
2021 Attendance with a poster presentation at "European Materials Research Society (E-MRS), Fall Meeting", September 20-23, Virtual  
2022 Attendance with an oral presentation at "European Materials Research Society (E-MRS), Fall Meeting", September 19-22, Poland, Warsaw

- 2022 Attendance with a poster presentation at “Graduate School of Functional Materials and Technologies (GSFMT) Scientific Conference”, May 17-18, Tartu, Estonia
- 2023 Attendance with an oral presentation at “Quantsol Summer School”, March 19-24, Rauris, Austria
- 2023 Attendance with a poster presentation at “Graduate School of Functional Materials and Technologies (GSFMT) scientific conference”, May 23-24, Tallinn, Estonia
- 2023 Attendance with a poster presentation at “ReNewPV Workshop”, June 15-16, Tallinn, Estonia

### Supervised dissertations

Mohammad Kadkhodaei, Master’s Degree, 2023, (sup) **Nimish Juneja**; Sajeesh Vadakkedath Gopi,  $\text{Sb}_2\text{S}_3$  thin film solar cell for semi-transparent applications, Tallinn University of Technology, School of Engineering, Department of Materials and Environmental Technology.

### List of publications

**Nimish Juneja**, Aistē Jegorovē, Raitis Grzibovskis, Atanas Katerski, Maryte Daskeviciene, Tadas Malinauskas, Aivars Vembris, Smagul Karazhanov, Nicolae Spalatu, Vytautas Getautis, Malle Krunks and Ilona Oja Acik, “Dopant-free fluorene based dimers linked with thiophene units as prospective hole transport materials for  $\text{Sb}_2\text{S}_3$  solar cells”, Sustainable Energy and Fuels, 8, 4324-4334, 2024, doi: 10.1039/D4SE00472H.

**Nimish Juneja**, Šarūnē Daškevičiūtē-Gegužienē, Nicolae Spalatu, Sreekanth Mandati, Atanas Katerski, Raitis Grzibovskis, Aivars Vembris, Smagul Karazhanov, Vytautas Getautis, Malle Krunks, and Ilona Oja Acik, “Employment of dopant-free fluorene-based enamines as innovative hole transport materials to boost the transparency and performance of  $\text{Sb}_2\text{S}_3$  based solar cells”, Materials Science in Semiconductor Processing, 169, 107934, 2024, doi: 10.1016/j.mssp.2023.107934.

Sreekanth Mandati, **Nimish Juneja**, Atanas Katerski, Aistē Jegorovē, Raitis Grzibovskis, Aivars Vembris, Tatjana Dedova, Nicolae Spalatu, Artiom Magomedov, Smagul Karazhanov, Vytautas Getautis, Malle Krunks, and Ilona Oja Acik, “4.9 % efficient  $\text{Sb}_2\text{S}_3$  solar cells from semitransparent absorbers with fluorene-based thiophene-terminated hole conductors”, ACS Applied Energy Materials, 6, 3822-33, 2023, doi: 10.1021/acsaem.2c04097.

Sreekanth Mandati, **Nimish Juneja**, Atanas Katerski, Aistē Jegorovē, Sarune Daskeviciute-Geguziene, Raitis Grzibovskis, Aivars Vembris, Nicolae Spalatu, Artiom Magomedov, Smagul Karazhanov, Vytautas Getautis, Malle Krunks, and Ilona Oja Acik, “Cost-effective fluorene and thiophene containing hole conductors towards semi-transparent  $\text{Sb}_2\text{S}_3$  absorber-based solar cells”, 8th World Conference on Photovoltaic Energy Conversion, 470-473, 2022, doi: 10.4229/WCPEC-82022-2BV.2.70.

**Nimish Juneja**, Sreekanth Mandati, Atanas Katerski, Nicolae Spalatu, Šarūnē Daškevičiūtē-Gegužienē, Aivars Vembris, Smagul Karazhanov, Vytautas Getautis, Malle Krunks, and Ilona Oja Açik, “ $\text{Sb}_2\text{S}_3$  solar cells with a cost-effective and dopant-free fluorene-based enamine as a hole transport material”, Sustainable Energy and Fuels 6, 13, 3220-29, 2022, doi: 10.1039/d2se00356b.

**Nimish Juneja**, Leonard Tutsch, Frank Feldmann, Andreas Fischer, Martin Bivour, Anamaria Moldovan, Martin Hermle, “Effect of hydrogen addition on bulk properties of sputtered indium tin oxide thin films”, AIP Conference Proceedings, 2147, 2019, doi: 10.1063/1.5123835.

# Elulookirjeldus

## Isikuandmed

Nimi: Nimish Juneja  
Sünniaeg: 07.03.1991  
Sünnikoht: Kanpur, India  
Kodakondsus: India

## Kontaktandmed

E-mail: nimish.juneja@taltech.ee

## Hariduskäik

2020–2024 Tallinna Tehnikaülikool, Eesti, Materjali- ja keskkonnatehnoloogia instituut – PhD  
2016–2019 Freiburg Ülikool, Saksamaa, säästvad süsteemid ja tehnika – MSc  
2010–2014 Sardar Vallabhbhai riiklik tehnoloogiainstituut, India, Elektrotehnika – B. Tech  
2004–2009 Dr Virendra Swarupi 21. sajandi kool, India

## Language competence

Hindi keel emakeel  
Inglise keel kõrgtase  
Saksa keel kesktase

## Teenistuskäik

2014–2015 Signode India, Insener

## Kaitstud väitekirjad

Magistrikraad, 2019, Läbipaistvate juhtivate oksiidkilede väljatöötamine kontaktide passiveerimiseks, Freiburg Ülikool ja Fraunhofer ISE, Freiburg, Saksamaa. Juhendajad: Dr. Stefan Glunz; Dr. Jürgen Wöllenstein

## Teadusprojektid

PRG627 “Antimoni kalkogeniidi õhukesed kiled järgmise põlvkonna poolläbipaistvatele päikesepatareidele, mida kasutatakse elektrit tootvates akendes (01.01.2020–31.12.2024)”, Asutaja: Eesti Teadusnõukogu.

ETAG21014 “Poolläbipaistvate bifacial õhukese kilega päikesepatareide arendamine uuenduslikeks rakendusteks (01.01.2021–31.12.2023)”, asutaja: Leedu teadusnõukogu.

TK210U8 “Säästvate roheliste vesiniku- ja energiatehnoloogiate tippkeskus GREENTECH (01.01.2024–31.12.2030)”, asutaja: Haridus- ja Teadusministeerium.

CA21148 “Research and International Networking on Emerging Inorganic Chalcogenides for Photovoltaics (06.10.2022–05.10.2026)”, Founder: European Commission.

CA21148 “Research and International Networking on Emerging Inorganic Chalcogenides for Photovoltaics (06.10.2022–05.10.2026)”, Asutaja: Euroopa Komisjon.

## Osalemise konverentsidel

2021 Osalemise suulise ettekandega “International School on Hybrid, Organic and Perovskite Photovoltaics (HOPE-PV 2021)”, 25.-27.11, Virtuaal

2021 Osalemise stendiettekandega “European Materials Research Society (E-MRS)”, Sügiskohtumine, 20.-23. september, Virtuaal

- 2022 Osalemine stendiettekandega „Funktsionaalsete materjalide ja tehnoloogiate kõrgkooli (GSFMT) teaduskonverentsil”, 17-18 mai, Tartu, Eesti
- 2023 Osalemine suulise ettekandega “Quantsoli suvekoolis”, 19-24 märts Rauris, Austria
- 2023 Osalemine stendiettekandega “Funktsionaalsete materjalide ja tehnoloogiate kõrgkooli (GSFMT) teaduskonverentsil”, 23.-24.mai Tallinn, Eesti
- 2023 Osalemine stendiettekandega “ReNewPV Workshopis”, juuni 15-16, Tallinn, Estonia

### Juhendatud lõputööd

Mohammad Kadkhodaei, magistrikraad, 2023, (sup) **Nimish Juneja**; Sajeesh Vadakkedath Gopi,  $Sb_2S_3$  õhukese kilega päikesepatarei poolläbipaistvatele rakendustele, Tallinna Tehnikaülikool, Inseneriteaduskond, Materjali- ja keskkonnatehnoloogia instituut.

### Teaduspublikatsioonid

**Nimish Juneja**, Aisté Jegorovè, Raitis Grzibovskis, Atanas Katerski, Maryte Daskeviciene, Tadas Malinauskas, Aivars Vembris, Smagul Karazhanov, Nicolae Spalatu, Vytautas Getautis, Malle Krunks and Ilona Oja Acik, “Dopant-free fluorene based dimers linked with thiophene units as prospective hole transport materials for  $Sb_2S_3$  solar cells”, Sustainable Energy and Fuels, 8, 4324-4334, 2024, doi: 10.1039/D4SE00472H.

**Nimish Juneja**, Šarūnė Daškevičiūtė-Gegužienė, Nicolae Spalatu, Sreekanth Mandati, Atanas Katerski, Raitis Grzibovskis, Aivars Vembris, Smagul Karazhanov, Vytautas Getautis, Malle Krunks, and Ilona Oja Acik, “Employment of dopant-free fluorene-based enamines as innovative hole transport materials to boost the transparency and performance of  $Sb_2S_3$  based solar cells”, Materials Science in Semiconductor Processing, 169, 107934, 2024, doi: 10.1016/j.mssp.2023.107934.

Sreekanth Mandati, **Nimish Juneja**, Atanas Katerski, Aisté Jegorovè, Raitis Grzibovskis, Aivars Vembris, Tatjana Dedova, Nicolae Spalatu, Artiom Magomedov, Smagul Karazhanov, Vytautas Getautis, Malle Krunks, and Ilona Oja Acik, “4.9 % efficient  $Sb_2S_3$  solar cells from semitransparent absorbers with fluorene-based thiophene-terminated hole conductors”, ACS Applied Energy Materials, 6, 3822-33, 2023, doi: 10.1021/acsaem.2c04097.

Sreekanth Mandati, **Nimish Juneja**, Atanas Katerski, Aisté Jegorovè, Sarune Daskeviciute-Gegužiene, Raitis Grzibovskis, Aivars Vembris, Nicolae Spalatu, Artiom Magomedov, Smagul Karazhanov, Vytautas Getautis, Malle Krunks, and Ilona Oja Acik, “Cost-effective fluorene and thiophene containing hole conductors towards semi-transparent  $Sb_2S_3$  absorber-based solar cells”, 8th World Conference on Photovoltaic Energy Conversion, 470-473, 2022, doi: 10.4229/WCPEC-82022-2BV.2.70.

**Nimish Juneja**, Sreekanth Mandati, Atanas Katerski, Nicolae Spalatu, Šarūnė Daškevičiūtė-Gegužienė, Aivars Vembris, Smagul Karazhanov, Vytautas Getautis, Malle Krunks, and Ilona Oja Açik, “ $Sb_2S_3$  solar cells with a cost-effective and dopant-free fluorene-based enamine as a hole transport material”, Sustainable Energy and Fuels 6, 13, 3220-29, 2022, doi: 10.1039/d2se00356b.

**Nimish Juneja**, Leonard Tutsch, Frank Feldmann, Andreas Fischer, Martin Bivour, Anamaria Moldovan, Martin Hermle, “Effect of hydrogen addition on bulk properties of sputtered indium tin oxide thin films”, AIP Conference Proceedings, 2147, 2019, doi: 10.1063/1.5123835.

ISSN 2585-6901 (PDF)  
ISBN 978-9916-80-228-1 (PDF)